

# Structure and properties of rare earth metaphosphate glasses

Brennan, Tessa

*Award date:*
1998

*Awarding institution:*
University of Bath

# Structure and Properties of Rare Earth Metaphosphate Glasses

Submitted by

**TESSA BRENNAN**

for the degree of PhD of the University of Bath

1998



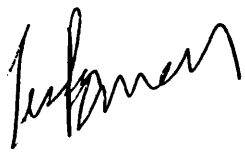





ProQuest LLC
789 East Eisenhower Parkway
P.O. Box 1346
Ann Arbor, MI 48106-1346

Your whole life is on the other side of the glass. And there is nobody watching.
A. Bennet

# ACKNOWLEDGEMENTS

Initially I would like to thank my supervisor Professor G. A. Saunders for his guidance and enthusiasm in the subject. I would also like to acknowledge Dr Jonathan Knight for acting as a sounding board during my optical studies, and allowing me to use his 'trusty' cleaving tile. Throughout my time at Bath University I have very been fortunate to work with some of our many collaborators. They have all been kind enough to share their expertise, time, and friendship. Thanks to the scattering group at The University of Kent at Canterbury led by Professor R. J. Newport, I would especially like to mention Ruth Anderson, Dr Jacqui Cole, Dr Gavin Mountjoy and Dr Daniel Bowron; they almost made the night shift at Daresbury fun! I would also like to thank Professor B. Rainford at the University of Southampton for allowing me to pick his brains on all things neutrons. I am indebted to the technical support I have received both at the University of Bath, Wendy Lambson, Eddy Lambson, Bob Draper, and Hugh Perrot, what they couldn't polish, fix, or make wasn't worth knowing; and the station masters at Rutherford and Daresbury Laboratories, Roger Ecclestone, Ron Smith, Graham Bushnell-Wye, and Laurie Murphy. There are several people on level five who more than deserve a mention, they have shared their knowledge with me, thanks Huijin for helping me get to grips with the subtleties of the ultrasonics equipment and to Mark and Owen for solving my numerous computing problems; more importantly though I would like to thank them for being mates, the best. This acknowledgements would not be complete without thanking Mum, Dad and Zoe. They have all contributed to my mental stability and have always offered me an ear to bend when things didn't quite go to plan; I'm sure this kind of support wasn't in their job description! Finally I would like to thank Bob for my BMX.

Everyone, Thanks!

# ABSTRACT

Metaphosphate glasses doped with rare earth ions $(R_2O_3)_{0.25}(P_2O_5)_{0.75}$ (REMGs) have been manufactured. X-ray diffraction and EXAFS have been used to determine the local structure. The x-ray scattering experiments have verified that the REMGs are constructed from a three-dimensional network of corner linked tetrahedra, with an average P-O, R-O and O-(P-)O correlation distance of 1.55Å, 2.31Å, and 2.57Å respectively. The EXAFS experiments were measured at 293K, 145K, and 79K to examine if there was any change in the short range structure with temperature; no significant change was found. The R-O distances were consistent with a co-ordination number of six and a valence of 3+. Lanthanide contraction was observed with increasing atomic number using both techniques. Inelastic magnetic neutron scattering experiments have been completed to examine the magnetic low lying energy levels in REMGs; a significant amount structure due to crystal field splitting was recorded. The potential of a new neutron scattering technique which can be used to examine the R-R correlation distance in REMGs has been examined, using $(Tb_2O_3)_{0.247}(P_2O_5)_{0.753}$. The elastic properties of ternary samarium lanthanum metaphosphate glass, as a function of temperature and pressure, have been measured using ultrasonics. The normal mode behaviour of lanthanum is found to negate the acoustic mode softening displayed by samarium metaphosphate glass. The acoustic mode Grüneisen parameters of $Sm^{3+}$ and $La^{3+}$ REMGs have been used to separate the long wavelength acoustic mode contribution to the thermal expansion from ones arising from the higher energy phonon states. The 'excess' modes provide negative contributions to the thermal expansion and the elastic modulus pressure derivatives. The fluorescence and absorption of a series of REMGs have been recorded and transitions assigned to the peaks. The effect of concentration quenching has been measured in $Nd^{3+}$ doped metaphosphate glasses; the number of ions which correspond to a halving of the fluorescence lifetime is $5.8\times10^{20}$ions $cm^{-3}$. A silica clad fibre of $(Nd_2O_3)_{0.010}(La_2O_3)_{0.260}(P_2O_5)_{0.730}$ has been pulled from a bulk sample (core diameter of 58.6μm). A number of basic experiments have been made to characterise the optical properties of the fibre.

# CONTENTS

# CHAPTER ONE

## INTRODUCTION

Glasses doped with rare earth elements have received increasing attention due to their potential in the fabrication of novel optoelectronic devices. However phosphate glasses have not developed at the same rate as silicate systems due to the fact that they can have a low resistance to moisture contamination, which would have an adverse effect in their practical employment. The development of phosphate glasses in the vicinity of metaphosphate, $(R_2O_3)_x(P_2O_5)_{1-x}$ (where R represents one of the rare earth elements, Ce, Pr, Nd, Sm, Eu, Gd, Tb, Dy, Ho, Er, Tm, Yb, and x is the mole fraction $\cong 0.25$), has revived interest. The rare earth elements are incorporated into the host material in relatively large modifier concentrations compared with the low dopant levels usually employed in devices; the resulting glasses exhibit stability to water as well as interesting acoustic, optical, and magnetic properties.

Amorphous materials exhibit features which are fundamentally different to those found in corresponding crystals. In crystalline materials the atoms occupy well defined positions and hence show a periodic arrangement. In contrast, the structure of amorphous materials has no long range transitional order, and is therefore characterised in terms of short and medium range order; which in turn is defined by nearest neighbour co-ordination, average bond length and angle. Debye theory assumes that a monatomic lattice may be regarded as an isotropic elastic continuum with no dispersion of wave propagation (Kelly and MacDonald 1953 and references therein, Kittel 1986, Hook and Hall 1994). This model has been successful in describing the lattice dynamics of a crystalline materials; furthermore in amorphous materials the acoustic phonons, in the long wavelength limit, can be considered to be Debye-like. The topological disorder, universal to all materials in the vitreous state,

introduces additional low energy 'excess' vibrational modes, which coexist and interact with the Debye-like phonons (Carini et al 1995a). The wide distribution of 'excess' modes is believed to be responsible for the characteristic anomalies present in the thermal, elastic and optical properties (sections 1.1) and has been described using the two level system and its extension the soft potential model (section 2.4).

The samples studied here are not strictly of the metaphosphate $R(PO_3)_3$ stoichiometry; however a structure in the region of metaphosphate appears to represent a stable form; the glasses exist in a range of composition close to $(R_2O_3)_{0.25}(P_2O_5)_{0.75}$, regardless of the starting quantities (mol%) of the constituent powders: phosphorus pentoxide and rare earth oxide (chapter three, Senin 1994). For ease, these amorphous materials are referred to as rare earth metaphosphate glasses (REMGs).

This chapter is divided into two sections. The first summarises the results obtained from previous experiments on the structure and properties of rare earth metaphosphate glasses. This brief overview of the subject is required to explain both the motivation behind this thesis and the starting point of its investigations. In section 1.2 a research overview, including details on chapter organisation, is presented.

## 1.1. STRUCTURE AND PROPERTIES OF RARE EARTH METAPHOSPHATE GLASSES

If the nature of glasses, in particular rare earth metaphosphate glasses, are to be fully understood, information must be collected on the atomic structure and the fundamental properties of these materials. Rare earth metaphosphate glasses exhibit a plethora of unusual properties. If these diverse properties are to be exploited in the production of novel optical and magneto-optical devices, detailed information on the structure and characteristics is essential.

### 1.1.1. STRUCTURE OF REMGs

There have been a number of short range structural investigations of rare earth metaphosphate glasses at room temperature using the complementary probes of x-ray diffraction, EXAFS (Bowron et al. 1994, 1996a, b) and neutron scattering (Hoppe et al. 1998a, b). These investigations have shown that the structure of rare earth doped

glasses in the vicinity of metaphosphate is based on a skeleton of linked $PO_4$ sharing one corner. One of the four oxygen atoms in a $PO_4$ tetrahedron is doubly bonded to the phosphorus and consequently it does not take part in the network bonding. The trivalent rare earth ions occupy sites inside the skeleton of linked $PO_4$ tetrahedra; each ion is surrounded by a nearest neighbour shell of oxygen atoms with average co-ordination number N between 6 and 8, an R-O distance of 2.25-2.40Å (following the lanthanide contraction, figure 2.7) and an average R-P bond length of approximately 2.90Å. The oxygen and phosphorus atoms are separated by 1.60Å; Hoppe et al. (1998a) used pulsed neutron scattering to study vitreous $P_2O_5$, and found that the P-O bond length for bridging atoms is larger than the non-bridging oxygen atoms. A rare earth - rare earth correlation distance has not been observed within the limits of the EXAFS technique; however the La-La distance in $LaP_3O_9$ glass has been measured (6.4Å) by Hoppe et al. (1998b) using x-ray diffraction. The structural observations are consistent with the rare earth ion environment in glass being similar to that of rare earth metaphosphate crystals (Hong 1974a, 1974b, and Matuszewski 1988). In these crystals the rare earth ions are co-ordinated to non-bridging oxygen atoms from the phosphate network, and the co-ordination number varies from 6 to 8 depending on the size of the rare earth ion.

### 1.1.2 OPTICAL PROPERTIES OF REMGs

Incorporation of rare earth ion modifiers into a glass network produces the energy level structure necessary for the manufacture of non-linear magneto-optical devices such as magnetically tuneable lasers and amplifiers for the telecommunication industry. The host material modifies the lanthanide ions' energy levels and therefore its optical properties, in two ways:

1) Crystal fields effect. The surrounding atoms act as sources of negative charge, and consequently lifts the degeneracy of the energy levels (section 2.5). The crystal field levels in a glass are much broader than in a crystal, due to the atomic disorder associated with amorphous materials, which means that each rare earth ion is situated in a slightly different environment.

2) Broadening of the energy levels. The two main mechanisms acting are the temperature dependent homogeneous phonon broadening, which produces a spread in

the energy of the emitted photons, and the inhomogeneous perturbations of the energy levels by the crystal field.

The optical spectra of the rare earth ions are mainly determined by electric and magnetic dipole transitions between states of the ground $f^n$ electronic configuration. In the rare earth ions the 4f electrons are partially shielded from perturbations by the external fields due to the presence of the 5s and 5p shells. However altering the environment of the rare earth ion does, to a certain extent, produce changes in the spectra. Phosphates have emerged with silicates as the principal glasses used for lasers and all of the lanthanides, except $Ce^{3+}$, $Eu^{3+}$, $Dy^{3+}$, have been reported to lase in a glass host. Neodymium has attracted the most attention due to the fact that it was the first rare earth element used in a glass laser in 1961, as well as having efficient pumping and operation at ambient temperatures (Rapp 1987, Hall and Weber 1991). The absorption and fluorescence spectra of rare earth metaphosphate glasses doped with samarium, europium and holmium have been measured by Farok et al (1992, 1994,1996 and to be published). These REMGs exhibit strong electronic absorption and fluorescence in the visible and infrared region. An effect of the alexandrite type has been observed in holmium metaphosphate glass: its perceived colour changes when this glass is viewed in different light sources (Farok et al. 1996). Samarium, and europium ions can be incorporated into host materials as either divalent or trivalent ions; they were both found to exist in binary metaphosphate glass with a valency of three.

### 1.1.3. ELASTIC PROPERTIES OF REMGs

Elastic properties are an important yet complex characteristic of an amorphous material. Vibrational properties in the long wavelength limit have been investigated using the techniques of ultrasonics to measure wave velocity and attenuation as a function of temperature. Ultrasonic velocity (longitudinal $v_L$ and shear $v_S$) measurements can be used to calculate the second order elastic stiffness tensor components (SOEC) $C_{IJ}$. For an isotropic material, such as glass, only two independent quantities $C_{11}$ ($\rho v_L^2$) and $C_{44}$ ($\rho v_S^2$) have to be considered. The elastic stiffness is related to the inter atomic binding forces, which determine long range attraction and short range repulsion. For materials exhibiting vibrational

anharmonicity the ultrasonic wave velocity (and consequently the SOEC) are expected to increase linearly with decreasing temperature, and at low temperatures the slope is expected to tend to zero. For all of the REMGs previously measured there is a continuous increase in the longitudinal and shear modes velocities, with a progressively increasing slope, as the temperature is lowered below approximately 150K (Senin et al. 1993a,b, 1994a,b, Farok et al. 1994, Saunders et al. 1994). This anomalous trend of a continuous increase in long wavelength mode velocity is governed by a combination of three contributions (Phillips 1981, Ilisavskii et al. 1989, Tielbürger et al. 1992, Carini et al. 1994,1995a, Sidek et al. 1998): at high temperatures the anharmonic term, at low temperatures an interaction between the acoustic phonons and the two level system (TLS) (section 2.4.1) and phonon scattering from soft anharmonic localised vibrational modes, described by the soft potential model (section 2.4.2). The temperature dependence of the ultrasonic wave attenuation in REMGs exhibits a broad peak centred at 75-100K. This peak is considered to originate from the same mechanism which governs the low temperature acoustic velocity, namely thermally activated relaxation of localised structural defects (Anderson and Bömmel 1955, Carini et. al 1988, 1990, 1994, Tielbürger et al 1992, Senin 1994, Sidek et al 1998).

By making ultrasonic velocity measurements under an applied pressure the hydrostatic pressure dependences of the SOEC and bulk modulus can be calculated. The Grüneisen parameters, $\gamma_L$ and $\gamma_S$ can be found from the SOEC and hydrostatic pressure derivatives. These represent the volume dependence of the long wavelength acoustic mode frequency $\omega$ i.e. $\omega = V^{\gamma}$, and are a measure of the strength of the associated vibrational anhamonicity. Properties, which depend on atomic thermal motion such as thermal expansion and non-linear acoustic properties, are governed by the anharmonicity of the vibrational states. The elastic behaviour of glasses under pressure can be divided into two main categories. In the majority of glasses ($As_2S_3$, $TeO_2$, chalcogencide, and fluorozirconate) the second order elastic constants and their pressure derivatives $(\partial C_{44}/\partial P)_{T,P=0}$, $(\partial C_{11}/\partial P)_{T,P=0}$ and $(\partial B/\partial P)_{T,P=0}$, are positive; this is termed normal behaviour. In contrast the nonlinear acoustic properties of silica and $BeF_2$ are anomalous; the temperature derivative of the bulk, longitudinal and shear moduli can be positive while the pressure derivatives and consequently the Grüneisen

parameters can be negative i.e. with increasing pressure the sample becomes easier to squeeze (Sidek et al. 1998 and refs. therein). Many of the glasses that show acoustic mode softening have structures based on tetrahedral units. A soft mode can be defined as a vibration whose frequency vanishes at a particular, finite, temperature. At this temperature the mode is time independent, and exhibits a permanent displacement; the modes become frozen in (Hooke and Hall 1994). Senin et al. (1994b) measured the hydrostatic pressure dependency of two lanthanum metaphosphate glass samples, $(La_2O_3)_{0.222}(P_2O_5)_{0.778}$ and $(La_2O_3)_{0.263}(P_2O_5)_{0.737}$, at room temperature. They found that the SOEC and hydrostatic pressure derivatives were positive for both the longitudinal and shear modes; however the shear mode Grüneisen parameter $\gamma_S$ was slightly negative. Phosphate glasses doped with Ce, Pr, Nd and Gd display intermediate behaviour (Senin et al. 1993a, 1994c), with $(\partial C_{ij}/\partial P)_{T,P=0}$ being small and either negative or positive. Previous ultrasonic studies on samarium and europium metaphosphate glasses has shown that these tetrahedrally bonded glasses have decreasing longitudinal and shear velocity with the application of pressure (Farok et al. 1994, Mierzejewski et al. 1988a, Carini et al. 1990, Senin et al. 1993b); under pressure the acoustic modes soften rather than stiffen. This softening is accompanied by negative SOEC, pressure derivatives and Grüneisen parameters $\gamma_L$ and $\gamma_S$ in the long wavelength limit. The physical microscopic origin of the anomalies is unknown. However it has been postulated by Sidek et al. (1998) that the force require to move two adjacent tetrahedra about the shared oxygen atom ($\phi$, $\theta$) is approximately two orders of magnitude smaller than the finite stiffness of a semi-rigid tetrahedral unit. Consequently as the sample is pressurised the corner linked tetrahedra will tend to move into regions of "free space" within the glassy matrix, resulting in an overall decrease in the volume and a subsequent reduction in the elastic stiffness. The extent to which there is a decrease in volume, and associated elastic constants, will be limited by the stearic hindrance between oxygen atoms on neighbouring tetrahedra, and the size of the dopant ions.

### 1.1.4. THERMAL PROPERTIES OF REMGs

All amorphous materials display characteristics in the low temperature specific heat and thermal conductivity measurements which are not present in corresponding crystalline structures. A comprehensive review of these anomalies has been edited by Phillips (1981).

In crystals the thermal conductivity increases as the temperature decreases to approximately 10K; this is the result of a reduction in scattering from the anharmonic Umklapp processes. A maximum is reached when the phonon mean free path becomes comparable to the dimensions of the sample ($K=C_v vl/3$, where K is the thermal conductivity, $C_v$ is the specific heat of the plane lattice waves with the Debye sound velocity $v$ and $l$ is the mean free path (Zeller and Pohl 1971)). If the temperature is reduced still further the thermal conductivity decreases due to increased scattering from the surface (see figure 1.1). In comparison a non-crystalline material has a much lower thermal conductivity, which reduces with decreasing temperature, suggesting that the phonon free path is much shorter in glasses than in crystals. The shape of the curve depends on the structure and not the composition of the sample, and displays a plateau of almost constant conductivity at approximately 10K. In a vitreous material phonons are scattered from the random network, as the atoms are seen as impurities, either vacancies or interstitials. Below 1K the thermal conduction changes less rapidly than it's crystalline counterpart (the mean free path varies as approximately $T^2$) (figure 1.1a); this is because a different scattering mechanism has become dominant at these temperatures. The soft potential model attributes the behaviour of the thermal conductivity below 10K to the presence of 'excess' localised modes which scatter thermal phonons. Jagannathan and Orbach (1990) suggested that the plateau defines a crossover in the density of states from extended to localised vibrational modes (see section 2.4.2). These localised states also contribute to the specific heat.

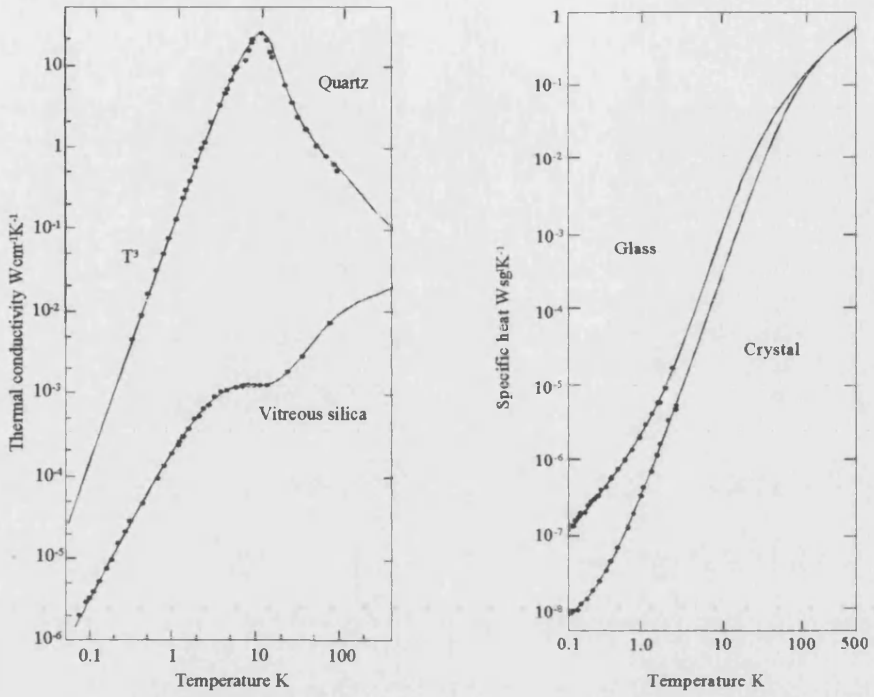


a) b)

Figure 1.1. The a) the thermal conductivity and b) the specific heat of vitreous and crystalline $SiO_2$ (after Zeller and Pohl 1971)

Comparing the specific heat data of crystalline and vitreous $SiO_2$ collected by Zeller and Pohl (1971) it can be seen, in figure 1.1b, that below 1K the specific heat capacity ($C_P$) of an amorphous material varies approximately linearly with temperature and therefore exceeds the predictions based on Debye theory. At elevated temperatures (T>10K) $C_P$ also rises more rapidly in glasses than the $T^3$ calculated using the Debye model; vitreous samples exhibit an excess contribution to the specific heat which can clearly be seen in plots of $C_P/T^3$ against T, where the experimental deviation from the theoretical model is characterised by a peak centred at about 11K (figure 1.2). This feature occurs at approximately the same temperature as the plateau in the thermal conductivity, and corresponds to the broad maximum in the total density of states (the boson peak) caused by the existence of 'excess' low energy vibrational states, which become significant at lower temperatures.

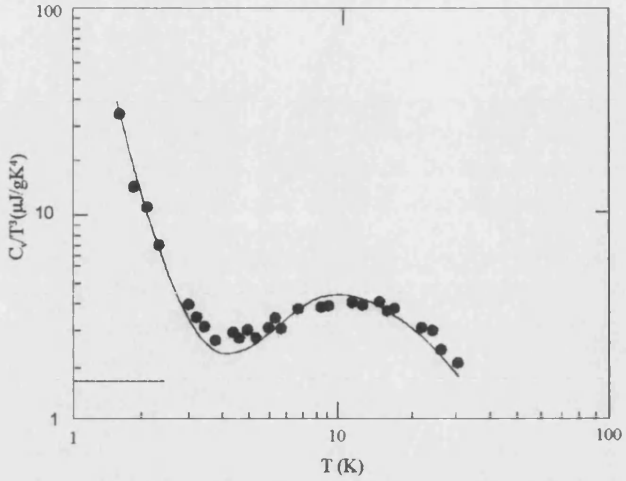


Figure 1.2. The temperature dependence of $C_v/T^3$ for samarium metaphosphate glass (after Carini et al. 1995b). The horizontal line indicates the calculated values using the Debye model.

The specific heat capacity of a non-conducting glass can be written as

$$C = C_{Debye} + C_{vib}, \tag{1.1}$$

where $C_{Debye}$ characterises the Debye contribution to the specific heat $((2\pi^2 k_B{}^4 T^3)/(5\hbar^3 \rho v^3))$ where v is the average sound velocity, $\rho$ is the sample density, $k_B$ is the Boltzmann constant and $\hbar$ is Plancks constant divided by $2\pi$); $C_{vib}$ describes the 'excess' contribution arising from quasi-local vibrational modes, as described by the soft potential model. These low temperature specific heat anomalies are universal to the amorphous state, and have been observed in rare earth metaphosphate glasses (Brodin et al. 1994, Carini et al 1995a, b, Fontana et al. 1995).

### 1.1.5. MAGNETIC PROPERTIES OF REMGs

Rare earth metaphosphate glasses contain large quantities of paramagnetic ions; consequently these glasses receive an additional contribution, $C_{mag}$, to the low temperature specific heat due to the magnetic nature of the material (Carini et al 1995, 1997, 1998). The magnetic effect shows itself, below 2K, as a rapid increase in $C_P/T^3$ with decreasing T (figure 1.2). Carini et al. (1997, 1998, to be published) found that on decreasing the temperature below 10K the specific heat in trivalent Gd and Dy doped metaphosphate glasses are approximately three orders of magnitude larger than the equivalent non-magnetic lanthanum doped sample. Lanthanum metaphosphate

glass does not exhibit contributions to the specific heat over those resulting from the vibrational states which are present in all amorphous materials. The magnetic specific heat $C_{mag}$ exhibits a $T^{-2}$ dependence, which is characteristic of the high temperature tail of the Schottky anomaly (Kittel and Kromer 1980, Carini et al. 1998):

$$C_{mag} = k_B \int_0^{\Delta_{max}} g(\Delta)\left[\frac{\Delta}{2k_BT}\,\mathrm{sech}\left(\frac{\Delta}{2k_BT}\right)\right]^2 d\Delta \qquad (1.2)$$

Here $g(\Delta)$ is the distribution of lowest energy crystal field excitations, $\Delta$ is the energy level splitting in reciprocal cm, $k_B$ is the Boltzmann constant, and T is the temperature. The Schottky anomaly which arises from energy level splitting, caused by hyperfine and crystal field interactions, has been observed in many paramagnetic materials. The REMG samples studied exhibit the largest magnetic contributions to the low temperature specific heats known in oxide glasses (Carini et al. 1997, 1998 and to be published).

The origin of the magnetic specific heat is a consequence of excess magnetic excitations. These are produced by electronic transitions between a quasi-continuous distribution of low-lying crystal field excitations (CF) arising from the variation of the local environments of magnetic ion sites in the glassy host matrix. The low frequency Raman scattering verified the existence of a large density of low lying magnetic excitations (Carini et al. 1997, 1998 and to be published). This is an extension of the fundamental aspect of glasses, namely the broad distribution of low-energy vibrational excitations due to the random structural disorder associated with an amorphous material (Carini et al. 1995a,b, Fontana et al. 1995 and refs. therein).

Several additional investigations on the magnetic properties of REMGs have been made using the techniques of NMR (Keartland et al. 1994, Goudermond et al. 1994, 1997), and magnetometery (Ford et al. 1994, Kang Sun and Risen 1986). It was concluded that the rare earth ions in $Nd^{3+}$ and $Gd^{3+}$ paramagnetic glass behave as non-interacting moments down to at least 2K (Ford et al. 1994).

## 1.2. RESEARCH OVERVIEW

The structure and properties of rare earth doped phosphate glasses in the vicinity of metaphosphate composition have been investigated. Experiments have been completed which both extend and complement existing data and increases the understanding of how the rare earth ions are incorporated into the metaphosphate host, and the effect of these modifiers on the fundamental properties of the glasses.

Several different methods have been adopted to investigate the structure and properties of trivalent rare earth doped phosphate glasses. The probes have been split into four groups; x-ray diffraction and EXAFS, elastic and inelastic neutron scattering, ultrasonics and finally optical investigations; consequently this breath of study has determined the format of the thesis. Each technique can be viewed as a separate investigation on the same series of glasses; hence each method has been isolated into groups of two chapters. The first chapter gives an overview of the basic theory and concepts involved with each experimental technique; that chapter also includes information on experimental and data correction procedures. In the second chapter, of each pair, the results and conclusion are presented. This grouping of chapters is intended to make it easier for the reader to extract desired information.

Chapter two serves as an introduction to the fundamental concepts of glasses, phosphates, rare earths, and the current models which have been developed to describe the structure and properties of the vitreous state. The concept of crystal fields, which are mentioned several times in this thesis, has also been included here. Chapter three describes the manufacturing process involved with the fabrication of bulk samples of this type. Chapters four and five are concerned with the experimental techniques of x-ray diffraction and EXAFS. X-ray diffraction measurements have been made on bulk samples containing Ce, Nd, Sm, Gd, Dy, Ho, and Er dopants. Previous measurements have only been made on metaphosphate glasses doped with trivalent praseodymium, europium and terbium, hence the current investigation has significantly extended the range of glasses examined. Although there have been several investigations on the structure of rare earth metaphosphate glasses using EXAFS, there has been no data recorded at any temperature other than room temperature. To investigate the possible effects of reduced temperature on the

structure of these glasses, an EXAFS investigation, using the rare earth $L_{III}$ absorption edges, has been made at temperatures of 293K, 145K and 79K. Results have been obtained for glasses modified with the rare earth ions La, Ce, Pr, Nd, Sm, Eu, Gd, Tb, Dy, Ho, and Er. Inelastic neutron scattering experiments have been employed in chapters six and seven to examine the presence of low energy magnetic excitations in a metaphosphate glass doped with trivalent Pr, Nd, Tb, Dy, Er and Tm. The magnetic neutron scattering spectra contains a number of features that can be attributed to a loss in neutron energy associated with promoting an electron into a higher crystal field energy level in the ground state. Total neutron scattering measurements can also give information on the local structure, and a new technique has been investigated which can be used to isolate the R-R correlation distances in REMGs. This method exploits the fact that neutrons are sensitive to changes in scattering lengths, and the scattering length of a paramagnetic rare earth ion, in an metaphosphate glass host, can be changed by applying a magnetic field. Chapters eight and nine are concerned with using the method of ultrasonics to determine the anharmonic properties of REMGs. The ultrasonic wave velocities and attenuations of mixed $(La_2O_3)_x(Sm_2O_3)_y(P_2O_5)_{0.75}$ (where $x + y = 0.25$) metaphosphate glasses have been measured as a function of temperature. The changes in the ultrasonic wave velocity induced by application of hydrostatic pressure, up to 0.16GPa, have also been measured in the mixed ternary samples, binary lanthanum $(La_2O_3)_{0.225}$ $(P_2O_5)_{0.775}$ and cerium metaphosphate glass $(Ce_2O_3)_{0.235}(P_2O_5)_{0.765}$, at selected temperatures between room temperature and 375 K. The experimental results provide the temperature dependences of the adiabatic elastic stiffnesses $C_{11}$ and $C_{44}$, and the hydrostatic-pressure derivatives $(\partial C_{11}/\partial P)_{P=0}$ and $(\partial C_{44}/\partial P)_{P=0}$ of the elastic stiffnesses and $(\partial B^S/\partial P)_{P=0}$ the bulk modulus. The results obtained for $C_{IJ}$ and $(\partial C_{IJ}/\partial P)_{P=0}$ are used to calculate the long-wavelength acoustic-mode Grüneisen parameters; these quantify the vibrational anharmonicity, which is essential information for determining the acoustic mode contribution to the thermal expansion of the glasses. Hence ultrasonic velocity measurements in metaphosphate glasses modified with $Sm^{3+}$ and $La^{3+}$ ions enable separation of these acoustic mode contributions from those due to the excess modes. The absorption and fluorescence spectra of the series of metaphosphate glasses doped with Pr, Nd, Sm, Eu, Tb, Dy, Ho and Er have been examined over the wavelength range 400-1750nm in chapters ten and eleven. These measurements extend previous investigations in both

wavelength range, and by the number of rare earth metaphosphate samples studied. By comparing the measured transition wavelengths with those found in the optical spectra known for other hosts of rare earth ions, it is possible to account for virtually all the observed optical features. The optical properties provide detailed information required for device applications, and allow for the determination of the valence states of rare earth ions in a metaphosphate host. Details on the fabrication of a neodymium metaphosphate glass fibre clad with silica are given, and preliminary measurements on Brewsters angle, concentration quenching and absorption have been made. Finally all the experimental data on the structure and properties of rare earth metaphosphate glasses are summarised in a conclusion chapter.

# CHAPTER TWO

## AN INTRODUCTION TO FUNDAMENTAL OXIDE GLASS CONCEPTS

An amorphous material can be defined as a substance which exhibits topological disorder; unlike crystals, vitreous materials possess no long range order. Glasses are a subset of amorphous materials, which undergo a glass transition at temperature $T_g$ provided the melt is cooled sufficiently quickly that crystallisation is avoided (figure 2.1). $T_g$ does not have a definite value because the glass transition occurs over a range of temperatures depending on the cooling rate. As the temperature is lowered there is an abrupt decrease in the heat capacity and thermal expansivity at $T_g$.

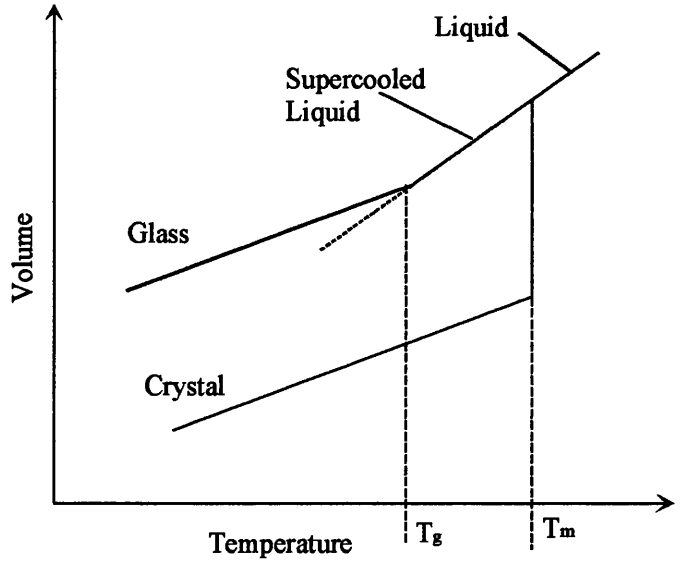


Figure 2.1. The volume-temperature characteristic of a glass compared with that of a crystal. $T_g$ is the glass transition, and $T_m$ is the melting temperature.

The amorphous phase is less thermodynamically stable than the corresponding crystalline form and is not in equilibrium. This is due to the fact that the atoms in a vitreous material do not have equivalent environments and therefore the system possesses extra degrees of freedom. Determination of the structure of a covalent amorphous material is complicated by the lack of long range order; this implies that the unit cell of a vitreous solid would contain an infinitely large number of atoms, and statistical interpretations are inevitable. Many investigations have attempted to understand the short (2-5Å) and medium (5-20Å) range order of oxide glasses. Short range order (SRO) defines the immediate connectivity between ions, and is usually expressed in terms of the co-ordination number $N_j$, the nearest neighbour bond length $R_{ij}$ and the bond angle $\theta_{ij}$ (Zachariasen 1932). Medium range order (MRO) can be split into three subsections. Near MRO (NMRO) $\leq$5Å, describes the connection between the adjacent structural units. Intermediate MRO (IMRO) ~5-8Å is concerned with the formation of 'super' structural units i.e. rings or clusters of atoms. Far MRO (FMRO) ~8-20Å is associated with the dimensions of the glass network (Elliot 1991, Gladden 1990).

This chapter provides an introduction to the basic theories and models that have been formulated to describe the structure and properties of amorphous materials. A resumé of crystal field effects has been included. Crystal field splitting modifies the energy level structure of a paramagnetic ion in a host material, thus effecting its magnetic and optical properties. Rare earth metaphosphate glasses are paramagnetic and hence this effect is particularly pertinent for the behaviour of these materials.

## 2.1. THE STRUCTURE OF GLASS

Several models have been proposed to describe the structure of non-crystalline materials. Two popular, but disparate, theories are:

a) Continuous random network (CRN) model (Zachariasen 1932, Warren and Biscoe 1939, Bell and Dean 1972, Gaskel and Tarrant 1980, Ching 1982, Gladden 1990)

b) Paracrystallite model (Phillips 1982 and 1984, Banavar and Phillips 1983, Galeener and Wright 1986, Hosemann et al.1986).

Both models have been reviewed by Wright et al. (1991). Neither model accounts for all of the experimental properties recorded in an oxide glass, especially as length scales increase e.g. in the MRO region.

### 2.1.1. CONTINUOUS RANDOM NETWORK MODEL

The seminal paper on the continuous random network (CRN) model was written by Zacharisen in 1932. He proposed that the atoms in an oxide glass form a three dimensional network. The arrangement lacks periodicity and symmetry, however it is not totally random as the atoms oscillate about equilibrium positions fixed by interatomic forces similar to those found in crystals. The CRN model was developed on the basis of four requirements, which Zacharisen suggested had to be met if glass formation was to be possible:

1) An oxygen is not linked to more than two glass forming atoms i.e. $P^{+5}$, $B^{+3}$, $Si^{+4}$.

2) The co-ordination of the glass forming atom is small; hence it is only surrounded by oxygen tetrahedra or triangles.

3) The oxygen polyhedra share corners with each other, not edges or faces.

4) At least three corners of each oxygen polyhedra must be shared.

Vitreous materials are built from units similar to their crystalline counterparts, which means that short range order and valence is retained. The randomness is generated from the bond angle $\theta$ and the dihedral angle $\phi$ (figure 2.2). The bond angle is concerned with deviations (120-180°) in the mutual orientation of connected units (for example the silicate or phosphate tetrahedron), and the dihedral angle describes the torsional rotation of the tetrahedron about the glass forming ion-oxygen bonds (Si-O or P-O); in a real glass the distribution of $\phi$ is limited by stearic hindrance

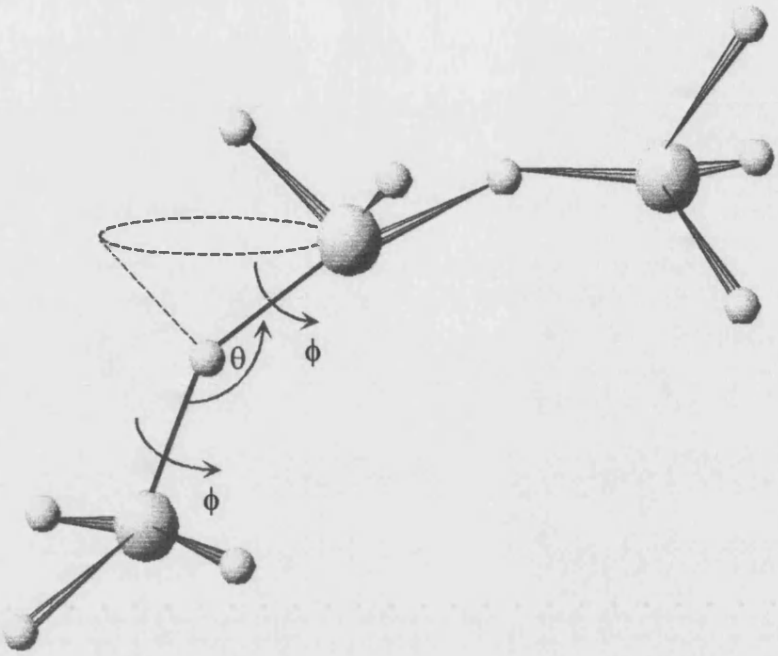


Figure 2.2. Schematic of a continuous random network. $\phi$ is the dihedral angle and $\theta$ is the bond angle.

Bell and Dean (1972) illustrated this model by constructing a ball and stick representation for $v$-$SiO_4$, using a tetrahedral base unit with a mean Si-O-Si bond angle of 153°, and varying molecular ring size, n (figure 2.3). The theoretical results were in agreement with x-ray diffraction experiments; this was attributed to the inclusion of rings containing four atoms (19%). However Gaskell and Tarrent (1980) showed that the strain energy within the structure did not correspond to experimental predictions and tried to extend the basic concept by relaxing the model. This was achieved by fixing the nearest neighbour distances and allowing $\theta$ and $\phi$ to rotate. As computer power has progressed, laborious modelling tasks have successfully been replaced by computer simulation (Ching 1982, Galeener and Wright 1986). Warren and Biscoe (1939) extended the CRN work by investigating the effect of adding sodium metal cations ($Na_2O_4$) to a silicate skeleton. The metal ion inclusions are chosen to be relatively large, and carry a small charge, in order to reduce the repulsion between them and the glass forming atoms. The dopants increase the ratio of oxygen atoms with respect to silicon; this means that a number of singularly bonded oxygen atoms are formed which are not present in a pure $v$-$SiO_4$ network. Non-bridging oxygen act as point defects but have the feature of reducing the overall strain within

the sample, and consequently decrease the probability of crystallisation. The sodium ions sit in holes in the network, see figure 2.3.

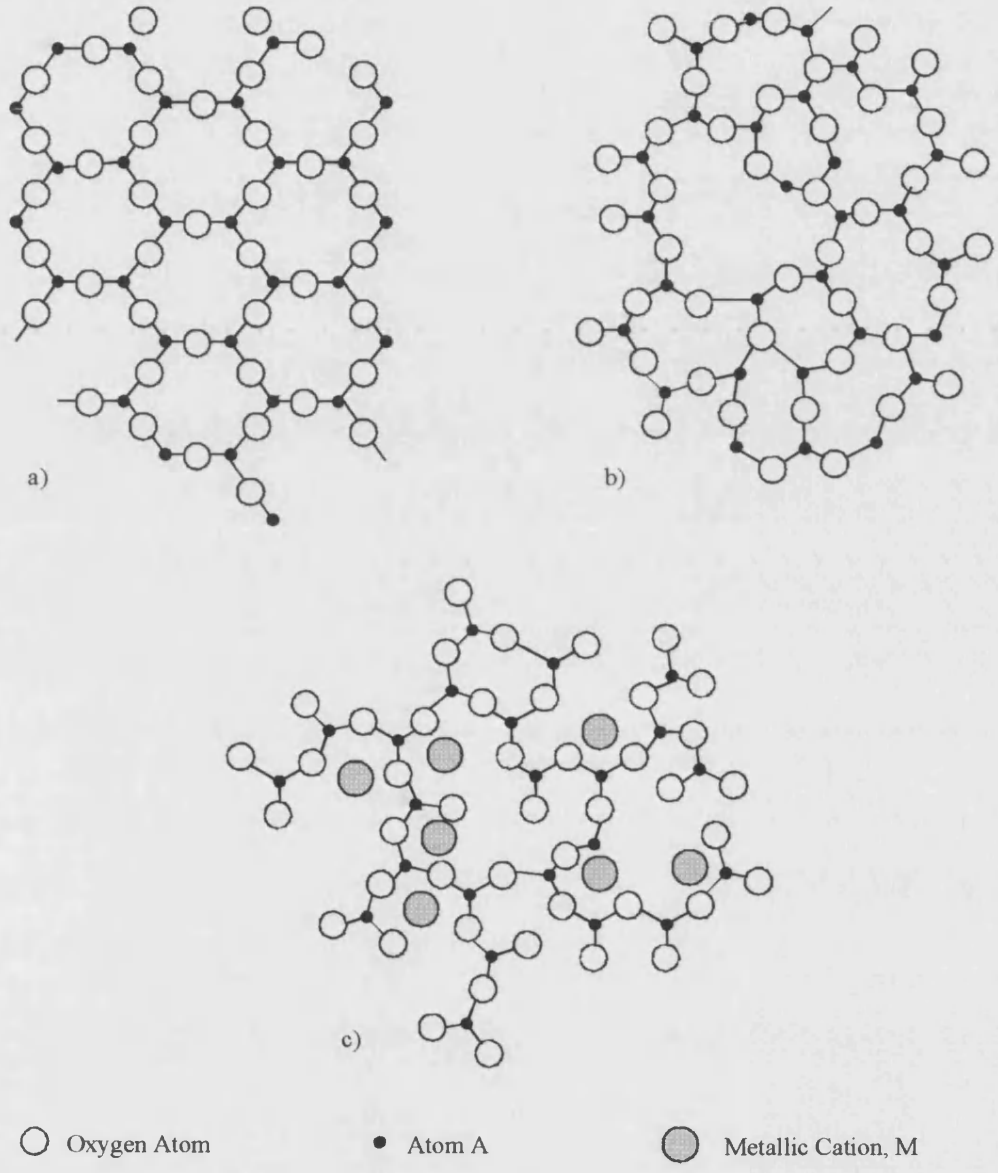


Figure 2.3. Structure of a typical two dimensional oxide glass $A_2O_3$; a) as a crystal b) as a glass (after Zacharisen 1932) c) as a binary glass of $A_2O_3$ and $M_2O$ (after Warren and Biscoe 1938).

### 2.1.2. PARACRYSTALLINE MODEL

The paracrystalline model was developed in a review paper by Phillips in 1982. Essentially the model assumes that small clusters (micro-clusters) of different crystalline phases exist in a liquid and, when the melt is cooled rapidly, the resulting glass exists as a mixture of these tiny microphases. Glass formation in oxides arises due to the ability of oxygen atoms to create double, rather than single, non-bridging bonds with little change in the enthalpy of the system. In silicate materials disorder is produced because the paracrystallites will remain as separate clusters, if the surface is saturated with these Si=O double bonds. The reconstructed bonds exhibit intercluster cross linking, as well as strong interactions to atoms within a crystallite; the bond stretching interaction on the surface of a cluster is 25% larger than that of the internal Si-O bonds. The most likely morphology for vitreous silica is based on microcrystallites (approximately 60Å in diameter) of $\beta$-cristobalite, which is a cubic $SiO_2$ crystalline material. The neutron vibrational spectrum of amorphous $SiO_2$ supports this model, with peaks in the glass occurring at similar values to the corresponding crystalline quartz data (Banavar and Phillips 1983, Phillips 1984). However, the peaks in the silica glass are broadened due to the small dimensions of the cluster. There are also other features present which can be attributed to the internal surface double bonds, and the associated break in the chemical order. Hosemann et al. (1986) examined the structure of silica based on microparacrystal principles (an extension of the paracrystallite model). This is a three dimensional model where randomness occurs due to twisting the tetrahedra in parallel but opposite directions by 22°. These units form six membered rings (Si-O-Si 145.0 ± 3.8°), which are octahedral in shape, and approximately 12.5Å in size. Larger angular distortions (i.e. >±3.8°) will occur at the grain boundaries between these microparacrystals.

Criticism of the paracrystallite model comes from Galeener and Wright (1986), who showed that it does not account for all the Raman spectroscopic and neutron diffraction data; experimental results ruled out the possibility of large concentrations of Si=O double bonds that are required by Phillips' model.

## 2.2 PHOSPHATE GLASSES

Phosphorus, atomic number 15, can exist as one of six different isotopes, although there is only one stable form $_{15}P^{31}$ with atomic weight 30.98. It is produced by the reduction of phosphate rock with coke in an electric furnace at approximately 1100°C. In 1959 Van Wazer produced a comprehensive review of phosphorus chemistry, and his work on amorphous phosphates has been reviewed and updated in an article by Martin (1991). Phosphorus bonds covalently to produce compounds, its most important reaction being oxidation. The final product of this reaction is primarily phosphorus pentoxide $P_2O_5$. Phosphate is the generic title for any material which is built from $PO_4$ tetrahedra. In this basic building block the phosphorus atom is surrounded by four oxygens (four fold co-ordination). Phosphorus has valency +5, hence the arrangement requires three single bonds and one terminal doubly bonded oxygen. There are four fundamental arrays from which all phosphates can be formed:

1) Branching unit. Three oxygen atoms are shared with neighbouring $PO_4$ tetrahedra. In $Q^n$ site notation this is equal to $Q^3$, where n is the number of P-O-P links on the $PO_4$ tetrahedron (figure 2.4.a)

2) Middle group. Two shared oxygen atoms $PO_4^{1-}$ ($Q^2$) (figure 2.4.b)

3) End unit. One shared oxygen atom $PO_4^{2-}$ ($Q^1$) (figure 2.4.c)

4) No bridging oxygens ($Q^0$).

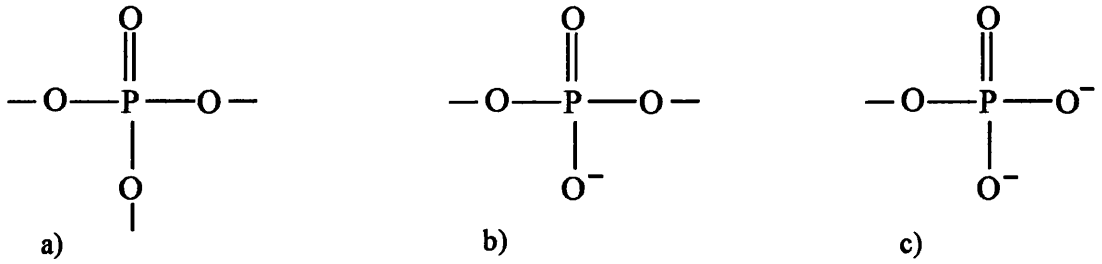


Figure 2.4. The elementary $PO_4$ tetrahedra building units: a) branching unit, b) middle unit, c) end unit.

By sharing oxygen atoms between tetrahedra, 'bridging oxygens', chains, rings, and branched polymers can be formed.

Pure phosphorus pentoxide can be super-cooled to produce a colourless glass with refractive index of approximately 1.55 in the visible region. Changes in the

composition, via the introduction of network modifiers, alter the extent to which the basic units are present in the system, and hence the structure of the amorphous material. According to Van Wazer's (1959) reorganisation theory, phosphate glasses can exist in many different ensembles such as ultraphosphate, metaphosphate, and pyrophosphate (figure 2.5). These structural units are determined by the ratio of metal oxide modifiers to phosphorus pentoxide $R=n(M_{2/x}O)/n(P_2O_5)$, where x is the valency of the metal dopant M (alkali, transition, rare earth, or actinide) (Hoppe 1996).

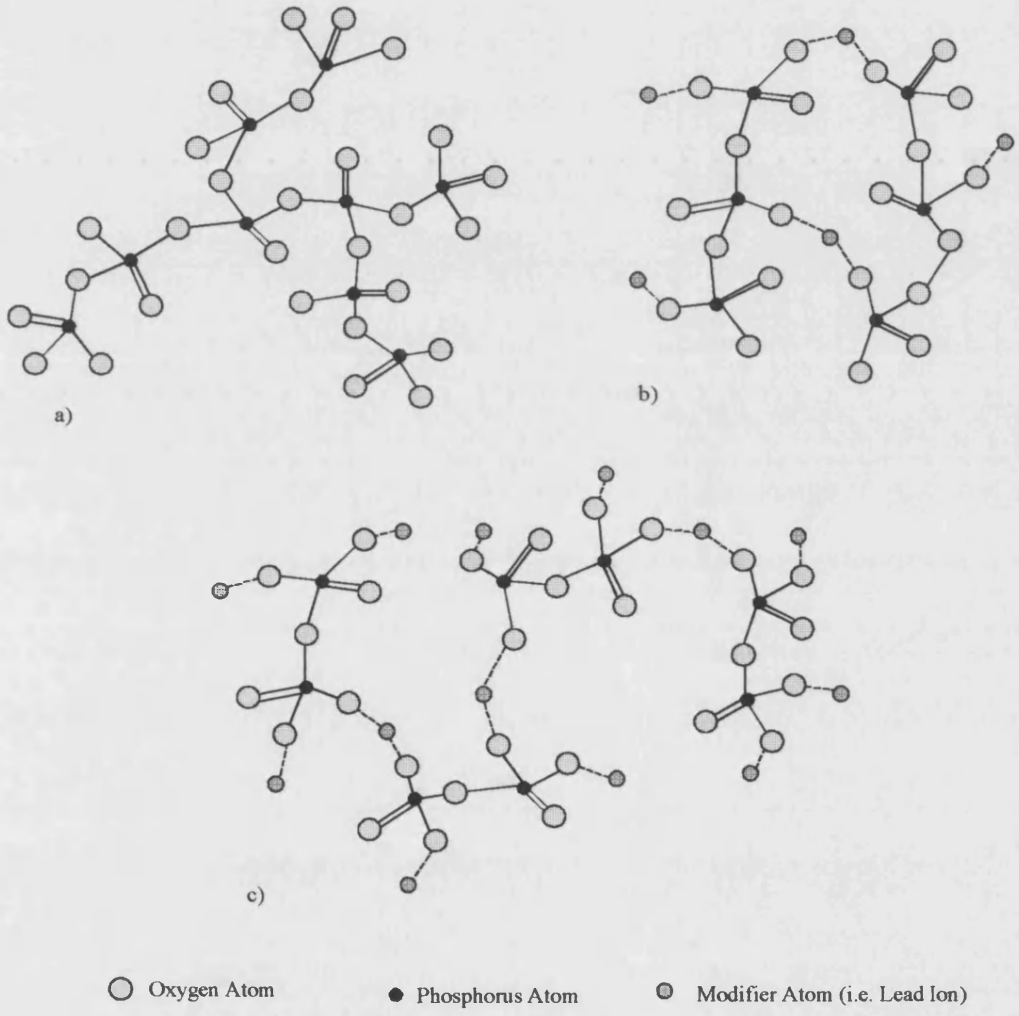


Figure 2.5. Schematic of phosphate glass structures: a) pure phosphate glass, b) metaphosphate network, c) pyrophosphate glass.

Galeener et al. (1979) studied the Raman spectra of *v*-$P_2O_5$ and concluded that the structure is based on a three-dimensional network of cross-linked $PO_4$ tetrahedra (figure 2.5.a); the $PO_4$ tetrahedra are connected at three of its four corners. As the

metal ion content is increased the $PO_4$ tetrahedra form linked chains (figure 2.5b). If the dopants are incorporated into the network in still larger quantities, the length of the chains becomes shorter until the network glass consists primarily of isolated pyrophosphate ensembles in a 'sea' of metal modifiers (figure 2.5c).

As metal oxide is added to the melt the basic phosphate structural groups pass through $Q^3$ to $Q^2$ to $Q^1$ to $Q^0$. The graphical representation, shown in figure 2.6, is based on Van Wazer reorganisation theory (1959). It is assumed that the basic units make and break many times during the period in which steady state is achieved.

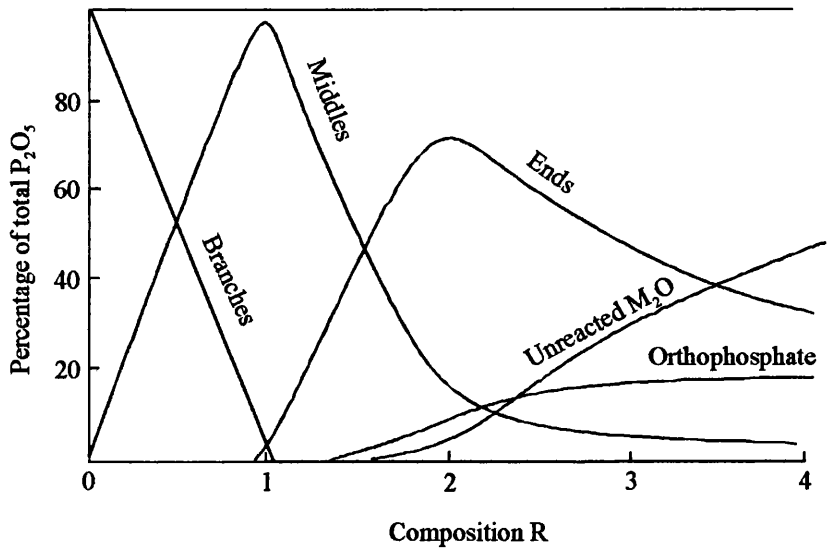


Figure 2.6. A hypothetical curve showing the relative proportions of branching, middle and end units as a function of R, the ratio of metal oxide to phosphorus pentoxide (after Van Wazer 1959).

Sales (1990) investigated the structure of binary lead doped phosphate glass. As metal oxide modifiers are added to the glass, bridging oxygens are broken to preserve the balance of charge, and incorporate the additional oxygen atoms; this results in the break up of the tetrahedra (this process is called depolymerization). When there are equal numbers of metal inclusions and $PO_4$ in the system, a metaphosphate composition results. Glasses with the stoichiometry $M(PO_3)_x$ where x is the valency of the metal dopant cation M, are called metaphosphate (R=1). Investigations (Greaves et al. 1988, Greaves 1989) on the structure of metal oxide doped metaphosphate

glasses suggest that the $PO_4$ tetrahedra form infinitely long chains attached by two branching oxygens, and interconnected by weaker links to the metal modifier atoms, which occupy sites between non bridging oxygens (figure 2.5.b). The stoichiometry lends itself to only middle units being present. In reality, a fraction of the tetrahedra may be associated with a ring structure which limits the chain length.

There have been numerous papers which investigate the structure of phosphate glasses (Greaves et al. 1988, Musinu et al. 1989, Sales 1990, Brow et al. 1990, Brow 1993, Hoppe et al. 1995a, b,1996), and recently, the specific case of REMGs (Kang Sun and Risen 1986, Bowron et al. 1994, 1995, 1996). In probing the structures, techniques such as elastic and inelastic neutron scattering, NMR and the complementary methods of EXAFS and x-ray diffraction have been employed. Diffraction results for glasses doped with lanthanides (Bowron et al. 1996b) are inconsistent with a network model based on $PO_4$ units linked in a chain arrangement, but instead favour a structure dominated by a three-dimensional phosphate skeleton. The rare earth ions are situated at the interstices and are found to be surrounded by six to eight oxygen atoms; this co-ordination adheres to a pseudo-octahedral or cubic arrangement, or a mixture of both configurations. (Bowron et al. 1996a).

The major problem with using phosphate glasses in practical devices, is that for most compositions the samples are highly susceptible to water contamination. However metaphosphate glasses have a large resistance to hydrolysis. Greaves et al. (1988, 1989), attributed this stability to water in lead iron metaphosphate glass to an increase in metal cations, and consequently the number of cross links between phosphate chains. In this 'modified random network' the percolation channels (pathways of ionically bonded modifiers) become truncated by the cross linking iron atoms, which because they are more tightly bound than the lead ions, form 'knots' in the percolation channel. This stops diffusion of hydroxonium ($H_3O^+$ or $OH^-$) ions, impairs ion exchange and therefore reduces corrosion. In REMGs the phosphate network is based on a three-dimensional skeleton, and hence does not have the percolation channel characteristic of a metaphosphate glass consisting of long chains; however it is assumed that the hydroxyl groups can not diffuse easily through the three dimensional network.

## 2.3. LANTHANIDES AS GLASS DOPANTS

Rare earths, is the name given to the group of elements which run from cerium (atomic number 58) to lutetium (71) in the periodic table, and corresponds to the systematic filling of the 4f shell with 1 to 14 electrons (table 2.1). This group of atoms is sometimes extended to include lanthanum (57) and yttrium (37), as these elements have an identical core arrangement and consequently exhibit similar properties.

| Atomic Number | Lanthanide Element. | Electronic Configuration. | Ground State $3^+$ Hund Notation |
|---|---|---|---|
| 75 | Lanthanum | [Xe] $5d6s^2$ | $^1S_0$ |
| 58 | Cerium | [Xe] $4f5d6s^2$ | $^2F_{5/2}$ |
| 59 | Praseodymium | [Xe] $4f^36s^2$ | $^3H_4$ |
| 60 | Neodymium | [Xe] $4f^46s^2$ | $^4I_{9/2}$ |
| 61 | Promethium | [Xe] $4f^56s^2$ | $^5I_4$ |
| 62 | Samarium | [Xe] $4f^66s^2$ | $^6H_{5/2}$ |
| 63 | Europium | [Xe] $4f^76s^2$ | $^7F_0$ |
| 64 | Gadolinium | [Xe] $4f^75d6s^2$ | $^8S_{7/2}$ |
| 65 | Terbium | [Xe] $4f^96s^2$ | $^7F_6$ |
| 66 | Dysprosium | [Xe] $4f^{10}6s^2$ | $^6H_{15/2}$ |
| 67 | Holmium | [Xe] $4f^{11}6s^2$ | $^5I_8$ |
| 68 | Erbium | [Xe] $4f^{12}6s^2$ | $^4I_{15/2}$ |
| 69 | Thulium | [Xe] $4f^{13}6s^2$ | $^3H_6$ |
| 70 | Ytterbium | [Xe] $4f^{14}6s^2$ | $^1S_0$ |

Table 2.1. The electronic configurations of the neutral rare earths and the Hund notation $^{2S+1}L_J$ (section 2.5), for the ground state of the trivalent ion ([Xe] = $1s^22s^22p^63s^23p^63d^{10}4s^24p^64d^{10}5s^25p^6$ ($nl^N$, where n is the principal quantum number and N is the number of electrons)).

Optical and magnetic characteristics are determined by the number of electrons in the 4f shell, but as these electrons do not partake in the bonding the chemical changes within the group vary only slightly with atomic number. The electronic configuration

of the neutral lanthanides is based on a xenon core ($1s^2 2s^2 2p^6 3s^2 3p^6 3d^{10} 4s^2 4p^6 4d^{10} 5s^2 5p^6$), with 3 electrons in the higher energy 5d and 6s orbitals. The 5d and 6s levels mix to give the conduction band, whereas the 4f electrons remain localised. The rare earths usually ionise to give a trivalent $R^{3+}$ configuration; typically two electrons are lost from the 6s shell, and one from either the 5d or 4f shell. The $5s^2$ and $5p^6$ shells remain intact and therefore act to partially shield to the 4f electrons.

Lanthanide contraction is an interesting property displayed by these elements (Moeller 1973). The atomic radius of neutral lanthanides decreases almost linearly with atomic number from lanthanum (1.83Å) to lutetium (1.73Å), with the exception of cerium, europium, and ytterbium Lanthanide contraction is the result of imperfect shielding of one 4f electron by another. The additional attractive force between the nucleus and the filled outer 5p shell, as the number of protons is increased, is not quite neutralised by the repulsive effect associated with the corresponding increase in f electrons, hence the outer shell contracts. Lanthanide contraction is most pronounced in the $R^{3+}$ ions (figure 2.7). The slight discontinuity which occurs at the gadolinium atom (atomic number 64) is probably related to the closed-shell arrangement of that ion.

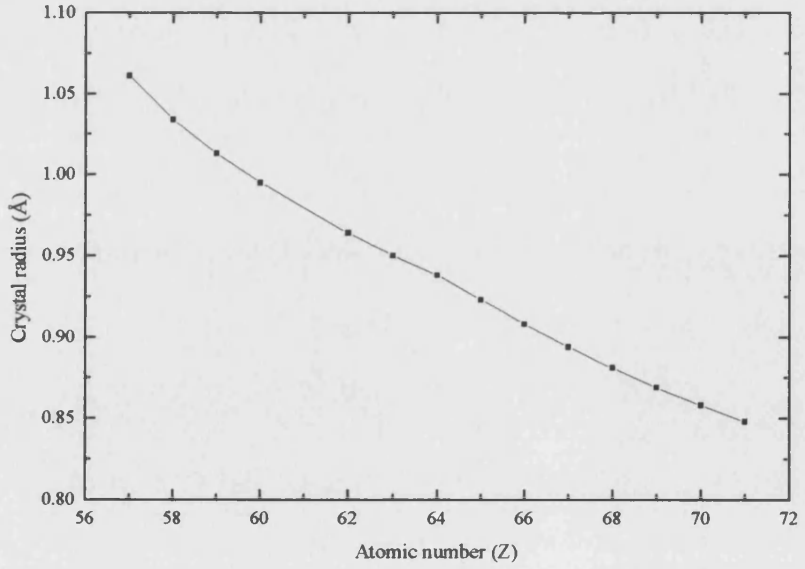


Figure 2.7. A graph of the crystal radius of trivalent lanthanides as a function of atomic number (after Moeller 1973).

When dopant elements, such as rare earth atoms, are added to an amorphous host, the energy levels of the ion change. This modification alters the magneto-optical properties of the sample. Magnetic and spectral substructure will be seen due to crystal field splitting (section 2.5), which also contributes to the broadening of characteristic features observed in a vitreous material. The amount of doping also effects the structure and properties of the glass. At present it is only possible to produce stable phosphate glasses with approximately 25mole% rare earth oxide (Senin 1994). However by mixing different rare earth elements the properties of the sample may be tuned; magnetism can be varied by changing the ratio of the paramagnetic ion to that of lanthanum or yttrium, while retaining the metaphosphate composition; $La^{3+}$ and $Y^{3+}$ have no 4f electrons and therefore give zero magnetic contribution.

## 2.4. MODELS TO DESCRIBE THE CHARACTERISTIC PROPERTIES OF GLASSES

Many hypotheses have been proposed to account for the anomalous properties exhibited by amorphous materials. These models have been constructed to find a common origin for all the anomalies found. Investigations have been made to develop understanding of REMGs, and check the applicability of proposed theoretical models, such as the two level tunnelling system and its' extension the soft potential model, to these materials.

### 2.4.1. THE TWO LEVEL SYSTEM

The two level system (TLS) was proposed independently by Phillips and Anderson et al. in 1972, to account for the presence of low energy excitations in amorphous materials. This phenomenological model is based on the assumption that a certain number of atoms (or groups of atoms) can exist in two (or more) equilibrium positions. These sites can be thought of as different energy minima separated by barriers with a broad distribution of heights; the simplest configuration is a one dimensional asymmetric double potential well, as illustrated in figure 2.8. The actual microscopic origin of the potential minima is unknown. Particular atoms could shift between two favoured positions, or perhaps whole $PO_4/SiO_4$ tetrahedra can occupy two orientations with equal probability. As the TLS is observed in the low

temperature properties of all glasses, it must be an intrinsic feature of the disordered amorphous state. The majority of the atoms, however, do not exhibit this extra degree of freedom, which arises from structure defects or difference in ion mobility, and are localised within a single potential well.

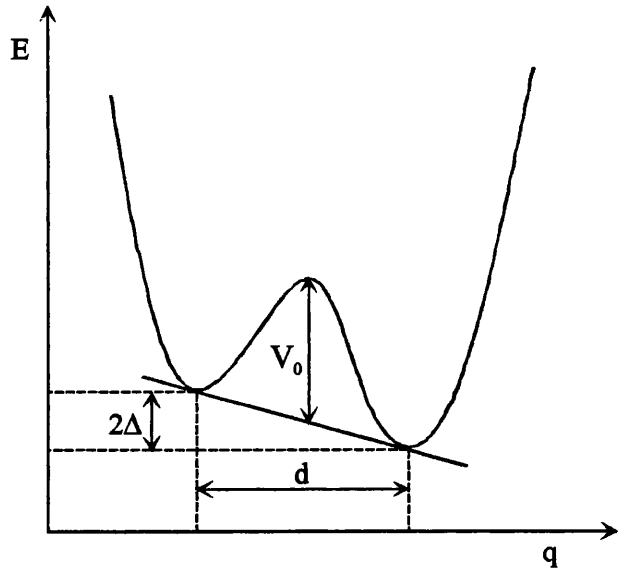


Figure 2.8. A schematic of the two level systems' double potential well, plotted as a function of energy E versus the generalised co-ordinate q.

The two energy minima differ by an amount 2Δ, which is known as the asymmetry, and $V_0$ and d defines the barrier height and width respectively. The width is not necessarily a linear distance and could represent a rotation, or a more complicated structural transition. Δ and $V_0$ are defined as random quantities with a uniform distribution; $P(\Delta, V_0)$ equals a constant.

When the atoms have a large thermal energy compared with the height of the barrier, they can 'hop' between the wells. This mechanism has been observed as thermally activated structural relaxations in ultrasonic long wavelength velocity and attenuation measurements (Phillips 1981, Buchenau et al. 1988, Tielbürger et al. 1992, Carini et al. 1994). The hopping process is defined by a wide distribution of relaxation times $\tau$,

$$\tau = \tau_0 \operatorname{sec}\left(\frac{\Delta}{2k_B T}\right) \exp\left(\frac{V_0}{k_B T}\right) \qquad (2.1)$$

where $\tau_0$ is a constant which can be found from the ultrasonic data, $k_B$ is Boltzmann's constant and T is the temperature. As the relative activation energy is reduced there is a finite probability the ions will tunnel through the barrier. At low temperatures, where quantum effects are dominant, the ground state of the system will be split by both the nature of the asymmetry $\Delta$ and by the tunnelling atoms. The ground states in the two local energy wells have relative energies $\pm E/2$ where $E^2=(\Delta^2+\Delta_0^2)$. The coupling energy $2\Delta_0$ is the energy difference between the two lowest states in a symmetric arrangement, and depends on the shape of the parabolas; $\Delta_0=-h\omega_0 e^{-\lambda}$, where the oscillation frequency of an individual well is $\omega_0$; the exponential factor describes the overlap of the wavefunctions of the two wells and $\lambda$ is the tunnelling parameter, which is approximately equal to $(2mV_0/\hbar^2)^{1/2}d$, if m is the mass of the tunnelling atom (or atoms); $V_0$ and d are illustrated in figure 2.8. Tunnelling only occurs due to perturbation of the potential well by processes such as phonon assisted tunnelling; here the transition between the two states is accompanied by the absorption or emission of a phonon to conserve energy. The extent of the tunnelling contribution to the thermal properties depend on $n(\varepsilon)d\varepsilon$, the number of tunnelling states within a given energy range $\varepsilon$ to $d\varepsilon$. The density of states of the TLS has the dual role of generating low energy excitations ($10^{-5}eV<E<10^{-4}eV$) and acting as resonant scatterers for acoustic phonons. The first contribution accounts for the specific heat anomaly, and the second mechanism controls the mean free path and hence the thermal conductivity (section 1.1.4) and ultrasonic attenuation. The two well system is believed to be a consequence of random disorder in an amorphous material, which results in a wide distribution of bond lengths and angles.

### 2.4.2. SOFT POTENTIAL MODEL

Above 1K the properties of an amorphous material deviate from predictions arising from the tunnelling model. The soft potential model (SPM) can be seen as an extension of the two level system created to account for the thermal anomalies present at higher temperatures, such as the plateau in the thermal conductivity, and the specific heat 'excess' observed as a 'bump' in the $C_v/T^3$ versus T plot (figure 1.2). The SPM is based on the assumption that in addition to the Debye-like phonons (non-dispersive thermal plane waves), there coexist excess vibrational states which have the

ability to interact strongly with acoustic phonons. These excess modes have been described as soft excitations and are localised to about 10-100 atoms. The modes are softened by the introduction of local strains into the material on passing through the glass transition. There are three types of soft modes present in an amorphous material. The limiting case is the anharmonic tunnelling mode, which describes the characteristics below 1K. If the frequency is increased (T<10K, f ≅ 20-100cm$^{-1}$), there is a growth in the quasi-harmonic soft vibrations, which gives rise to a peak in the density of low energy vibrational modes (boson peak), and whose scattering intensity varies with temperature according to the Bose-Einstein distribution. The boson peak has been observed in amorphous materials using Raman spectroscopy (Brodin et al. 1994, Fontana et al. 1995, Carini 1997, Guillot and Yves 1997, Surotsev et al. 1998), low temperature specific heat (Buchenau et al. 1986, Carini et al. 1995a, b, Fontana et al. 1995) and neutron scattering (Buchenau et al. 1986, 1988). At low frequencies and increased temperatures (T>15K, f<20 cm$^{-1}$) there is a cross-over into a regime dominated by harmonic classical relaxation; this mechanism is responsible for quasi-elastic scattering, sometimes called the light scattering excess. The magnitude of the quasi-elastic scattering increases with increasing temperature faster than the Bose population factor, and is attributed to relaxation mechanisms (Parshin 1994, Carini et al. 1995a, 1997). All the soft modes interact in the same manner with the extended vibrations, and are hence believed to have the same origin. The SPM tries to unify the three regions in one distribution of anharmonic potentials. The additional excitations are predominately due to local deviations in mass and/or force constants which result in the incorporation extra degrees of freedom into the vitreous materials. Buchenau et al. (1986) suggested that the localised modes could correspond to the coupled rotation of several tetrahedra. The SPM was initially employed by Karpov et al. (1983) to describe the tunnelling, soft vibrations and low temperature relaxation motion in an amorphous material. It has since been developed by Buchenau et al. (1988, 1991, 1992) and Parshin (1994). The anharmonic potential of a single mode can be written as,

$$V(x) = \varepsilon\left[\eta\left(\frac{x}{a}\right)^2 + \xi\left(\frac{x}{a}\right)^3 + \left(\frac{x}{a}\right)^4\right]. \qquad (2.2)$$

Here x is the displacement of the atom with the largest amplitude in the mode and $\varepsilon$ is the binding energy and is equivalent to $1/2m_s\omega_c^2a^2$ where $m_s$ is the effective mass of the soft mode and $\omega_c$ is the frequency of the soft mode in ordered ('crystal-like') surroundings. The distance a is of the order of interatomic spacing; its exact value is chosen so the fourth order soft mode is equivalent to that of a harmonic 'crystal-like' mode. The dimensionless random local parameters $\eta$ and $\xi$ ($\ll 1$) determine the nature of the modes; if $\eta<0$, the system can be represented by a double well potential, if $\eta>0$, the excitations are quasi-local anharmonic oscillators confined to a single well potential, and when $\xi = 0$ the potential is symmetric (Parshin 1994). The distribution of the parameters $\eta$ and $\xi$ can be expressed as $P(\eta,\xi) = 1/2P_0|\eta|$ where $P_0$ is a slow varying function of $\eta$ and $\xi$; as $|\eta|\rightarrow 0$, $P_0$ exhibits the 'seagull singularity' due to the distruction of the soft potentials by small linear perturbations (Buchenau et al. 1991, 1992, Parshin 1994). Once the distribution of $\eta$ and $\xi$ are known, the resulting states of the system are characterised in terms of the three parameters which govern $\varepsilon$. The soft mode frequency $\omega_c$ can be found directly from neutron scattering data as it corresponds to the position of the first maximum in the density of states (Buchenau et al. 1986). The values of $m_s$ and a can be extracted, in combination, from specific heat data. As the frequency is lowered, there is cross-over from classical relaxations to tunnelling states (corresponding to several K). The cross-over occurs at an energy W, where

$$W=\varepsilon\left(\frac{\hbar^2}{2m_s a^2\varepsilon}\right)^{\frac{2}{3}}. \qquad (2.3)$$

The product $m_sa^2$ can be evaluated by defining a quantity $T^*$, which is the temperature at which the two contributions are equal (W is approximately equal to $1.6k_BT^*$) (Buchenau et al. 1991). In theory $T^*$ occurs where specific heat $C_p$ changes from a T to a $T^5$ dependency (corresponding to $g(\omega) \propto \omega^4$) see figure 2.9 (Buchenau et al. 1991). The heat capacity in rare earth metaphosphate glasses shows a much weaker temperature dependency, approximately $C_p \propto T^{3.6}$ (Fontana et al. 1995).

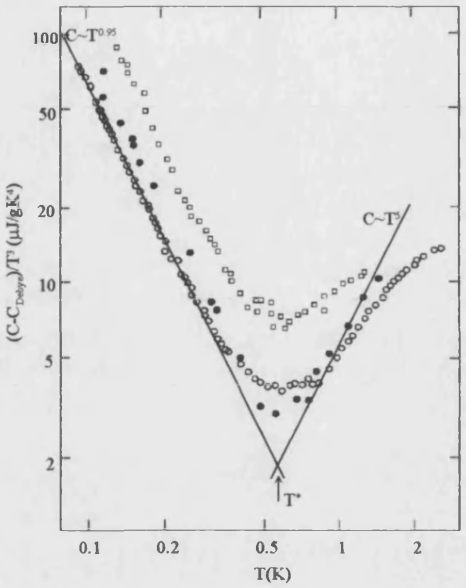


Figure 2.9. Specific heat (Debye contribution subtracted) versus temperature, on a log-log plot, for vitreous selenium samples. The different symbols refer to data taken by different groups, see Buchenau et al. (1991).

From experimental data such as specific heat, Raman spectroscopy and ultrasonic measurements, the temperature and frequency dependence of phonon scattering by thermal relaxing soft vibrations have been calculated and generally are found to be in qualitative agreement with predictions made by the SPM. The main conflict between soft potential model and experiment occurs in the low temperature and low frequency Raman scattering data of rare earth metaphosphate glasses. At sufficiently low temperatures the quasi-elastic scattering can be ignored and the first order Raman intensity $I^{exp}$ can be expressed in terms of the density of states $g(\omega)$ modulated by the light-vibration coupling constant $C(\omega)$:

$$I^{exp}\omega/[n(\omega, T) + 1] = C(\omega)g(\omega). \qquad (2.4)$$

Here $n(\omega, T)+1$ is Bose-Einstein population factor, which acts to normalise the scattering data. Based on the general assumption that soft mode configuration does not depend on eigenfrequency (Buchenau et al. 1992), the SPM predicts that the coupling constant $C(\omega)$ is frequency independent; however the Raman spectrum of REMGs has a near linear frequency dependence (Brodin et al. 1994, Fontana et al. 1995, Carini et al. 1995a).

## 2.5. CRYSTAL FIELD THEORY

The magnetic properties of rare earth ions can be attributed to the presence of unpaired 4f electron. These electrons can be considered localised, and contribute to the magnetic moment of the atom through their intrinsic spin s, and orbital angular motion about the nucleus l. Hunds rules give values of total orbital L, spin S and angular J momentum, which produces the most stable ground state (table 2.1):

1) Intratomic exchange interaction. The value of $S = \sum s$ must be maximum in accordance with the exclusion principle; as many electrons as possible will have their spins aligned parallel.

2) Non-central coulomb force. The value of $L = \sum l$ must also be maximum, while remaining consistent with S, but without violating the exclusion principle. The electrons will occupy the state with the largest orbital angular momentum followed by the state with the next largest orbital angular momentum, and so on.

3) L-S coupling. The total angular momentum J equals |L-S| for a shell less than half filled, and J = |L+S| for a shell more than half filled. When a shell is exactly filled, L=0 and J=S.

Crystal field effects also plays an important role in determining the properties of a magnetic ion in a host network. In crystal field theory the nearest neighbour atoms are assumed to act as sources of negative charge, this leads to destruction of the spherical symmetry of the ion, lifts the (2J+1) degeneracy associated with a given J, and results in a change in the energy levels of the system. The crystal field acts by modifying the wavefunction associated with a free ion; consequently the problem becomes one of identifying the perturbing Hamiltonian and calculating its matrix elements. The effective Hamiltonian, which is the total energy operator describing the magnetic system, consists of a symmetric free ion part $H_f$, arising from the electrostatic and spin-orbit interactions, and the smaller crystal field contribution $H_{CF}$ ($H_{CF} = -eV$). The energy levels of the system are found by evaluating the matrix elements of the perturbing Hamiltonian $\langle i|H_{CF}|f\rangle$, and subsequently diagonalizing it to find the eigenfunctions (Hutchings 1964). The electrostatic potential V which the paramagnetic ion feels due to the surrounding charges can be determined from the sum of the potential function acting on all of the electrons in the unfilled shells; it can be calculated using either Cartesian co-ordinates or spherical harmonics. This Stark

splitting is usually the order of a few $100cm^{-1}$, which is small compared with the separation between different J multiplets. As the symmetry of the host crystal can be described using group theoretical notation the degeneracy of the ground state can also be labelled with a corresponding irreducible representation; the dimensions of the matrix are equal to the degeneracy of the energy level (Bethe 1929). Rare earth atoms can be split into two groups; Kramers ions (Ce, Nd, Sm, etc.) have an odd number of f electrons, and are at least two-fold and evenly degenerate in the ground state provided that no external magnetic field is present (maximum degeneracy J+1/2). In a cubic field the degeneracy of a Kramers ion can be described using the irreducible representations $\Gamma_6$ - $\Gamma_8$. Non-Kramers ions (Pr, Eu, Tb etc.) have an even number of f electrons, and thus an integral J, and form singlets in the ground state (maximum degeneracy 2J+1) (in a cubic field the crystal field levels can be labelled $\Gamma_1$- $\Gamma_5$) (Lea et al. 1962). The crystal field effect can be characterised by the crystal field parameter $A_k^q$, which measures the strength of interaction between the open shell (4f) electrons and the surrounding environment. The superposition model of CF's was introduced by Bradbury and Newman (1967), to separate the geometrical and physical properties of the crystal field parameter. The superposition model is solely a phenomenological model and gives no insight into the mechanisms responsible for the splitting. A comprehensive summary is given in the review article by Newman and Betty Ng (1989). The model is based on four postulates:

1) The crystal field acting on the open shell electrons of a paramagnetic ion is the resultant of a sum of contributions coming from the individual ions in the crystal.

2) Only contributions from the nearest neighbour ligands are taken into account.

3) Each single ion contribution in the sum is axially symmetric about the line joining its centre to that of the paramagnetic ion.

4) Single ligand contributions depend only on the nature of the ligand and its distance from the paramagnetic ion.

In the superposition model each crystal field parameter is constructed as follows

$$A_k^q \langle r^k \rangle = \sum K_{kq}(\theta_i \phi_i) A_k(R_i) \qquad (2.5)$$

where i labels the ionic position $(R_i, \theta_i, \phi_i)$ and the co-ordination factors $K_{kq}$ are determined by the angular co-ordination of the ligands, and transforms the intrinsic parameter $A_k(R_i)$ from a local to common reference frame; $A_k(R_i)$ is the CF parameter

for a single ligand a distance R from the paramagnetic ion. The subscript k represents the rank/degree (2, 4, 6) of the crystal field parameter and q = 0 to k in integer steps. The number of terms needed to completely define the potential function is governed by the symmetry and orbital angular momentum of the magnetic ion. The general rule is that for terms greater than 2l the corresponding matrix elements vanish; hence for rare earth ions (4f) the electrostatic expansion needs only to be sixth degree ($k \leq 6$). The even k terms determine the degree of the Stark splitting of the J multiplet, and the odd k terms admix higher states into the system and account for electric dipole transitions in otherwise parity forbidden inter f shells; hence within a given configuration (a given l) the odd k terms are zero (Hutching 1964). A popular and convenient way to express the crystal field is by using Stevens operator equivalent method (Stevens 1952). Successive terms in the electrostatic potential expansion can be replaced by angular momentum operators (spherical tensor operators), which act on the angular momentum part of the of the wavefunction, and transform under rotation in the same way as the spherical harmonics. The operator equivalent Hamiltonian $H_{CF}$ can be written as

$$H_{CF} = \sum B_k^q O_k^q, \tag{2.6}$$

where $B_k^q$ is a crystal field parameter corresponding to Stevens normalisation and is usually determined empirically. The Stevens operator $O_k^q$ expresses the Cartesian function f(x,y,z) of a given $H_{CF}$ in terms $\alpha_{kq}$, $J_x$, $J_y$, $J_z$, where $\alpha_{kq}$ is a multiplicative factor depending on l, J, and N, the number of electrons in the unfilled shell (Hutching 1964). Using operator equivalent notation, equation 2.5 can be expressed as

$$A_k^q \langle r^k \rangle = B_k^q \alpha_{kq}, \tag{2.7}$$

numerical values of the multiplicative factor $\alpha_{kq}$ for rare earth ions can be found in the review article by Newman and Betty Ng (1989).

There have been many investigations on the effect of different host materials on the crystal field parameters (Newman and Stedman 1971, Stedman and Newman 1971, Lésniak 1990). Comprehensive studies have been made on magnetic ions situated in a host with cubic symmetry, (Lea et al. 1962, Hutching 1964, Birgeneau 1972). In a cubic arrangement the second order crystal fields vanish and the operator equivalent Hamiltonian is $B_4(O_4^0+5O_4^4)+B_6(O_6^0-21O_6^4)$. Hutchings (1964) tabulated the Stevens

equivalent operators $O_q^k$ of some commonly occurring potential functions and their non zero matrix elements for J states between 2 and 15/2. Lea, Leask and Wolf (1962) have calculated the eigenstates and eigenvalues for J = 2 - 8, (in steps of J = 1/2) as a function of the parameter x which characterises the ratio of fourth ($B_4$) and sixth ($B_6$) degree cubic fields splitting, and have displayed their results in energy level diagrams. The order of the energy levels depends directly upon x. There are several interesting points of high degeneracies in these graphs, which represent clustering of the energy levels: for J=8, E=300cm$^{-1}$, and x=+0.8, the ion exhibits a 6 fold degeneracy, a similar degeneracy is found when J=4, E=15 and x =+0.85. Lea et al. (1962) questioned the physical likelihood of the occurrence of these 'accidental' degeneracies, however several experimental examples have been recorded; Yeung and Newman (1985b) cited the presence of energy level clustering in $DyVO_4$, $Er^{3+}$ in garnets and $Tb^{3+}$ in $CaF_2$. Fulde and Lowenhamp (1985) demonstrated that several $PrX_2$ crystal field ground states have degeneracy close to six fold.

### 2.5.1. CRYSTAL FIELD SPLITTING IN AN AMORPHOUS MATERIAL

The topological disorder associated with the different environments of the rare earth ion introduces a randomly varying crystal field at each atomic site (Kaneyoshi 1984). Harris et al. (1972) tried to explain the continuous crystal field acting on the rare earth ions by the random anisotropy model. This assumes that there exists an uniaxial crystal field acting on each rare earth site i equal to

$$H_{CF}=-DJ_{zi}^2, \tag{2.8}$$

where $J_{zi}$ is the component of the rare earth moment along the random local axis $z_i$, and D is a constant. Experimental results suggests that D is positive; hence the lowest crystal field states are $|J_z=\pm J\rangle$. Fert and Campbell (1978) have proposed a different model based on the assumption of a general quadrupole electric field Hamiltonian;

$$H_{CF}= \alpha J_x^2 +\beta J_y^2 + \gamma J_z^2. \tag{2.9}$$

Here x, y, z, are the principle axes of each atom and $\alpha$, $\beta$, $\gamma$ have random values such that equation 2.9 is equivalent to the assumption of an uniaxial field with D always positive (at least for large J); the trace $\alpha+\beta+\gamma$ equals zero, where $\alpha$ is the most positive coefficient and $\gamma$ is the most negative. Expression 2.9 can be rewritten as

$$H_{CF}=\sum C\left(\frac{3-\eta}{6}J_{xi}^2+\frac{\eta}{3}J_{yi}^2-\frac{3+\eta}{6}J_{zi}^2\right), \tag{2.10}$$

C is a positive coefficient and $\eta$, equal to $3\beta/(\alpha-\gamma)$, is the asymmetry parameter; $\eta$ can vary between -1 ($\beta=\gamma$), corresponding to an axial field gradient along the x axis with D negative, and +1 ($\beta=\alpha$) an axial field gradient along the z axis with D positive. Fert and Campbell (1978) assumed that $(\alpha-\gamma)$ is constant, which gives an approximately constant overall crystal field splitting. For a non-Kramer ion when $\eta=1$ the ground state is a doublet $|J_z=\pm J\rangle$; as $\eta$ decreases the doublet splits into two singlets. At the limit $\eta=-1$ the ground state is a singlet $|J_x=0\rangle$ and the other singlet joins a higher state and forms a doublet $|J_x=\pm J\rangle$. For large J values ($J\geq 6$) a classical limit is reached, and the ground state doublet is only split for the value $\eta=-1$; these ions can be described within the axial field model with positive D. For Kramers ions the crystal field Hamiltonian is doubly degenerate in the ground state. When J is large the ground state doublet is $|J_z=\pm J\rangle$, and follows the uniaxial field model. When J is small the doublet changes from $|J_z=\pm J\rangle$ to $|J_x=\pm 1/2\rangle$ with decreasing $\eta$.

# CHAPTER THREE

## THE MANUFACTURE OF RARE EARTH METAPHOSPHATE GLASSES

This chapter outlines the procedures involved in the manufacture and structural characterisation of rare earth metaphosphate glasses. REMGs were fabricated from phosphorus pentoxide $P_2O_5$ and 99.9% pure rare earth (R) oxides (R=Ce, Pr, Nd, Sm, Gd, Tb, Dy, Ho, Er). The method used for the production of each of the samples is essentially the same, with the only variation arising from the different melting temperatures of the metal oxides. Senin (1994) found that the technique outlined in this chapter resulted in glasses that all had a similar metaphosphate composition $(R_2O_3)_x(P_2O_5)_{1-x}$ (where $x \sim 0.25$), regardless of the initial ratio of the constituent powders. He concluded that this stoichiometry must represented a stable form. All the samples the were prepared on the premises of the University of Bath.

### 3.1. PRODUCTION DETAILS

The proportions of phosphorus pentoxide and rare earth oxide which would produce a 40g ingot of metaphosphate (approximately 25mole% ($R_2O_3$), and 75mole% ($P_2O_5$)) glass were calculated. The powders were weighed on an electronic balance (accuracy ±1mg) and placed into an alumina crucible (100cm$^3$ capacity). Extra $P_2O_5$ (approximatly 2g) was added to the mixture to compensate for its' volatile nature. Phosphorus pentoxide is extremely hydroscopic; hence it is added to the crucible first, and the rare earth oxide acts as a protective shield over the top. The powders are then mixed thoroughly, so that the rare earth oxide is homogeneously distributed throughout the sample. The mixing was completed in a fume cupboard; however weighing and stirring of the constituent oxides would have been carried out in a dry box, if one had been available. The crucible is then covered with a lid and carefully put

into the first furnace. Phosphorus pentoxide has a relatively low melting point 580°C, and sublimes at 395°C under atmospheric pressure, so the material has to be melted in three stages, to minimise loss. It is believed that as consequence of this low vapourisation point, the samples will always have the ability to tend to the apparently stable metaphosphate composition. The crucible is transferred between three preheated muffle electric furnaces (Carbolite, UK). The furnace features are shown in figure 3.1.

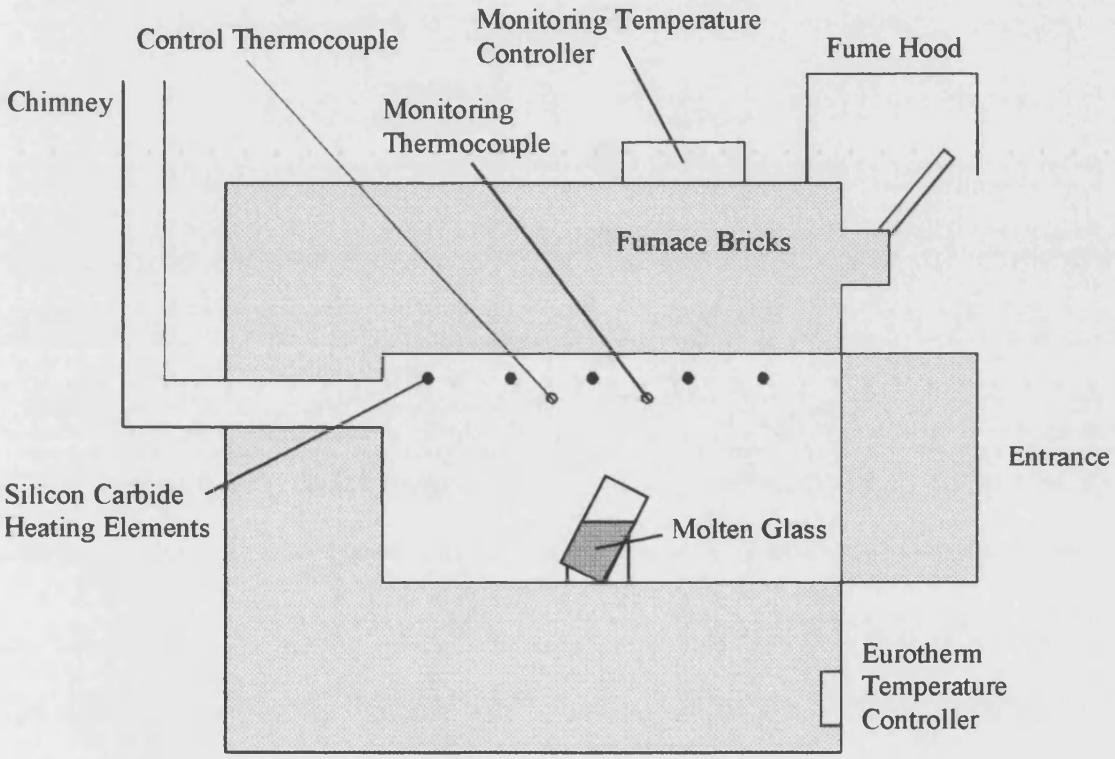


Figure 3.1. An electric muffle furnace.

1) The crucible is placed in the first furnace pre-heated to a temperature of 500°C for about one hour. During this stage the phosphorus pentoxide reacts with the rare earth oxide. The sample is neither powder or liquid, but resembles a ceramic, and due to this interaction the compound is relatively stable.

2) The mixture is then transferred to the second furnace at 1000°C. It is kept there for approximately one hour while the temperature is raised to 1400°C to ensure the sample is melted.

3) The third furnace is initially at a temperature of 1400°C and is raised until the mixture is completely molten. This depends on the melting point of the rare earth oxides (see table 3.1). The temperature is then raised and lowered approximatly a 100°C above and below the melting point, to decrease/increase the viscosity of the liquid. It is during this 'refining' process that air bubbles, which are unavoidably present in the molten sample, rise to the surface and are eradicated. The crucible stays in this furnace for 30 minutes.

The third furnace has a maximum temperature of 1400°C, which is not high enough to melt the majority of the rare earth oxides. However the furnace elements reach greater temperatures, which are achieved by `backing off` the control thermocouple, by adding an external millivolt source. With this arrangement the high temperature furnace it capable of reaching 2000°C; this is at the expense of the lifetime of the elements and furnace. The actual temperature is monitored by a digital thermometer via a platinum-rhodium/platinum thermocouple (accuracy ±5°C).

The contents of the crucible is then, via tongs, poured into a split cylindrical graphite mould. The mould (inside diameter 10mm, height 40mm) is preheated to the relative annealing temperature (table. 3.1) to reduce the possibility of thermal shock. The cast is then returned into the first furnace where it is annealed over a period of twenty-four hours. This process reduces the internal residual stresses, which would make the glass brittle and increase the probability of it fracturing during the cutting and polishing stages. Finally the furnace is turned off and the sample cools to room temperature at an approximate rate of 0.5°C minute$^{-1}$.

Safety is one of the most important factors in making these glasses. When weighing out, and mixing the powders, gloves and dust mask are worn, as protection against the highly water absorbent and corrosive nature of phosphorus pentoxide. During the heating stages high temperature reflective jacket, gloves, and protective face shield with darkened visor were donned so the sample could be viewed, and the crucible was transported between furnaces using long handled (0.5m) tongs.

| Rare earth dopant (Glass colour) | Standard for analysis | Melting Temperature (K) | Annealing Temperature (K) |
|---|---|---|---|
| Cerium (Orange) | Ce coil | 1440 | 500 |
| Praseodymium (Green) | $PrP_5O_{14}$ | 1400 | 500 |
| Neodymium (Purple) | $NdAl_2$ | 1650 | 600 |
| Samarium (Yellow) | SmS | 1650 | 600 |
| Europium (Pink) | EuS | 1550 | 600 |
| Gadolinium (Colourless) | $GdAl_2$ | 1450 | 500 |
| Terbium (Colourless) | $Tb_3Fe_5O_{12}$ | 1650 | 600 |
| Dysprosium (colourless) | $Dy_3F$ | 1600 | 600 |
| Holmium (Orange/pink) | $Ho_3F$ | 1800 | 650 |
| Erbium (Light pink) | $Er_3F$ | 1620 | 500 |

Table. 3.1. The melting and annealing temperatures of various REMGs. The standard column refers to the material used for the quantitative analysis of the rare earth metaphosphate glass composition (see section 3.2).

The resulting REMG will be an ingot of transparent glass, whose colour is determined by the rare earth dopant (table. 3.1). The final samples are stored in a desiccator. In each of the experiments, the glasses had to be prepared in different ways. For neutron investigations the samples needed no further work; to use EXAFS and x-ray diffraction techniques the materials had to be crushed, and the glasses were polished

flat and parallel for the ultrasonic and optical work. All precision cutting and polishing has been completed by Wendy Lambson, at the University of Bath. The processes involved have been documented by Senin (1994), and they allow for the surfaces to be prepared to a flatness of within one wavelength of sodium light, and a parallelism of $10^{-3}$ rad for a sample with a thickness of 5mm.

As part of the classification of the different samples the density was measured using Archimedes principle. The glass was weighed using an electronic balance, with an accuracy of ±1mg, both in air and a liquid of known density, i.e. water. The density of the sample, $\rho_s$, was then calculated using;

$$\rho_s = \rho_f \times \frac{W_a}{(W_a - W_f)} \tag{3.1}$$

where $\rho_f$ is the density of the known fluid, and $W_a$ and $W_f$ are the weight of the sample measured in air and in the fluid respectively. The density of the fluid had to be corrected for temperature dependence, to limit the error.

### 3.2. QUANTITATIVE ANALYSIS OF REMG COMPOSITION

To find out the exact composition of each of the samples, they were analysed using an electron probe microanalyser (EMPA), Joel JXA 8600M. Electron probe microanalysis works by monitoring the characteristic x-rays emitted from atoms within a specimen, after excitation by an incident electron beam. The incoming electrons are focused in to a point, to increase the sensitivity of the apparatus (figure 3.2). A portion of the glass must initially be mounted and polished. The sample is set in Fastech, a ceramic filled acrylic resin, supplied by Buehler. The mount/sample is then polished on a Buehler Metaserve Motopol 12 polishing jig. Initially the turntable is layered with 240 grit paper, rotating at 150 revolutions per minute and a pressure of 5lb per sample; after 30 seconds the coarseness of the paper is then reduced to a 1200 grit. Finally the sample is polished for 5 minutes using a combination of a Texmet diamond cloth with a steady flow colloidal silica, the rotation of the plate is reduced to 100 rev/min and the pressure increased to 7.5lbs per sample. As this resin is non-conducting the mount must be coated with a layer of carbon, prevent the build up of unwanted charge in the material during the EMPA process. This is achieved by evaporation of carbon fibre on the surface using chemical deposition. The emitted x-

ray spectrum consists of a series of peaks. These peaks have a wavelength characteristic of the excited atom, and an intensity proportional to the quantity of the element present. The electron probe microanlyser is fitted with four wavelength dispersive crystals; these are orientated at varying angles and hence detect different ranges of energy. Each crystal is specifically chosen to correspond to the emitted x-ray wavelength of one of the elements, and allows for the simultaneous measurements of up to four different atoms (phosphorus, oxygen, and the rare earth ion). For quantitative analysis standard samples, containing elements matching those in the REMG, were used as a comparison. These could be in pure or compound form as long as the exact stoichiometry is known. The standards were required to normalise the intensity data, so the composition of each material could be found. The standards used to analyse the samples investigated are listed in table 3.1, and to calculate the concentration of lanthanum, phosphorus and oxygen in the glasses, the monocrystalline ultraphosphate $LaP_5O_{14}$ was used.

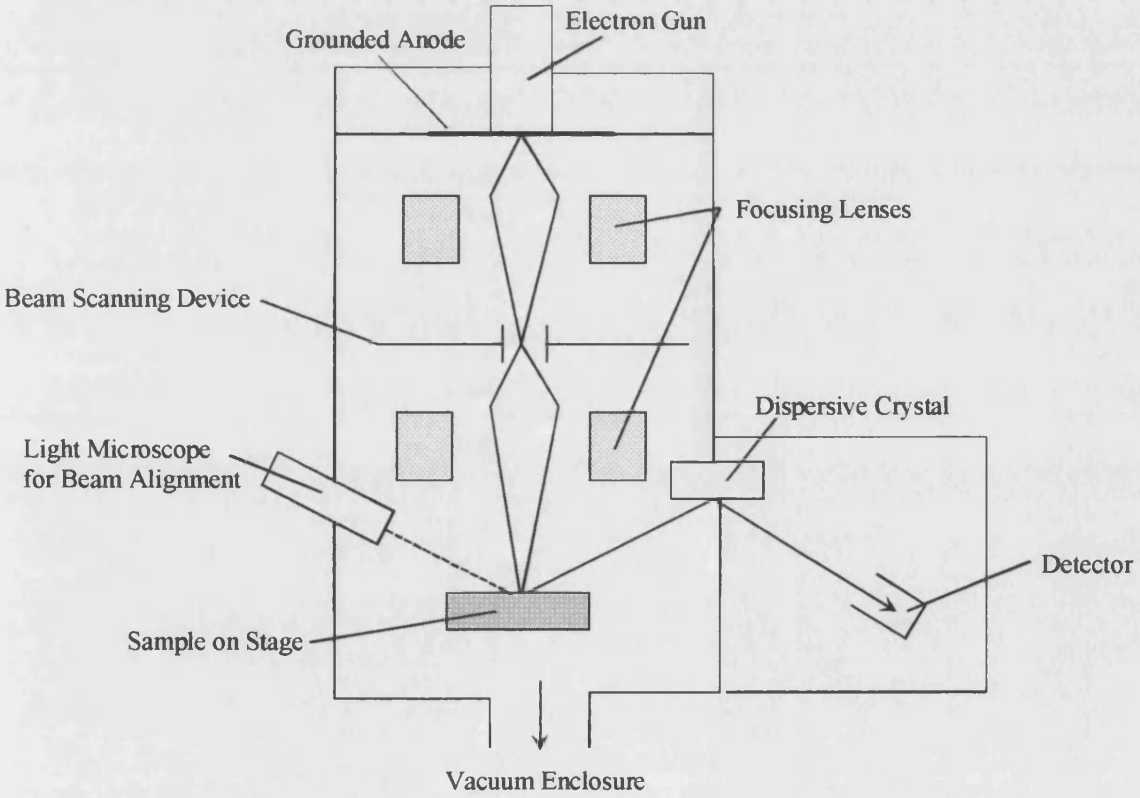


Figure 3.2. An electron probe microanalyser.

# CHAPTER FOUR

## BASIC THEORY AND INSTRUMENTATION OF X-RAY DIFFRACTION AND EXAFS EXPERIMENTS

Two key techniques in the structural analysis of vitreous materials are the complementary methods of x-ray diffraction and extended x-ray absorption fine structure (EXAFS) spectroscopy. X-ray diffraction characterises the local structure and provides information about the glass forming (phosphate in the present instance) network. EXAFS, an atom specific probe, helps define the environment surrounding the rare earth ions. Knowledge of the local atomic structure is essential to the understanding of the anomalous thermal, optical and magnetic properties exhibited by rare earth metaphosphate glasses. Many investigations have used these methods to examine phosphate glasses (Greaves et al.1985, 1988, 1989 Matsubara et al.1988, Musinu et al 1989,1995, Bruni et al. 1995) and several of those carried out by Bowron and co-workers (1994, 1995, 1996a, 1996b) focus solely on rare earth metaphosphate glasses. X-ray diffraction and EXAFS experiments have been performed at the synchrotron radiation source at Daresbury Laboratory, UK. This chapter is split into three sections: section 4.1 describes the synchrotron radiation source, sections 4.2 and 4.3 summarise the basic theory, experimental method, and data correction procedures involved with making x-ray diffraction and EXAFS measurements respectively.

### 4.1. SYNCHROTRON RADIATION SOURCE (SRS)

A synchrotron radiation source (SRS) produces a broad spectrum of 'white' radiation, with wavelengths varying from far infrared to gamma rays. This is achieved by accelerating charged particles (electrons) travelling at high velocities, which induces the emission of intense electromagnetic radiation, called synchrotron radiation.

Acceleration takes place by bending the electron beam into a circle using a series of magnets along an evacuated pipe (the storage ring), figure 4.1. The particles radiate in a direction tangential to their orbit. The intensity of the radiation will peak at a wavelength determined by the radius of curvature of the storage ring, and the energies of the electrons.

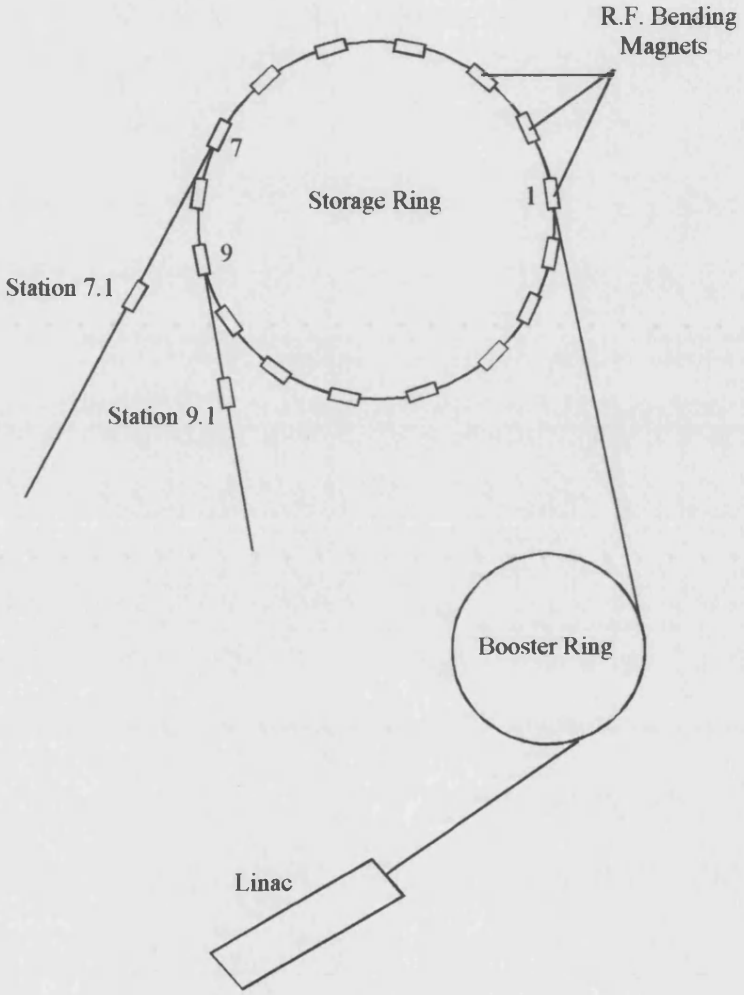


Figure 4.1 The synchrotron radiation source at Daresbury.

The SRS at the CCLRC Laboratory, Daresbury, UK can be divided into three sections, the linac (linear accelerator), the booster ring, and the storage ring, figure 4.1. The linac acts as an electron gun, particles produced at a cathode are accelerated as they travel through a series cylindrical electrodes which are alternately connected positive and negative, each possessing an increasing RF potential. The electrons, which are travelling at (near) relativistic speeds, emerge with energies of approximately 12MeV. The booster ring increases this energy still further, and the particles enter the storage ring with energies up to 600MeV. The storage ring is an

evacuated pipe with a circumference of 96m and is surrounded by sixteen 1.2 Tesla dipole bending electromagnets, which accelerate the electron to 2GeV, with typical beam currents of 200mA. The storage ring acquires its name from the fact that the electrons remain in the ring producing radiation for 10 to 20 hours. The bending magnets are at equidistant intervals, in which are placed quadrupole focusing magnets and RF cavities which are necessary to keep the beam in motion. RF pulses are applied to maintain the acceleration of the bunches of electrons and to replace the energy, which is lost when radiation is emitted at each of the bending magnets. The system is kept under a ultra high vacuum ($10^{-12}$ to$10^{-13}$ bar), which reduces the probability of scattering the charges particles. Each bending magnet has been given a number which represents its position from the point at which the electron beam is injected (1-16). This label is also shared by the beamlines, the evacuated tangential pipes which carry the synchrotron radiation to the workstations. All the stations along the line are also named numerically, number 1 corresponding to a position closest to the storage ring, see figure 4.1. The EXAFS experiments have been completed on stations 7.1, and 8.1, and the x-ray diffraction work performed on station 9.1. A wiggler has been added to beamline 9, to produce what is known as 'hard' x-ray radiation. A wiggler is a superconducting magnet that generates local high intensity fields, which results in a sharp bend in the particle's trajectory. This induces a shift in the frequency of the radiation; the peak in the intensity occurs at shorter wavelengths. On beamline 9, the wiggler is a 5 Tesla, three pole magnet which has to be kept at 4K so that it retains its superconducting properties. In each station wavelength selection is achieved by Bragg scattering from a crystal monochromator. Bragg's law determines the angle at which the crystal has to be orientated so a particular wavelength $\lambda$ is transmitted:

$$n\lambda = 2d\sin\theta \qquad (4.1)$$

where n is the harmonic number, d the separation distance of the crystal planes, and $\theta$ is the angle of incidence of the beam. The monochromators are mainly of the cut channel variety, where a single crystal (in station 9.1 this is silicon) has an angled channel cut into it for the beam to travel along, bouncing off the sides twice, before emerging from the other end. Equation 4.1. shows that higher harmonics are transmitted in this arrangement. These extra wavelengths can be suppressed by using two independent crystals that can be angled slightly differently, so their faces are not

parallel; hence the higher harmonics are attenuated more than the fundamental. This process is called harmonic rejection. In x-ray experiments harmonic rejection is usually between 40 and 60%

## 4.2. INTRODUCTION TO X-RAY DIFFRACTION

When an x-ray is incident on an atom two processes can occur: either the radiation is absorbed, this is coupled with the ejection of an electron, or the beam is scattered. The incoming x-rays mainly interact with the electrons of the atom, and the resulting scattering can be elastic or inelastic. In x-ray diffraction the elastic scattering (intensity versus $2\theta$) profile of the beam emerging from the sample is examined. This carries information of co-ordination number and atomic separation.

### 4.2.1. THEORY

X-ray diffraction can be analysed using either classical electromagnetic or quantum mechanical theory. This section outlines the main concepts of the classical approach; if an extensive review is required see X-ray diffraction by Warren (1969). Classical theory simplifies the processes involved as it ignores Compton modified scattering. Compton scattering is the term given to inelastic, incoherent scattering, during which an incoming photon scatters from an electron, producing a less energetic photon and a scattered electron. The reduction in energy of the scattered photon and accompanying increase in wavelength depends on the effective mass of the electron and the angle at which the scattered x-rays are observed. Initially consider elastic scattering from a single electron, which can be viewed as a point charge, figure 4.2.

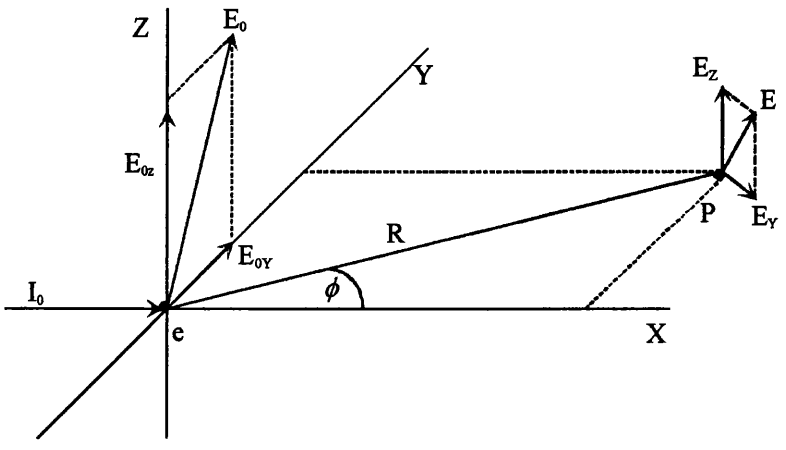


Figure 4.2. The scattering of an unpolarized x-ray beam by a single electron

R is the distance of an arbitrary point P, in the XY plane, from a single free electron and at an angle $\phi$ with the X axis. $I_0$ represents the intensity of the unpolarized incoming beam, $E_0$ is the amplitude of the electric field, and $E_{0(x,y)}$ are the resolved components of the wave. $E_0$ can take any orientation with equal probability. The incident x-ray beam can be described in terms of a sinusoidal electric field:

$$\varepsilon = E_0 \sin 2\pi\nu t \tag{4.2}$$

where $\nu$ is the frequency of the incoming wave, and t is time. A corresponding time dependent force will be exerted on the free electron causing an acceleration. An accelerated charged particle radiates, and the frequency of this radiation is determined by the frequency of the incident beam. The observed intensity (energy per unit area per unit time) of classical scattering from a single free electron is given by the Thomson equation:

$$I_{eu} = \frac{I_o}{R^2}\left(\frac{e^2}{4\pi\varepsilon_o mc^2}\right)^2 \frac{(1+\cos^2\phi)}{2} \tag{4.3}$$

m is the mass of the electron, e is the electron charge, c is the speed of light, and $(1+\cos^2\phi)/2$ is the polarisation factor for an unpolarized primary beam. All scattered intensities are measured in terms of the right hand side of equation 4.3; the unit is an electron unit, eu.

To increase the accuracy of this simple model, consider scattering from an electron whose charge is distributed over a volume. The electron is assumed to be a diffuse cloud of continuous negative charge, defined by a charge density $\rho$ in a volume dV. The scattering from this 'cloud' is a factor $\rho$dV greater than that from a single (point charge) electron. To find the intensity at an arbitrary position P, the individual contributions must be integrated over the volume, making allowances for the different path lengths, and hence phases, of the various elements. It is possible to define the scattering factor per electron $f_e$ as the amplitude of unmodified (i.e. non-Compton) scattering in electron units.

$$f_e = \int \exp\left[\frac{i2\pi}{\lambda}(\mathbf{s}-\mathbf{s}_o)\cdot\mathbf{r}\right]\rho\, dV \tag{4.4}$$

where $\lambda$ is the wavelength of the incident beam, $\mathbf{s}$, $\mathbf{s}_o$, are the incoming and scattered vectors respectively, and $\mathbf{r}$ is a position vector, see figure 4.3.

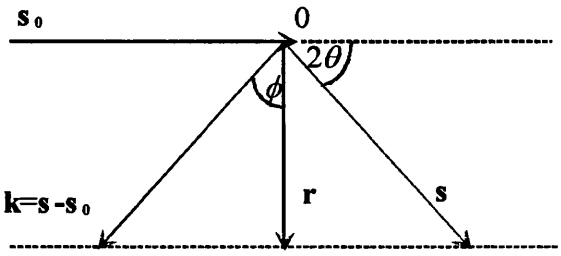


Figure 4.3. Diagram showing the relationship between the scattering vectors $\mathbf{s}_o$, $\mathbf{s}$. $\mathbf{k}$ is the difference vector ($\mathbf{k} = \mathbf{s}-\mathbf{s}_o$).

Using the following relationship,

$$k = \frac{4\pi \sin\theta}{\lambda} \tag{4.5}$$

and assuming spherical symmetry (this premis becomes more accurate as the atomic number, increases), equation 4.4 can be rewritten by substituting $\rho$ with $\rho(r)$, $(\mathbf{s}-\mathbf{s}_o).\mathbf{r}$ with $2\sin\theta r\cos\phi$, and dV by $2\pi r^2 \sin\phi\, d\phi\, dr$. Integrating $\phi$ between 0-$\pi$ the electron scattering factor becomes,

$$f_e = \int_{r=0}^{\infty} 4r^2\pi\rho(r)\frac{\sin kr}{kr}dr. \tag{4.6}$$

For an atom containing n electrons, the individual amplitudes can be summed to produce f, the 'form factor' or 'atomic scattering factor':

$$f = \sum_n f_{en} = \sum_n \int_0^{\infty} 4r^2\pi\rho_n(r)\frac{\sin kr}{kr}dr \tag{4.7}$$

The total coherent scattered intensity is $I_{eu}=ff^*$ ($f^*$ is the complex conjugate of f). These equations hold when the wavelength of the incident beam is smaller than the absorption edge wavelengths of the atom. If this condition is not met, a correction term must be included to rectify for dispersion effects (Warren 1969).

Finally expression 4.7 has to be applied to an amorphous material. For an array of randomly distributed atoms, of different types m, n, and having positions $\mathbf{r}_m$ and $\mathbf{r}_n$, the product of the atomic scattering factor for each individual atom must be found:

$$I_{eu} = \sum_m f_m \exp\left[\frac{i2\pi}{\lambda}(\mathbf{s}-\mathbf{s}_o)\cdot\mathbf{r}_m\right]\sum_n f_n \exp\left[-\frac{i2\pi}{\lambda}(\mathbf{s}-\mathbf{s}_o)\cdot\mathbf{r}_n\right] \tag{4.8}$$

Introducing the vector $\mathbf{r}_{mn}=\mathbf{r}_m-\mathbf{r}_n$, equation 4.8 becomes,

$$I_{eu}=\sum_m\sum_n f_m f_n \exp\left[\frac{i2\pi}{\lambda}(\mathbf{s}-\mathbf{s}_0)\cdot\mathbf{r}_{mn}\right] \qquad (4.9)$$

In an isotropic material the atoms have no preferential direction; hence $\mathbf{r}_{mn}$ has an equal probability of taking any orientation on the surface of a sphere, see figure 4.4.

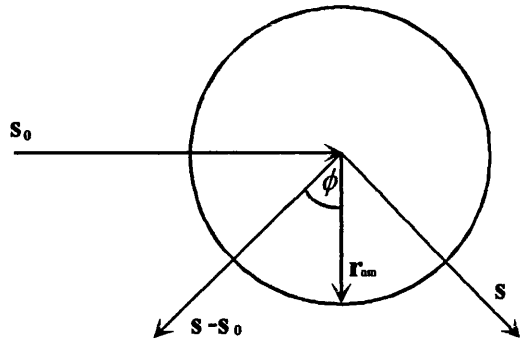


Figure 4.4. The relationship between the scattering vectors as $\mathbf{r}_{nm}$ takes all orientations in space.

By averaging over all spatial orientations, the unmodified scattering is defined by the Debye scattering equation:

$$I_{eu}=\sum_m\sum_n f_m f_n \frac{\sin kr_{mn}}{kr_{mn}} \qquad (4.10)$$

In an amorphous solid the atoms have permanent positions, well defined sizes and nearest neighbour distances, but no repeating structure. The arrangement of atoms are defined in terms of a radial distribution function J(r):

$$J(r)=4\pi r^2\rho(r) \qquad (4.11)$$

such that J(r)dr is the number of atoms between r and r+dr from the centre of an arbitrary origin atom, and the density function, $\rho(r)$, is the atomic pair correlation function. When $r < r_1$ (where $r_1$ is the nearest neighbour interatomic separation) $\rho(r)=0$, and when $r >> r_1$, $\rho(r)$=constant $\rho^0$, in-between these limits $\rho(r)$ will oscillate about $\rho^0$, the peaks in the probability function representing average interatomic separations.

If a multi-atom system is being analysed it is necessary to define a basic unit uc, which represents the overall stoichiometry of the material. Equation 4.9 can be rewritten as;

$$I_{eu}=\sum_m f_m^2+\sum_m f_m\sum_{n\neq m} f_n \exp\left[\frac{i2\pi}{\lambda}(\mathbf{s}-\mathbf{s}_o)\cdot\mathbf{r}_{nm}\right] \qquad (4.12)$$

By letting $\rho_m(\mathbf{r}_{nm})dV_n$ be the number of atoms, weighted by $f_n$, in a volume element at position $\mathbf{r}_{nm}$ from an origin atom type m, the summation over n atoms can be replaced with a volume integral. Equation 4.12 becomes:

$$I_{eu}=\sum_m f_m^2+\sum_m f_m\int_s \rho_m(\mathbf{r}_{nm})\exp\left[\frac{i2\pi}{\lambda}(\mathbf{s}-\mathbf{s}_o)\cdot\mathbf{r}_{nm}\right]dV_n. \qquad (4.13)$$

The average value of $\rho_m(\mathbf{r}_{nm})dV_n$ equals:

$$\left(\frac{N}{V}\right)\sum_{uc} f_j dV_n \qquad (4.14)$$

where N is the number of uc units per unit volume, and the subscript j represents the atom type. The above term is now added and subtracted from the equation 4.13:

$$I_{eu}=\sum_m f_m^2+\sum_m f_m\int_s\left[\rho_m(\mathbf{r}_{nm})-\frac{N}{V}\sum_{uc} f_j\right]\exp\left[\frac{i2\pi}{\lambda}(\mathbf{s}-\mathbf{s}_o)\cdot\mathbf{r}_{nm}\right]dV_n$$
$$+\sum_m f_m\int_s\frac{N}{V}\sum_{uc} f_j\exp\left[\frac{i2\pi}{\lambda}(\mathbf{s}-\mathbf{s}_o)\cdot\mathbf{r}_{nm}\right]dV \qquad (4.15)$$

The third term represents scattering in the forward direction. This peak falls in the incident beam and hence in practice it is not observed. If it is assumed that $\mathbf{r}_{nm}$ has equal probability in all directions, the exponential can be averaged over all orientations and the intensity can then be written as:

$$I_{eu}=\sum_m f_m^2+\sum_m f_m\int_s\left[\rho_m(\mathbf{r}_{nm})-\frac{N}{V}\sum_{uc} f_j\right]\frac{\sin kr_{nm}}{kr_{nm}}dV_n \qquad (4.16)$$

The $\rho_m(\mathbf{r}_{nm})$ term was only introduced to allow for averaging; hence resubstituting in $\sum f_n$, leads to:

$$I_{eu}=\sum_m f_m^2+\sum_m f_m\sum_{n\neq m} f_n\frac{\sin kr_{nm}}{kr_{nm}}-\sum_m f_m\int_s\frac{N}{V}\sum_{uc} f_j\frac{\sin kr_{nm}}{kr_{nm}}dV_n \qquad (4.17)$$

The sum over n can be replaced by the sum over the shell of neighbours i, at a distance $r_{ij}$ from atom type j. If q(r) is also introduced, and defined as being the average fraction of atoms within a sphere of radius r from atom m, equation 4.17 can be rewritten and rearranged to give:

$$k\left(\frac{I'_{eu}}{N}-\sum_{uc} f_j^2\right)=\sum_{uc} f_j\sum_i\frac{N_{ij}}{r_{ij}}f_i\sin kr_{ij}-\frac{N}{V}\left(\sum_{uc} f_j\right)^2 4\pi\int_0^\infty rq(r)\sin krdr \qquad (4.18)$$

The integral above is extended to infinity as q(r) tends to zero at large distances. To improve the convergence of the experimental signal, equation 4.18 must be multiplied by a window function W(k). This suppresses errors at high k, and thus reduces spurious data points when the interference spectrum is Fourier transformed. A sharpening factor, $1/g^2(k)$, must also be applied; this corrects the data so that it represents information arising from point scatters, and not diffuse electron distributions. A suitable g(k) is $f_e$, the average electron scattering form factor. Using the standard abbreviations:

$$i(k)=\left(\frac{I_{eu}}{N}-\sum_{uc} f_j^2\right)\frac{1}{g^2(k)} \tag{4.19}$$

$$Y(k)=4\pi\int_0^\infty rq(r)\sin krdr \tag{4.20}$$

where i(k) is called the interference function and Y(k) is negligible except for small values of k. Therefore equation 4.18 takes the form:

$$ki(k)W(k) = \sum_{uc} f_j \sum_i \frac{N_{ij}}{r_{ij}} f_i \frac{W(k)}{g^2(k)} \sin kr - \frac{N}{V}\left(\sum_{uc} f_j\right)^2 \frac{W(k)}{g^2(k)} Y(k) \tag{4.21}$$

Multiplying by sin kr and integrating from k=0 to $k=k_{max}$:

$$\int_0^{k_m} ki(k)W(k)\sin krdk = \sum_{uc}\sum_i \frac{N_{ij}}{r_{ij}} \int_0^{k_m} \frac{f_j f_i}{g^2(k)} W(k)\sin kr_{ij}\sin krdk$$

$$-\frac{N}{V}\int_0^{k_m}\left(\sum_{uc} f_j\right)^2 \frac{W(k)}{g^2(k)} Y(k)\sin krdk \tag{4.22}$$

Due to the nature of Y(k) the slow varying quantities in last term in the equation 4.22 can be replaced with the values at k=0, and integrating to ∞:

$$\frac{N}{V}\left(\sum_{uc} Z_j\right)^2 \int_0^\infty Y(k)\sin krdk \tag{4.23}$$

where $\Sigma Z_j$ is the total number of electrons in the scattering unit. As Y(k) is the Fourier transform of rq(r), it is possible to write:

$$2\pi^2 rq(r) = \int_0^\infty Y(k)\sin krdk \tag{4.24}$$

If it is assumed q(r)=1.0 for small values of r, and $\rho_e$ is the average electron density, equation 4.22 becomes:

$$\sum_{uc}\sum_{i}\frac{N_{ij}}{r_{ij}}\int_{o}^{k_m}\frac{f_i f_j}{g^2(k)}W(k)\sin kr_{ij}\sin krdk = 2\pi^2 r\rho_e\sum_{uc}Z_j + \int_0^{\infty} ki(k)W(k)\sin krdk \quad (4.25)$$

To simplify the above equation the pair function $P_{ij}(r)$, is introduced;

$$P_{ij}(r) = \int_0^{k_m}\frac{f_i f_j}{g^2(k)}W(k)\sin kr_{ij}\sin krdk \quad (4.26)$$

Using the trigonometric identity, $\sin kr_{ij} \sin kr = [\cos(r-r_{ij})k - \cos(r+r_{ij})]/2$ an auxiliary formula can be created:

$$Q_{ij}(x) = \frac{1}{2}\int_0^{k_m}\frac{f_i f_j}{g^2(k)}W(k)\cos xkdk \quad (4.27)$$

Where: $$P_{ij}(r) = Q_{ij}(r - r_{ij}) - Q_{ij}(r + r_{ij}) \quad (4.28)$$

The first term in equation 4.28 dominates, and the second term can be neglected. Finally equation 4.25 can be written as:

$$\sum_{uc}\sum_{i}\frac{N_{ij}}{r_{ij}}P_{ij}(r) = 2\pi^2 r\rho_e\sum_{uc}Z_j + \int_0^{k_m} ki(k)W(k)\sin krdk \quad (4.29)$$

The right hand side of this expression is evaluated from the experimental results. A number of data correction procedures initially have to be executed see Bowron (1994) (summarised in section 4.2.3) to isolate the interference function i(k). Structural information is then obtained from the electron distribution function t(r), which is evaluated using the Fourier transform relation (this is essentially defined by equation 4.29),

$$t(r) = 2\pi^2 r\rho_e\sum_{uc}Z_j + \int_0^{k_m} ki(k)W(k)\sin krdk \quad (4.30)$$

The t(r) function is a complex distribution function representing the electron density variations within the sample, and although is contains useful information, extra independent data i.e. from EXAFS, is required to assist in extracting it. Once the function t(r) has been acquired and plotted against distance r, see figure 4.5, the positions and areas of the peaks can be found by fitting a series of gaussian curves to the t(r) spectrum. The gaussian peaks were fitted to the data using a method of non-linear least squares testing, which iterated the heights, widths and positions. The position of the peaks in the data correspond to the various interatomic correlation distances $r_{ij}$ i.e. P-O, R-O. By comparing the area of gaussian peaks with the area of the pair functions $P_{ij}$, the co-ordination numbers can be determined (equation 4.26).

However, the co-ordination numbers are only approximate as the majority of peaks lack the isolation required by the fitting program to assign accurate weighting to the individual gaussian profiles. The values for $P_{ij}$, calculated at the different $r_{ij}$, also have an associated error resulting from the uncertainty in the magnitude of the area contained in the 'tails' of the transformed function (equation 4.26).

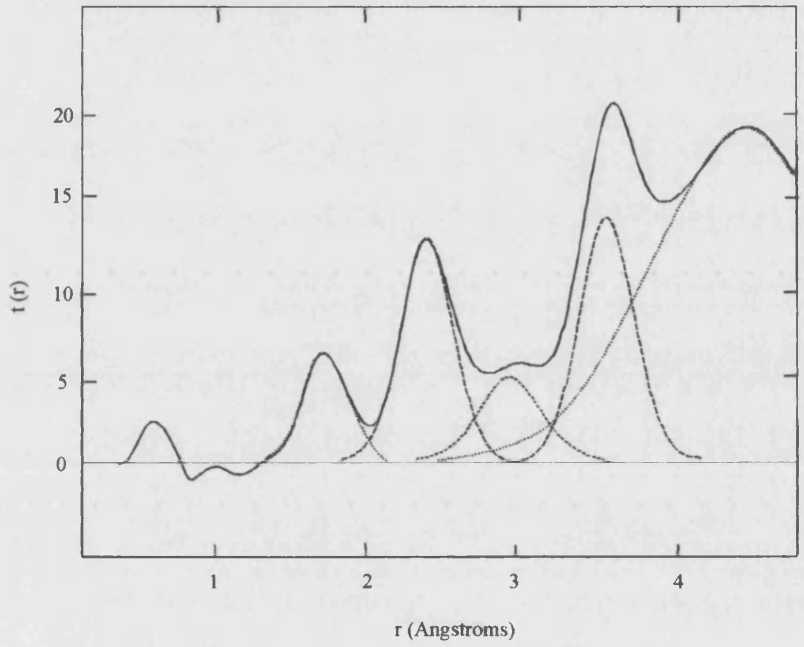


Figure 4.5. Example of an electron distribution function, t(r), fitted with Gaussian profiles

### 4.2.2 $\theta/2\theta$ DIFFRACTION APPARATUS

The experiments performed at Daresbury Laboratory UK used a conventional $\theta/2\theta$ geometry where $\phi$, the scattering angle, is fixed to always be twice $\theta$, the angle of sample orientation, see figure 4.6. A $\theta/2\theta$ geometry is adopted as it allows for simplification of the correction procedures i.e. absorption corrections (Bowron 1994). The approaching x-rays are passed through a monochromator to select an individual wavelength (~0.5Å). A piece of kapon foil is placed between the monochromator and the sample. This scatters a small portion of the incident beam towards a scintillation counter, the recorded count rate is subsequently used to normalise the data. The radiation diffracted from the sample passes through a pair of beam profile definition slits, and is detected at an angle of $2\theta$, ($\phi$). This counter is mounted on a rotating arm,

whose axis coincides with the samples centre of rotation. Typical scan ranges are between $\phi = 2°$ to 130° in steps of 0.2° (in k (=$(4\pi\sin\theta)/\lambda$) terms 0.4 - 23 $Å^{-1}$). The detector either collects photons for an equal time interval at each angle, or for a fixed number of counts; the REMG experiments employed the first method, recording scattering events for the duration of 10 seconds. The samples are prepared for x-ray diffraction experiments by crushing the bulk glass into coarse granules between two metal plates. It is then ground still further with a pestle and mortar, and the subsequent powder (~1$\mu$m) is layered onto sticky tape and placed into the path of the beam. It was important to keep the layer thin as the x-ray absorption properties of REMGs are quite servere.

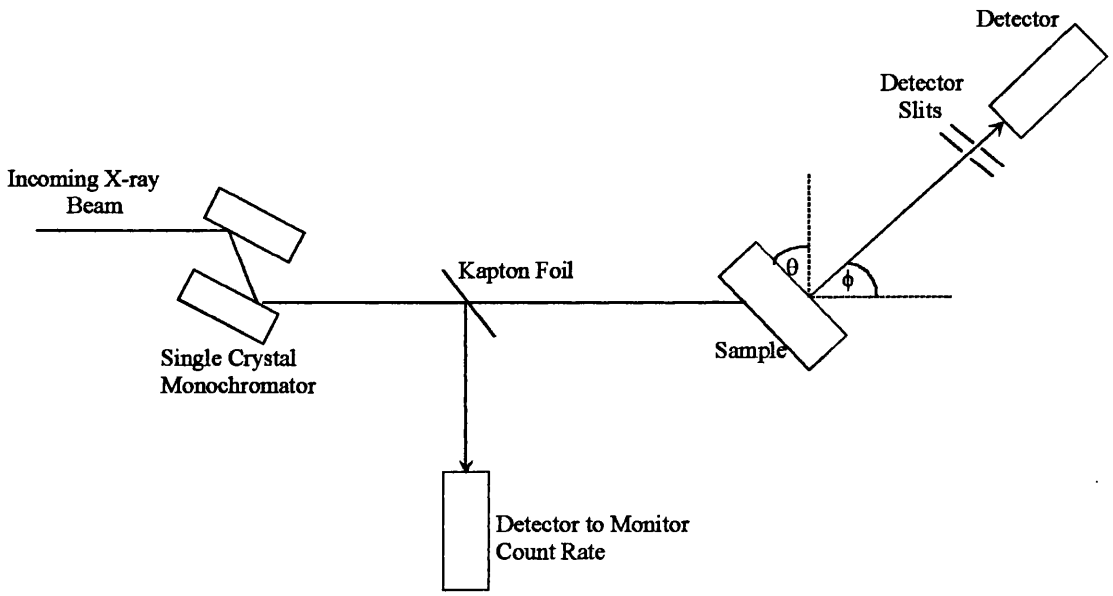


Figure 4.6. Schematic of a diffraction experiment.

### 4.2.3. DATA CORRECTION PROCEDURES

A brief description of the x-ray diffraction data correction procedures required to isolate the interference function i(k) are listed below, for a full account see Bowron 1994. The subsequent extraction of structural information has been discussed in section 4.2.1.

a) Dead time corrections. The dead time $\tau$ is defined as the minimum time interval required by the detector electronics to resolve two individual scattering events. Corrections have to be made to account for increases in the incident photon flux on

the detector, and hence the loss in resolution of different events. If the dead time of the detector is ignored, the error in 10000cps is the order of 1%, if $\tau = 10^{-6}$s.

b) Polarization factors. The intensity of the diffracted beam depends on the polarization ($P_{\parallel}$, parallel and $P_{\perp}$, perpendicular to the scattering plane) of the incident x-ray beam (see equation 4.3). The polarization of the incoming x-ray beam is source dependent; for station 9.1 at the SRS, Daresbury, UK., 90% of the x-rays are $P_{\perp}$ polarized and 10% have $P_{\parallel}$ polarization.

c) Normalisation. Normalisation corrects for time dependent fluctuations in the incident x-ray flux, and accounts for the different collection times required at varying detector angles to ensure uniform statistics. The counts were re-scaled using the data scattered from a kapon foil placed before the sample (see figure 4.6).

d) Background corrections. These eliminate scattering that arises from the sample holder, air, etc. A background scan is made of an empty sample holder, over the same angular range, in order that the subtractions can be implemented. This extra scan also has to be corrected for dead time and beam polarization corrections.

After the sample and instrumental corrections have been implemented the wavelength dependent corrections have to be applied.

e) Compton Scattering. Compton scattering defines the incoherent scattering intensity, and can be modelled and subtracted using either theoretical, or experimental methods (Warren et al. 1965, Bushnell-Wye et al. 1992).

f) Absorption correction. As the x-rays travel through the sample, the beam suffers a degree of attenuation, resulting in a reduction of the intensity. The magnitude of this effect depends on the absorption coefficient and the path length of the x-rays through the sample.

g) Atomic self scattering. Self or independent scattering describes the scattering from the electron distributions of individual atoms within the system. The correction depends on the sum of the squares of the atomic scattering factor, $f_j$, for each atom in a unit of composition. Once this has been calculated, the experimental intensity can be scaled so that it oscillates about the self scattering function; this is equivalent to normalising the data so that it represents scattering from a unit of composition. The self-scattering function is then subtracted from the scaled intensity and the remaining difference function is divided by the square of the sharpening factor $g^2(k)$ (typically

having the form $f_e^2$, the average electron scattering form factor)(equation 4.19). Defining a unit of composition in the phosphate glass is problematic due to the $P_2O_5$ volatilization losses during sample manufacture. A good approximation to the composition of the samples studied is the metaphosphate glass stoichiometry $R(PO_3)_3$.
f) Binning of data into k space. Finally the intensity is transformed from a function of angle $\theta$, to a function of scattering vector k (= $4\pi\sin\theta/\lambda$). The data is binned so that the results are evenly distributed spaced in k. This improves the statistical accuracy of the data at large momentums.

The interference function i(k) is now in a condition where it can multiplied by the window function, and subsequently Fourier transformed (equation 4.30). The resulting radial distribution function t(r) contains the structural information. The window function truncates the spectrum and is required to reduce the errors introduced by the fact that the i(k) is recorded over a finite k range. The window function has to be chosen and used with care as it can also produce artificial ripples in the t(r) data (Fourier series termination effects). For the analysis of the rare earth metaphosphate glasses, W(k) has the following characteristics

$$\begin{aligned} &= 1-3(k/k_{max})^2 && |k|< k_{max}/3 \\ W(k) \quad &= 3/2(1-2|\,k/k_{max}|+(k/k_{max})^2) && k_{max}/3< |k|< k_{max} \\ &= 0 && |k| >k_{max} \end{aligned} \qquad (4.31)$$

Another popular window function has the form $W(k)=\sin(\pi k/k_{max})/(\pi k/k_{max})$, this has the advantage that it produces a much gentler cut off than the traditional step functions, however the there is a trade off in resolution (broadening of the peaks in the transform) (Cusack 1987). The electron density function is fitted with pair functions $P_{ij}$ defined in equation 4.26. The peak positions give the interatomic correlation distances $r_{ij}$, and the ratio of the area given by the pair function to the area under the peaks in the t(r) curve gives the co-ordination number $N_{ij}$, corresponding to the number of distances $r_{ij}$ in the scattering unit.

## 4.3 INTRODUCTION TO EXAFS

Extended x-ray absorption fine structure (EXAFS) spectroscopy is concerned with determining the short range interatomic correlation between a given ion and the surrounding atoms. This atom specific probe studies the high energy side of the

absorption edge spectrum corresponding to a particular atom. Close to the edge the absorption coefficient of the outgoing excited photoelectrons is modulated by electron scattering processes, and it is this complex oscillatory form, see figure 4.7, which is known as EXAFS.

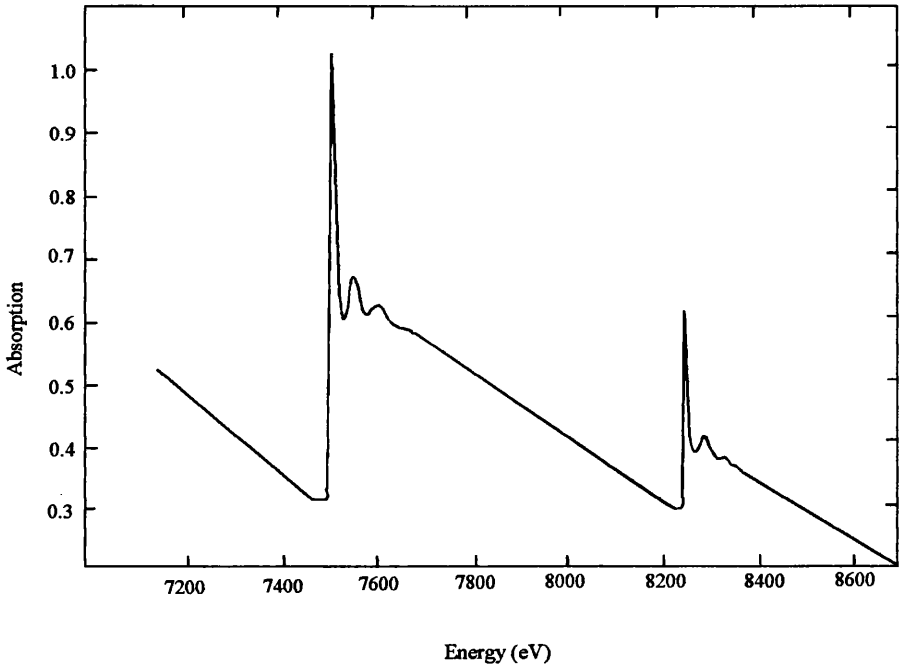


Figure 4.7. Example of the $L_{II}$ and $L_{III}$ absorption edges for terbium (Bowron 1994).

### 4.3.1 THEORY

The theory and application of EXAFS has been extensively documented, and this synopsis follows the arguments presented in the review paper by Haynes and Boyce (1982), and the books by Eberhart (1991) and Elliott (1990).

If a photon incident on an atom has an energy greater than the ionisation threshold of that atom, it will be absorbed with the ejection of a photoelectron from the K or L shell. This is called an absorption edge and manifests itself as a step function in the x-ray absorption (figure 4.7). For an isolated atom the photoelectron propagates to infinity, and the absorption coefficient decreases smoothly from the absorption edge. For an atom in a condensed material the departing photoelectron is back scattered by the surrounding particles. The outgoing and partially back scattered waves interfere, producing constructive and destructive interference fringes, which depend on the photon energy and the corresponding wavelength, figure 4.8. The oscillations are

characteristic of the number of nearest neighbours, the type of atom, and how far away they are.

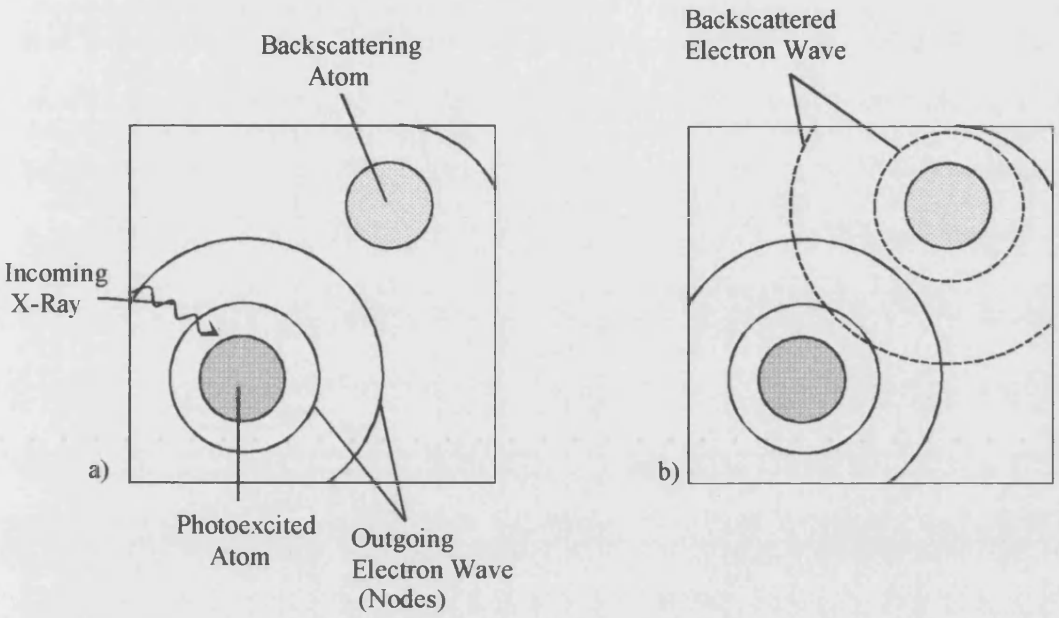


Figure 4.8. The interference process involved in producing extended x-ray absorption fine structure (after Haynes and Boyce 1982).

The process can be treated using a semi-classical approach, assuming that absorption can be modelled on first order perturbation theory. The probability P that the x-ray photon is absorbed can be calculated from Fermi's golden rule (a general rule describing transition rates):

$$P = \frac{2\pi^2 e^2}{hc^2\omega}\left|\int \psi_f^* \varepsilon \, \mathbf{r} \psi_i \, d^3r\right| \rho(E_f) \qquad (4.32)$$

Here $\psi_f$ and $\psi_i$ are the initial and final state wavefunctions of the core electron/photoelectron, $\omega$ is the angular frequency of the x-ray photon, $\rho(E_F)$ is the density of final states to which the electron is excited, $E_F$ is the Fermi energy level, **r** is the position vector of the electron, $\varepsilon$ the polarization state vector of the incoming x-ray, e is the charge of an electron, h is Planck's constant, and c is the speed of light in free space. For energies beyond the absorption edge, the final density of states, $\rho(E_F)$, can be approximated to a free electron. Therefore, it can be seen from studying equation 4.32, that the matrix element $\psi_f$ is the only term which can vary and hence must give rise to the observed oscillations. This is due to a final state interference

effect between the outgoing photoelectron wavefunction and the coherent, but phase shifted, back scattered wave. The phase difference occurs predominately due to the distance the wave travels, although there are energy dependent contributions arising from the backscattering atoms potentials. The oscillations are damped (see figure 4.7) because when the photoelectron propagates outwards from the core, as a spherical wave, an excited electron relaxes into the remaining empty 'hole' causing alterations to the wavefunction, and deterioration of the coherency. The absorption coefficient $\mu$ can be written as a combination of two factors, $\mu_0$(k) is the absorption if there is no backscattering, and $\chi$(k) is the modulation function:

$$\mu\ (\mathrm{k}) = \mu_0(\mathrm{k})\big(1+\chi\ (\mathrm{k})\big). \qquad (4.33)$$

Here k represents $|\mathbf{k}|$ for the wave vector $\mathbf{k} = 2\pi/\lambda$ (the absorption coefficients can also be expressed as functions of energy, E), and $\lambda$ is the wavelength of the electron. EXAFS can hence be considered as a problem of solving $\chi$(k). Interpretation of the data can be based upon classical interference arguments for two waves, and are simplified by introducing three approximations.

1) Only a single photoelectron is generated, and this suffers no other interactions as it leaves the atom.

2) A single backscattering process is considered, multiple scattering is ignored.

3) The atoms are small compared to the interatomic distances, and hence the spherical wavefront is viewed as planar. This assumption improves with high photoelectron energy (80eV from the edge).

An expression for $\chi$(k) can then be formulated by using a simple heuristic plane wave equation:

$$\chi\ (\mathrm{k}) = \mathrm{A}(\mathrm{k})\sum_{ij}\frac{\mathrm{N_j}}{\mathrm{kR_{ij}^2}}\left|\mathrm{f_j}(\mathrm{k}\pi)\right|\sin(2\mathrm{kR_{ij}}+2\delta_i+\varphi_j)\exp\left(-\frac{2\mathrm{R_{ij}}}{\lambda}\right)\exp\left(-2\sigma_{ij}^2\mathrm{k}^2\right) \qquad (4.34)$$

where $N_j$ are the number of backscattering atoms j, at distance $R_{ij}$ from the absorbing atom i. $f_i(k\pi)$ is the backscattered amplitude from the jth shell, and A(k) is an amplitude reduction factor (between 0.6-0.8) that accounts for inelastic scattering within the sample and depends on the atomic number of the excited atom. The attenuation of the beam is represented by both the mean free path for the inelastic scattering $\lambda$, which characterises the loss of coherence caused by the finite lifetime of the core hole, and a Debye-Waller term, which involves displacements $\sigma_{ij}$ about the

equilibrium bond length due to thermal and structural disorder. The $\delta$ and $\varphi$ terms represent the phase shift of the electron wave arising from modulation by the atomic potentials of the emitting and backscattering atom; both are functions of the electrons momentum |**k**|. Each shell produces a sinusoidal contribution (of varying frequency) to the EXAFS function, and hence it has a complex form. Structural information is extracted by fitting gaussian peaks to the EXAFS spectrum. However in equation 4.34 the atom distribution of the $i^{th}$ shell of neighbouring atoms is asymmetric arising from the inclusion of the $\exp(-2R_{ij}/\lambda)$ term. Consequently the fitted $R_{ij}$ distance is shorter than the actual mean distance by $(2\sigma^2/R_{ij})(1+R_{ij}/\lambda)$; this factor is small and in most cases can be ignored (Crozier 1997). The effect of the anharmonic potentials, for strong thermal or static disorder, can be integrated into equation 4.34 using a method of cumulant fitting (Crozier 1997, Anderson et al. 1998), this effectively introduces extra terms to produce skewed gaussians:

$$\chi(\mathrm{k}) = \mathrm{A(k)} \sum_{ij} \frac{\mathrm{N_j}}{\mathrm{kR_{ij}^2}} \left| \mathrm{f_j}(k\pi) \right| \sin\left( 2\mathrm{kR_{ij}} + 2\delta_i + \varphi_j + \frac{4}{3}\mathrm{C_3 k^3} \right) \exp\left( -\frac{2\mathrm{R_{ij}}}{\lambda} \right) \exp\left( -2\sigma_{ij}^2 \mathrm{k}^2 + \frac{2}{3}\mathrm{C_4 k^4} \right) \quad (4.35)$$

The constants $C_3$ and $C_4$ are the third and fourth cumulants respectively. For the rare earth metaphosphate glasses studied, the constants were found to have values of approximatly $C_3$=0.001Å$^3$ and $C_4$=0.0001Å$^4$ and consequently are not highly significant. Structural information is extracted from the EXAFS signal using a suite of correction programs at the Daresbury Laboratory, EXCALIB, EXBACK, EXCURV92; these allow for the summation of multiple data sets and edge calibration, carry out pre- and post-edge energy subtractions and normalisation, and finally fits the EXAFS spectrum using fast curved waved theory, described by Gurman et al. (1984, 1986). Co-ordination numbers, and nearest neighbour distances can be extracted from the Fourier transform of the isolated $\chi$(k) functions, which gives the pair distribution function of the short range order.

### 4.3.2 TRANSMISSION EXAFS APPARATUS

The absorption spectrum can be measured using either a fluorescence or transmission geometry. At the synchrotron radiation source at Daresbury Laboratory, stations 7.1

and 8.1, the latter arrangement was utilised and a schematic representation is shown in figure 4.9.

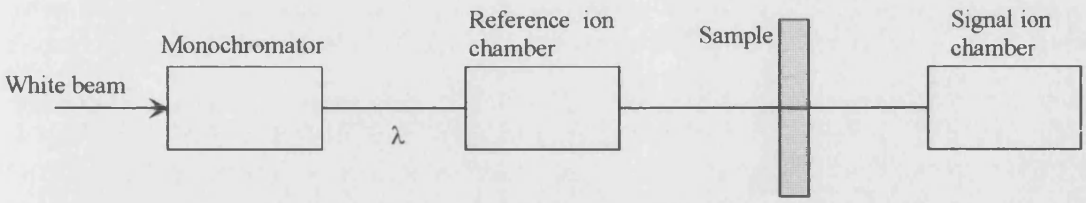


Figure 4.9. Schematic of a transmission geometry EXAFS experiment.

The wavelength of the incoming beam is selected using a monochromator (station 7.1 uses a double crystal Si(111) and station 8.1 uses either a Si(111) or a Si(220)). By changing the angle of the monochromating crystals the absorption edge of an individual atom can be selected and scanned as a function of the corresponding photon energy. The K and $L_{III}$ adsorption edges are predominantly probed; the $L_I$ and $L_{II}$ edges suffer interference from the preceding, lower energy edges (i.e. the $L_{II}$ and $L_{III}$), which complicates data extraction. As the x-rays pass through the sample, the beam is attenuated;

$$I_t = I_0 \exp^{-(\mu(E)x)} \tag{4.36}$$

$I_t$, $I_0$ are the intensities before and after the sample, x is the sample thickness, and $\mu(E)$ is the linear attenuation coefficient, see equation 4.33. $I_0$ and $I_t$ are measured directly by the reference, and the signal ion chamber (filled with a mixture of helium and argon gasses), respectively. The samples are prepared for EXAFS measurements in the same way as for x-ray diffraction experiments (section 4.2.2); the sample is ground and the resulting powder is layered onto sticky tape and placed into the beam. Several layers were usually required to achieve uniformity across the beam and a near-optimum absorption edge step, corresponding to a pre-edge to post-edge step of 0.5 - 1.5. The sample is mounted in a variable temperature cryostat for the 145K, and 77K measurements. The k range of the rare earth ion $L_{III}$ edge is limited by the presence of the $L_{II}$ edge, and spans approximatly 2 to 12Å$^{-1}$ (which corresponds to 4 to 24 Å$^{-1}$ in conventional x-ray diffraction terms, equation.4.5). Once $\mu(E)$ has been defined $\chi(E)$ can be found by subtracting the slow varying background $\mu_0$ and normalising (equation 4.33). Background absorption occurs as a result of the excitation of

electrons in higher (less tightly bound) shells. Finally the interference function can be Fourier transformed, so the structural information can be extracted.

### 4.3.3. DATA CORRECTION PROCEDURES

The data correction procedures involved in the isolation of the oscillatory signal (figure 4.7), can be divided into five sections.

a) Summation of data sets and energy scale calibration. Initially the transmitted x-ray intensity $I_t$ is normalised by the incident intensity $I_0$ (see equation 4.36), and multiple 'like' spectrums (same sample and temperature) are subsequently summed to improve the statistics of the data; these process are completed using the EXCALIB program. The position of the absorption edge is then calibrated, to check for any misalignment of the monochromator. The calibrant samples used were 5μm thick metal foils (Cr, Fe, Co, Ni) that had a precisely known $K_\alpha$ absorption edge, at an energy close to the $L_{III}$ edge of the glass sample being studied.

b) Glitch removal. This correction procedure eliminates any relatively large sharp structure in the EXAFS signal that have arisen from multiple reflections in the monochromator crystal. Points are interpolated from data on either side of the unwanted glitch.

c) Pre-edge background removal. All unwanted contributions to absorption, such as Compton scattering and lower energy absorption edges, are removed. This is achieved by fitting a linear function to the pre-edge data, extrapolating it over the total energy range, and then subtracting it from the signal.

d) Post-edge fitting, background removal and normalisation. The unmodulated background absorption for the post-edge, $\mu_0(k)$, is determined and on evaluating this the EXAFS signal can be isolated. There are several method for modelling the background of the post edge, the simplest evolves fitting a low order polynomial, which ignores the oscillations. This is a critical stage in the data correction procedure and failure to produce a satisfactory fit will lead to non-physical artefacts in the spectrum. The data is then corrected and normalised using the following equation:

$$\chi(k) = \frac{\mu(k) - \mu_o(k)}{\mu_o(k)} \qquad (4.37)$$

All background subtractions (pre and post edge) and normalisation processes have been accomplished using a program called EXBACK.

e) Extraction of structural information. Final stage of the data corrections is completed using a computer program called EXCURV92 (Joyner et al 1987). This analyses the modulation function using the small atom approximation (or fast curved wave theory) as developed by Gurman et al (1984, 1986). EXCURV92 is essentially a non-linear least squares fitting procedure which uses statistical significance tests to isolate experimental parameters, such as A(k) the amplitude reduction factor, $\lambda$ the mean free path length, $R_i$ the distance from the absorbing atom i, $N_i$ co-ordination number of shell i, and $\sigma^2$ a thermal and structural disorder parameter, equation 4.34. The fit parameters can be determined using correlation maps between strongly correlated parameters, i.e. $N_i$ and $\sigma$, or $R_i$ and $E_F$ a phaseshift (effective energy fit) parameter (figure 4.10). The map consists of a series of contours showing the variation in goodness of fit for a interrelated pair of parameters. The bold contour on figure 4.10 represents 95% confidence interval around the least sum of squares (marked by the cross on the plot), and it is the projection of this ellipse on the relevant axis which gives the error.

An EXAFS spectrum from monocrystalline neodymium ultraphosphate $NdP_5O_{14}$ has been recorded as a standard, to allow calibration of the data analysis parameters used in EXCURV92. Data calibration has been achieved by defining the structural parameters of the Nd ultraphosphate, as previously determined by x-ray diffraction (Hong 1974a), in EXCURV92. Once the bond length and co-ordination numbers have been fixed, data fitting can be performed to give a suitable amplitude reduction factor A(k), and the lifetime of the photoelectron. This process allows confirmation of the rare earth phase shifts $\delta$ and $\varphi$ between experiment and theoretical calculation (equation 4.34). The data demonstrates that a suitable amplitude factor would be 0.7; this is consistent with previous investigations by Bowron et al. (1996 a, b), and was held at this value for the following rare earth metaphosphate glass calculations. During the final stages of the analysis, the data is $k^3$ weighted, which has the effect of increasing the reliability of the results at higher energies, where the signal is weak, and suppressing low energy data which is complicated by multiple scattering processes. Multiple scattering can be significant (up to 10% of single scattering value) for k values up to $7Å^{-1}$ depending on the structure. However the effect is negligible at distances corresponding to the nearest neighbour shell (Crozier 1997, Anderson et al

1998). The fitting procedures does not included multiple scattering corrections, hence interpretation of data exceeding the first shell must be made with care.

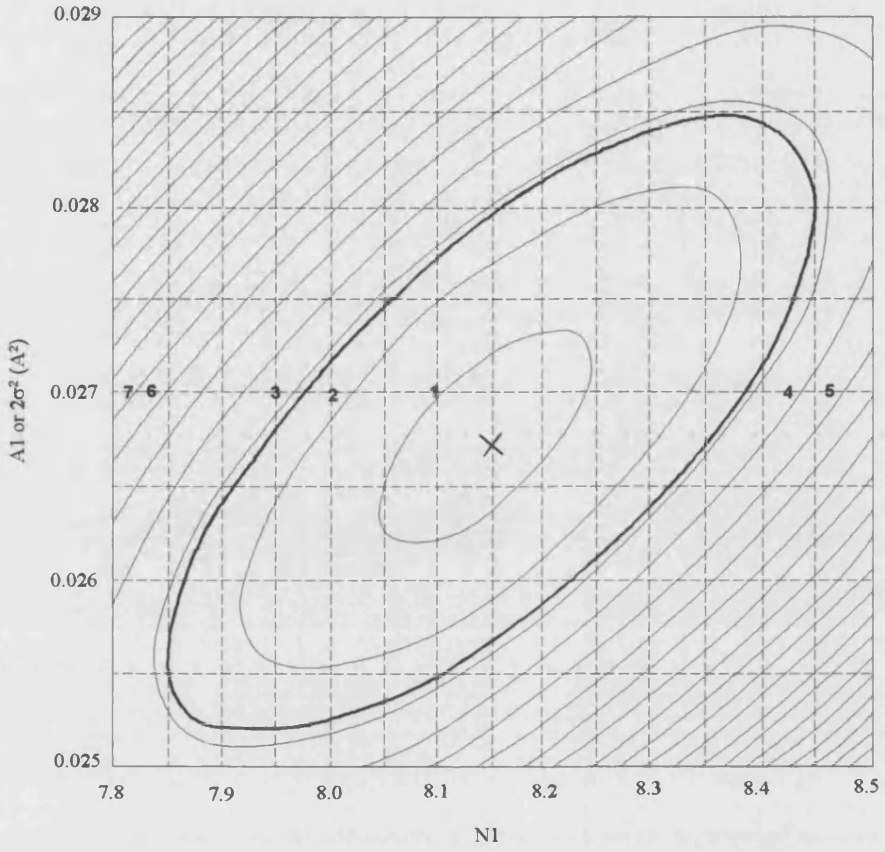


Figure 4.10. Correlation map for neodymium metaphosphate glass $(Nd_2O_3)_{0.187}$ $(P_2O_5)_{0.813}$, at 79K showing the goodness of the fit for the parameters N1 (number of neighbouring oxygen atoms in the first shell) and A1 or $2\sigma^2$ (the Debye-Waller factor for the first shell). The cross represents the least sum of squares.

# CHAPTER FIVE

## RESULTS AND DISCUSSION OF X-RAY DIFFRACTION AND EXAFS EXPERIMENTS

Knowledge of the short range structure of rare earth metaphosphate glasses on an atomic scale is essential if the properties of these materials are to be fully understood. Previous investigations using the complementary probes of x-ray diffraction and EXAFS (Bowron et al. 1994, 1995, 1996a, 1996b, Anderson et al 1998) have shown the structure of REMGs are based on a three-dimensional network of corner linked $PO_4$ tetrahedra, with trivalent lanthanide ions occupying sites within the phosphate skeleton. The majority of the structural work on REMGs has been carried out using EXAFS techniques; however, there is no information on the temperature dependence of the co-ordination numbers and nearest neighbour distances. This investigation aimed to satisfy the need for temperature based structural data, and hence establish whether the anomalous properties seen in rare earth doped phosphate glasses may, in part, be attributed to the changes in the microscopic structure as the temperature is changed. X-ray diffraction investigations are scarce on these glasses (previous measurements only include metaphosphate glasses doped with $La^{3+}$, $Pr^{3+}$, $Eu^{3+}$, and $Tb^{3+}$ (Bowron et al. 1995, 1996b, Hoppe et al 1998b)); hence the present experiments vastly increase the available data. Analysis of the data has been completed by Ruth Anderson and Jacqui Cole from The University of Kent at Canterbury; a synopses of the procedures are given in sections 4.2.3 and 4.3.3. The results are tabulated and compared with the existing data on REMGs.

## 5.1. X-RAY DIFFRACTION, RESULTS AND DISCUSSION

The x-ray diffraction spectra have been measured for seven metaphosphate glasses doped with trivalent Ce, Nd, Sm, Gd, Dy, Ho, and Er. All the samples have been investigated at room temperature (293K).

Typical data sets are shown in figures 5.1 to 5.6 for cerium and erbium doped metaphosphate glass. There are three graphs for each sample. Figures 5.1 and 5.4 contain the diffraction intensity spectra (solid lines) corrected for experimental background effects and scaled to the self (or independent) scattering function. The self-scattering polynomial is the sum of the squares of the atomic scattering factors and has been determined by taking the unit of composition for a metaphosphate glass to be $R(PO_3)_3$. After subtraction of the self-scattering function from the experimental data, the results have been normalised by dividing by a sharpening factor g(k) ($=f_e^2$ where $f_e$ is the average electron scattering function) (equation 4.19). The resultant is the interference function i(k) (figures 5.2 and 5.5). The Fourier transformation of the interference function gives the electron density distribution function t(r) of the system, figure 5.3, 5.6 (equation 4.30). Seven gaussian profiles have been fitted to the t(r) curve, and can be interpreted as representing the scaled pair distribution function $P_{ij}$ evaluated at various $r_{ij}$. The peak positions of the gaussians correspond to correlations between known atom parings such as P-O and R-O and the ratio of the area given by the pair function to the area under the gaussians determines the co-ordination number $N_{ij}$. A summary of all the data collected is presented in table 5.1. The gaussians were fitted to the t(r) data by allowing the defining parameters (peak position, height and width) to vary in a range of values determined by taking metaphosphate and ultraphosphate compositions (plus an error margin) as the extremes; the theoretical compositions were based on a combination of crystal structure data and computer simulations. The error in the peak positions is estimated to be ±0.02Å and the error in the co-ordination number is approximatly ±10%. The error in the co-ordination number varies depending on the whether the peaks in the experimental t(r) can be represented by an individual or combination of gaussians. Apart from the first P-O peak, overlap between neighbouring gaussians increases the difficulty in assigning unique weightings to the individual fits, an effect which increases the errors at larger r(Å)'s. The co-ordination number of the last peak (R-(O-P)-O) includes errors

resulting from all the other gaussian fits as well as from features which occur, and have not been modelled, at distances in excess of ~ 4.5 Å; consequently it is thought of as a 'buffer zone' and is effectively ignored.

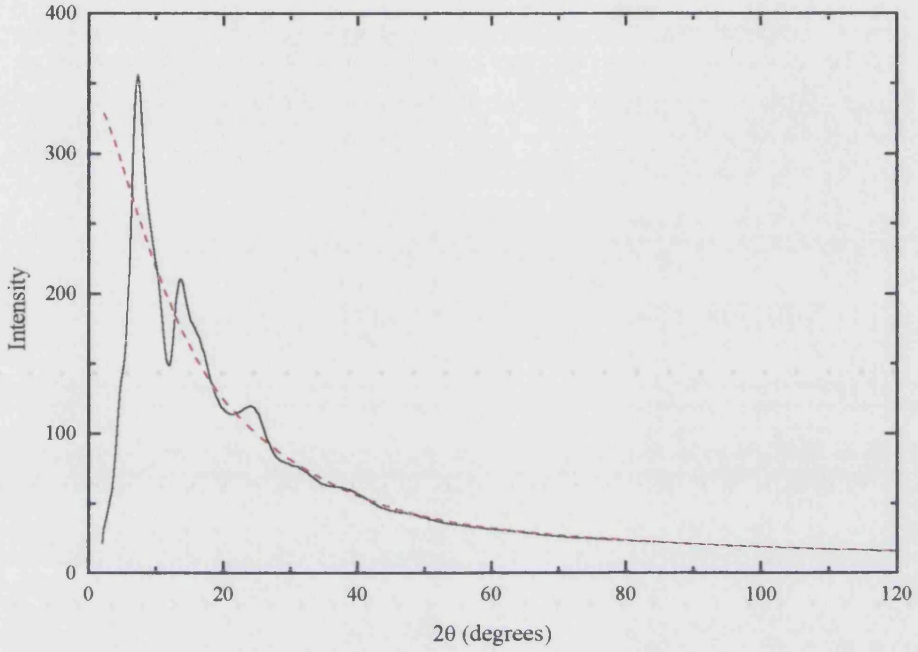


Figure 5.1. The x-ray diffraction spectrum of $(Ce_2O_3)_{0.235}(P_2O_5)_{0.765}$ (solid line), and the self-scattering (red line).

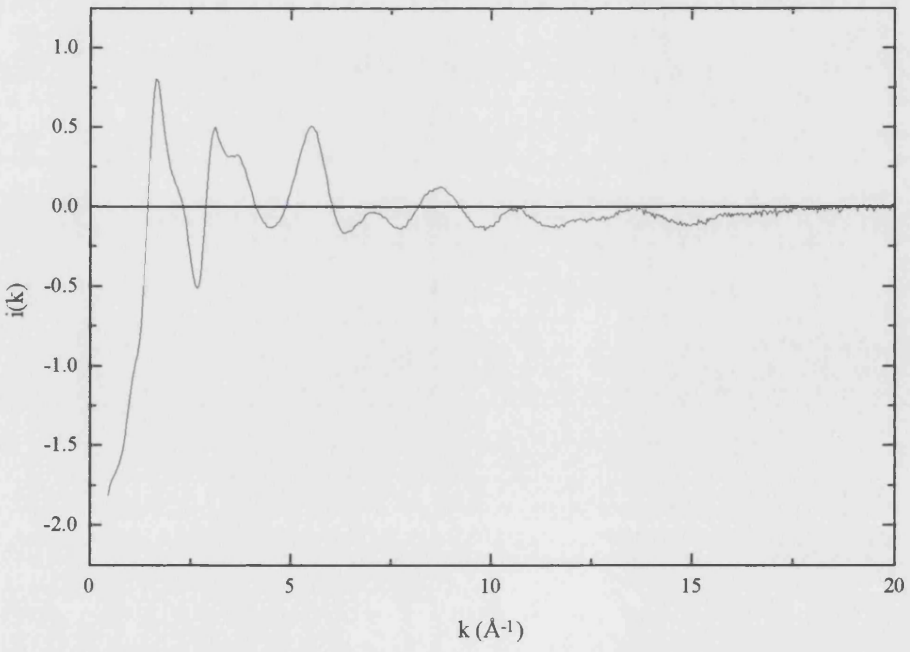


Figure 5.2. The interference function i(k) of $(Ce_2O_3)_{0.235}(P_2O_5)_{0.765}$.

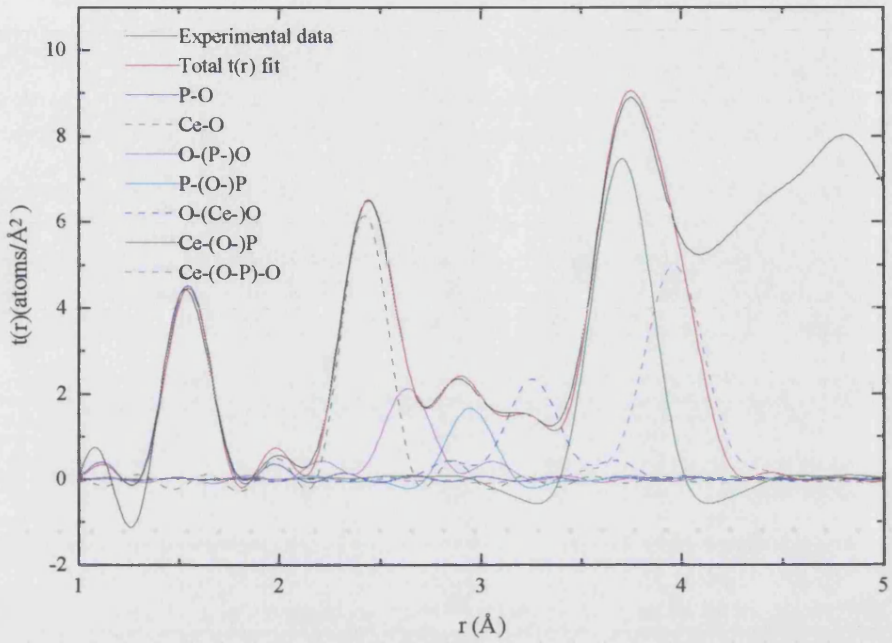


Figure 5.3. The electron density distribution t(r) for $(Ce_2O_3)_{0.235}(P_2O_5)_{0.765}$. The experimental data is given by the solid black line, the red line is a seven gaussian fit, where the individual gaussian profiles have been assigned to the correlations given in the key.

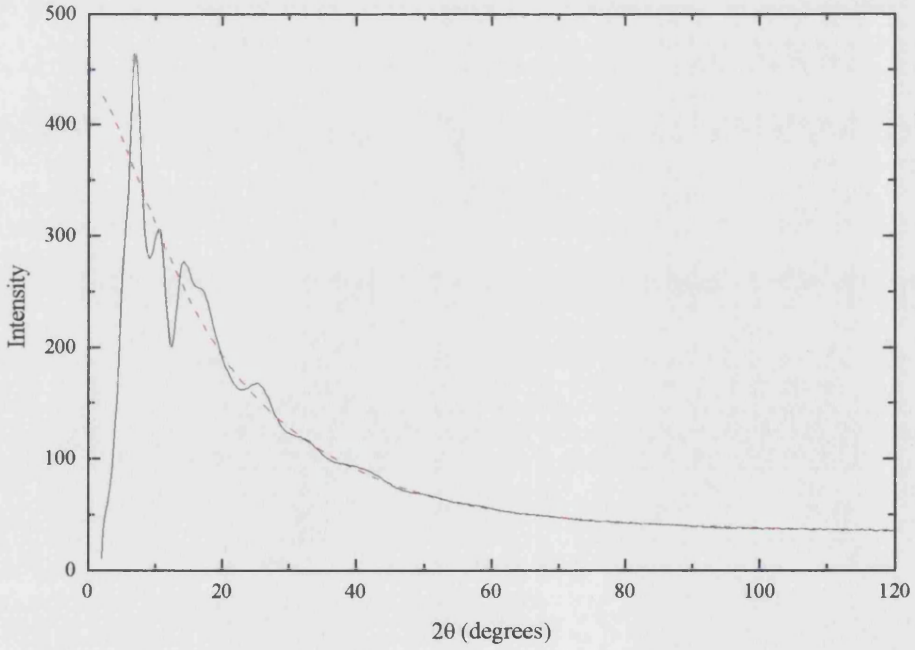


Figure 5.4. The x-ray diffraction spectrum of $(Er_2O_3)_{0.239}(P_2O_5)_{0.761}$ (solid line), and the self-scattering (red line).

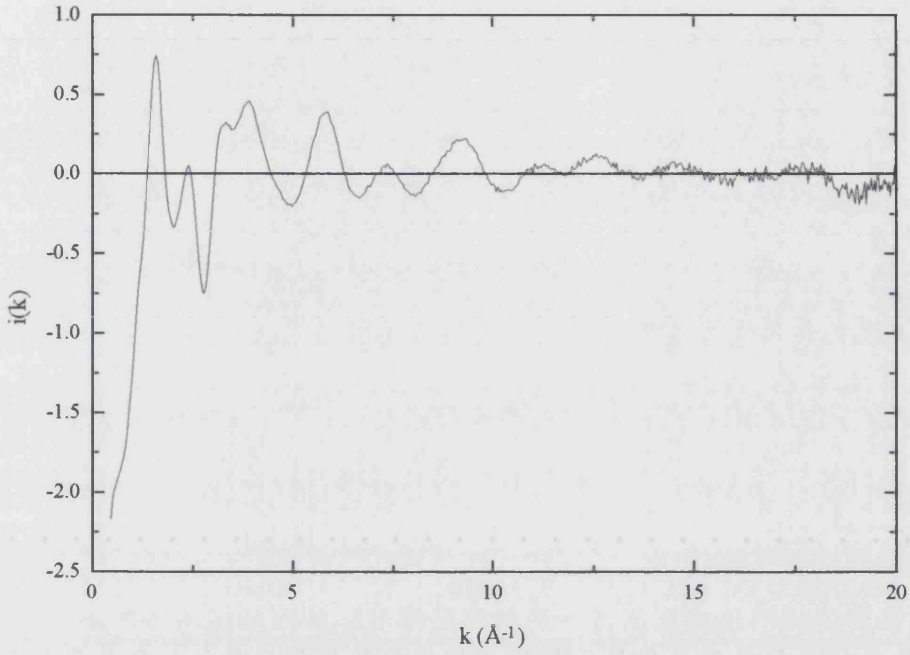


Figure 5.5. The interference function i(k) of $(Er_2O_3)_{0.239}(P_2O_5)_{0.761}$.

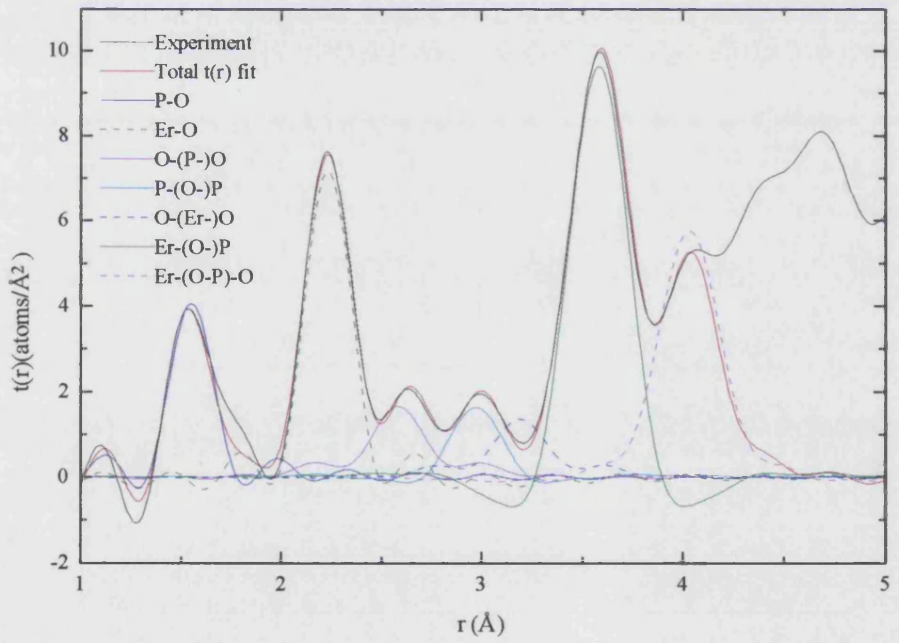


Figure 5.6. The electron density distribution t(r) for $(Er_2O_3)_{0.239}(P_2O_5)_{0.761}$. The experimental data is given by the solid black line, the red line is a seven gaussian fit, where the individual gaussian profiles have been assigned to the correlations given in the key.

| Sample | Peak position (±0.02Å) | Co-ordination number of correlation (±10%) | Atomic correlation(s) assigned |
|---|---|---|---|
| $(Ce_2O_3)_{0.235}$ $(P_2O_5)_{0.765}$ | 1.54 | 3.90 | P-O |
| | 2.42 | 6.50 | Ce-O |
| | 2.63 | 4.70 | O-(P-)O |
| | 2.94 | 2.40 | P-(O-)P |
| | 3.25 | 7.30 | O-(Ce-)O |
| | 3.70 | 7.60 | Ce-(O-)P |
| | 3.96 | 12.0 | Ce-(O-P)-O |
| $(Nd_2O_3)_{0.187}$ $(P_2O_5)_{0.813}$ | 1.55 | 3.80 | P-O |
| | 2.36 | 6.40 | Nd-O |
| | 2.56 | 4.70 | O-(P-)O |
| | 2.95 | 2.50 | P-(O-)P |
| | 3.27 | 8.20 | O-(Nd-)O |
| | 3.67 | 8.60 | Nd-(O-)P |
| | 4.00 | 15.9 | Nd-(O-P)-O |
| $(Sm_2O_3)_{0.212}$ $(P_2O_5)_{0.788}$ | 1.56 | 3.70 | P-O |
| | 2.33 | 6.50 | Sm-O |
| | 2.57 | 5.30 | O-(P-)O |
| | 2.80 | 2.96 | P-(O-)P |
| | 3.28 | 7.10 | O-(Sm-)O |
| | 3.67 | 9.50 | Sm-(O-)P |
| | 4.07 | 14.2 | Sm-(O-P)-O |
| $(Gd_2O_3)_{0.229}$ $(P_2O_5)_{0.771}$ | 1.55 | 4.00 | P-O |
| | 2.30 | 7.10 | Gd-O |
| | 2.55 | 4.70 | O-(P-)O |
| | 2.95 | 2.70 | P-(O-)P |
| | 3.25 | 5.10 | O-(Gd-)O |
| | 3.64 | 9.70 | Gd-(O-)P |
| | 4.07 | 13.3 | Gd-(O-P)-O |

| | | | |
|---|---|---|---|
| $(Dy_2O_3)_{0.225}$ $(P_2O_5)_{0.775}$ | 1.57 | 3.50 | P-O |
| | 2.26 | 6.50 | Dy-O |
| | 2.61 | 4.90 | O-(P-)O |
| | 3.00 | 3.60 | P-(O-)P |
| | 3.19 | 3.90 | O-(Dy-)O |
| | 3.60 | 9.60 | Dy-(O-)P |
| | 4.08 | 16.5 | Dy-(O-P)-O |
| $(Ho_2O_3)_{0.231}$ $(P_2O_5)_{0.769}$ | 1.55 | 3.90 | P-O |
| | 2.24 | 5.80 | Ho-O |
| | 2.55 | 5.90 | O-(P-)O |
| | 2.98 | 3.40 | P-(O-)P |
| | 3.24 | 5.30 | O-(Ho-)O |
| | 3.59 | 8.70 | Ho-(O-)P |
| | 4.01 | 14.3 | Ho-(O-P)-O |
| $(Er_2O_3)_{0.239}$ $(P_2O_5)_{0.761}$ | 1.55 | 3.90 | P-O |
| | 2.23 | 6.60 | Er-O |
| | 2.58 | 4.90 | O-(P-)O |
| | 2.97 | 3.40 | P-(O-)P |
| | 3.19 | 5.00 | O-(Er-)O |
| | 3.58 | 8.90 | Er-(O-)P |
| | 4.03 | 13.3 | Er-(O-P)-O |

Table 5.1. Summary of x-ray diffraction results for rare earth metaphosphate glasses.

The position of the first peak in the evaluated t(r) occurs at approximately 1.55Å in all of the REMGs studied, and has been assigned to the phosphorus-oxygen bond length. In previous x-ray diffraction studies of metal doped phosphate glasses the P-O distance has been recorded between 1.53-1.58Å, which is consistent with a network of linked $PO_4$ tetrahedra (Matsubara et al. 1988, Musinu et al. 1989, 1995, Bowron et al. 1994, 1995, 1996b, Cervinka et al.1995). The number of oxygen ions surrounding each phosphorus atom ($N_{P\text{-}O}$) is between 3.5-4.0. The slight deviations of the P-O co-ordination from the expected fourfold correlation, in some of the REMGs, can be

attributed to data extraction methods, and is not a real structural feature. Fourier series termination effects can produce 'ripples' within the experimental peaks area at low r; either depressions, hence producing the reduced co-ordination number, or positive 'bumps', which accounts for the shoulders on the right hand side of the t(r) P-O peak in Dy and Er doped glasses (figure 5.6). The second feature in the t(r) spectra was found at about 2.44Å. At low atomic numbers (Z) this peak is a conglomerate of the gaussians representing the R-O, and O-(P-)O distances, at higher atomic numbers these fits become separated (compare figures 5.3 and 5.6). This separation is due to the lanthanide contraction. As the atomic number increases there is a systematic reduction in the size of a rare earth ion, and consequently the R-O distance (from 2.42Å for $(Ce_2O_3)_{0.235}(P_2O_5)_{0.765}$ to 2.23Å for $(Er_2O_3)_{0.239}(P_2O_5)_{0.761}$). In contrast the O-O correlation is essentially static as it has no direct involvement with the lanthanide contraction. The two gaussian peaks start to become separate at gadolinium doped metaphosphate glass. The R-O correlations are compatible with the Me-O (where Me = Zn, Mg, Ca, Ba) distances measured in binary phosphate glasses by Hoppe et al (1995a) and in REMGs doped with $Pr^{3+}$, $Eu^{3+}$ and $Tb^{3+}$ (Bowron et al, 1995, 1996b). The average number of oxygen atoms surrounding each rare earth ion was determined to be 6.49. This is consistent with a co-ordination number of 7.0±1 found in REMGs using EXAFS (Bowron et al. 1995, 1996a) and in crystal rare earth metaphosphates which have a co-ordination of 6 or slightly larger (Hong 1974a). The oxygen-oxygen distances (~2.57Å) are also in agreement with O-O separations measured in other amorphous phosphate glasses using x-ray diffraction, 2.50-2.56Å (Matsubara et al. 1988), 2.50-2.55Å. (Musinu et al. 1995), and neutron scattering, 2.49-2.76Å (Hoppe et al 1995b, 1998b). The O-O correlations have increased accuracy at higher atomic numbers where the gaussian is more easily resolved from the neighbouring R-O profile (figure 5.6). The average P-(O-)P positions was calculated to be 2.94Å and the corresponding co-ordination number is 2.99 phosphorus ions. The gaussians describing the O-(R-)O separation occurred between 3.19-3.28Å, with an average co-ordination of 5.9 oxygen atoms. The O-(R-)O co-ordination exhibits an abrupt change at $(Gd_2O_3)_{0.229}(P_2O_5)_{0.771}$; the samples studied with atomic numbers between 58-62 have an average correlations number of 8.47 oxygen atoms, and the corresponding $N_{O-(R-)O}$ in REMGs doped with Gd, Dy, Ho and Er is 4.02 atoms. This trend is due to a combination of effects. As the atomic number

increases the O-(R-)O peak in the experimental t(r) becomes less distinguished until erbium where it seems to disappear completely from the total t(r) spectrum (figures 5.3 and 5.6). Lanthanide contraction causes the O-(R-)O distance to decrease with increasing Z, however as the P-(O-)P correlation is approximatly static the two peaks becomes partially overlapped. At high atomic numbers this produces an artificial enhancement of the P-(O-)P correlation and a corresponding (artificial) decrease in the O-(R-)O co-ordination number. However the low atomic number data is not consistent with a metaphosphate composition either. A six fold R-O correlation, would lead to an estimate that an oxygen atom, situated in an octahedral site, would be co-ordinated to four other oxygen atoms (the remaining oxygen atom, situated opposite, is significantly further from it than the other four). However as the glass is metaphosphate two of the three oxygen atoms are non-bridging, so for the whole system the O-(R-)O co-ordination number is predicted to be approximatly 8/3. At low Z values the correlation is much higher. This is due to the presence of a very broad peak in the range 3.5-4.2Å arising from the P-(O-P-)O correlation. As this peak was so broad (due to the fact that there is free rotation about the P-O bond) it was not modelled, however it will contribute to the correlation of all the gaussians profiles in this range, giving artificially high co-ordination numbers. An R-(O-)P correlation has been assigned to the peak situated between 3.70 to 3.58Å. The peak positions exhibit lanthanide contraction and the R-(O-)P distance decreases from cerium to erbium doped metaphosphate glass. Lanthanide contraction also leads to the separation of the R-(O-)P and R-(O-P)-O gaussians as the periodic table is transversed; at low atomic numbers both the fits contribute to the same feature in the t(r) (figure 5.3 and 5.6). The rare earth-phosphorus co-ordination number ($N_{RP}$) has an average value of 7.8, however this is physically unlikely as $N_{RP}$ cannot be greater than $N_{RO}$ because each non-bridging oxygen can only be bonded to one P atom. This high co-ordination number is due to presence of the P-(O-P-)O correlation which has not been modelled. The R-(O-P)-O distance has been calculated as 4.03 Å, and each rare earth ion was found to be surrounded by 14.2 oxygen atoms. Both the R-(O-)P and R-(O-P)-O distance have been measured using the complementary probe of EXAFS (section 5.2); the rare earth phosphorus, and rare earth oxygen distances were determined to be 3.29Å and 4.00Å respectively.

## 5.2. EXAFS, RESULTS AND DISCUSSION

EXAFS is an atom specific probe which gives detailed information on the local atomic structure of a chosen element; in the present study it is used to determine the short range environment of rare earth ions in a phosphate network. The correction steps involved in converting the raw data into a useful form from which data can be extracted, are based mainly on the isolation and normalisation of the extra fine spectra on the high energy side of an absorption edge. The data analysis was performed using EXCALIB, EXBACK and EXCURV92, a suite of programs available at Daresbury Laboratory (section 4.3.3). The composition of the eleven metaphosphate glasses studied by the EXAFS method are given in table 5.2.

| Rare earth dopant | Atomic number | Rare earth oxide content (mol%) |
|---|---|---|
| La | 57 | $(La_2O_3)_{0.1999}(Gd_2O_3)_{0.0001}(P_2O_5)_{0.8000}$ |
| Ce | 58 | $(Ce_2O_3)_{0.235}$ $(P_2O_5)_{0.765}$ |
| Pr | 59 | $(Pr_2O_3)_{0.254}(P_2O_5)_{0.746}$ |
| Nd | 60 | $(Nd_2O_3)_{0.187}$ $(P_2O_5)_{0.813}$ |
| Sm | 62 | $(Sm_2O_3)_{0.195}$ $(P_2O_5)_{0.805}$ |
| Eu | 63 | $(Eu_2O_3)_{0.218}(P_2O_5)_{0.782}$ |
| Gd | 64 | $(Gd_2O_3)_{0.229}$ $(P_2O_5)_{0.771}$ |
| Tb | 65 | $(Tb_2O_3)_{0.263}$ $(P_2O_5)_{0.737}$ |
| Dy | 66 | $(Dy_2O_3)_{0.225}$ $(P_2O_5)_{0.775}$ |
| Ho | 67 | $(Ho_2O_3)_{0.231}$ $(P_2O_5)_{0.769}$ |
| Er | 68 | $(Er_2O_3)_{0.239}$ $(P_2O_5)_{0.771}$ |

Table 5.2. Compositions of the rare earth metaphosphate glasses studied using EXAFS.

The $L_{III}$ absorption edges have been probed using the standard EXAFS transmission mode experiment. The range studied, 2-12Å$^{-1}$ (corresponding to $4<k<24$Å$^{-1}$ in conventional diffraction formalism), is limited by the position of the $L_{II}$ edge, and this determines the resolution in real space. A typical example of the isolated EXAFS

spectrum $\chi(k)$ and its pair distribution function, are shown in figure 5.7, and 5.8, for neodymium metaphosphate glass at 79K.

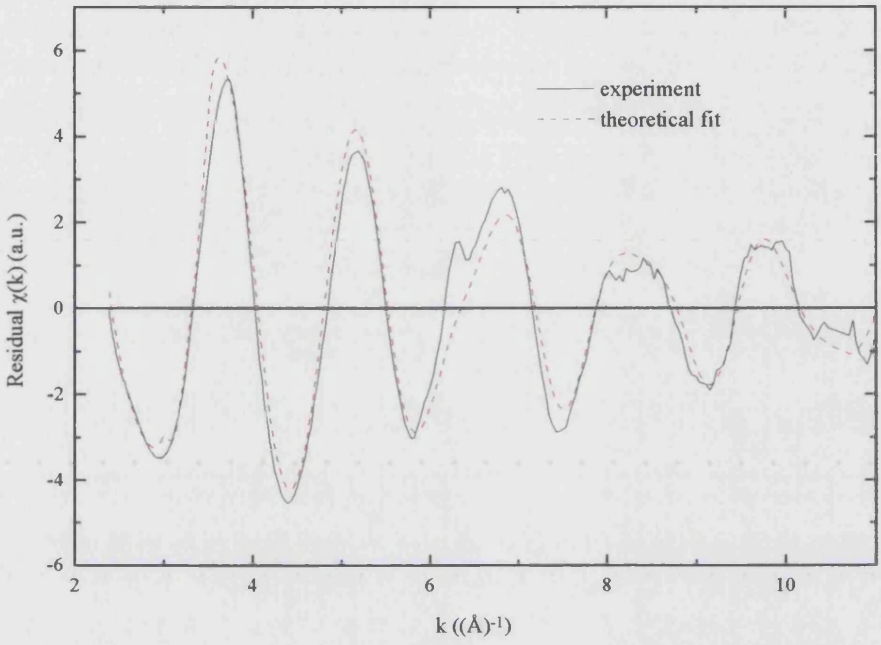


Figure 5.7. EXAFS $\chi(k)$ for neodymium metaphosphate glass $(Nd_2O_3)_{0.187}$ $(P_2O_5)_{0.813}$, at 79K, experimental data (solid line), and the theoretical fit (dotted line).

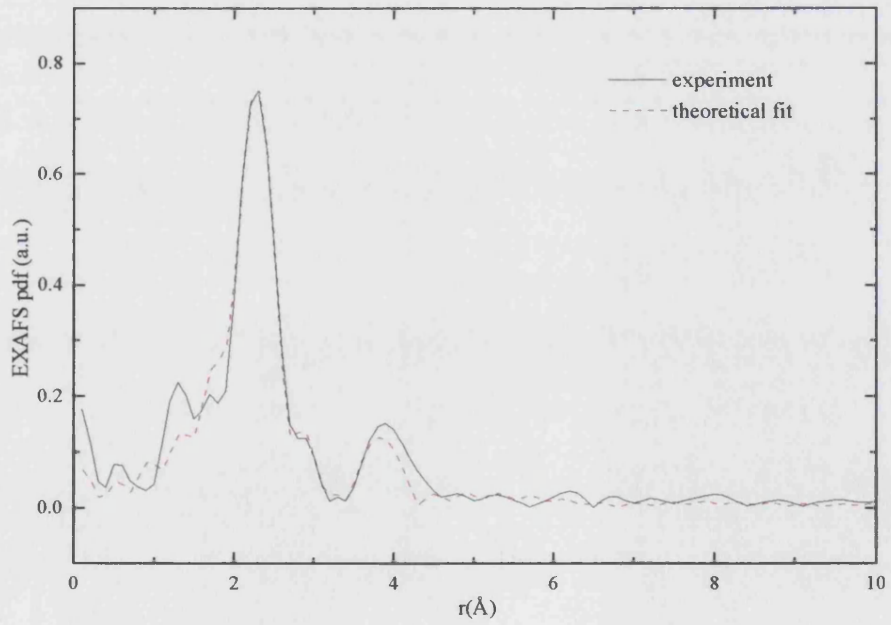


Figure 5.8. EXAFS pair distribution function for neodymium metaphosphate glass $(Nd_2O_3)_{0.187}$ $(P_2O_5)_{0.813}$, at 79K, experimental data (solid line), and the theoretical fit (dotted line).

In the spectra of La, Ce, Pr, and Nd metaphosphate glass an anomalous feature occurs between k = 5.5 to 6.5 $Å^{-1}$, see figures 5.9. This feature is believed to be the double electron excitation of the 2p and 4d electrons (Chaboy and Tyson 1994) as seen in previous EXAFS studies of rare earth metaphosphate glasses (Bowron et al 1996a, b). Evidence of the excitation occurs at a position corresponding to the electron binding energies and results in a discontinuity in the background x-ray absorption. The event can produces unphysical peaks, at low interatomic distances, in the Fourier transform of the data. Such a problem arose when analysing the lanthanum data. A method of Fourier filtering was successfully employed to remove contributions at small r distances, (the original feature in k-space was also removed from the back-transformed spectrum, as expected).

The experimental data and the theoretical best fits for all of the samples at 145K are shown in figures 5.9, 5.10 and 5.11. The corresponding residual R values (Anderson et al. 1998), wh

$$R = \sum_i \left(\frac{1}{\sigma(i)}\right)\left(\left|\exp(i) - \text{theory}(i)\right|\right) \times 100\%$$

$$R = \sum_i \left(\frac{1}{\sigma(i)}\right)\left(\left|\exp(i) - \text{theory}(i)\right|\right) \times 100\%$$

$$\left(\frac{1}{\sigma(i)}\right) = k(i)^3 \Big/ \sum_i \left(k(j)^3 \left|\exp(j)\right|\right) \quad , \qquad (5.1)$$

are given for all temperatures in table 5.3. The R values indicate how well the theoretical fit matches the experimental data; for a perfect match R = 0 and for EXAFS measurements results where $R \leq 25$ are considered to be good

| Glass modifier | R | Glass modifier | R | Glass modifier | R |
|---|---|---|---|---|---|
| La (293K) | 34.2 | Nd (79K) | 16.1 | Tb (145K) | 19.5 |
| La (145K) | 31.2 | Sm (293K) | 16.6 | Tb (79K) | 18.5 |
| La (79K) | 31.0 | Sm (145K) | 19.1 | Dy (293K) | 20.0 |
| Ce (293K) | 26.4 | Sm (79K) | 25.0 | Dy (145K) | 23.6 |
| Ce (145K) | 29.5 | Eu (293K) | 18.5 | Dy (79K) | 38.8 |
| Ce (79K) | 26.9 | Eu (145K) | 18.1 | Ho (293K) | 20.2 |
| Pr (293K) | 14.5 | Eu (79K) | 16.2 | Ho (145K) | 19.2 |
| Pr (145K) | 14.1 | Gd (293K) | 20.6 | Ho (79K) | 20.4 |
| Pr (79K) | 14.8 | Gd (145K) | 17.8 | Er (293K) | 18.1 |
| Nd (293K) | 16.0 | Gd (79K) | 16.4 | Er (145K) | 20.7 |
| Nd (145K) | 20.8 | Tb (145K) | 12.7 | Er (79K) | 20.5 |

Table 5.3 Residual (R) values for each rare earth phosphate glass EXAFS spectrum.

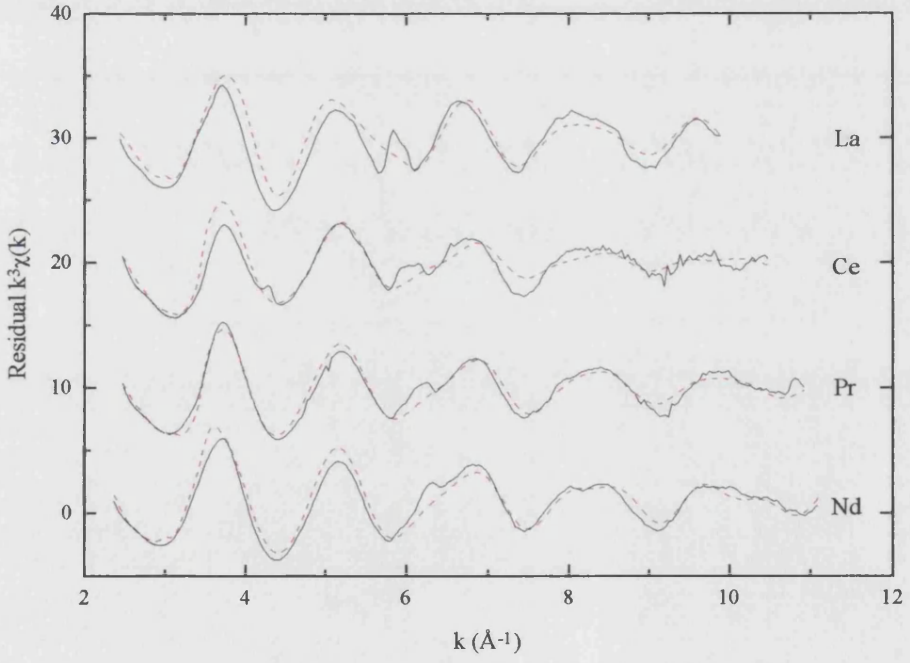


Figure 5.9. La, Ce, Pr, and Nd metaphosphate glass EXAFS $k^3\chi(k)$, experimental data (solid line) and theoretical fit (red dashed line) at 145K. Note that each spectrum exhibits the double electron feature.

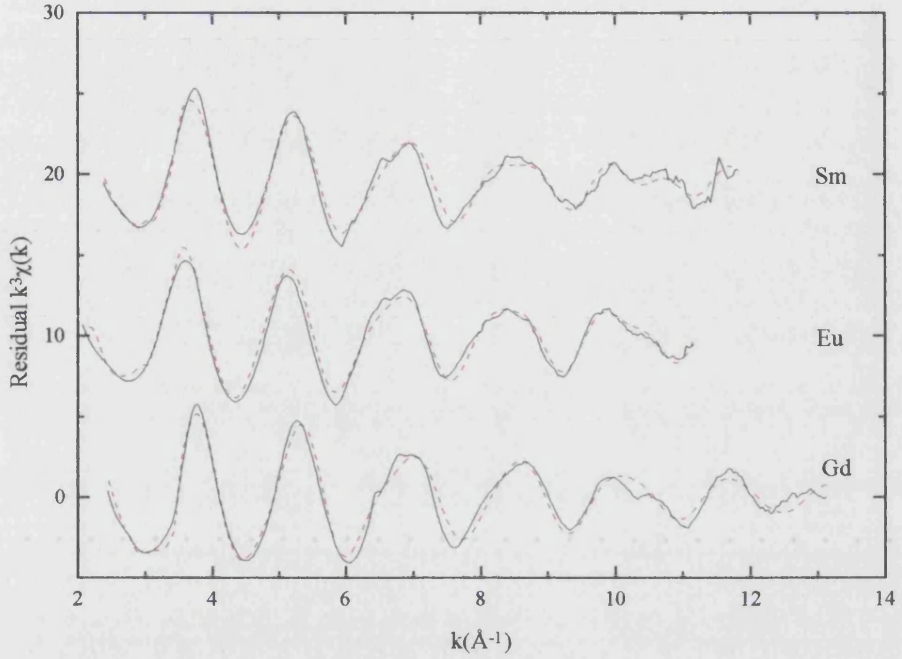


Figure 5.10. Sm, Eu, and Gd metaphosphate glass EXAFS $k^3\chi(k)$, experimental data (solid line) and theoretical fit (red dashed line) at 145K.

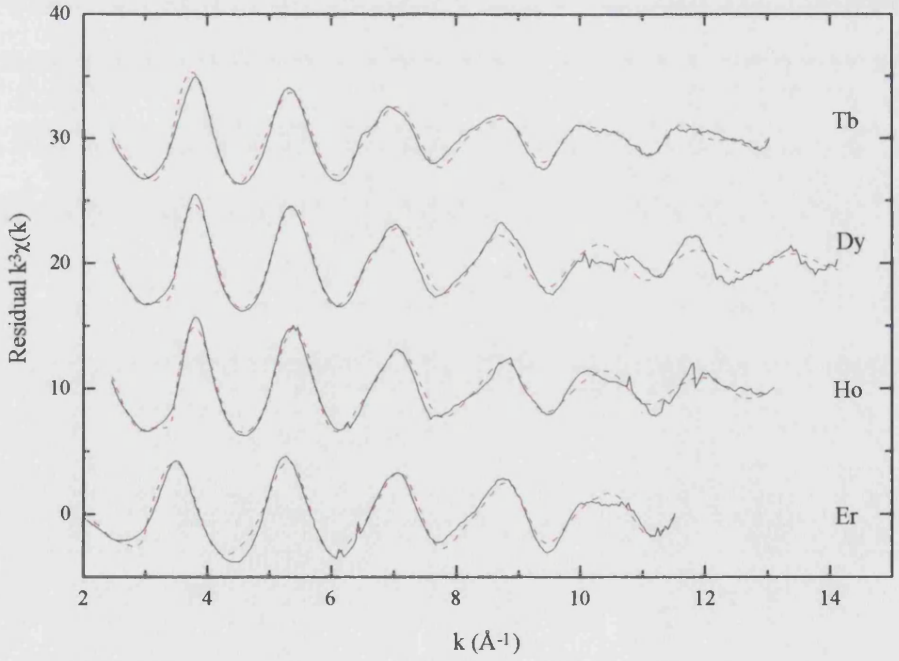


Figure 5.11. Tb, Dy, Ho, and Er metaphosphate glass EXAFS $k^3\chi(k)$, experimental data (solid line) and theoretical fit (red dashed line) at 145K.

The nearest neighbour distances, co-ordination numbers and Debye-Waller factors for the series of rare earth metaphosphate glasses determined from the EXAFS spectra, at 293K, 145K and 79K, are presented in table 5.4.

| Glass Dopant | Z | Correl-ation | Co-ord-ination (atoms) | Distance (Å) | $2\sigma_{ij}^2$ (Å$^2$) | Temp. (K) |
|---|---|---|---|---|---|---|
| La | 57 | La-O | 7.3 ± 1.2 | *2.42 ± 0.03 | 0.030 ± 0.012 | 293 |
| | | La-P | 5.9 ± 4.4 | 3.54 ± 0.04 | 0.042 ± 0.046 | |
| La | 57 | La-O | 6.0 ± 0.6 | *2.42 ± 0.02 | 0.017 ± 0.005 | 145 |
| | | La-P | 3.0 ± 1.5 | 3.60 ± 0.03 | 0.017 ± 0.019 | |
| La | 57 | La-O | 5.9 ± 0.4 | *2.41 ± 0.02 | 0.013 ± 0.004 | 79 |
| | | La-P | 3.6 ± 2.1 | 3.61 ± 0.04 | 0.028 ± 0.030 | |
| Ce | 58 | Ce-O | 4.8 ± 0.5 | 2.35 ± 0.01 | 0.013 ± 0.004 | 293 |
| Ce | 58 | Ce-O | 6.2 ± 1.8 | 2.39 ± 0.03 | 0.023 ± 0.013 | 145 |
| Ce | 58 | Ce -O | 4.8 ± 0.5 | 2.38 ± 0.01 | 0.006 ± 0.003 | 79 |
| Pr | 59 | Pr-O | 6.7 ± 0.3 | 2.37 ± 0.01 | 0.022 ± 0.003 | 293 |
| | | Pr-P | 2.9 ± 1.1 | 3.40 ± 0.04 | 0.041 ± 0.017 | |
| | | Pr-(P-)O | 5.0 ± 0.7 | 4.13 ± 0.02 | 0.015 ± 0.010 | |
| Pr | 59 | Pr-O | 6.3 ± 0.2 | 2.37 ± 0.01 | 0.017 ± 0.013 | 145 |
| | | Pr-P | 2.8 ± 1.2 | 3.40 ± 0.04 | 0.042 ± 0.022 | |
| | | Pr-(P-)O | 4.9 ± 0.8 | 4.13 ± 0.02 | 0.016 ± 0.010 | |
| Pr | 59 | Pr-O | 6.3 ± 0.3 | 2.37 ± 0.01 | 0.017 ± 0.002 | 79 |
| | | Pr-P | 2.6 ± 1.1 | 3.39 ± 0.04 | 0.041 ± 0.022 | |
| | | Pr-(P-)O | 5.2 ± 0.8 | 4.13 ± 0.02 | 0.015 ± 0.009 | |
| Nd | 60 | Nd-O | 8.6 ± 0.3 | 2.34 ± 0.01 | 0.037 ± 0.001 | 293 |
| | | Nd-P | 6.0 ± 2.7 | 3.44 ± 0.03 | 0.062 ± 0.027 | |
| | | Nd-(P-)O | 3.1 ± 0.7 | 4.08 ± 0.02 | 0.004 ± 0.006 | |
| Nd | 60 | Nd-O | 7.7 ± 0.4 | 2.33 ± 0.01 | 0.021 ± 0.003 | 145 |
| | | Nd-P | 7.2 ± 5.9 | 3.41 ± 0.04 | 0.076 ± 0.055 | |
| | | Nd-(P-)O | 2.8 ± 1.0 | 4.08 ± 0.02 | 0.001 ± 0.007 | |
| Nd | 60 | Nd-O | 8.1 ± 0.3 | 2.34 ± 0.01 | 0.027 ± 0.002 | 79 |

| | | | | | | |
|---|---|---|---|---|---|---|
| | | Nd-P | 8.1 ± 3.2 | 3.42 ± 0.03 | 0.080 ± 0.027 | |
| | | Nd-(P-)O | 3.2 ± 0.8 | 4.07 ± 0.02 | 0.003 ± 0.006 | |
| Sm | 62 | Sm-O | 6.9 ± 0.3 | 2.31 ± 0.01 | 0.019 ± 0.002 | 293 |
| | | Sm-P | 16.3 ± 7.1 | 3.40 ± 0.02 | 0.124 ± 0.037 | |
| | | Sm-(P-)O | 3.5 ± 0.7 | 4.03 ± 0.01 | 0.008 ± 0.005 | |
| Sm | 62 | Sm-O | 6.4 ± 0.3 | 2.33 ± 0.01 | 0.016 ± 0.002 | 145 |
| | | Sm-P | 5.7 ± 9.1 | 3.41 ± 0.05 | 0.071 ± 0.063 | |
| | | Sm-(P-)O | 3.5 ± 1.1 | 4.07 ± 0.02 | 0.004 ± 0.005 | |
| Sm | 62 | Sm-O | 6.9 ± 0.9 | 2.32 ± 0.01 | 0.013 ± 0.005 | 79 |
| | | Sm-P | 10.8 ± 13.4 | 3.42 ± 0.05 | 0.095 ± 0.067 | |
| | | Sm-(P-)O | 4.3 ± 1.3 | 4.08 ± 0.01 | 0.012 ± 0.005 | |
| Eu | 63 | Eu-O | 6.2 ± 0.3 | 2.31 ± 0.01 | 0.016 ± 0.002 | 293 |
| | | Eu-P | 5.0 ± 4.1 | 3.34 ± 0.05 | 0.082 ± 0.055 | |
| | | Eu-(P-)O | 3.8 ± 0.9 | 4.07 ± 0.02 | 0.007 ± 0.007 | |
| Eu | 63 | Eu-O | 6.0 ± 0.3 | 2.32 ± 0.01 | 0.012 ± 0.002 | 145 |
| | | Eu-P | 3.9 ± 3.4 | 3.33 ± 0.05 | 0.072 ± 0.052 | |
| | | Eu-(P-)O | 3.5 ± 0.8 | 4.03 ± 0.02 | 0.006 ± 0.006 | |
| Eu | 63 | Eu-O | 6.0 ± 0.3 | 2.30 ± 0.01 | 0.012 ± 0.002 | 79 |
| | | Eu-P | 4.0 ± 3.7 | 3.34 ± 0.05 | 0.074 ± 0.056 | |
| | | Eu-(P-)O | 3.6 ± 0.9 | 4.04 ± 0.02 | 0.005 ± 0.006 | |
| Gd | 64 | Gd-O | 6.5 ± 0.4 | 2.29 ± 0.01 | 0.014 ± 0.002 | 293 |
| | | Gd-P | 1.9 ± 2.6 | 3.18 ± 0.06 | 0.034 ± 0.050 | |
| | | Gd-(P-)O | 8.6 ± 8.0 | 4.01 ± 0.03 | 0.027 ± 0.080 | |
| Gd | 64 | Gd-O | 6.0 ± 0.2 | 2.29 ± 0.01 | 0.011 ± 0.001 | 145 |
| | | Gd-P | 1.4 ± 1.5 | 3.21 ± 0.14 | 0.020 ± 0.025 | |
| | | Gd-(P-)O | 6.8 ± 1.2 | 4.01 ± 0.02 | 0.020 ± 0.012 | |
| Gd | 64 | Gd-O | 6.1 ± 0.3 | 2.30 ± 0.00 | 0.009 ± 0.001 | 79 |
| | | Gd-P | 2.2 ± 2.5 | 3.17 ± 0.03 | 0.029 ± 0.050 | |
| | | Gd-(P-)O | 6.7 ± 1.2 | 4.01 ± 0.02 | 0.017 ± 0.010 | |
| Tb | 65 | Tb-O | 5.8 ± 0.2 | 2.27 ± 0.01 | 0.016 ± 0.001 | 293 |
| | | Tb-(P-)O | 6.5 ± 1.1 | 4.01 ± 0.01 | 0.027 ± 0.012 | |
| Tb | 65 | Tb-O | 5.5 ± 0.2 | 2.25 ± 0.01 | 0.013 ± 0.002 | 145 |

| | | | | | | |
|---|---|---|---|---|---|---|
| | | Tb-(P-)O | 2.4 ± 0.8 | 3.94 ± 0.02 | 0.003 ± 0.005 | |
| Tb | 65 | Tb-O | 5.3 ± 0.2 | 2.25 ± 0.01 | 0.012 ± 0.001 | 79 |
| | | Tb-(P-)O | 2.4 ± 0.7 | 3.95 ± 0.01 | 0.002 ± 0.004 | |
| Dy | 66 | Dy-O | 5.5 ± 0.3 | 2.22 ± 0.01 | 0.014 ± 0.002 | 293 |
| | | Dy-(P-)O | 2.3 ± 0.9 | 3.92 ± 0.02 | 0.004 ± 0.008 | |
| Dy | 66 | Dy -O | 5.8 ± 0.4 | 2.25 ± 0.01 | 0.011 ± 0.003 | 145 |
| | | Dy-(P-)O | 6.9 ± 2.8 | 3.98 ± 0.02 | 0.027 ± 0.023 | |
| Dy | 66 | Dy-O | 5.5 ± 0.5 | 2.25 ± 0.01 | 0.011 ± 0.002 | 79 |
| | | Dy-(P-)O | 2.9 ± 1.9 | 3.94 ± 0.04 | 0.009 ± 0.021 | |
| Ho | 67 | Ho-O | 5.8 ± 0.4 | 2.23 ± 0.00 | 0.012 ± 0.002 | 293 |
| | | Ho-P | 2.9 ± 5.0 | 3.12 ± 0.06 | 0.047 ± 0.060 | |
| | | Ho-(P-)O | 7.3 ± 2.5 | 3.95 ± 0.03 | 0.025 ± 0.020 | |
| Ho | 67 | Ho-O | 6.0 ± 0.3 | 2.24 ± 0.01 | 0.012 ± 0.001 | 145 |
| | | Ho-P | 4.8 ± 6.0 | 3.11 ± 0.07 | 0.061 ± 0.060 | |
| | | Ho-(P-)O | 7.4 ± 1.9 | 3.98 ± 0.02 | 0.021 ± 0.012 | |
| Ho | 67 | Ho-O | 5.6 ± 0.3 | 2.23 ± 0.01 | 0.010 ± 0.002 | 79 |
| | | Ho -P | 1.3 ± 8.7 | 3.15 ± 0.07 | 0.021 ± 0.010 | |
| | | Ho-(P-)O | 6.5 ± 2.7 | 3.96 ± 0.02 | 0.018 ± 0.017 | |
| Er | 68 | Er-O | 5.7 ± 0.4 | 2.23 ± 0.01 | 0.010 ± 0.002 | 293 |
| | | Er-(P-)O | 6.5 ± 3.2 | 3.97 ± 0.02 | 0.016 ± 0.020 | |
| Er | 68 | Er-O | 5.7 ± 0.3 | 2.22 ± 0.01 | 0.009 ± 0.002 | 145 |
| | | Er-(P-)O | 6.3 ± 3.7 | 3.95 ± 0.02 | 0.013 ± 0.016 | |
| Er | 68 | Er-O | 5.7 ± 0.4 | 2.22 ± 0.01 | 0.010 ± 0.002 | 79 |
| | | Er-(P-)O | 6.8 ± 2.2 | 3.95 ± 0.02 | 0.014 ± 0.011 | |

Table 5.4. Summary of EXAFS results from spectra for the rare earth metaphosphate glasses. The results marked with an * were obtained using Fourier filtering.

The nearest neighbours to the rare earth ion are the oxygen and phosphorus atoms; no information could be gathered on the lanthanide-lanthanide (R-R) relationship within the limits of the experimental method ~4Å. Clustering of the rare earth ions significantly effects the magnetic and optical properties of the sample, and thus their

absence in short range is pertinent for the theoretical understanding of the magneto-optical properties displayed by these glasses. The R-R separation distance is estimated in the range 4-6Å, the upper limit is approximated using density considerations.

The first shell surrounding the rare earth ion in all the glasses studied was found to contain oxygen atoms. The variation of the R-O distance with atomic number of the rare earth ion, from lanthanum doped phosphate glass (2.42Å) to erbium (2.23Å), is shown in figure 5.12. The decrease in R-O distance with increasing atomic number clearly demonstrates the lanthanide contraction (as already observed in the x-ray diffraction data, section 5.1). The values obtained for the R-O distance compare well with the selection of rare earth metaphosphate glasses (at 293K) studied by Bowron et al (1996a), and distances calculated from the tables of ionic radii (Shannon 1976), assuming a co-ordination number of 6 and a valence of $3^+$ for all of the rare earth elements studied here (radius of the $O^{2-}$ ion was 1.35Å). The comparisons, also shown in figure 5.12 between the measured distances and those calculated for trivalent ions having a co-ordination numbers of either 7 (long dashed line) or 8 (short dashed line) do not give such a reasonable fit. However the data for lanthanum, cerium and praseodymium metaphosphate glass may equally be in accord with a co-ordination of either 6 or 7. A co-ordination of 7, and a La-O distance of 2.46Å, have recently been determined for a La metaphosphate glass by Hoppe et al (1998b) using the combined methods x-ray and neutron diffraction.

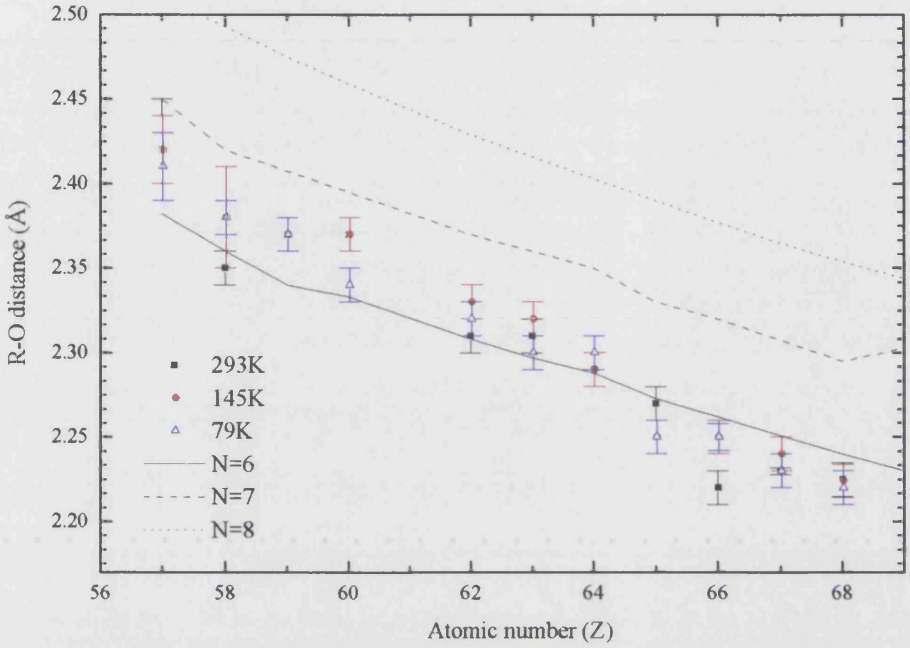


Figure 5.12. The variation of the rare earth-oxygen distance as a function of the lanthanide atomic number. The lines on the plot represent the values for the R-O distance calculated from the tables of ionic radii for $R^{3+}$ and for co-ordination 6 (solid line), 7 (long dashed line) and 8 (short dashed line) (Shannon 1976)

If the nearest neighbour distance is studied as a relative deviation from the $R_{RO}$ calculated for trivalent ions with co-ordination number 6 (see solid line in figure 5.12), an increase in the measured nearest neighbour distance is observed, with decreasing atomic number Z. For lanthanide glasses doped with rare earths having large Z, the $R_{RO}$ distance falls below that expected for co-ordination value of 6. However, a co-ordination of less than 6 is unlikely, in view of the known co-ordinations of rare earth ions. This low correlation number could be attributed to a small systematic error, such as the neglected $(2\sigma^2/R_{ij})(1+R_{ij}/\lambda)$ correction (section 4.3.1, Crozier 1997). The inclusion of this term would produce an increase of 0.01Å in the $R_{RO}$ values (assuming $\lambda$ is 10Å). Hence the rare earth glasses with lower Z have $R_{RO}$ values which are intermediate between those calculated for co-ordination of 6 and 7. Rare earth-oxygen nearest neighbour distances determined from tables for ionic radii (Shannon 1976) assuming valences of $2^+$ and $4^+$ and co-ordination numbers of 6, 7 and 8 were in poor agreement with the results (and in consequence are not illustrated in figure

5.12). A valence state of three is in agreement with optical evidence: the fluorescence and absorption spectra of Sm (Farok et al. 1992) and Eu (Farok et al. 1994) metaphosphate glasses show features arising solely from trivalent ions. Other valence states, which can occur in certain lanthanide's, such as $2^+$ (La, Ce, Pr, Nd, Sm, Eu, Gd, Dy) or $4^+$ (Ce, Pr, Tb) or an intermediate valence, appear not to be favoured in these glasses.

The first shell co-ordination numbers of the oxygen atoms surrounding the rare earth ions ($N_{RO}$) are shown in figure 5.13. $N_{RO}$ is found to vary between 5 and 8. This is slightly lower than the range of 6 to 10 found by Bowron et al (1995, 1996a). Bowron et al. (1996b) proposed that this co-ordination number may arise from a mixture of cubic and pseudo-octahedral arrangements (rare earth oxides normally have an octahedral configuration). The values of co-ordination numbers $N_{RO}$ have a lower associated precision than the measured R-O distances. However the variation in $N_{RO}$ with atomic number appears to exhibit a similar trend as the $R_{RO}$. The $N_{RO}$ increases as Z decreases with values intermediate between 6 and 7 for rare earths with smaller Z, and slightly below 6 for lanthanides with larger Z. As a co-ordination of less than 6 is considered unlikely, there is the possibility that one of the fitting parameters is introducing a systematic error, i.e. the fixed amplitude reduction factor A(k) (see equation 4.34). An increase in A(k) from 0.7 to 0.75 would give a measured co-ordination nearer to 6 for the rare earths with larger Z's. The neodymium co-ordination number breaks with the above trend; $N_{Nd\text{-}O}$ is inconsistently large. It should also be noted that the Debye-Waller term $2\sigma^2$ is also larger for the neodymium sample than the other rare earth doped glassses.

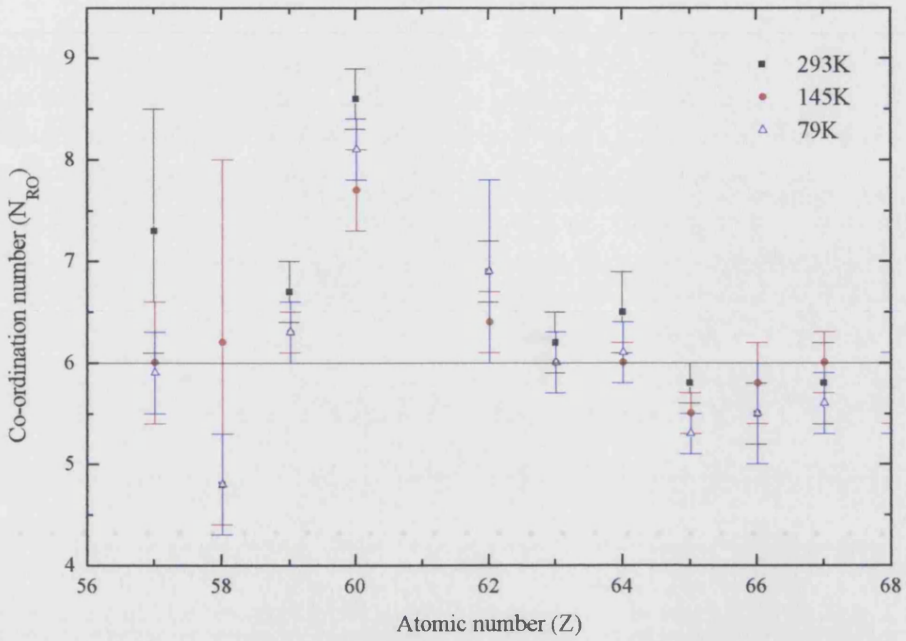


Figure 5.13. Rare earth - oxygen co-ordination number in metaphsophate glasses as a function of lanthanide atomic number. A solid guideline is included showing $N_{RO} = 6$

The observed atomic number dependence of the nearest neighbour structural parameters can be understood in terms of the variation in the rare earth size with Z. Rare earth with smaller Z's have larger radii, and are less likely to be co-ordinatively saturated by six ions (Wang et al 1993). Crystal rare earth metaphosphates also show a Z dependence. Metaphosphate crystals doped with La to Gd exhibit an orthorhombic structure, and for Sm to Yb monoclinic structures have been observed. The monclinic structure has a co-ordination of 6, and the othorhombic structure is synonymous with a co-ordination 6 also, but with 2 additional oxygen atoms at an approximatly 15% greater distances. Hence the overall co-ordination of an othorhombic crystal can be considered larger than 6, but less than 8 (Anderson et al. 1998 and references therein). In the boundary between the two different structures lie samarium, europium and gadolinium doped crystals. These rare earths also fall approximatly in the middle of the trends seen for the glass (figure 5.12, 5.13).

Another factor which might influence the structure of the glasses is composition. The ratio of non-bridging oxygen to rare earth ions increases as the proportion of rare

earth ions decreases. In the case of divalent metal metaphosphate glasses, Hoppe (1996) has argued that this can enable an increased oxygen co-ordination of cations. In crystal rare earth metaphosphates x=0.25 the co-ordination is 6 or slightly larger, in ultraphosphates with x=0.17 the co-ordination number is 8 (Hong 1974a). To check for composition effects the variation of $N_{RO}$ with rare earth oxide content is plotted in figure 5.14. If the error bars are considered the majority of glasses do not show a departure from $N_{RO}$=6. The exception to this is the neodymium sample which has $N_{RO}$ values of 8, but also has the lowest $R_2O_3$ concentration (x=0.187). However this is not consistent with the R-O distance results (figure 5.12). The samarium (x=0.195), and lanthanum (x=0.199) samples also have compositions closer to the ultraphosphate regime than metaphosphate; the results for these samples do not depart from the trends seen in the other rare earth glasses (within experimental error). Hence it is concluded from the co-ordination number and $R_{RO}$ data, that there is no clear evidence to support the idea that composition affects in trivalent rare earth metaphosphate glasses.

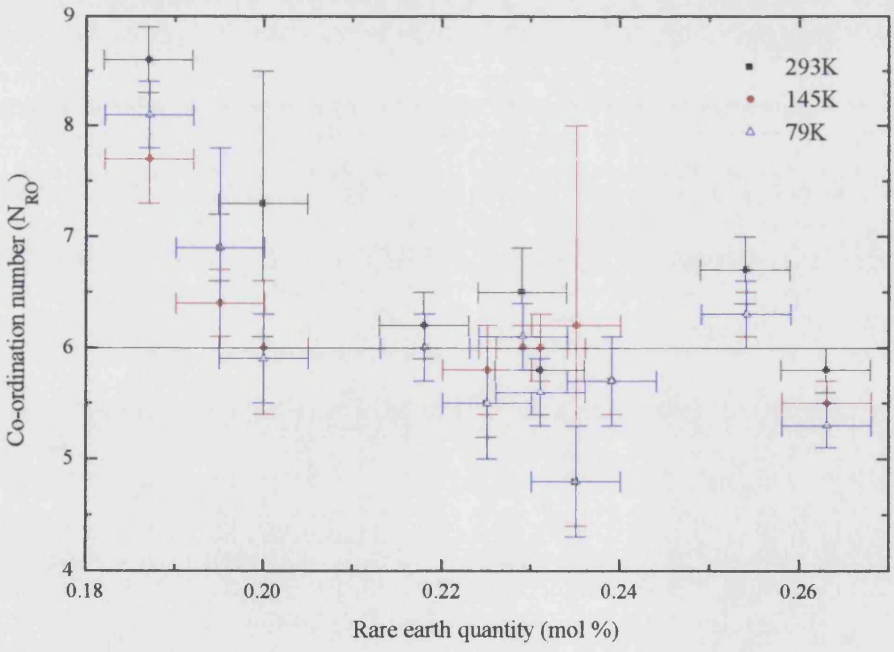


Figure 5.14. Rare earth - oxygen co-ordination number variation with rare earth oxide ($R_2O_3$) dopant (mol%). A solid guideline is included showing $N_{RO}$ = 6

A second co-ordination shell was obtained for all of the rare earth metaphosphate glasses except for $Ce^{3+}$ $Tb^{3+}$ $Dy^{3+}$ and $Er^{3+}$, giving R-P correlation distances of between 3.2 and 3.5Å. This is consistent with the distance expected from the crystalline analogues of the metaphosphate glasses (Hong 1974a and b, Matuszewski et al. 1988). The co-ordination numbers ($N_{RP}$) have relatively large errors, as tends to be the case for EXAFS-determined co-ordination numbers for shells further away from the central excited atom. However, the measured $N_{RP}$ of between 3-7 are compatible with an R-P co-ordination of 6, which occurs in the rare earth metaphosphate crystals. Note that $N_{RP}$ cannot be greater than $N_{RO}$ because each non-bridging oxygen can be bonded to at most one P.

A second rare earth-oxygen correlation was observed at approximately 4Å in nine of the rare earth doped samples (Pr, Nd, Sm, Eu, Tb, Gd, Ho Er, and Dy glasses). The co-ordination numbers for this shell, obtained from a straightforward EXCURV92 fit, were too small. In the metaphosphate crystals, the second R-O shell extends from approximately 4.0 to 4.5Å, with a total co-ordination number of 20 to 25. Thus it is possible that the EXAFS results correspond only to the start of the second R-O shell. It should be noted that the 2nd and 3rd shells can be expected to include multiple scattering contributions.

Within the limitations of the $L_{III}$-edge EXAFS experiments, no change in fit parameters was observed at different temperatures, except for the expected decrease in the Debye-Waller factors with decreasing temperature resulting from a reduction in thermal disorder (table 5.4). If the Debye-Waller term for the first shell $A_{RO}=2\sigma_{RO}^2$ is averaged at given temperature (293K 145K and 79K) over all the samples, the $A_{RO}$ factor reduces with decreasing temperature 0.019Å$^2$, 0.015Å$^2$ and 0.013Å$^2$ (statistical error of 0.001 Å$^2$) . The averaged $A_{RO}$ is not physically meaningful, however it does highlight the trend, and can be considered as a rough estimate of $2\sigma_{RO}^2$ for intermediate values of Z. The linear temperature dependence of $A_{RO}$ means that the data can be extrapolated to 0K to find the static disorder contribution to the mean square deviation in the R-O distance ($\sigma_{RO}^2 = A_{RO}/2$). The static disorder for rare earth doped glasses is approximatly 0.0055Å$^2$. This is in good agreement with the mean

square deviation in the R-O distance of monoclinic ytterbium metaphosphate crystal 0.005Å$^2$. Hoppe et al. (1998b) have reported a value of $\sigma_{RO}^2$=0.006Å$^2$ for lanthanum metaphosphate glass at room temperature, which is lower than the value found here.

It is concluded that there is no change in short range order around the rare earth ion at temperatures down to that of liquid nitrogen, within experimental uncertainty. Anomalous changes present at low temperatures in the acoustic, thermal and optical properties of these glasses are not due to observable changes in structure, within the limits of sensitivity of the EXAFS technique used here and the temperature range available. However there is evidence for a degree of Z dependence of the structure with some correspondence to that seen for rare earth metaphosphate crystals. These EXAFS results do not eliminate the possibility that subtle structural changes occurring at longer distances account for the behaviour of REMGs.

## 5.3. CONCLUSIONS

The short range structure of a series of rare earth metaphosphate glasses have been investigated using the complementary probes of x-ray diffraction and EXAFS. The EXAFS measurements have been made at several different temperatures. The following conclusions can be made

1) The presence of the lanthanide contraction has been demonstrated for the set of rare earth ions using both x-ray diffraction and EXAFS methods.

2) The x-ray diffraction data determines the average nearest neighbour distances to be: P-O = 1.55Å, R-O = 2.31Å, O-(P-)O = 2.57Å, P-(O-)P = 2.94Å, O-(R-)O = 3.24Å, R-(O-)P = 3.64Å, R-(O-P)-O = 4.03 Å. Using the EXAFS probe the R-O distance was measured between 2.23Å and 2.42Å, an R-P correlation distance of about 3.3Å, and a second rare earth-oxygen correlation was observed at approximately 4Å

3) The trivalent rare earth ions, $R^{3+}$, have a similar local environment to that of rare earth ions in the metaphosphate crystals, with rare earth ions co-ordinated to

approximately 6 non-bridging oxygens. One possible exception to this is La, which according to the EXAFS data, may have a co-ordination of 7.

4) The rare earth ions in the glass are separated by distances greater than 4Å. This can be compared with the lower limit of approximatly 3.5Å which exists in the case of R-O corners sharing octahedra.

5) Using the EXAFS probe the near-neighbour rare earth oxygen distances and co-ordination numbers where found to exhibit a degree of Z dependence. The results for rare earths with smaller Z are consistent with co-ordination numbers of between 6 and 7, whereas the results for the larger Z rare earths are consistent with a co-ordination of 6. The change between these two types of co-ordinations occur around Gd.

6) There is no significant change in the short range structure surrounding the rare earth ion, either in near-neighbour distances or in co-ordination numbers, in the temperature range from 79K to 293K within the experimental error associated with the EXAFS method. This indicates that the anomalous thermal, acoustic and optical properties of these glasses at low temperature do not result directly from significant temperature induced changes in rare earth environment.

# CHAPTER SIX

## BASIC THEORY AND INSTRUMENTATION OF NEUTRON SCATTERING EXPERIMENTS

Neutrons possess many unique traits which make them attractive as a complementary method to x-rays as a means of structural determination. The main features are summarised below:

1) Neutrons have zero charge which allows them to interact with the nucleus. This means that they are a highly penetrating probe (low absorption), and can be used to study the bulk properties of a sample. As scattering is nuclear dependent, neutrons have the capability of being able to distinguish between different isotopes of the same material. When neutrons are incident on the nucleus of an atom, the nucleus can be considered to behave as a point potential and the scattering is essentially isotropic.

2) The neutron also has a magnetic moment which interacts with the unpaired electrons present in the material. This phenomena can be exploited to look at magnetic excitations, arrangement of electron spins, etc. In magnetic scattering the resulting spectrum is proportional to the square of the magnetic form factor.

3) The de Broglie wavelengths associated with neutrons are the same order of magnitude as interatomic distances present in condensed matter, and therefore they can be used to perform diffraction experiments.

4) Neutrons have energies comparable to excitations in materials; thus information on dynamic and static features can be simultaneously measured.

There are numerous books and papers dedicated to studies of the production, application, and analysis of neutrons. For those wishing to gain a general overview of the principles involved the author recommends the texts by Willis (1970), Squires (1978), Windsor (1981), Balcar and Lovesey (1989) and Furrer (1995).

Two different neutron experiments have been employed to study the structure of rare earth metaphosphate glasses. The basic theory of both experiments and the corresponding measurement procedures are outlined in this chapter. Investigations of these types were executed at ISIS, the pulsed spallation neutron source at Rutherford Appleton Laboratory, Didcot, UK.

## 6.1. PULSED NEUTRON SOURCE

Neutron production can be split into two different methods. Traditionally a continuous beam of neutrons was created in steady state fission reactors. These neutrons emerge from the moderator with a band of wavelengths, and a high flux. However the wavelength range is restricted by the limited temperatures available in the reactor core. Spallation sources, such as ISIS, generate neutrons by bombarding heavy metal targets with energetic particles, and have the advantage that they produce less heat, have broad spectrum, and can be pulsed (see figure 6.1). The time averaged heating effect at ISIS is 160KW compared with the tens of MW produced in the core of a reactor source.

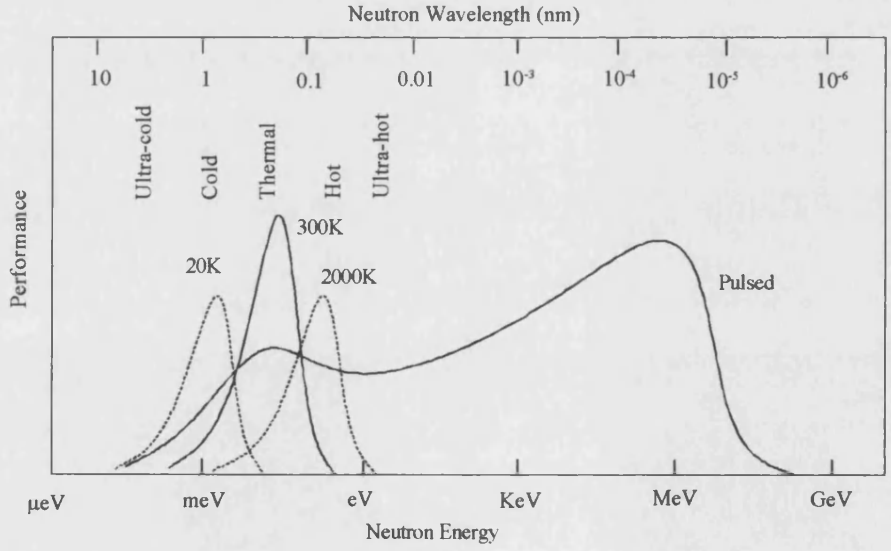


Figure 6.1. The neutron spectrum for thermal neutrons and pulsed sources (After Windsor 1981). The curves show the Maxwellian distributions of neutrons from an ambient moderator (300K), and a cold (20K) and hot (2000K) moderator. The pulsed source spectrum depends on the flux and pulse width. The neutron wavelength was calculated using $E=h^2/2m\lambda^2$.

Pulsed sources use 'epithermal' neutrons which are slowing down, instead of neutrons which are in thermal equilibrium with the core. The wavelength and energy of the neutrons present can be analysed using time-of-flight methods.

The typical components of a pulsed source are shown in figure 6.2.

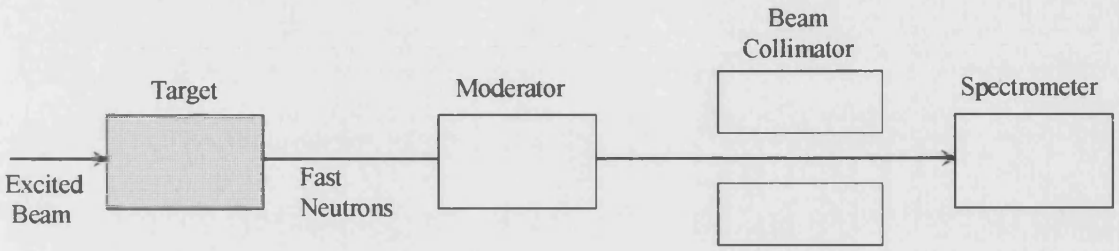


Figure 6.2. A schematic diagram of the components present in a pulsed neutron source.

The excited beam comprises of bunches of protons, accelerated to high energies 500-800MeV. This is achieved by producing $H^-$ atoms in an ion source, and accelerating them in a pre-injector column to 66KeV. In a second stage the ions pass through a linear accelerator consisting of four RF cavities, in which the particles reach energies of 70MeV. Finally the $H^-$ ions are passed through sheets of aluminium foil (0.25μm), in a synchrotron, which strips them of their electrons. The synchrotron has a 52m diameter and accelerates $2.5 \times 10^{13}$ protons per pulse to 800MeV, at a rate of 50 times a second. The protons are steered in a circular orbit by a series of bending and focusing magnets. On reaching an energy of 800MeV the protons are directed towards a spallation target, constructed from a heavy metal, usually tantalum or uranium. The following collisions either produce excited states within the target, which decay instantly, or extract fragments from the nucleus such as neutrons n, gamma particles $\gamma$, neutrinos $\nu$, or $\pi$-mesons. The emerging neutrons, in turn, interact with other tantalum/uranium molecules, producing a cascade effect (see figure 6.3).

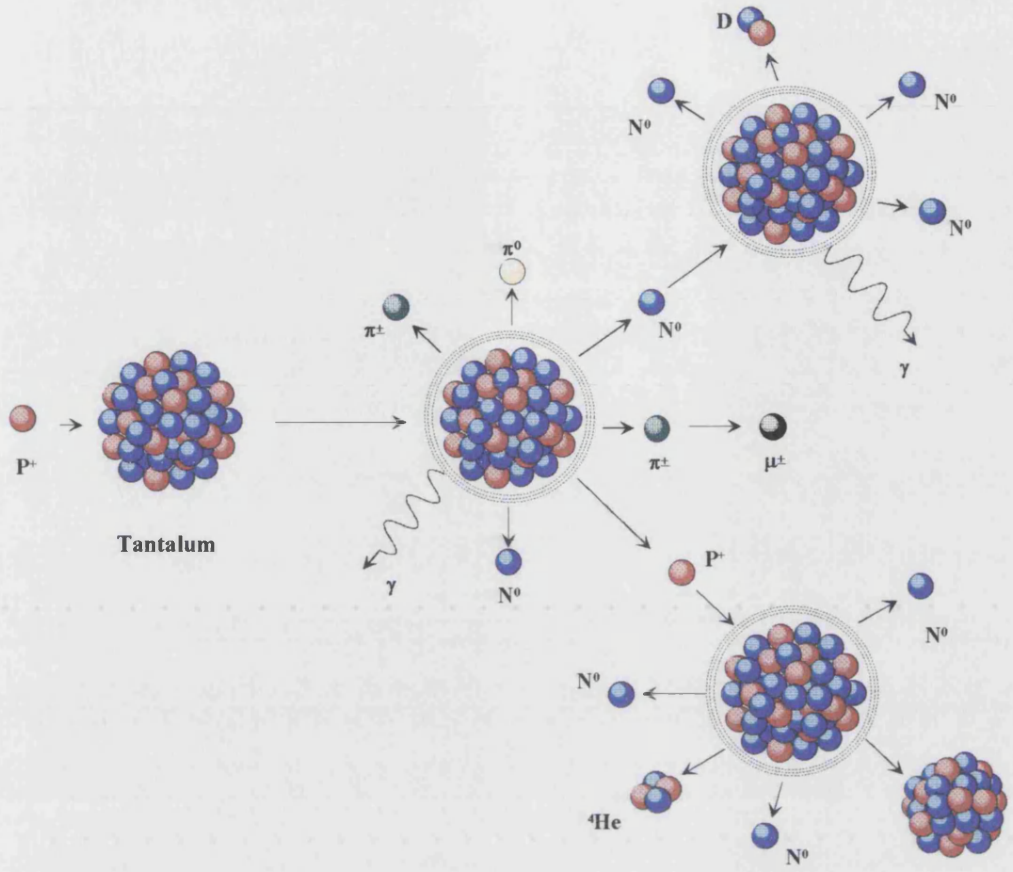


Figure 6.3. Schematic of the spallation process.

On leaving the target the neutrons have energies which are far greater than that required by diffraction experiments; they are slowed by partaking in a number of inelastic collisions with hydrogen atoms in the surrounding arrays of moderators. The moderators have various temperatures, water at 316K, liquid methane at 100K and liquid hydrogen at 20K, so different wavelength distributions can be obtained. Unfortunately during this process, the beam suffers a degree of broadening. The energy spectrum of the emerging neutrons can be seen to compose of two sections. An epithermal region in which the intensity varies inversely with energy, and a Maxwellian distribution which manifests itself as a 'hump' due to the neutrons reaching the same temperature as the moderator. The beam leaves the moderator in all orientations and consequently needs to be collimated. The collimator requires a trade off between good angular resolutions and acceptable count rates. When studying the diffraction patterns from a sample, it is convenient to use time-of-flight techniques. In pulsed time-of-flight diffraction experiments there is no monochromator and the full

energy spectrum of neutrons is incident on the sample. The time, t, it takes for a neutron to travel a distance, L, is measured by an electronic timing device, which is started by an electron pulse emitted when the protons hit the target, and is terminated when the neutron is recorded in the detector. The detectors are the $^3$He gas variety. Each neutron is labelled corresponding to the number of the detector in which it was observed and its' time of arrival. The de Broglie wavelength can thus be calculated;

$$\lambda = \frac{h}{mv} = \frac{ht}{mL} \tag{6.1}$$

where h is Plancks constant, and m and v are the mass and velocity of the neutron respectively. The energy can also be calculated from this equation.

## 6.2. INTRODUCTION TO INELASTIC NEUTRON SCATTERING

The technique of inelastic neutron scattering has been employed to probe the presence and form of the magnetic contribution to the low energy excitations in the rare earth metaphosphate glasses. In addition to the excess localised soft harmonic vibrations proposed by the soft potential model and observed in REMGs (Carini et al. 1995a), investigations of the low temperature specific heat of these glasses have shown the coexistence of excitations due to the magnetic moment of the lanthanide ion (Carini et al, 1997, 1998, to be published). The magnetic moment of neutrons, incident on a paramagnetic sample, interacts with the unpaired electrons in the partially filled shells (4f shell in lanthanides). The neutrons can either suffer elastic or inelastic magnetic scattering. Elastic magnetic scattering gives information on the arrangement of the electron spins and the density distribution of the unpaired electrons. Inelastic magnetic scattering investigates the energy of the magnetic excitations and hence provides information on the crystal field transitions and the local environment. The experiments were performed at the High Energy Transfer (HET) station at the Rutherford Appleton Laboratory in Oxfordshire.

### 6.2.1. THEORY

The concepts introduced in this section are based on the Theory of Magnetic and Neutron Scattering (Balcar and Lovesey, 1989) and Magnetic Neutron Scattering (ed. Furrer 1995); these texts are recommended if a comprehensive description is required. In all neutron scattering experiments the principal aim of the investigation is to

determine the probability that a neutron incident on the sample with a wave vector $\mathbf{k}_i$ is scattered into a state with a wave vector $\mathbf{k}_f$. The intensity of the scattered neutron spectrum is consequently measured as a function of momentum transfer:

$$\hbar\mathbf{Q} = \hbar(\mathbf{k}_i - \mathbf{k}_f) \tag{6.2}$$

where $\mathbf{Q}$ is called the scattering vector. Neutron scattering experiments are usually measured in terms of the partial differential cross section. This is defined by equation 6.3 and is depicted pictorially in figure 6.4.

$$\frac{d^2\sigma}{d\Omega d\omega} = (\text{ the number of neutrons scattered per second into a small solid angle } d\Omega \text{ in the direction } \mathbf{k}_f(\theta,\phi) \text{ with final energy between E and E')}/\Phi d\Omega dE' \tag{6.3}$$

Here $\sigma$ is the scattering cross section (total number of neutrons scattered per second)/$\Phi$), $d\Omega$ is the small solid angle subtended by a detector at position $\theta$, $\phi$, and $\Phi$ is the flux of the incident neutrons.

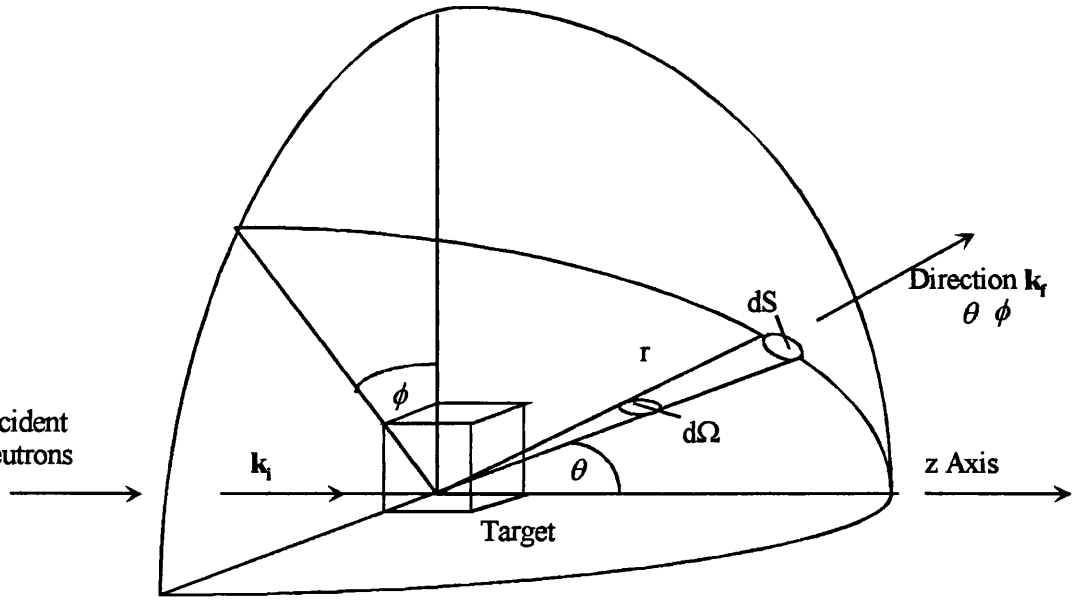


Figure 6.4. The geometry of a neutron scattering experiment.

A formal expression of the partial differential scattering cross section originates from Fermis' Golden Rule which describes the transition from an initial state, which is a function of the initial states of the neutron $\mathbf{k}_i$ and scattering system *i*, to a final composite state f( $\mathbf{k}_f$ *f*). Assuming that the neutron can be modelled as a plane wave, the corresponding transition probability is proportional to:

$$\left|\langle f|\int d\mathbf{r}\exp(-i\mathbf{k}_f\mathbf{r})\,\hat{U}(\mathbf{r})\exp(i\mathbf{k}_i\mathbf{r})|i\rangle\right|^2=\left(\frac{2\pi\hbar^2}{m}\right)^2\left|\langle f|\,\hat{V}(\mathbf{Q})\,|i\rangle\right|^2 \qquad (6.4)$$

m is the mass of the neutron ($1.675\times10^{-27}$Kg), **r** is the position vector of the neutron, $\hat{U}(\mathbf{r})$ is the neutron-matter interaction operator and $\hat{V}(\mathbf{Q})$ is defined by the above equality i.e the Fourier transform of the neutron-matter interaction, and depends on the scattering process. If the transition probability is multiplied by the density of the final states $\rho(\mathbf{k}_f)$ and divided by the initial flux of the neutrons i.e. multiply equation 6.4 by the factor $(k_f/k_i)(m/2\pi\hbar^2)^2$, it becomes,

$$\left(\frac{d^2\sigma}{d\Omega dE'}\right)_f^i=\frac{k_f}{k_i}\left|\langle f|\hat{V}(\mathbf{Q})|i\rangle\right|^2\delta(\hbar\omega+E_i-E_f). \qquad (6.5)$$

The delta function represents the energy conservation of the scattering process in which the target sample is changed from energy state $E_i$ to a state with energy $E_f$, resulting in a corresponding change in the neutron energy $\hbar\omega$. To increase the accuracy of expression 6.5, the partial differential cross section should include the probability distribution of the initial spin states of the neutron $\rho_\sigma$ and the target $\rho_i$: $\rho_i$ is equal to $\exp(-E_i/k_BT)/Z$, where $k_B$ is the Boltzmann constant, T and $E_i$ are the temperature and energy of the system and Z ($=\sum\exp(-E_i/k_BT)$) is the partition function.

$$\frac{d^2\sigma}{d\Omega dE'}=\frac{k_f}{k_i}\sum_{\sigma\sigma'}\rho_\sigma\sum_{ii}\rho_i\left|\langle f\sigma'|\hat{V}(\mathbf{Q})|i\sigma\rangle\right|^2\delta(\hbar\omega+E_i-E_f). \qquad (6.6)$$

In evaluating equation 6.5 and 6.6 a suitable interaction potential must be chosen. In general $\hat{V}(\mathbf{Q})$ has the form:

$$\hat{V}(\mathbf{Q})=\hat{V}_M(\mathbf{Q})+\hat{V}_N(\mathbf{Q}). \qquad (6.7)$$

$\hat{V}_M(\mathbf{Q})$ and $\hat{V}_N(\mathbf{Q})$ are the magnetic and nuclear interaction respectively. In inelastic magnetic neutron scattering the neutrons interact with the magnetic field **H**; hence the magnetic interaction potential is applied:

$$\hat{U}_m=-\hat{\mu}\,\hat{\mathbf{H}}=-\gamma\,\mu_N\,\hat{\sigma}\,\hat{\mathbf{H}} \qquad (6.8)$$

where $\hat{\mu}$ is the magnetic moment operator of the neutron, $\mu_N$ is the nuclear magneton, $\gamma$= -1.91 is the neutron gyromagnetic ratio and $\hat{\sigma}$ the Pauli spin operator

defines the spin state of the neutron. In rare earth metaphosphate glasses the magnetic field **H** contribution arises from the unpaired electrons. The Fourier transform of equation 6.8 gives the corresponding matrix element:

$$\hat{V}_M(\mathbf{Q}) = r_o \hat{\sigma} \hat{T}(\mathbf{Q}) \tag{6.9a}$$

Here the interaction operator **T(Q)** characterises the scattering sample:

$$\hat{T}(\mathbf{Q}) = \sum \exp(i\mathbf{Q}\mathbf{r}_v) \frac{1}{Q^2} \left[ \mathbf{Q} \times \left( \hat{\mathbf{s}}_v \times \mathbf{Q} - \frac{im_e}{\hbar} \hat{\mathbf{V}}_v \right) \right] \tag{6.9b}$$

where $r_0$ is the classical radius multiplied by the neutron gyromagnetic ratio ($\gamma e^2/m_e c^2 = 0.54 \times 10^{12} cm^{-1}$), $\mathbf{r}_v$ and $m_e \mathbf{V}_v$ are respectively the position vector and momentum of the electron $v$, and $\hat{\mathbf{s}}$ is the spin angular momentum, which arises due to the magnetic dipole interaction between the neutron and the electron. If a limitation of scattering over small **Q** is applied, i.e. scattering between states within an electronic configuration, equation 6.9 becomes,

$$V_M(\mathbf{Q}) = r_o \hat{\sigma} \frac{1}{2Q^2} \left( \mathbf{Q} \times \left[ (\hat{\mathbf{l}} + 2\hat{\mathbf{s}}) \times \mathbf{Q} \right] \right) \tag{6.10}$$

where **l** and **s** are the electron angular and spin moment operators. If the ion is a multi-electron system, the total spin $\hat{\mathbf{S}}$ ($=\sum \hat{\mathbf{s}}$) and the total orbital momentum $\hat{\mathbf{L}}$ ($=\sum \hat{\mathbf{l}}$) couple (L-S coupling, see Hunds rules section 2.5), to give a total angular momentum operator $\hat{\mathbf{J}}$ ($=\hat{\mathbf{L}} + \hat{\mathbf{S}}$). Hence the expression ($\hat{\mathbf{l}} + 2\hat{\mathbf{s}}$) in the above equation can be replaced by $g\hat{\mathbf{J}}$ ($=\hat{\mathbf{L}} + 2\hat{\mathbf{S}}$), g is the Landé splitting factor ($g = 1 + 1/2J(J+1)[J(J+1) - L(L+1) + S(S+1)]$). However, although the small **Q** approximation for the neutron-electron interaction operator describes most of the fundamental characteristics of a scattering experiment, the dipole approximation gives improved interpretation of the data. The dipole approximation is used to simplify the neutron-electron interaction operator by describing $V_M(\mathbf{Q})$'s **Q** dependence, and hence the scattering amplitude, in terms of the magnetic form factor; $f(\mathbf{Q}) = \langle j_0 \rangle + (1 - 2/g)\langle j_2 \rangle$ where $\langle j_0 \rangle$ and $\langle j_2 \rangle$ are the radial averages of spherical Bessel functions (these contain the **Q** variation) and g is the gyromagnetic ratio. The magnetic form factor is the Fourier transform of the magnetic distribution of a single atom. The dipole approximation reduces to the small **Q** result as $\mathbf{Q} \rightarrow 0$. Equation 6.9 can be rewritten as,

$$\hat{V}_M(\mathbf{Q}) = r_0\hat{\sigma}\left[\mathbf{Q}\times(\mathbf{X}^D(\mathbf{Q})\times\mathbf{Q})\right] \quad \text{where} \quad \mathbf{X}^D(\mathbf{Q}) = \frac{1}{2}gf(\mathbf{Q})\hat{\mathbf{J}} \qquad (6.11)$$

$\mathbf{X}^D(\mathbf{Q})$ is the dipole approximation for the intermediate scattering function $\mathbf{X}(\mathbf{Q})$ (=exp(i$\mathbf{Qr}$)[$\mathbf{s}$-(i/$\hbar$ $\mathbf{Q}^2$)($\mathbf{Q}\times\mathbf{p}$)] where $\mathbf{p}$ (=-i$\hbar\nabla$) is the momentum operator).

The coupling between rare earth ions is weak in these amorphous materials; hence scattering can be approximated to a single (isolated) ion problem. There are essentially two types of inelastic magnetic scattering that can be considered when a neutron hits a target. Either transitions occur between different $\mathbf{J}$ (=$\mathbf{L}$+$\mathbf{S}$) values in a multiplet, or there is excitation between different crystal field levels, both processes involve the absorption/creation of phonons. In the former, if the small $\mathbf{Q}$ approximation is considered, all the matrix elements $\left|\langle f|V(\mathbf{Q})|i\rangle\right|^2$ vanish except for the diagonal transition elements J'=J±1; these represent the dipole allowed transitions. If a dipole approximation is employed, higher order transitions contribute to the cross-section; however these are small compared to the dipole allowed ones. The experiments completed at Rutherford Appleton Laboratory probed the crystal field transitions within the amorphous sample. To isolate excitations due to the crystal field, the nuclear scattering contribution (in the form of inelastic phonon interactions) has to be modelled and subtracted. The partial differential cross section for such a problem can then be written in terms of a transition between two irreducible representations that characterise the crystal field states $\Gamma_n\rightarrow\Gamma_{n'}$ (see section 2.5):

$$\frac{d^2\sigma}{d\Omega dE'} = r_0^2\frac{k_f}{k_i}\sum_{\upsilon\upsilon'}p_n\left|\langle\Gamma_n\upsilon|\hat{\mathbf{T}}(\mathbf{Q})|\Gamma_{n'}\upsilon\rangle\right|^2\delta\left(\hbar\omega+E_n-E_{n'}\right). \qquad (6.12)$$

Here $p_n$ is a product of the occupation probability of the $\Gamma_n$ state (a Boltzmann factor) and a weighting factor due to the degeneracy of the wave functions $\upsilon$, and $E_n$ and $E_{n'}$ are the corresponding energies of the levels. Dipole allowed transitions only occur when there are non-zero matrix elements for the dipole approximation $\langle\Gamma_n\upsilon|\hat{\mathbf{J}}|\Gamma_{n'}\upsilon\rangle\neq0$. For data analysis it is convenient to introduce a quantity called the magnetic scattering function, $S(\mathbf{Q},\omega)$;

$$S(\mathbf{Q},\omega) = Np_n\langle\Gamma_n\upsilon|\hat{\mathbf{J}}^\alpha|\Gamma_{n'}\upsilon\rangle\langle\Gamma_n\upsilon|\hat{\mathbf{J}}^\beta|\Gamma_{n'}\upsilon\rangle\delta\left(\hbar\omega+E_n-E_{n'}\right) \qquad (6.13)$$

where $\alpha,\beta$ are Cartesian co-ordinates (x,y,z) and N is the total number of magnetic ions in the scattering system. Using the above expression, and equations 6.9 and 6.11, the partial differential cross section (equation 6.12) can be rewritten as

$$\frac{d^2\sigma}{d\Omega dE'} = \left(\frac{1}{2}gr_0\right)^2 \frac{k_f}{k_i} \exp(-2W(\mathbf{Q}))f^2(\mathbf{Q})S(\mathbf{Q},\omega). \qquad (6.14)$$

The exponential term is the Debye-Waller factor and is included to correct for thermal motion, which causes the ions to vibrate about their equilibrium positions, thus modifying the cross section. The experimental quantities measured are the total $S(\mathbf{Q},\omega)$ (which contains nuclear, magnetic and multiple scattering interactions) as a function of either energy $\hbar\omega$ or momentum transfer $\hbar\mathbf{Q}$.

### 6.2.2. HET APPARATUS

The inelastic neutron scattering experiments were completed on the High Energy Transfer (HET) station at the Rutherford Appleton Laboratory, UK HET is a direct geometry time-of-flight spectrometer, see figure 6.5.

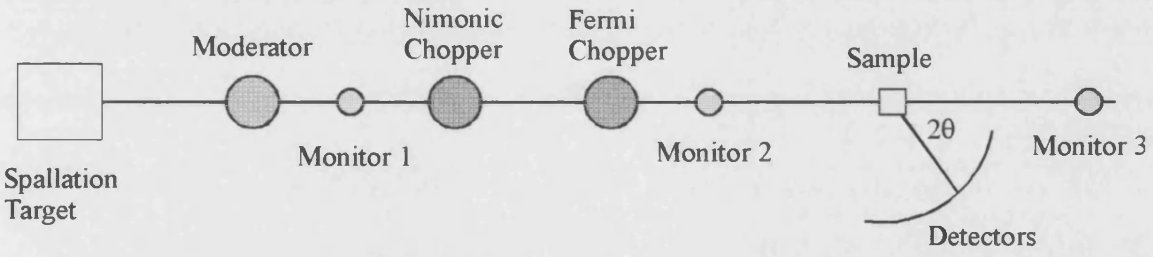


Figure 6.5. Schematic of the HET neutron chopper spectrometer.

The neutrons leave the heavy metal spallation target with various high speeds and energies. They are slowed to useable energies in the moderator, see section 6.1. The nimonic chopper is employed to suppress the background radiation, which arises mainly from the production of gamma rays in the proton-tantalum/uranium collision. This acts by closing the beam tube to the spectrometer when the proton is incident on the target. The neutrons arrive at the sample in monochromatic pulses of known energy (beam size 45×45mm). Energy selection is achieved by using a fast Fermi chopper (Windsor 1981). The Fermi chopper is an aluminium and boron drum

(aluminium is neutron transparent, and boron is highly absorbing) which rotates in phase with the ISIS pulse (50Hz or an integer multiple of this value). A curved channel is cut into the drum and as it sweeps across the path of the beam the ends act like two slits moving in opposite directions; hence only at certain positions will neutrons, of a specific velocity, be allowed to pass. Increasing the frequency of the rotating drum selects a different neutron velocity. After impact with the sample the scattered neutrons are monitored in a fixed array of $^3$He detectors, as a function of time-of-flight; combining this with the known sample-detector length, the final energies $E_f$ (and wave vector $\mathbf{k}_f$) can be found. Monitor 1 records the incident beam and monitors 2 and 3 are used to calculate the incident energy of the neutrons by recording the time, $t_{m2\text{-}3}$, it takes a neutron to travel between the monitors without scattering ($E_i = \hbar \mathbf{k}_i^2/2m = mL^2_{m2\text{-}3}/2t^2_{m2\text{-}3}$). This arrangement can also be used to calculate the momentum transfer (by applying the cosine rule to the initial and final wave vectors):

$$\mathbf{Q}^2 = \mathbf{k}_i^2 + \mathbf{k}_f^2 - 2\mathbf{k}_i\mathbf{k}_f \cos 2\theta \qquad (6.15)$$

For a given detector ($2\theta$ = constant, see figure 6.5) all energies of the final wave vector have the same direction, its' magnitude however depends on the velocity of the incident neutrons. There are five low angled detectors with average $2\theta$ values varying between 4.9° and 26.5°; these banks predominantly observe magnetic scattering. In addition there are two high angle banks (115° and 133°) which mainly record scattering produced by the phonons. The efficiency of the detectors are normalised to an absolute scale by replacing the sample with a vanadium control rod, which has the property of almost totally incoherent scattering. The vanadium data used to measure the wavelength distribution of the incident 'white' neutron beam and the wavelength dependent variation in efficiency of the $^3$He gas detectors. The REMGs were prepared for the inelastic neutron scattering experiments by placing bulk samples in an aluminium foil envelope (which has negligible absorption) and shrouding the support apparatus with cadmium; cadmium has a large absorption cross section and hence should reduce the Bragg scattering. The sample was then lowered into the beam using a top loading two stage cryostat, which meant that the experiment could be performed at different temperatures. Several measures were taken within the apparatus to reduce background intensity; in addition to the nimonic chopper, the system is evacuated to

reduce scattering from the air, and all internal surfaces are lined with a low hydrogen $B_4O$ resin which absorbs neutrons with high energies.

### 6.2.3. DATA CORRECTION PROCEDURES

The inelastic neutron scattering data corrections were executed using the HET data analysis program HOMER (Eccleston et al. 1998). HOMER performs the following functions:

a) The incident energies of the neutrons are calculated from the measured monitor time-of-flight spectrum.

b) The data from different detectors are summed into workspaces (W1-W8) with similar resolution using a mapping file. The default mapping file was used which defined the following workspaces: W1 to W5 contain data from the low angles banks which have an average scattering angle of 4.9°, 11.5°, 16.5°, 21.5° and 26.5° respectively; W6 and W7 are the high angled bank at 115.0° and 133.0°. All the detectors are situated at 2.5m, except the banks at 4.9° and 115.0° which are at 4m. Workspace 8 calculates the average of the scattering in the second to fifth workspaces. The spectra recorded at low angles are dominated by the magnetic scattering factor $f^2(\mathbf{Q})$, which describes the interaction of the neutron with the electrons, and hence describes the magnetic properties of the system. At higher angles (or larger values of $\mathbf{Q}$ or elevated temperatures) the crystal field transitions are eclipsed by a $\mathbf{Q}^2$ term, which characterises the neutron interaction with the nucleus, via inelastic phonon scattering. All of the measurements are taken at low temperatures (20-100K) in order to suppress the unwanted phonon contributions.

c) A time-modulated or time-independent background is subtracted from the workspaces. The time-modulated background depends on the speed of the chopper.

d) The data is converted into $S(\mathbf{Q}\omega)$ i.e. displayed in terms of energy transfer (in meV) and corrected for $k_f/k_i$ and detector efficiency. A vanadium rod spectrum is required to normalise the data for variations in input flux, solid angle and detector efficiency.

Data manipulation is executed using Genie, which is the ISIS graphics software. To isolate the form of the excess magnetic contribution to the rare earth metaphosphate glass spectra, the phonon spectrum must be modelled and subtracted from the raw

data. The easiest way to achieve this is to assume that the vibrational components of all the rare earth metaphosphate glasses are identical; this is a reasonable postulate as all the lanthanides are based on a xenon core, and are situated in the same host material. Therefore the phonon spectrum can be measured directly from the inelastic neutron scattering of lanthanum metaphosphate glass, as $La^{3+}$ has a filled 4f shells i.e. it possess no magnetic moment. However the lanthanum spectrum has to be scaled before subtraction can be performed. The scaling factor $\alpha$ is calculated by comparing the spectrum of the lanthanum data with the intensity from the magnetic rare earth sample at high detector angles (W7), where the scattering flux is dominated by the phonons. This $\alpha$ factor is then used to adjust the low angle scattering (W8) from the lanthanum sample, the resultant is an estimation of the phonon scattering in the magnetic lanthanide glasses over the measured **Q** range. The scaled low angle lanthanum spectrum is subsequently subtracted from W8 of $Pr^{3+}$, $Nd^{3+}$, $Tb^{3+}$, $Dy^{3+}$, $Er^{3+}$ and $Tm^{3+}$ glasses; this isolates the magnetic contribution to the inelastic neutron scattering for the different rare earth metaphosphate glasses.

## 6.3. INTRODUCTION TO TOTAL NEUTRON SCATTERING

Neutrons incident on a sample are diffracted by nuclei and are therefore particularly sensitive to changes in the characteristic nuclear scattering length, b, of the target atom. The scattering cross section is uniquely isotopic dependent and hence the partial structure factors can be determined using a method of isotopic substitution. As rare earth metaphosphate glasses are paramagnetic, the scattering length of the lanthanide ions can be changed by the application of a magnetic field; this acts to align the magnetic moments of the atoms; hence the effective scattering length becomes the sum of the nuclear and magnetic scattering length. These traits were exploited to study the rare earth-rare earth correlation distances in a terbium metaphosphate glass $(Tb_2O_3)_{0.247}(P_2O_5)_{0.753}$. The data was collected on Polaris station at ISIS, Rutherford Appleton Laboratory, UK.

### 6.3.1. THEORY

There are two terms used to describe the nuclear elastic scattering from a target sample: coherent and incoherent (or diffuse) scattering. The former gives information

on correlation between the positions of identical, and different, nuclei at different times, and hence incorporates interference effects. Incoherent scattering depends only on the positions of the same nucleus at various times, and arises from random deviations in the scattering length ($b_j$) from their mean value $\bar{b}_j$ (where the bar denotes an average over isotopes and nuclear spin directions). In structural determination this term can be considered background, and is consequently subtracted. Interpretation of elastic scattering data is initially identical to inelastic theory, section 6.2.1, except that in the partial differential cross section (equation 6.5/6.6) the magnetic interaction $V_M(\mathbf{Q})$ operator is replaced by the nuclear interaction operator $V_N(\mathbf{Q})$ (equation 6.7):

$$\hat{V}_N(\mathbf{Q}) = \sum_j \exp\left(i\mathbf{Q}\mathbf{r}_j\right)\left(A_j + \frac{1}{2}B_j\hat{\sigma}\hat{\mathbf{I}}_j\right) \qquad (6.16)$$

where $\hat{\mathbf{I}}$ is the spin angular momentum of the nucleus, $\hat{\sigma}/2$ is the spin of the neutron, and $A_j$ and $B_j$ describe the low energy neutron-nucleus scattering/absorption, and their values are atom (and isotope) dependent. There are two essential terms required to determine elastic cross section: the average scattering length, $\bar{b}$, and the average of the square of the scattering length $\overline{|b|^2}$, both can be defined in terms of A and B;

$$\bar{b} = \sum_\xi c_\xi A_\xi \qquad \text{and} \qquad \overline{|b|^2} = \sum_\xi c_\xi\left(\left|A_\xi\right|^2 + \frac{1}{4}I_\xi\left(I_\xi + 1\right)\left|B_\xi\right|^2\right) \qquad (6.17)$$

$c_\xi$ is the fractional concentration of the $\xi^{th}$ isotope with an associated nuclear spin $I_\xi$. Using this terminology the total single atom cross section is

$$\sigma = 4\pi\overline{|b|^2}, \qquad (6.18)$$

the coherent cross section is

$$\sigma_c = 4\pi\left|\bar{b}\right|^2, \qquad (6.19)$$

and the incoherent cross section is

$$\sigma_i = 4\pi\left(\overline{|b|^2} - \left|\bar{b}\right|^2\right), \qquad (6.20)$$

For a binary system the average scattering length is $\bar{b} = c_1\,\bar{b}_1 + c_2\,\bar{b}_2$; if $b_1 \neq b_2$, incoherent scattering is present; this contributes to the cross section through the $Nc_1c_2(b_1\text{-}b_2)$ term, where N is the number of scattering nuclei. Focusing on the

coherent contribution only, the partial differential cross section for a monatomic fluid/glass can be written in terms of the scattering function $S(\mathbf{Q},\omega)$:

$$\frac{d^2\sigma}{d\Omega dE'} = \left(\frac{N\sigma_c k'}{8\pi^2\hbar k}\right)\int_{-\infty}^{\infty} e^{-i\omega t}\left\langle \hat{\rho}_{\mathbf{Q}}\hat{\rho}_{-\mathbf{Q}}(t)\right\rangle = \left(\frac{N\sigma_c k'}{k}\right)S(\mathbf{Q},\omega) \qquad (6.21)$$

$\rho_{-Q}(t)$ ($=\rho^{+}_{Q}(t)$) is the Hermitian conjugate of $\rho_Q(t)$ i.e. $\langle\mu|\rho_{\mathbf{Q}}(t)|\mu\rangle^{*} = \langle\mu|\rho^{+}_{\mathbf{Q}}(t)|\mu\rangle$, and $\rho_Q(t)$ is the spatial Fourier transform of the particle density at position **r** and time t, in terms of the Dirac delta function $\rho(\mathbf{r},t) = \sum_j \delta\left[\mathbf{r} - \mathbf{R}_j(t)\right]$:

$$\hat{\rho}_{\mathbf{Q}}(t) = \int e^{-i\mathbf{Q}\mathbf{r}}\rho(\mathbf{r},t)\,d\mathbf{r} \qquad (6.22)$$

where $\mathbf{R}_j$ is the position of the $j^{th}$ nucleus. The zeroth energy moment of the scattering function is called the (static) structure factor $S(\mathbf{Q})$, i.e t=0, $\omega$=0:

$$NS(\mathbf{Q}) = \int S(\mathbf{Q}\omega)d\omega = \int \rho(\mathbf{r}_1)\exp(i\mathbf{Q}\mathbf{r}_1)d\mathbf{r}_1 \times \int \rho(\mathbf{r}_2)\exp(-i\mathbf{Q}\mathbf{r}_2)d\mathbf{r}_2$$

$$= \int \rho(\mathbf{r}_1)\rho(\mathbf{r}_2)\exp\left[i\mathbf{Q}(\mathbf{r}_1 - \mathbf{r}_2)d\mathbf{r}_1 d\mathbf{r}_2\right]. \qquad (6.23)$$

On changing the variables $\mathbf{r}_2=\mathbf{r}'$ and $\mathbf{r}_1-\mathbf{r}_2=\mathbf{r}$, the above equation becomes; $NS(\mathbf{Q}) = \int P(\mathbf{r})\exp(i\mathbf{Q}\mathbf{r})d\mathbf{r}$ where

$$P(\mathbf{r}) = \int \rho(\mathbf{r}+\mathbf{r}')\rho(\mathbf{r}')d\mathbf{r}' = \sum_{i,j}\delta(\mathbf{r} + \mathbf{R}_j - \mathbf{R}_i). \qquad (6.24)$$

$P(\mathbf{r})$ is call the autocorrelation function. Letting $\mathbf{R}_j=\mathbf{R}_1$ be the origin of the system, and summing over all i, the autocorrelation function becomes $\sum_i\delta(\mathbf{r}-\mathbf{R}_i)$, which is the density function at a distance **r** away from the point $\mathbf{R}_1$ - a, a being the position of another particle. The average of this value defines the pair distribution function, $g(\mathbf{r})$,

$$\left\langle \sum_i \delta(\mathbf{r} - \mathbf{R}_i)\right\rangle = \rho_o g(\mathbf{r}) + \delta(\mathbf{r}) \qquad (6.25)$$

$\rho_o$ is the average particle density (=N/V), and $g(\mathbf{r})$ gives the particle density with respect to an arbitrary origin particle ($= \sum\langle\delta(\mathbf{r}-\mathbf{R}_i+\mathbf{R}_o)\rangle$); the $\delta(\mathbf{r})$ function arises from inclusion of the origin atom in the calculations. The average autocorrelation can be expressed in terms of $g(\mathbf{r})$. This formulation can be extended for $\mathbf{R}_j=\mathbf{R}_2$, and $\mathbf{R}_j=\mathbf{R}_3$, giving N similar terms.

$$\langle P(\mathbf{r})\rangle = N(\rho_o g(\mathbf{r}) + \delta(\mathbf{r})) \qquad (6.26)$$

This can be substituted into equation 6.23 to find the average static structure factor:

$$\langle S(\mathbf{Q})\rangle = \int\left[\rho_o(g(\mathbf{r})-1)+\rho_o+\delta(\mathbf{r})\right]\exp(i\mathbf{Qr})d\mathbf{r}\,. \qquad (6.27a)$$

U $$\langle S(\mathbf{Q})\rangle = \int\left[\rho_o(g(\mathbf{r})-1)+\rho_o+\delta(\mathbf{r})\right]\exp(i\mathbf{Qr})d\mathbf{r}\,. \qquad (6.27a)$$

$\delta$Using the properties of the delta function i.e. $\int\delta(\mathbf{r})\exp(i\mathbf{Qr})d\mathbf{r}=1$, and

$$\langle S(\mathbf{Q})\rangle = \rho_o\int_V(g(\mathbf{r})-1)\exp(i\mathbf{Qr})d\mathbf{r}+(2\pi)^3\rho_o\delta(\mathbf{Q})+1\,. \qquad (6.27b)$$

The second term in expression 6.27b depends on the size and shape of the sample; Cusack (1987) stated that it is equivalent to $\rho_o V^{-1}\left|\int\sigma(\mathbf{r})\exp(i\mathbf{Qr})d\mathbf{r}\right|^2$ where $\sigma(\mathbf{r})=1$ inside the sample and $\sigma(\mathbf{r})=0$ outside the sample. The delta function contains structural information in the small **Q** limit (scattering in the forward direction only: **Q** $\cong$ 0), where the signal is swamped by the incident radiation. Hence to a good approximation the structure factor can be written as

$$S(\mathbf{Q}) = 1+\rho_o\int[g(\mathbf{r})-1]\exp(i\mathbf{Qr})d\mathbf{r}\,; \qquad (6.28)$$

$S(\mathbf{Q})\rightarrow 1$ as $\mathbf{Q}\rightarrow\infty$ .The structure factor is proportional to the coherent scattering intensity $I^{coh}(\mathbf{Q})$;

$$S(\mathbf{Q}) = \frac{I^{coh}(\mathbf{Q})}{Nf^2(\mathbf{Q})}. \qquad (6.29)$$

The form factor $f(\mathbf{Q})$ is constant for a given sample. For a binary system the total scattered intensity $I(\mathbf{Q})$ is

$$I(\mathbf{Q}) = N\left[\sum_i c_i b_j^2+\sum_i\sum_j c_i c_j b_i b_j\left(S_{ij}(\mathbf{Q})-1\right)\right]=I^{inc}(\mathbf{Q})+I^{coh}(\mathbf{Q}). \qquad (6.30)$$

Here N is the number of scatters, and c is the concentration of each atom type i, j (Soper et al. 1989). The first term incorporates the incoherent contribution (sometimes called the self scattering term), and the second term describes the coherent (or interference) scattering from the sample. If a method of isotopic substitution is employed, it is possible to change the scattering length b, while keeping all other variables constant. This allows the determination of individual scattering functions $S_{ij}(\mathbf{Q})$, and their Fourier transform, the partial distribution functions $g_{ij}(r)$. As terbium metaphosphate glass is paramagnetic, the coherent scattering length was changed from $b_{Tb}$ to $b_{Tb}\pm(1/2)gr_0f(\mathbf{Q})\langle J_z\rangle$) by the application of a strong magnetic

field. The magnetic form factor f(**Q**) quantifies the contribution due the space distribution of the 4f electrons within the terbium atom; $r_0$ is the magnetic interaction strength (equal to $\gamma e^2/m_e c^2$ where $m_e$ is electron the mass, and $\gamma$ is the neutron gyromagnetic ratio), $\pm 1/2$ enters into the equation as the beam is unpolarized hence half of the neutrons will have spin up orientation (+ve sign) and the other half will have spin down (-ve sign), g is the Landé splitting factor and $\langle J_z \rangle$ is the total angular momentum in the direction of the applied magnetic field. If the total neutron scattering data from terbium metaphosphate glass is simplified to a binary system (equation 6.30) (phosphorus and oxygen have similar scattering lengths, 5.13, 5.83fm respectively), the resulting first order difference pattern (high field minus zero field data), depends only on the $S_{Tb,Tb}(\mathbf{Q})$,

$$I(\mathbf{Q}) = N\{c_{Tb}(g/2)^2 f^2(\mathbf{Q}) r_0^2 \langle J_z \rangle^2 + c_{Tb}^2 (g/2)^2 f^2(\mathbf{Q})\, r_0^2 \langle J_z \rangle^2 [S_{Tb,Tb}(\mathbf{Q})-1]\} \qquad (6.31)$$

and not on the scattering function between oxygen and terbium atoms, $S_{Tb,O}(\mathbf{Q})$, and oxygen-oxygen correlation's $S_{O,O}(\mathbf{Q})$. Hence the Fourier transform of $S_{Tb,Tb}(\mathbf{Q})$ gives the terbium-terbium correlation distance. In practice a pseudo binary approximation has not been used, see section 7.2. Development of this technique could be used to examine paramagnetic ion clustering within an amorphous sample. Atomic clustering has an adverse effect on the optical properties of a materials as it can increase non-radiative losses.

### 6.3.2 POLARIS APPARATUS

The total neutron scattering experiment was performed on the Polaris station (ISIS beamline S1) at Rutherford Appleton Laboratory. Polaris is a high intensity, medium resolution, powder diffractometer. It receives white beam neutrons (beam cross section 40 × 25mm) from a 295K $H_2O$ moderator. As with the HET station, the sample tank is evacuated ($\sim 10^{-1}$mbar) to reduce background scattering from the air. The terbium metaphosphate glass sample (6.87g) was loaded into an 11mm diameter thin walled vanadium sample can and placed inside an Oxford Instruments cryomagnet, the design of which is based around a standard helium cryostat into which has been incorporated a superconducting magnet capable of generating a homogeneous magnetic field of up to 7.5T over the entire sample volume. The $Tb^{3+}$

glass sample was cooled to 4K and scattering spectra were collected at zero field and in a magnetic field of 7.5T, applied vertical to the sample. The sample was cooled to 4K, as to calculate the terbium-terbium correlation distance full alignment of the dipole moments is required, and at this temperature the random thermal motion of the ions are significantly suppressed. The zero field data was also measured at this temperature, to keep all external factors constant. Time-of-flight neutron diffraction patterns were recorded in the horizontal plane using the low angle 'A' ($28° < 2\theta < 42°$, $Q_{min}$ ~$0.8Å^{-1}$) and back scattering 'C' ($135° < 2\theta < 160°$, $Q_{min}$ ~$2.0Å^{-1}$) $He^3$ detector banks, see figure 6.6. The low angled 'A' banks are the most informative, as they record mainly low momentum transfer, **Q**, scattering. (There are two other sets of detectors on Polaris, ZnS scintillators, but as a large field was applied they could not be used).

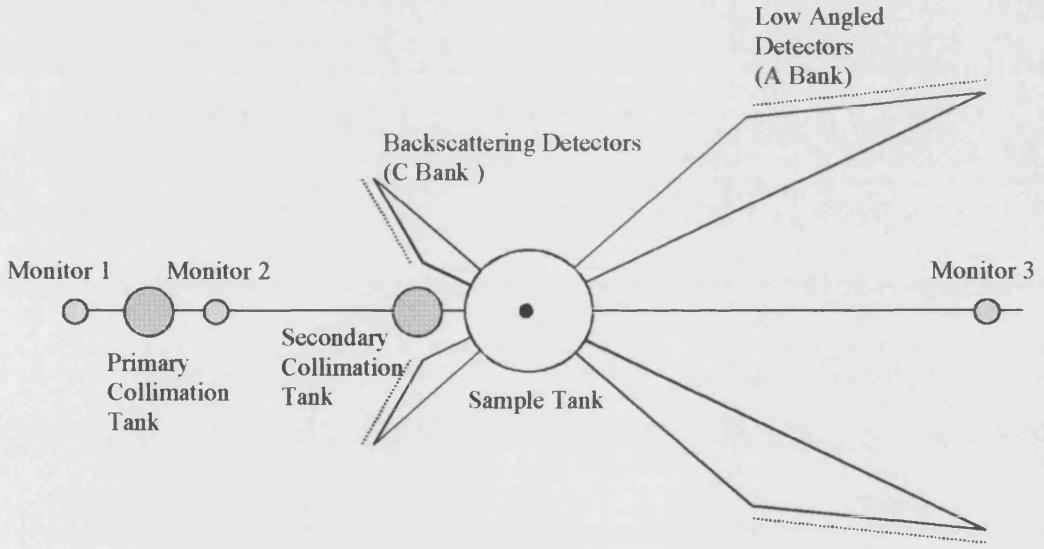


Figure 6.6 Schematic layout of Polaris's detectors

The collimating tanks are used to reduce the dimensions of the beam, and align it (horizontally and vertically) with the centre of the sample. Monitors 1 and 2 observe the incident neutron beam, and the third monitor records the transmitted beam, providing information about the incident energy of the neutrons. Polaris is designed to give constant resolution in each of the detector elements within each bank. For Bragg reflection $2d\sin\theta = n\lambda = nht/mL$ (using equation 6.1), where $2\theta$ is the scattering angle,

$\lambda$ is the neutron wavelength, t is the total time-of-flight, L flight path and d is the interplaner spacing, the resolution can be written as,

$$R(d) = \Delta d/d = [(\Delta\theta\cot\theta)^2 + (\Delta t/t)^2 + (\Delta L/L)^2]^{1/2} . \qquad (6.32)$$

As the scattering angles decreases, the uncertainty in the resolution due to the angular contribution increases. For bank 'C' the error in the angular position is relatively small, and resolution is dominated by time uncertainties. For 'A' bank, the theta term dominates, so it is necessary that $\Delta\theta\cot\theta$ is constant across the elements; this is achieved by positioning the detectors almost parallel to the incident beam. To correct and normalise the data, several additional runs had to be made. Scattering from a vanadium rod acts as an absolute efficiency calibration, as it produces approximatly completely incoherent scattering, and empty vanadium can runs are used to eliminate Bragg peaks arising from sample tank, cryostat windows etc. Finally, all the background scattering that occurs prior to the sample, can be measured, by filling the vanadium can with boron carbide, as this absorbs all the neutrons which would have been diffracted by the sample (see section 6.3.3). If the terbium-terbium correlation distance is to be calculated, it is necessary to check that there is total alignment of the paramagnetic dipole moments under the applied field experimental conditions (7.5T and 4K). This was tested by recording the magnetic moment as a function of applied field using the vibrating sample magnetometer (VSM) at Southampton University. In a VSM (Jiles 1995) a sample is moved between the poles of an electromagnet and the difference in magnetic induction ($V=-Nd\Phi/dt$ where V is the induced emf, N is the number of turns in the coil of the electromagnet and $d\Phi/dt$ the rate of change of the magnetic flux) between areas where there is, and is not, a sample present, can be directly related to the magnetisation **M**. The change in magnetic flux density $\Delta\mathbf{B}$ ($=\Phi/A$ where A is the coil cross section) for a coil with a sample, $\mathbf{B}_m$, and free space, $\mathbf{B}_o$, centre is,

$$\Delta\mathbf{B} = \mathbf{B}_m - \mathbf{B}_o = \mu_o(\mathbf{H}+\mathbf{M}) - \mu_o\mathbf{H} = \mu_o\mathbf{M} \qquad (6.33)$$

where **H** is the magnetic field strength and $\mu_0$ is the permeability. Therefore flux change as the sample is moved depends only on the magnetisation of the sample, and not on **H**, consequently so does the VSM output;

$$\int V dt = -NA\mu_o\mathbf{M} \qquad (6.34)$$

The magnetic moment **m** (= **M**V, where V is the volume of the sample) was measured as the applied field, **B**, was increased up to 10T at 10K, 5K and 1.8K, with respect to finding the conditions under which saturation magnetisation was reached.

### 6.3.3. DATA CORRECTION PROCEDURES

Before the extraction of the terbium-terbium partial structure factor from the neutron scattering data (with and without applied field), the spectra must initially be corrected and normalised (Soper et al. 1989). Data analysis has been executed using Polaris specific commands on the Genie data display and manipulation program (Smith and Hull 1997). The accuracy of the data corrections may be affected by the high level of multiple scattering, which is likely to be present in such a large sample.

Initially all the raw data sets have to be input into different workspaces (in Genie workspaces are used to store a single spectrum, or the result of some arithmetic operation involving several spectra); these are then Afocused. Afocus is a command file, which sums the counts from different detectors in the 'A' bank, in order to improve statistics. The resultant is subsequently divided by the incident monitor counts to normalise to the data to the counting time. This process is employed to eliminate fluctuations due to variation in the incident beam, caused by small changes in the temperature of the moderator or proton beam steering. The normalised data sets from 'like' runs (i.e. same sample, temperature, and field) are then ready to be summed. To isolate the terbium-terbium correlation distance, five different environments have to be measured: terbium metaphosphate glass in a vanadium can (no field, NF), terbium metaphosphate glass at 7.5T in a vanadium can (high field, HF), (see figure 6.7) 10mm vanadium rod in a vanadium can (VR), and two background runs in the form of empty vanadium can (EVC), and boron carbide in a vanadium can (BC); all runs were recorded at 4K.

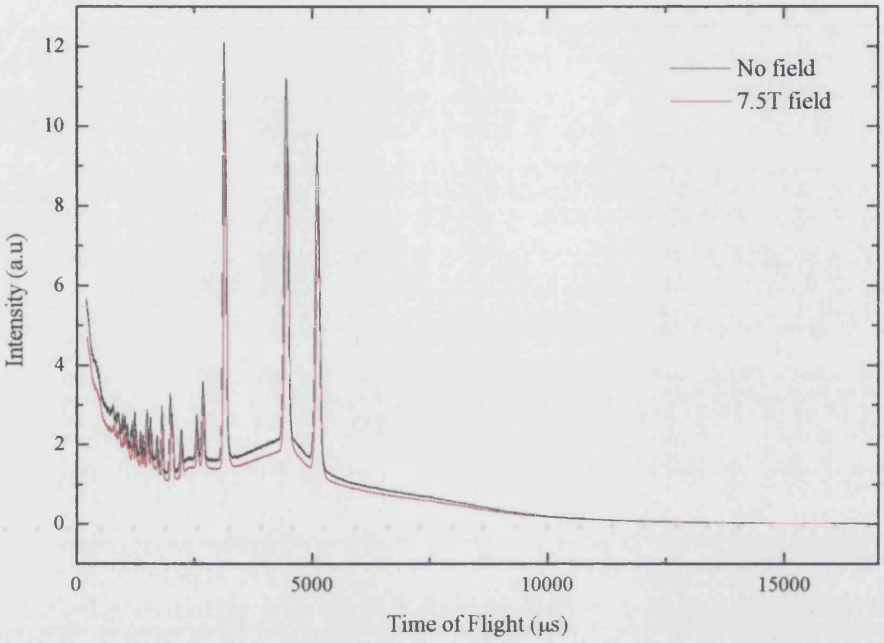


Figure 6.7. The Afocused and summed raw neutron scattering data sets for terbium metaphosphate glass, $(Tb_2O_3)_{0.247}(P_2O_5)_{0.753}$, with (red line) and without (black line) an applied magnetic field. The graph features a number of Bragg peaks, these are the result of background scattering from the cryomagnet, sample holder etc.

The vanadium spectrum, which exhibits almost pure incoherent scattering and has a known differential cross section, is used to normalise the data to the energy distribution of the incident flux and also corrects for the variation in detector efficiency with neutron wavelength. Boron carbide is totally absorbing; hence the run only records the scattering that occurs before the sample (i.e. the windows of the cryostat) $B_2$ in figure 6.8. The spectrum from the EVC is a combination of scattering from before and after (cryostat walls) the sample ($B_1$+$B_2$). The measured (Afocused) scattering, C, from the different runs can be written in terms of the total scattering from the sample $S_S$ and the vanadium $S_V$, and the self shielding factor $\alpha$

$$C_S = \alpha_S S_S + \alpha_S B_1 + B_2$$

$$C_{EVC} = B_1 + B_2$$

$$C_V = \alpha_V S_V + \alpha_V B_1 + B_2$$

$$C_{BC} = B_2 \qquad (6.35)$$

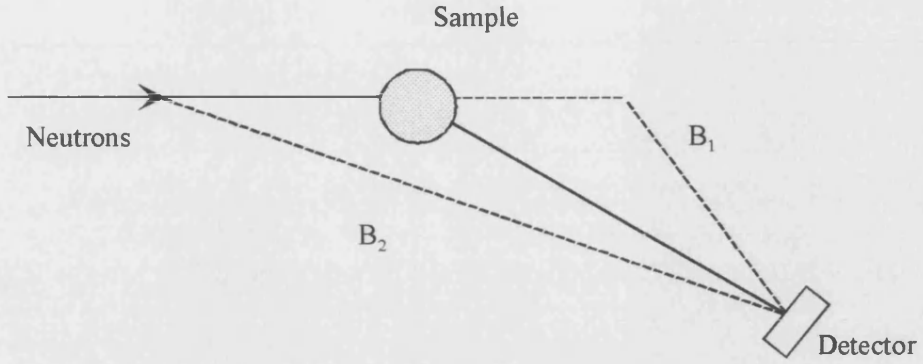


Figure 6.8. Schematic of the experimental set up. $B_1$ represents the background scattering that occurs to the neutrons after leaving sample and $B_2$ is the background contribution due to the scattering of the incoming neutrons prior to the sample.

Both the terbium metaphosphate glass, and vanadium rod data have to be corrected for scattering from the vanadium can and instrumental background. Attenuation and multiple scattering depends on the energy of the incoming neutrons ($E=mL^2/2t^2$ where m is the mass of the neutron, L is the path length (14m for the low angle banks) and t is the time of flight). The wavelength dependent sample absorption ($\lambda = \alpha_V^{-1}$) for the vanadium rod can be calculated using a routine in Genie called CORRECT. To run this calculation, the cylindrical radius (5mm), number density ($7.21\times10^{22}$ vanadium ions $cm^{-3}$), and the total scattering and absorption cross section (5.1 and 5.08 barns respectively) of the vanadium sample need to be known. The vanadium absorption corrected spectrum is then divided by the raw vanadium data to find the wavelength dependent absorption $\alpha_V^{-1}$. The necessary background corrections required to isolate the total vanadium neutron scattering, $S_V$, can be found by rearranging equation 6.35:

$$S_V = \alpha_V^{-1}\times(C_{VR}-C_{BC})-(C_{EVC}-C_{BC}) \qquad (6.36)$$

This spectrum is shown in figure 6.9. Finally the vanadium rod data can be smoothed using a VSPLINE fitting programme.

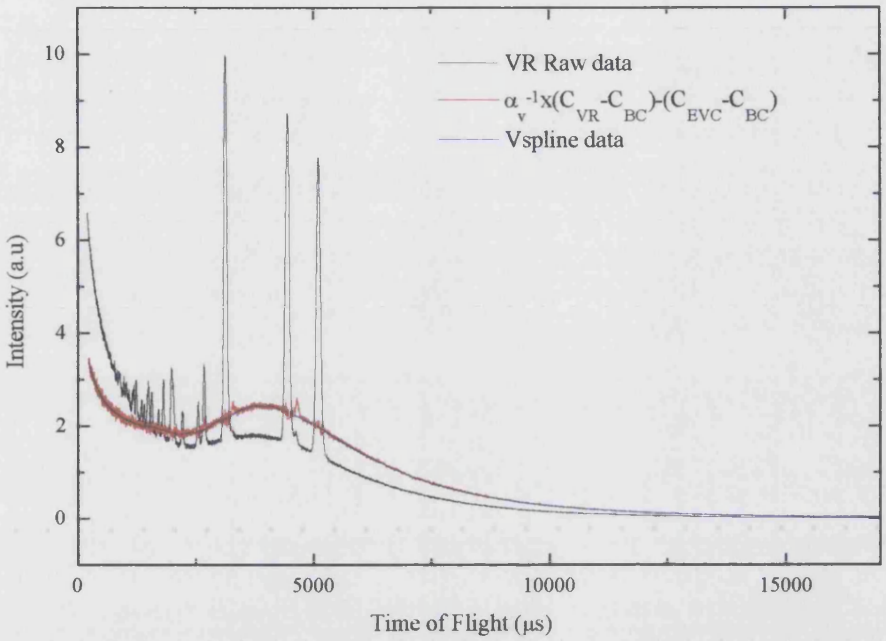


Figure 6.9. The different correction stages of the 10mm vanadium rod neutron scattering data.

A similar procedure can be implemented when correcting the no field and high field terbium metaphosphate glass sample. To find the wavelength dependent absorption correction factor (which is the same for the sample with and without applied field), the sample was also analysed using the CORRECT program (radius = 4.1cm, number density = $0.549\times10^{22}$ terbium ions $cm^{-3}$, total scattering cross section 54.86barns, and total absorption cross section 23.92barns). The total scattering from the no field and high field can be calculated using:

$$S_{NF}= \alpha_S^{-1}\times(C_{NF}-C_{BC})-(C_{EVC}-C_{BC})$$
$$S_{HF}= \alpha_S^{-1}\times(C_{HF}-C_{BC})-(C_{EVC}-C_{BC}). \quad (6.37)$$

The total scattering spectra from terbium metaphosphate glass are subsequently divided the by the smoothed vanadium data, ($S_S/S_V$). This has the effect of allowing the absolute normalisation of I(**Q**) to be estimated, and removes any discrepancies incurred due to the incident monitor (used to normalise the measured spectra) and detectors having different efficiencies, see figure 6.10.

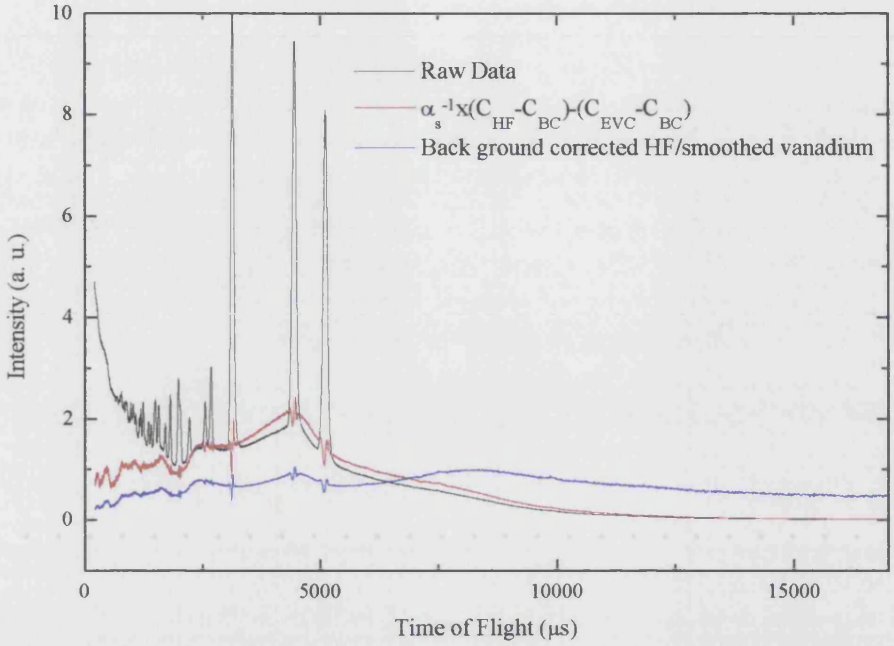


Figure 6.10. The different correction stages of the high field terbium metaphosphate glass $(Tb_2O_3)_{0.247}(P_2O_5)_{0.753}$ neutron scattering data.

The normalised terbium glass spectra can now be converted into an absolute cross section. This is achieved by finding the ratio of the corrected scattering from the terbium metaphosphate sample $S_S$ (either $S_{NF}$ or $S_{HF}$) to that of the vanadium sample $S_V$:

$$S_s = N_S \times \left[\frac{d\sigma}{d\Omega}\right]_S$$

$$S_V = N_V \times \left[\frac{d\sigma}{d\Omega}\right]_V$$

Hence

$$\left[\frac{d\sigma}{d\Omega}\right]_S = \frac{N_V S_S}{N_S S_V}\left[\frac{d\sigma}{d\Omega}\right]_V \qquad (6.38)$$

where Ns and $N_V$ are the number of $Tb(PO_3)_3$ molecules and vanadium atoms per unit volume ($5.5\times10^{21}cm^{-3}$, and $7.2\times10^{22}cm^{-3}$ respectively), and $[d\sigma/d\Omega]_V$ is the vanadium differential cross section ($5.1/4\pi$ barns steradian$^{-1}$), hence $[d\sigma/d\Omega]_S = 5.33S_S/S_V$. If the normalised spectra are now multiplied by this value, the no field and high field terbium

metaphosphate glass data can be expressed in terms of barns/steradian/terbium atom, see figure 6.11.

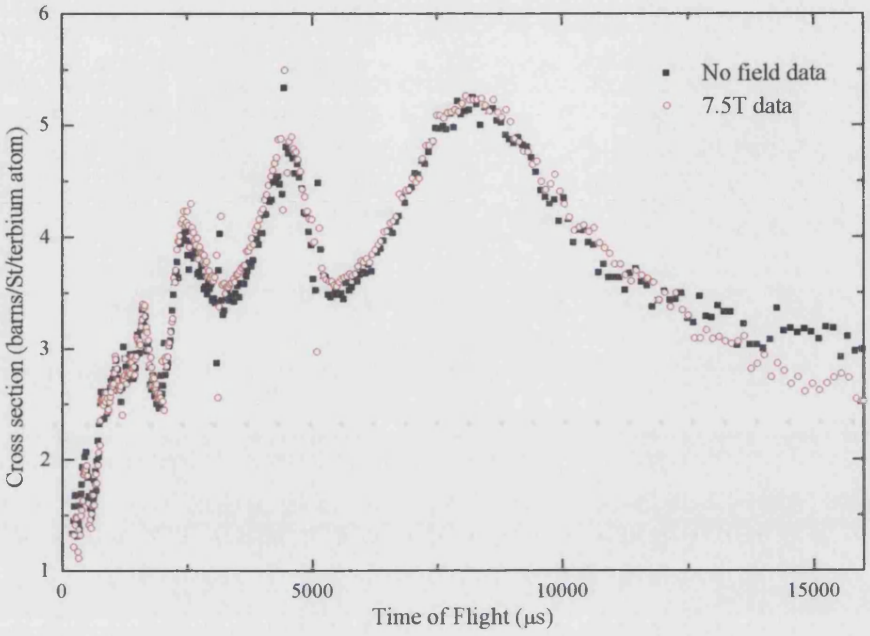


Figure 6.11. The no field (▪) and high field (○) neutron scattering data for terbium metaphosphate glass $(Tb_2O_3)_{0.247}(P_2O_5)_{0.753}$.

At long times-of-flight (small wavevectors) the scattering is suppressed by the field; however in contrast it appears to enhance the first peaks of the scattering factor. These characteristics are consistent with the picture of random paramagnetic ions contributing a general smoothed background to the zero field terbium structure factor. When the magnetic field is applied the dipoles are aligned, this is accompanied by a reduction in this incoherent scattering (i.e. a diminishing paramagnetic form factor), but an increase in their contribution to the coherent structured scattering i.e. $\mathbf{S(Q)}$. If the sample is fully aligned, the correlation between magnetic moments of different sites $\langle J_i J_j \rangle$ is going to be the same as the nuclear correlations $\langle b_i b_j \rangle$, so the effective scattering length becomes a combination of the magnetic and nuclear scattering lengths. The high field data can now be subtracted from the zero field spectrum and the resulting first order difference equation can be Fourier transformed to find the terbium-terbium correlation distance.

# CHAPTER SEVEN

## RESULTS AND DISCUSSION OF NEUTRON SCATTERING EXPERIMENTS

Neutron scattering techniques have been employed to explore the environment of trivalent rare earth ions situated in an amorphous phosphate host. Inelastic scattering has been used to probe the magnetic contribution, arising from the partially filled 4f shell, to the scattered neutron intensity; thus giving information on the splitting of the energy levels. Carini et al. (1997, 1998) examined praseodymium metaphosphate glass using specific heat and low frequency Raman scattering. They observed excess contributions due to low lying magnetic excitations and suggested these originate from a continuous distribution of crystal field interactions. However, other contributory effects such as hyperfine interactions or co-operative transitions have not been discounted; these processes arise when there is ion clustering within the sample. Clustering has a negative effect on the optical properties of a system, due to cross relaxation's producing reduced recombination times (section 10.1.3). EXAFS data (Bowron et al. 1994, 1996a, section 5.2) has found no evidence to support rare earth ions being nearest neighbours in the short lengths scales probed by this technique. Here a novel method of neutron scattering has been used to determine the correlation distance between terbium ions. The terbium-terbium partial distribution function has been calculated using a neutron scattering technique similar to isotropic substitution; however the scattering length of the terbium ion is changed by the application a magnetic field.

## 7.1. INELASTIC NEUTRON SCATTERING, RESULTS AND DISCUSSION

The spectra from the HET inelastic scattering experiments for metaphosphate glasses doped with lanthanum, praseodymium, neodymium, terbium, dysprosium, erbium and thulium have been compared with previously published results on the crystal field splitting of lanthanides in different host materials. The inelasticity of the magnetic scattering arises from the neutron exciting crystal field transitions of the 4f electrons. In the measured spectra the observed peak positions are equal to the energy separation between two crystal field states, and the intensity is proportional to the transition probability. In all the REMGs studied the first excited multiplet state is not thermally populated at the temperatures the measurements were made, and it is also located outside the neutron energy range used (see figure 10.1, where 1meV is equivalent to $8.066cm^{-1}$ and 11.6K); hence transitions from the ground state to higher energy levels are not observed The crystal field spectra recorded in rare earth phosphate glasses suffer a significant degree of broadening compared to their crystalline counterparts. This is a consequence of the topological disorder associated with all amorphous materials, which has the effect of producing deviations in the local environment, and hence a distribution of closely spaced (quasi-continuous) crystal field energies. The error in the data is proportional to $\sqrt{N}$, where N is the number of measured scattering events, and is thus determined by the quantum efficiency of the detectors, the total flux, the counting time and the binning of the detectors. All the graphs in this section (figure 7.1-7.9) show the data collected in workspace W8, which is the average of the low angled detectors positioned at 2.5m (see section 6.2.3). The shape of the spectra are expected to be symmetric about the elastic scattering region (i.e. $\Delta \hbar\omega = 0$), and consist of features on both sides representing energy gained by the neutrons (or energy loss in the sample) $\hbar\omega < 0$, and the energy lost by the neutrons $\hbar\omega > 0$. This is not observed in the experimental data as the detailed balance factor $\exp(-\hbar\omega/k_BT)$ (where T is the temperature and $k_B$ is the Boltzmann factor) attenuates scattering at neutron energy gains greater than a few $k_BT$ ($S(-\mathbf{Q},-\omega)=\exp(-\hbar\omega/k_BT)S(\mathbf{Q},\omega)$) (Squire 1978, Furrer 1995). The exponential term corresponds to the difference in probability between an initial scattering system being in a higher energy state rather than a lower one. As the temperature is reduced the thermal population damping acts to suppress energy gained by the neutrons. The

majority of the neutron scattering data was recorded at low temperatures (20-22K) because as the temperature is raised the quasi-local vibrational modes make up an increasing proportion of the total scattering, hence the error in the magnetic scattering becomes increasingly significant. All the data exhibit a central peak, which is not totally removed by subtraction of the phonon contributions; this is a consequence of quasi-elastic scattering within crystal field split doublets, triplets etc. The rare-earth ions are expected to occupy low symmetry sites in glasses: orthorhombic, monoclinic or triclinic (Van Deun et al. 1998). This would correspond to the total removal of the crystal field degeneracy. For several of the samples it has been assumed, for data comparison purposes, that the ions are situated in a site with symmetry being close to cubic (cubic is a sub-set of orthorhombic). This hypothesis is plausible as the splitting observed in the fluorescence spectrum of samarium metaphosphate glass is consistent with a near cubic local symmetry about the $Sm^{3+}$ ion (Farok et al to be published). The assumption is also supported by EXAFS data (Bowron et al. 1994, 1996a) which places the number of nearest neighbour oxygen atoms about a rare earth ion as $7 \pm 1$ atoms. Unfortunately due to the broadening of the transitions no conclusion about the symmetry of the rare earth ions in metaphosphate glasses can be made from the inelastic neutron scattering.

The total inelastic scattering spectrum of lanthanum metaphosphate glass (17.49g) excited with neutrons which had an incident energy ($E_0$) of 30meV is shown in figure 7.1. The total scattering spectrum is the raw data corrected for $k_i/k_f$, solid angle, background and normalised to the incident neutron flux (section 6.2.3). The lanthanum glass spectrum, which in the absence of 4f electrons, can be assumed to include only vibrational contributions due to inelastic nuclear scattering from the phonons. The lanthanum glass was also measured using neutrons with energies of 90meV; two energy ranges have been recorded as, although the 30meV spectrum gives improved resolution, some of the samples show crystal field structure in excess of 30meV.

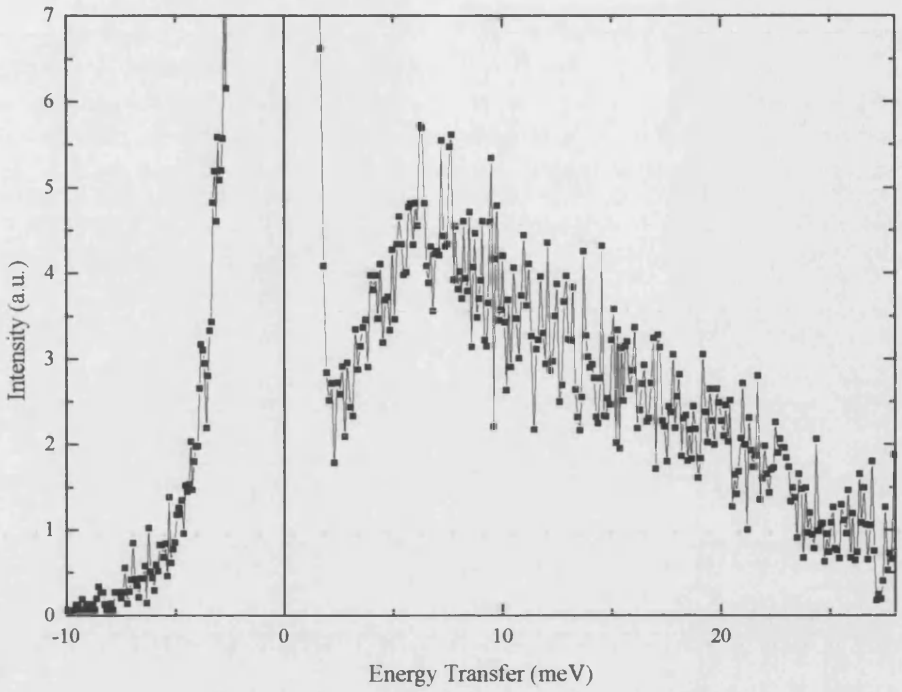


Figure 7.1. The total inelastic neutron scattering spectrum of lanthanum metaphosphate glass at 22K, with an incident neutron energy of 30meV.

Terbium (8.76g, figure 7.2 and 7.3), thulium (1.87g, figure 7.4) and praseodymium (20.43g, figure 7.5. and 7.6), are non-Kramers ions, i.e. in low symmetry sites the ion is expected to form a singlet in the ground state. The terbium (figure 7.2 and 7.3), and thulium spectra (figure 7.4) are similar in shape. They both display a single inelastic feature in the total and magnetic scattering data: a broad shoulder ranging from the elastic peak to ~40meV. The lowest multiplet of the terbium and thulium ions both have a total angular momentum (J) of six. Lea, Leask and Wolf (1962) calculated that the thirteen fold degeneracy would be partially lifted in a cubic field to give two singlets ($\Gamma_1$, $\Gamma_2$) one doublet ($\Gamma_3$) and three triplets ($\Gamma_4$ $\Gamma_5^{(1)}$ $\Gamma_5^{(2)}$). The relative order in which the energy levels occur depends on x, the ratio of the fourth and sixth-order coefficients, and the scale of the overall splitting (W), which is determined by the magnitude of the crystal field parameters. The matrix element $\left|\langle \Gamma_i | J_Z | \Gamma_f \rangle\right|^2$, which describes the probability (and hence the intensity) of a magnetic dipole transition between an initial $\Gamma_i$ and final $\Gamma_f$ crystal field level, has been calculated by Birgeneau et

al. (1971) for J between 2 and 8. The allowed inelastic transitions for terbium and thulium ions are ($\Gamma_1$ - $\Gamma_4$), ($\Gamma_5^{(2)}$ - $\Gamma_2$), ($\Gamma_2$ - $\Gamma_5^{(1)}$), and all combinations of $\Gamma_3$, $\Gamma_4$, $\Gamma_5^{(1)}$ and $\Gamma_5^{(2)}$; quasi-elastic scattering is expected to arise from transitions within the $\Gamma_4$, $\Gamma_5^{(1)}$,$\Gamma_5^{(2)}$ energy levels but obviously not from the non-magnetic $\Gamma_1$ and $\Gamma_2$ levels. The individual peaks are too close to be resolved experimentally in these amorphous samples. The inelastic scattering of terbium (figure 7.2) and praseodymium (figure 7.5) metaphosphate glass has been measured at several temperatures. The total inelastic scattering data has been presented in these figures rather than the magnetic neutron scattering, which has also been calculated, as the total scattering exhibits the same characteristics as the magnetic scattering in these samples (see figure 7.3 and 7.6) but suffers less from data fluctuations, making it easier to compare trends in the spectra. The results clearly illustrate the effect of the detailed balance factor on the negative side of the graph i.e. a reduction in energy gained by the neutron as the temperature is lowered. This population damping is expected to be accompanied by a decrease in the elastic peak, due to a reduction of the population in higher energy ground states, and therefore associated quasi-elastic scattering. In the terbium metaphosphate glass data (figure 7.2), at low energy transfers (<10meV), increasing the temperature from 22 to 91K increases the height of the shoulder intensity ($\propto S(\mathbf{Q},\omega)$); at higher energy transfers the magnetic inelastic scattering is the same for all three temperatures within experimental error. As $S(\mathbf{Q},\omega)$ is proportional to the density of states, this phenomena is probably a consequence of a population increase in the higher crystal field levels, and therefore a corresponding increase in transitions between closely spaced higher energy levels i.e. lowering the temperature depopulates the high energy crystal field states of the ground multiplet and only transitions from the lowest lying $\Gamma_i$'s are expected to contribute to the scattering intensity. The additional transitions manifest themselves as a 'smooth bump' in the spectrum, as the crystal fields in an amorphous material can be considered quasi-continuous. Loong et al. (1993c) found similar trends in the inelastic neutron scattering data of terbium orthophosphate ($TbPO_4$), measured at several temperatures between 4.2 and 150K. $TbPO_4$ crystallises in a tetragonal zircon structure, and the corresponding crystal field effect on the terbium ion is to split the ground state into seven singlets and three doublets. They recorded major transition peaks at 0.46, 0.97, 2.6, 6.8, 9.2, and 20.2

meV, and found that the intensity of the 6.8meV peak increases with increasing temperature, while all the other magnetic peaks decrease as the temperature is raised.

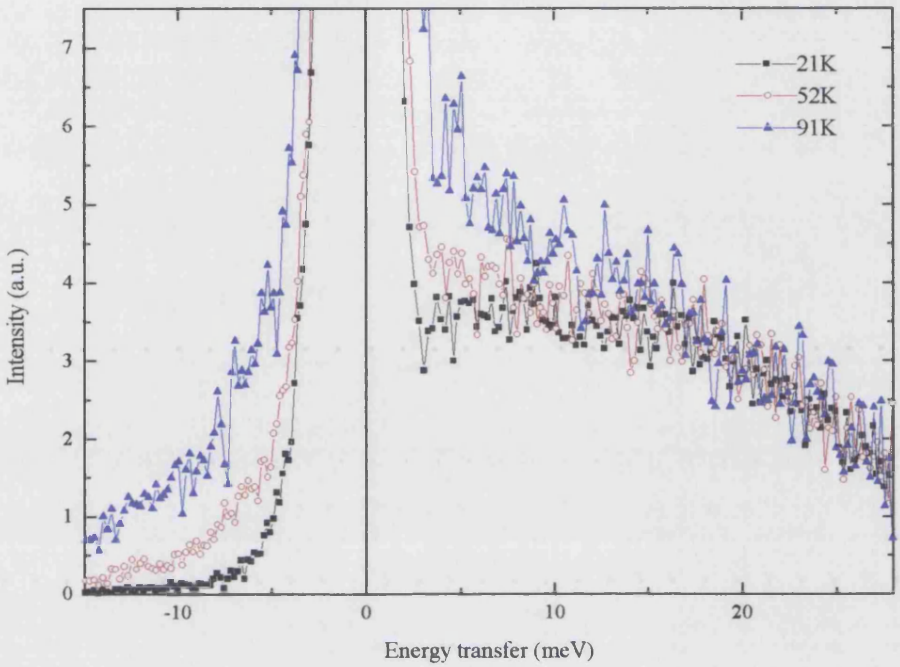


Figure 7.2. The total inelastic neutron scattering from terbium metaphosphate glass at 21K, 52K and 91K, with an incident neutron energy of 30meV.

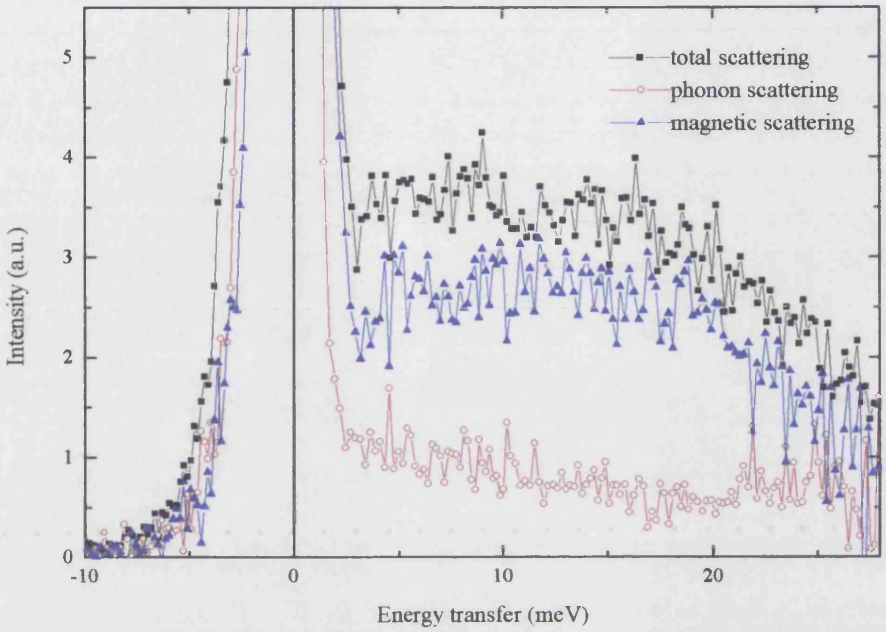


Figure 7.3. The inelastic neutron scattering from terbium metaphosphate glass at 21K, with a neutron incident energy of 30meV. The phonon scattering is the scaled low angle lanthanum spectrum (see section 6.2.3), and the magnetic scattering is the resultant of the total scattering minus the estimated phonon contribution.

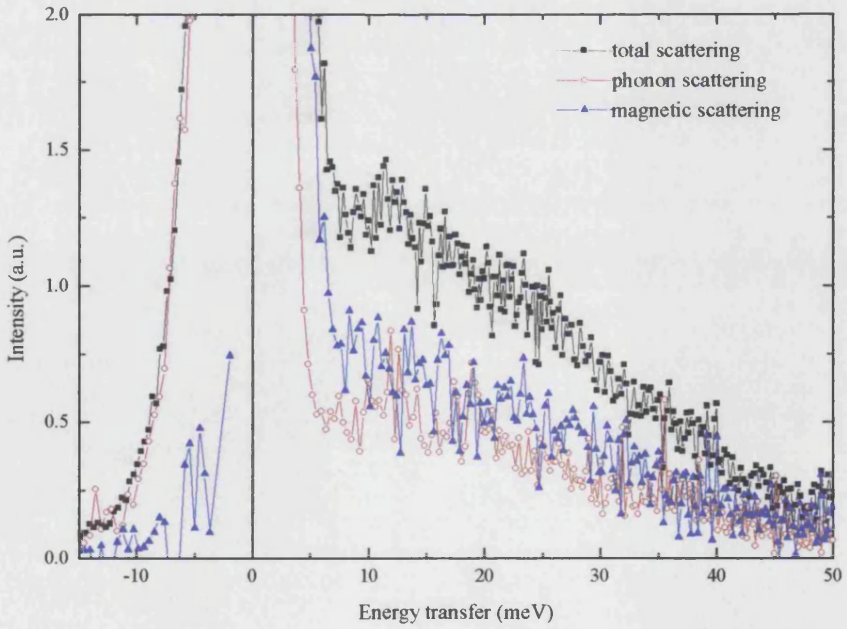


Figure 7.4. The inelastic neutron scattering from thulium metaphosphate glass at 21K, with an incident neutron energy of 60meV.

The inelastic peak in the praseodymium metaphosphate glass (figure 7.5 and 7.6) has considerably improved definition, and occurs centred at 4.5meV (22K). The spectrum also consists of a long tail in the positive (neutron energy loss) direction which may be due to transitions between the broad spread of states resulting from the different environments of the $Pr^{3+}$ ion. The ground level of trivalent praseodymium is the J = 4 manifold $^3H_4$, which splits into a singlet ($\Gamma_1$), a non-magnetic doublet ($\Gamma_3$), and two triplets ($\Gamma_4, \Gamma_5$) in a cubic environment (Lea et al. 1962, Tuberfield et al. 1970, 1971, Loewenhaupt and Prager 1986). The inelastic spectrum originates from ($\Gamma_5$ - $\Gamma_3$), ($\Gamma_4$ - $\Gamma_5$), ($\Gamma_4$ - $\Gamma_3$) and ($\Gamma_1$ - $\Gamma_4$) transitions, and the quasi-elastic scattering is due to ($\Gamma_4$ - $\Gamma_4$) and ($\Gamma_5$ - $\Gamma_5$). Tuberfield et al. (1970, 1971) studied the inelastic neutron scattering from praseodymium monopnictides (PrBi, PrSb, PrP). They were able to correlate the four inelastic transitions to peaks in their spectra: for PrSb, ($\Gamma_3$ - $\Gamma_4$) occurs at a position of 4.5 meV, ($\Gamma_4$ - $\Gamma_1$) at 6.3 meV, ($\Gamma_5$ - $\Gamma_3$) at 9.8 meV, ($\Gamma_5$ - $\Gamma_4$) at 14.3 meV. Assuming a degree of similarity between the samples being studied, the main peak in figure 7.5 and 7.6 probably arises from a combination of the ($\Gamma_3$ - $\Gamma_4$) and ($\Gamma_4$ - $\Gamma_1$) excitations. The two remaining transitions are not resolvable within the fluctuations in the data, but they are assumed to contribute to the shape of the tail. In the measurements made by Turberfield et al (1970, 1971) they observed a reduction in the intensity of the higher energy transfer peaks ($\Gamma_5$ - $\Gamma_3$) and ($\Gamma_5$ - $\Gamma_4$) with decreasing temperature; at 80K the intensity of these peaks were only approximately 13% of the ($\Gamma_4$ - $\Gamma_1$) transition strength. In contrast the height of the inelastic features in the PrSb spectra due to the ($\Gamma_3$ - $\Gamma_4$) and ($\Gamma_4$ - $\Gamma_1$) excitations increased with falling temperature. This trend was observed in the inelastic neutron scattering spectrum of praseodymium metaphosphate glass at temperatures of 142K, 72K, and 22K (the 142K data is not included in figure 7.5 for clarity). As the temperature is increased the phonon contribution rises, but the magnetic contribution decreases, this leads to the overall reduction in the total scattering as seen in figure 7.5. Carini et al. (1997, 1998) studied praseodymium metaphosphate glass, using a method of low frequency Raman scattering (below 100 $cm^{-1}$) (LFRS), to examine a peak in the density of low lying magnetic excitations which occurred at 37$cm^{-1}$ (corresponding to 4.6meV). They also found that lowering the temperature increases the intensity of this peak and shifts its maxima to lower frequencies. In a subsequent paper by Carini et al. (to be published)

they compared the LFRS and specific heat of praseodymium metaphosphate glass with monocrystalline $PrP_5O_{14}$ and concluded that the results could be described within the frame work of a singlet-singlet interaction. This suggests that the $Pr^{3+}$ ion is not situated a cubic site in a metaphosphate glass.

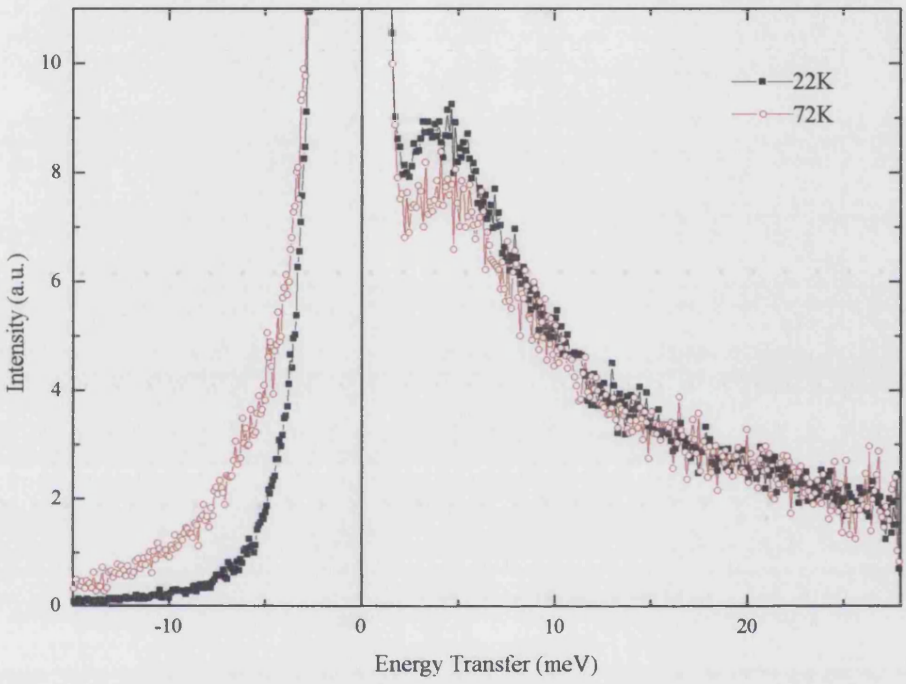


Figure 7.5. The total inelastic neutron scattering from praseodymium metaphosphate glass at 22K and 72K, with an incident neutron energy of 30meV.

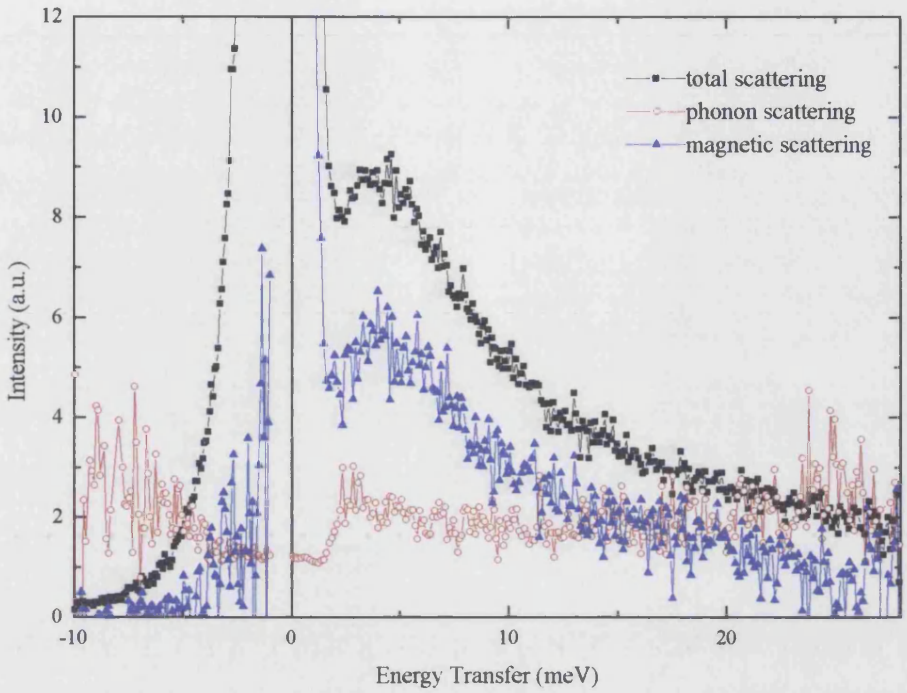


Figure 7.6. The inelastic neutron scattering from praseodymium metaphosphate glass at 22K, with an incident neutron energy of 30meV.

Neodymium (8.08g, figure 7.7), dysprosium (4.83g, figure 7.8) and erbium (2.04g, figure 7.9) are Kramers ions, and hence the ground state degeneracy is a doublet. At all temperatures Kramers ions should display a central peak which is characteristic of quasi-elastic scattering between the two closely spaced ground state levels. The inelastic magnetic neutron scattering spectra of neodymium (figure 7.7), and dysprosium (figure 7.8) glass contain similar characteristics: a prominent peak at 6.5 or 4.6 meV respectively, faint structural features which occur in neodymium at approximately 13, and 19meV, and in dysprosium at 14meV, and both glasses exhibit broad tail which may be the consequence of the superposition of several smaller peaks. The ground multiplet of neodymium $Nd^{3+}$ ($4f^3$, $^4I_{9/2}$), can be partially quenched into one doublet ($\Gamma_6$), and two quartets ($\Gamma_8^{(1)}$, $\Gamma_8^{(2)}$) by a cubic field (Lea et al 1962). All combinations of inelastic and elastic transitions are allowed according to magnetic dipole selection rules (Birgeneau 1972). The spectrum of neodymium situated in cubic hexaboride was recorded by Loewenhaupt and Prager (1985) using inelastic neutron scattering. Their sample exhibits peaks at similar positions to the ones observed in

figure 7.7, two strong transitions occur at 12meV (($\Gamma_8^{(2)}$ - $\Gamma_8^{(1)}$) and ($\Gamma_8^{(1)}$ - $\Gamma_6$)) and a weaker one at ~24meV ($\Gamma_8^{(2)}$ - $\Gamma_6$); however there is no evidence of the prominent peak which occurs at 6.5meV in the metaphosphate glass sample. The results taken by Loewenhaupt and Prager (1985) were recorded at 150K which suggests that their spectrum would experience a significant contribution from thermal broadening, and as Carini et al. (1997) observed, in LFRS measurements of praseodymium metaphosphate glass, an increase in the temperature can also produce in an increase in the frequency (or energy) at which the maxima occurs. The neodymium neutron scattering spectra recorded by Soderholm et al (1991) in $RBa_2Cu_3O_7$ exhibited similar characteristics to Loewenhaupt and Prager (1985). The crystal field site symmetry of their orthorhombic sample splits the ground state of $Nd^{3+}$ into five doublets, and sharp peaks are observed at 12, 20.8, 36, and 117meV. A degree of variation in peak positions due to the different hosts is expected, especially as the rare earth ion may well be situated in the metaphosphate glass with a symmetry lower than orthorhombic.

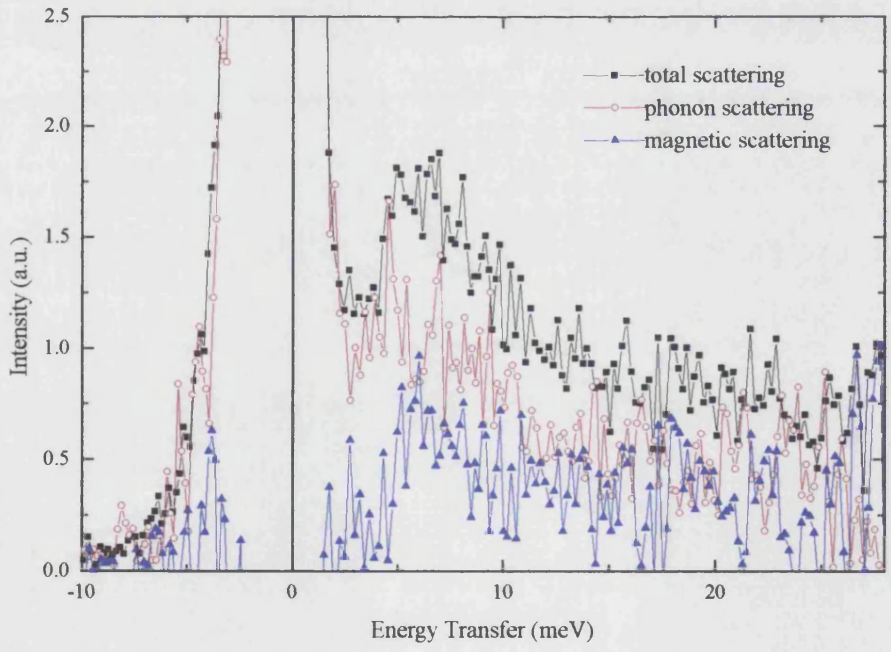


Figure 7.7. The inelastic neutron scattering from neodymium metaphosphate glass at 22K, with an incident neutron energy of 30meV.

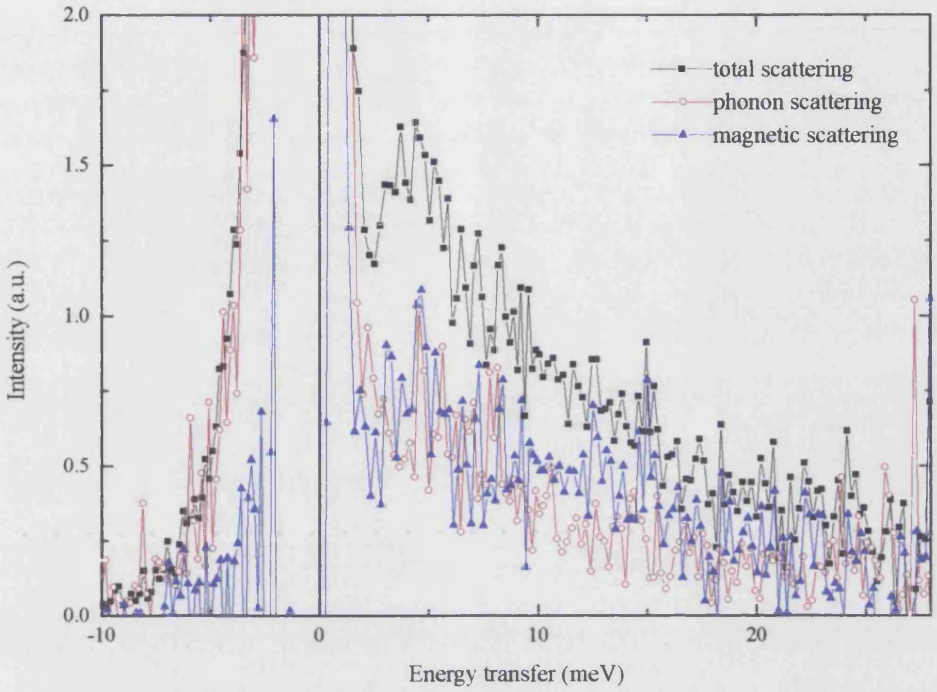


Figure 7.8. The inelastic neutron scattering from dysprosium metaphosphate glass at 20K, with an incident neutron energy of 30meV.

Erbium and dysprosium (J = 15/2) in a cubic site split into two doublets ($\Gamma_6$, $\Gamma_7$), and three quartets ($\Gamma_8^{(1)}$, $\Gamma_8^{(2)}$, $\Gamma_8^{(3)}$) (Lea et al. 1962). Once again, all of the quasi-elastic excitations are viable, and so too are all of the inelastic combinations except ($\Gamma_6$ - $\Gamma_7$) (Birgeneau 1972). Lesniak (1990) calculated crystal field splitting of the $^6H_{15/2}$ manifold of trivalent dysprosium, situated in cubic fluorite sites, using spectroscopic techniques. The energy levels for $Dy^{3+}$ in $CaF_2$ gives rise to the following transitions: 2.85meV ($\Gamma_8^{(1)}$ - $\Gamma_7$), 10.04meV ($\Gamma_6$ - $\Gamma_8^{(3)}$), 11.28meV ($\Gamma_7$ - $\Gamma_8^{(2)}$), 14.13meV ($\Gamma_8^{(1)}$ - $\Gamma_8^{(2)}$) and five other transitions which occur at energies outside the range that was examined. The transition ($\Gamma_8^{(1)}$ - $\Gamma_7$) which accounts for the 2.85meV peak in $CaF_2$ could be responsible for the 4.6meV feature in $Dy^{3+}$ phosphate glass; Lesniak (1990) found that in $BaF_2$ the ($\Gamma_8^{(1)}$ - $\Gamma_7$) transition corresponded to an energy of 3.97meV. The three remaining peaks probably contribute to the feature seen in the magnetic scattering data of dysprosium metaphosphate glass centred at 14meV (figure 7.8). As the sample is amorphous and the transitions have similar energies, it is reasonable that

the individual peaks are not resolvable. The erbium sample shows the most pronounced structure of all the rare earth metaphosphate glasses studied (figure 7.9), exhibiting two peaks situated at approximately 4 and 9.5meV. Knopp et al. (1985) studied the inelastic neutron scattering spectrum from erbium in mixed crystals of cubic symmetry. The initial peak occurs at a position similar to the Er metaphosphate glass and has been assigned to excitations between $\Gamma_8^{(3)}$ and $\Gamma_6$, $\Gamma_8^{(2)}$ levels. Loong et al. (1993a, and 1993b) have investigated the neutron scattering from polycrystalline erbium orthophosphate ($ErPO_4$) based on a tetragonal crystal field (space group $D_{2d}$ or $4\bar{2}m$), which splits the ground state into eight doublets ($4\times\Gamma_6$, $4\times\Gamma_7$). The selection rules for magnetic dipole transitions allow excitations (or de-excitation) between any two doublet states. The magnetic origin of the strong, low energy, crystal field peaks in $ErPO_4$, which occur at 4.08 and 6.60 meV, arose from the ($\Gamma_7^{(1)}$ - $\Gamma_6$) and ($\Gamma_7^{(1)}$ - $\Gamma_7^{(2)}$) transitions respectively. At 22K there is a finite probability that in addition to the ground crystal field level, the first two excited CF states ($\Gamma_6^{(1)}$ and $\Gamma_7^{(2)}$) will be thermally populated; the relative concentrations of the first three crystal field levels, $\Gamma_7^{(1)}$, $\Gamma_6^{(1)}$ and $\Gamma_7^{(2)}$, according to Boltzmann statistics are 85.4%, 11.6% and 3% respectively, the next higher crystal field state, the $\Gamma_7^{(3)}$, only contains 0.01% of the total number of electrons, and hence can be effectively ignored. In the spectrum measured by Loong et al. (1993b) there are four closely spaced weaker transitions in the energy range 10.6 - 13.8meV, corresponding to excitations from the $\Gamma_6^{(1)}$ and $\Gamma_7^{(2)}$ energy levels to $\Gamma_7^{(3)}$ and $\Gamma_6^{(2)}$. The above characteristics are similar to the features seen in figure 7.9.

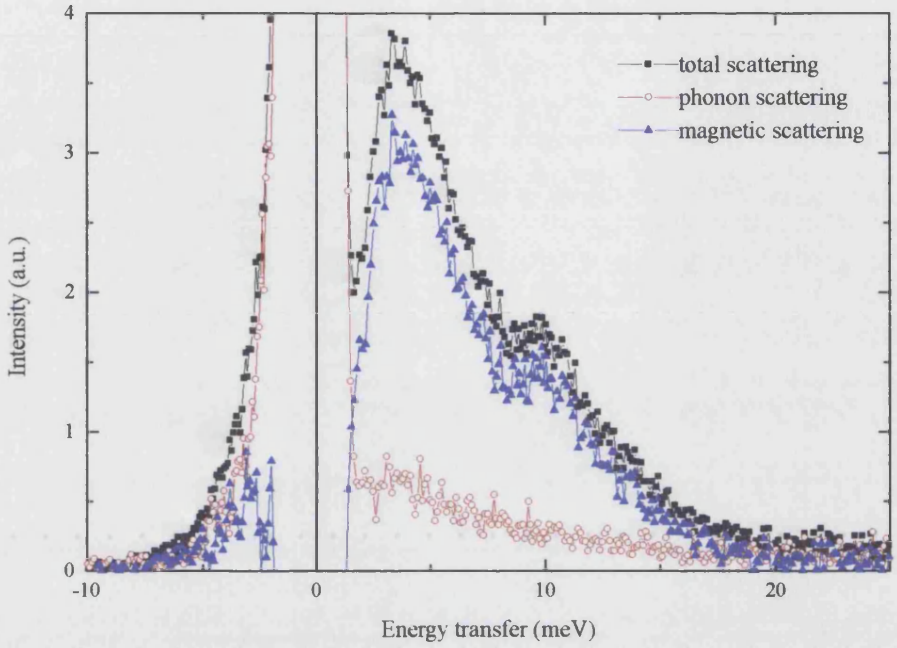


Figure 7.9. The inelastic neutron scattering from erbium metaphosphate glass at 22K, with an incident neutron energy of 30meV.

From this data it is evident that a large distribution of low energy crystal field excitations exist in all the rare earth metaphosphate glasses and at low temperatures the magnetic properties of these glasses will be strongly influenced by the symmetry of metaphosphate host surrounding the rare earth ion.

A description of the inelastic neutron scattering spectra can be made in terms of the semi-classical crystal field model (Newman 1995). The semi-classical crystal field model for the splitting of low lying states in ions having large J values, describes the ground states in terms of angular momentum vector hopping/tunnelling between energy minima. The approximate degeneracy (d) of the ground state corresponds to the number of energy minima of the crystal field; this is usually larger than the degeneracy associated with the symmetry of the ion. If these metaphosphate glasses are approximated to a cubic symmetry state (as suggested by the EXAFS data (Bowron 1994, 1996a)), the minimum energy directions are expected to have high symmetry: towards the faces of the cube (d=6), the corners (d=8) or the edges (d=12). Although such large ground state degeneracies appear unlikely, degeneracies

of 6 and 8 have been observed in theoretical and experimental data. Lea, Leask and Wolf (1962) calculated clustering of crystal field levels in cubic site symmetries i.e. for J=8, an exact 6-fold degeneracy occurs at E,x=300cm$^{-1}$, 0.8 and E,x=-100cm$^{-1}$, 0.8, and for J=6, 6-fold and 8-fold degeneracies appear at positive energies for x values of 0.8 and -0.5 respectively. Yeung and Newman (1985b) have cited experimental data on trivalent erbium in $DyVO_4$, and $Tb^{3+}$ in $CaF_2$ as ions exhibiting these high 'accidental' degeneracies (section 2.5). One restriction of the semi-classical approach is that despite the ground state being defined by this model, it may not be true to express the first excited state by precessing angular momenta occupying the same set of energy minima. For both sites to be equally represented it is necessary for the ground (2J + 1) manifold to be greater or equal to twice the degeneracy 2d; this implies that J must be at least 11/2 (and accuracy increase with larger J values). The semi-classical model predicts that only magnetic dipole transitions between $|J_m=J\rangle$ to $|J_m=J-1\rangle$ states are allowed. Hence a single transition would be expected in the inelastic neutron scattering data. In many of the trivalent rare earth metaphosphate glasses the spectra is dominated by a single peak; however this is usually accompanied by weaker (semi-classically dipole forbidden) features.

## 7.2. TOTAL NEUTRON SCATTERING, RESULTS AND DISCUSSION

The neutron scattering produced by the application of a magnetic field to terbium metaphosphate glass ($(Tb_2O_3)_{0.247}(P_2O_5)_{0.753}$) can be isolated by subtracting the no field cross section spectrum from the high field data (figure 6.11); the resultant spectrum is the first order difference cross section, proportional to $S_{Tb,Tb}(\mathbf{Q})f^2(\mathbf{Q})$ where $S_{Tb,Tb}(\mathbf{Q})$ is the terbium-terbium partial structure factor and $f(\mathbf{Q})$ is the magnetic form factor.

On the basis of arguments presented by Lovesey (1987) the cross section of the magnetic scattering from a paramagnet can be written as,

$$\frac{d\sigma}{d\Omega}_M = r_0^2\left(\frac{1}{2}gf(\mathbf{Q})\right)^2 \sum_{\alpha\beta}\left(\delta_{\alpha\beta} - \breve{Q}_\alpha \breve{Q}_\beta\right)\sum_{jj'} \exp^{i\mathbf{Q}(\mathbf{R}_j - \mathbf{R}_{j'})}\left\langle J_j^\alpha J_{j'}^\beta \right\rangle. \qquad (7.1)$$

Here $r_0$ the magnetic interaction strength, g is Landé splitting factor, J is the total angular momentum, and the subscripts $\alpha,\beta$ =x,y,z, and j and j′ denote different ion

sites at position $\mathbf{R}_j$ and $\mathbf{R}_{j'}$. $\breve{Q}_\alpha$ is the $\alpha$ component of the unit vector in the direction of $\mathbf{Q}$; $\breve{Q}_\alpha \breve{Q}_\beta$ (its' analogue in the $\beta$ direction) are included in equation 7.1 in order to account for the vector nature of the neutrons interaction with the magnetic electrons. For a paramagnet in zero field, $\mathbf{B}=0$, the magnetic moments act as a collection of independent ions and there is no spatial correlation between spins on different sites. Hence, if $j \neq j'$ $\langle J_j^\alpha . J_{j'}^\beta \rangle = 0$, and consequently these terms do not contribute to the cross section. The $\langle J_j . J_{j'} \rangle$ correlation between spins on the same site $j=j'$ becomes $\langle (J_j^x)^2 \rangle = \langle (J_j^y)^2 \rangle = \langle (J_j^z)^2 \rangle = J(J+1)/3$. Therefore the magnetic scattering in zero applied field can be written as

$$\frac{d\sigma}{d\Omega_M} = N\left(\frac{r_0}{2}\right)^2 \frac{2}{3} g^2 J(J+1) f^2(\mathbf{Q}), \qquad (7.2)$$

where N is the number of atoms (equal to 1, if the cross section per ion is required). There is no coherent scattering because the paramagnetic ions are randomly orientated. The only scattering vector $\mathbf{Q}$ dependence comes from the magnetic form factor $f(\mathbf{Q})$ of the 4f electrons, which describes the spatial distribution of the magnetic electrons within the paramagnetic atom. The cross section of the magnetic form factor falls off as a function of $\mathbf{Q}$; this reflects the destructive interference of the neutron wave as it scatters from different parts of the magnetisation density within the atom. The paramagnetic ions are polarized by the application of a magnetic field $\mathbf{B} \neq 0$ at low temperatures. If a saturating magnetic field is applied along the z axis (normal to xy plane, which contains the scattering vector), $\langle J_j^x, J_{j'}^y \rangle = \langle J_j^x, J_{j'}^z \rangle$ etc. still equal zero, and $\langle (J_j^x)^2 = \langle (J_j^y)^2 \rangle = 1/2(J(J+1) - \langle (J_z)^2 \rangle)$. However the magnetic field produces an associated magnetic moment $\langle m \rangle = g\mu_B \langle J_j^z \rangle$ on every site. Therefore if $j \neq j'$, $\langle J_j^z . J_{j'}^z \rangle = \langle J_j^z \rangle^2 = \langle J_z \rangle^2$, while if $j = j'$, $\langle J_j^z . J_{j'}^z \rangle = \langle (J_z)^2 \rangle$; $\langle J_z \rangle$ is the thermal average of the total angular momentum in the local quantisation direction z. The magnetic scattering from a paramagnet in a field is

$$\frac{d\sigma}{d\Omega_M} = N\left(\frac{r_0}{2}\right)^2 g^2 \left( \langle J_z \rangle^2 S(\mathbf{Q}) + \frac{1}{2} J\langle J+1 \rangle + \frac{1}{2}\langle J_z^2 \rangle - \langle J_z \rangle^2 \right) f^2(\mathbf{Q}). \qquad (7.3)$$

In a magnetic field the scattering cross section is a combination of a coherent part, proportional to $\langle J_z \rangle^2 S(\mathbf{Q})$, and a reduced form factor, which is diffuse in nature. The structure factor $S(\mathbf{Q})$ is introduced into equation 7.3 due to the correlation between the now aligned spins sites; $S(\mathbf{Q})$ is the Fourier transform of the pair distribution. The

difference cross section for the magnetic scattering (high field-no field expression) has the form,

$$\frac{d\sigma}{d\Omega_M} = N\left(\frac{r_0}{2}\right)^2 g^2\left(\frac{1}{2}\langle J_z^2\rangle - \frac{1}{6}J(J+1) + \langle J_z\rangle^2\left(S(\mathbf{Q})-1\right)\right)f^2(\mathbf{Q}). \qquad (7.4)$$

If the total scattering of a multicomponent glass such as terbium metaphosphate glass is considered, equation 7.2 and 7.3 needs to be modified so it contains additional contributions due to the nuclear scattering from correlations between the terbium, phosphate and oxygen atoms ($\langle b_i,b_j\rangle$ is not equal to zero). These extra terms will depend on the concentration c of the different atom types i,j, the partial structure factors $S_{i,j}(\mathbf{Q})$ and the respective scattering lengths $b_i$, $b_j$ (in a magnetic field the terbium scattering length becomes an effective scattering length equal to $b_{Tb}+ r_0(g/2)f(Q)\langle J_z\rangle$, see equation 6.30). However as the sample is being probed with unpolarised neutrons the scattering from the cross terms (of the type $b_P[b_{Tb}\pm r_0(g/2)f(Q)\langle J_z\rangle](S_{PTb}(\mathbf{Q})-1)$) cancel. The difference cross section for terbium metaphosphate glass will have the same form as equation 7.4 with the partial structure factor $S(\mathbf{Q})$ being due to the terbium-terbium correlations $S_{Tb,Tb}(\mathbf{Q})$. The partial difference cross section for terbium doped phosphate glass is plotted as a function of time-of-flight in figure 7.10 and scattering wavevector **Q**, in figure 7.11.

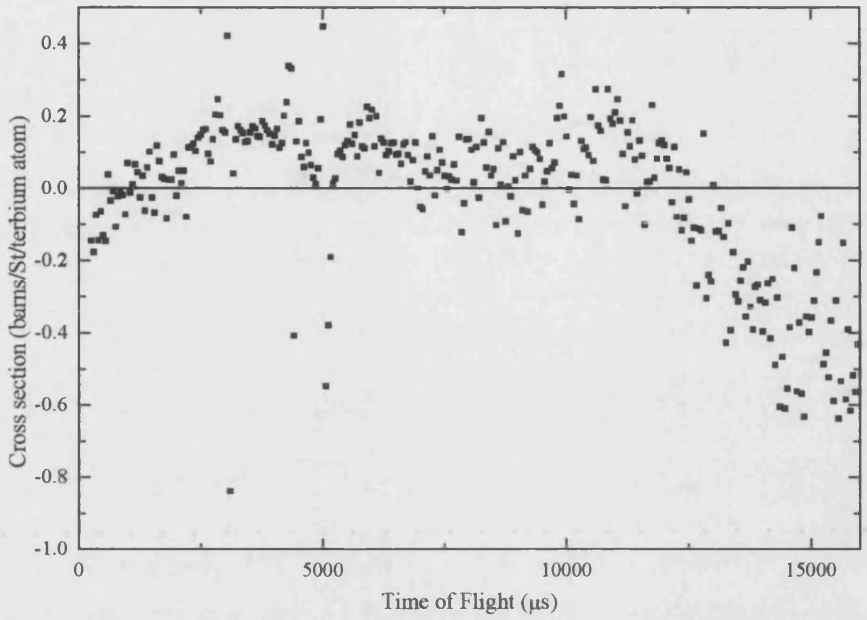


Figure 7.10. The first order neutron scattering difference pattern $S_{Tb,Tb}(\mathbf{Q})f^2(\mathbf{Q})$ for terbium metaphosphate glass $(Tb_2O_3)_{0.247}(P_2O_5)_{0.753}$ as a function of time of flight.

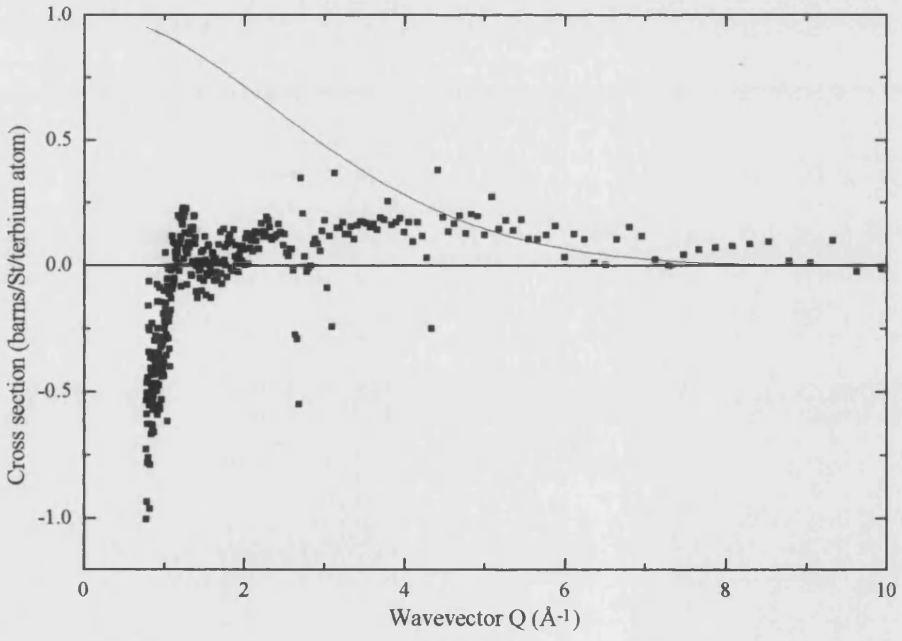


Figure 7.11. The first order difference pattern $S_{Tb,Tb}(\mathbf{Q})f^2(\mathbf{Q})$ for terbium metaphosphate glass $(Tb_2O_3)_{0.247}(P_2O_5)_{0.753}$ as a function of wavevector. The curved line represents the square of the magnetic form factor (calculated using equation 7.5a).

The square of the magnetic form factor has also been plotted in figure 7.11. If a dipole approximation is applied (see section 6.2.1), the magnetic form factor only comprises of the $\langle j_0 \rangle$ and $\langle j_2 \rangle$ spherical Bessel functions (Lovesey 1987),

$$f(\mathbf{Q}) = \langle j_0(\mathbf{Q}) \rangle + (g-2)/g \times \langle j_2(\mathbf{Q}) \rangle \qquad (7.5a)$$

where

$$\langle j_0(\mathbf{Q}) \rangle = A\exp(-aQ^2) + B\exp(-bQ^2) + C\exp(-cQ^2) + D$$

$$\langle j_2(\mathbf{Q}) \rangle = AQ^2\exp(-aQ^2) + BQ^2\exp(-bQ^2) + CQ^2\exp(-cQ^2) + DQ^2. \qquad (7.5b)$$

The prefactors A, B, C, D, and a, b, c, have been tabulated for the lanthanide ions by Brown (1988), and g is the Landé splitting factor.

At high **Q** values the experimental $S_{Tb,Tb}(\mathbf{Q})f^2(\mathbf{Q})$ in figure 7.11 does not fall off as quickly as the square of the theoretical magnetic form factor. This might be due to shifting of the sample in the beam or incorrect wavelength dependent absorption corrections. The structure factor $S_{Tb,Tb}(\mathbf{Q})$ is not as prominent in a glass as a crystal due to the topological disorder characteristic of all amorphous materials.

The magnetic moment of terbium metaphosphate glass has been investigated, as a function of applied magnetic field, to gain additional insight into scattering mechanisms and to increase understanding the first order difference pattern (figures 7.12, and 7.13). The main features of graph 7.12 is that by 10T the magnetisation of the 5K and 1.8K temperature runs have almost saturated, and there is no indication of hysteresis at any of the temperatures. Hence it can be concluded that, to a good approximation, all the magnetic dipoles are aligned under the conditions on Polaris. The maximum magnetic moment **m** for the 18.86 ± 0.01mg terbium glass sample is approximately 1.26emu (this is estimated by extrapolating the data); therefore the corresponding paramagnetic moment per gram is 66.8 emu $g^{-1}$. The magnetic moment of terbium metaphosphate glass is in accord with the magnetisation measured in $Gd^{3+}$ doped metaphosphate glass at 10kOe and 2K (65 emu $g^{-1}$) (Ford et al. 1994). The resultant saturation magnetisation, **M**, (magnetic moment per unit volume) equals $2.41\times10^5 Am^{-1}$ (using density = 3609 $Kgm^{-3}$), and the magnetic susceptibility per unit volume ($\chi = \mu_0\mathbf{M}/\mathbf{B}$) is approximately 0.040 at field strengths of 7.5T.

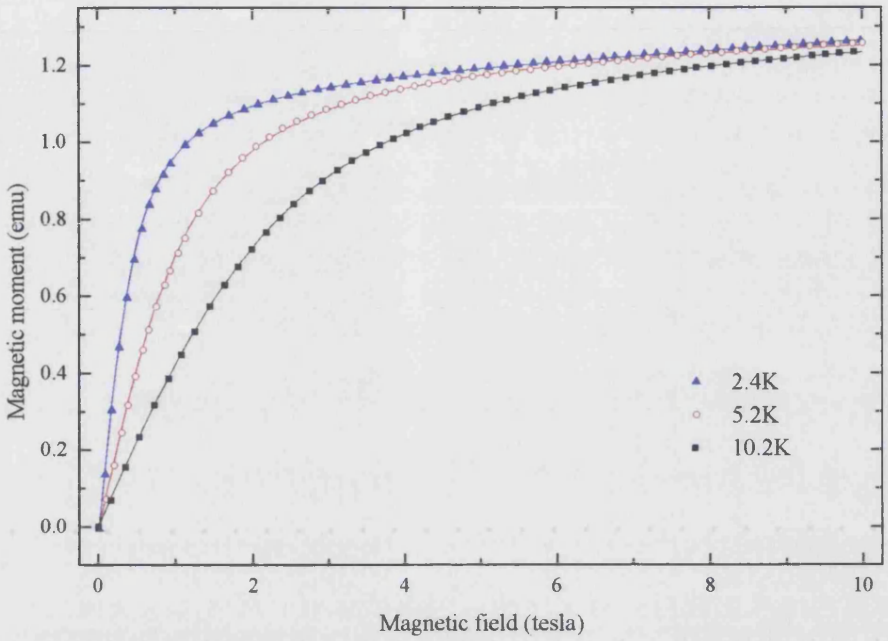


Figure 7.12. The magnetic moment of terbium metaphosphate glass $(Tb_2O_3)_{0.247}(P_2O_5)_{0.753}$. The symbols are the raw data points, and the line fits are calculated using non-linear least squares techniques.

In figure 7.12 the raw data for the paramagnetic moment **m**, has been fitted with modified Brillouin function ($B_J(g\mu_B\mathbf{B}/k_BT)$) (Jiles1995), using a non-linear least square fitting program with three parameters (written by Professor Rainford, Southampton University):

$$\mathbf{m} = \mathbf{m}_0 B_J\left(\frac{g\mu_B\mathbf{B}}{k_BT}\right) + \chi\,\mathbf{B} \tag{7.6a}$$

where

$$B_J\left(\frac{g\mu_B\mathbf{B}}{k_BT}\right) = \frac{2J+1}{2J}\coth\left(\frac{2J+1}{2}\frac{g\mu_B\mathbf{B}}{k_BT}\right) - \frac{1}{2J}\coth\left(\frac{g\mu_B\mathbf{B}}{2k_BT}\right), \tag{7.6b}$$

$k_B$ is the Boltzmann constant, T is the temperature (in K), $\mu_B$ is the Bohr magneton ($\mu_B = e\hbar/2m_e$) and g is the Landé splitting factor. The Brillouin function assumes that in a magnetic field an ion, with total angular momentum J, has 2J+1 equally spaced ground state energy levels; in real materials effects such as crystal fields and Zeeman splitting perturb the energy levels. Initially the data was fitted using a single parameter $\mathbf{m}_0$, the saturation magnetic moment; however this curve had a shallower gradient than

the experimental data at higher applied fields. Two extra parameters were added to improve the fit, $\chi$ is a high field susceptibility incorporated through the addition of the $\chi\mathbf{B}$ term (7.6a), and $J_{eff}$ is the effective total angular moment, which was used to replace J in equation 7.6b. By introducing these two parameters the displacement of the energy levels due to crystal field splitting has been acknowledged (the crystal field effects in these glasses are significant, see section 7.1). The $\chi\mathbf{B}$ correction term describes the behaviour of the second order crystal field perturbation of the energy levels called the Van Vleck temperature independent susceptibility (Van Vleck 1965, Jiles1995). It characterises the susceptibility at high (saturating) fields, where B and T are no longer proportional. Figure 7.13 is a plot of the magnetic moment versus the scaled magnetic induction B/T. The different measured temperatures have had to be scaled to get agreement in the initial gradients of the **m** versus B/T curve. The 1.8K run becomes 2.4K, 5K becomes 5.2K and 10K scales to 10.2K. These discrepancies are not surprising as the temperature is not measured immediately next to the sample and calibration of the vibrating sample magnetometer at very low temperatures becomes less accurate (usual working temperature for the VSM at Southampton University is 50-100K).

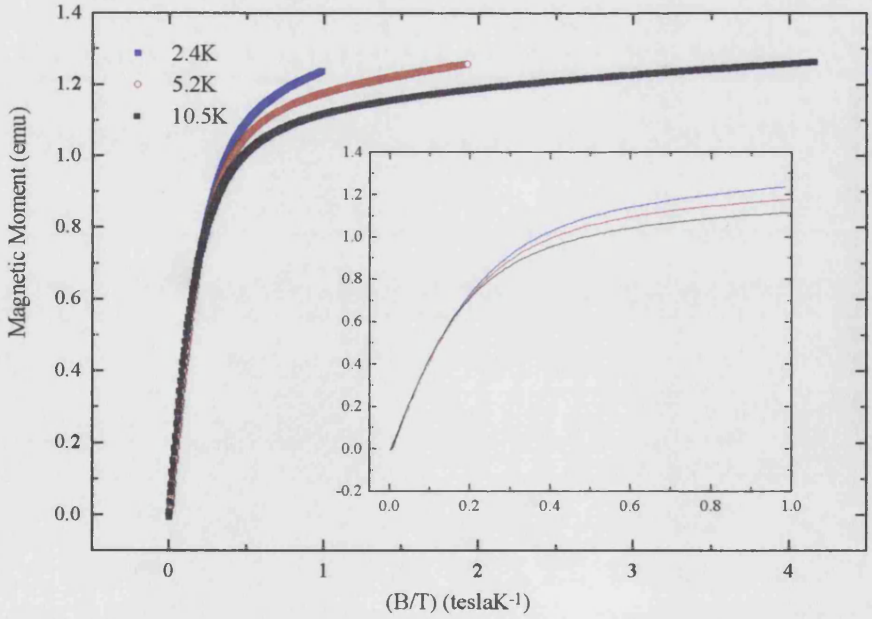


Figure 7.13. The magnetic moment of terbium metaphosphate glass $(Tb_2O_3)_{0.247}(P_2O_5)_{0.753}$ plotted against the scaled applied magnetic field. The insert is an expansion of the data up to $1TK^{-1}$.

The three parameter model described by equation 7.6 generates very good fits to the experimental data (see figure 7.12); however the parameters deviate fairly significantly from the theoretical values for a free ion of trivalent terbium: $J_{eff}$ is approximately 9 (it varies between 8.4 and 9.8 at the three different temperatures), the ground state of a terbium ion has a theoretical total angular momentum J of 6, the saturation magnetisation $\mathbf{m_0}$ is 0.51×calculated $\mathbf{m_0}$ (where the calculated $\mathbf{m_0}$ ($Ng\mu_B J$) is equal to 2.38emu) and the average high field susceptibility is ~0.007. The low saturation magnetic moment may be a consequence of the fact that the ground level can be split in three directions (x, y, z) by the crystal field and the resulting magnetic moment depends on the population of these levels relative to the direction of the applied field (Professor Rainford, private communication). These results suggests that the terbium ions are not fully aligned in the z direction. For an improved representation of the magnetic moment data as a function of applied field the crystal field effect on the energy levels of the terbium ion can be explicitly incorporated into the Hamiltonian $H_{tot}$ of the system:

$$H_{tot} = H_{CF} + H_{Zeeman} = -D(J_z)^2 - g\mu_B \mathbf{JB}. \qquad (7.7)$$

The crystal field contribution ($-D(J_z)^2$ where D is a constant (Fert and Campbell 1978) section 2.5.1) to the Hamiltonian of a paramagnetic ion in an applied field requires knowledge of the symmetry of the rare earth ion site. Unfortunately information of this type in REMGs limited due to the topological disorder producing broadening of the crystal field spectra, section 7.1. If the rare earth ion is assumed to be situated in an environment lower than cubic (triclinic or monoclinic) the splitting can be described in terms of the second order crystal fields $B_2^0O_2^0$ where $B_2^0$ determines the scale of the crystal field splitting and $O_2^0$ is the second order Stevens operator, section 2.5. The Stevens operator can be written in terms of the total angular momentum, hence $H_{CF}$ becomes $B_2^0(3J_Z^2 - J(J+1))$. The crystal field generated by the atoms surrounding the $Tb^{3+}$ ion act to lift the 13 fold degeneracy associated with the $^7F_6$ ground state. The crystal field term is relatively large compared with the Zeeman splitting term. The Zeeman effect describes the lifting of the degeneracy of an atom when it is placed into a strong magnetic field; the splitting is proportional to the applied field. The crystal field and Zeeman interactions combine to change the energy levels in two different ways. If the magnetic field is turned on parallel to the z axis, the diagonal elements of the perturbing matrix act to split the $|\pm J_m\rangle$ doublets equally up

and down. When the magnetic field is applied parallel to the x or y direction, the off diagonal matrix elements gives rise to the Van Vleck high field susceptibility term, and results in a quadratic perturbation between $|\pm J_m\rangle$ and $|\pm J_m+1\rangle$ levels. A schematic of the energy levels are shown in figure 7.14; for an appropriate sign of D the lowest energy state is $|\pm 6\rangle$ and the next highest state is the $|\pm 5\rangle$ (section 2.5.2).

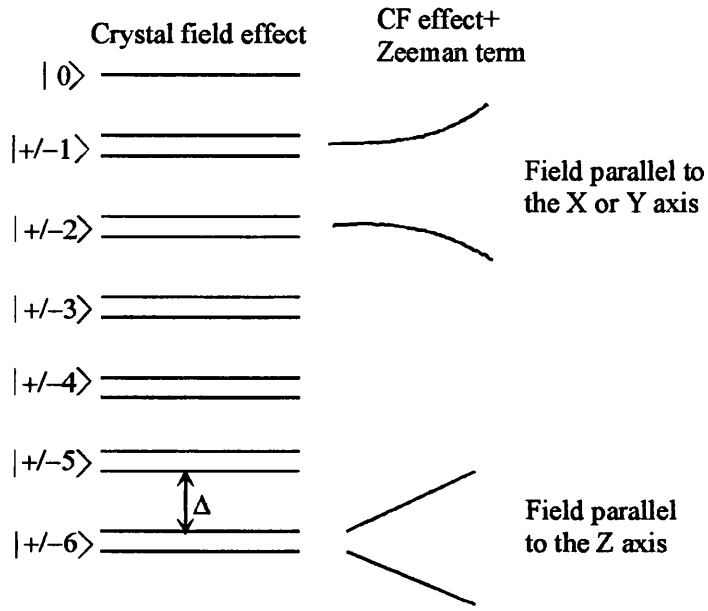


Figure 7.14. A schematic of the perturbed energy level diagram of the ground state of terbium in metaphosphate glass. Δ is a measure of the crystal field splitting.

In the following simple analysis only the bottom two doublets $|\pm 6\rangle$ and $|\pm 5\rangle$ of the terbium ion have been considered; it was assumed that interactions between the two lowest crystal field excitations give rise to the majority of the magnetic moment at low temperatures. To calculate the crystal field Hamiltonian matrix elements ($H_{CF}=B_2^0(3J_z^2-J(J+1))$ where J=6), the $J_z$ acting on each state has to be calculated: $J_z$ acting on $|\pm 6\rangle$ gives $\pm 6|\pm 6\rangle$ and $J_z^2|\pm 6\rangle = \pm 36|\pm 6\rangle$. Hence the crystal field Hamiltonian operating on the eigenstate $|\pm 6\rangle = 66\ B_2^0|\pm 6\rangle$ and the $H_{CF}$ on $|\pm 5\rangle$ equals $33B_2^0|\pm 5\rangle$. Consequently the crystal field splitting $\Delta = (66-33)B_2^0 = 33B_2^0$. The magnetic moment per atom $m_{atom}$ can be defined as

$$m_{atom} = \frac{1}{Z}\sum\langle i|J_Z|i\rangle g\mu_B \exp\left(-\frac{E_i}{k_B T}\right) = \frac{1}{Z}\sum m_i \exp\left(-\frac{E_i}{k_B T}\right). \qquad (7.8)$$

Here Z is the partition function equal to $\Sigma\exp(-E_i/k_BT)$, and $\mathbf{m}_i$ (= $Ng\mu_BJ$) is the magnetic moment of the $i^{th}$ level. The exponential term describes the probability (using Boltzmann statistics) of an electron occupying the $E_i$ energy level (where $E_i$= $g\mu_B\mathbf{B}J_m$).

First consider the magnetic moment of the terbium atom when the **B** field is applied parallel to the z axis. The energy of the $i^{th}$ level can be found by calculating the matrix elements $\langle i|H_{tot}|i\rangle$ of the total Hamiltonian, taking the crystal field splitting to be $\Delta$ = $33B_2^0$, and the Zeeman term as $-g\mu_BJ_Z\mathbf{B}$.

| $H_{tot}$ | $\|+6\rangle$ | $\|-6\rangle$ | $\|+5\rangle$ | $\|-5\rangle$ |
|---|---|---|---|---|
| $\|+6\rangle$ | $-6g\mu_B\mathbf{B}$ | | | |
| $\|-6\rangle$ | | $+6g\mu_B\mathbf{B}$ | | |
| $\|+5\rangle$ | | | $\Delta-5g\mu_B\mathbf{B}$ | |
| $\|-5\rangle$ | | | | $\Delta+5g\mu_B\mathbf{B}$ |

Substituting these values into the equation 7.8, the magnetic moment per atom in the z direction can be written as

$$m_z=\frac{g\mu_B}{Z}\left[6\left(\exp\left(\frac{6g\mu_B\mathbf{B}}{k_BT}\right)+\exp\left(-\frac{6g\mu_B\mathbf{B}}{k_BT}\right)\right)+5\exp\left(-\frac{\Delta}{k_BT}\right)\left(\exp\left(\frac{5g\mu_B\mathbf{B}}{k_BT}\right)+\exp\left(-\frac{5g\mu_B\mathbf{B}}{k_BT}\right)\right)\right] \tag{7.9}$$

where

$$Z=\exp\left(\frac{6g\mu_B\mathbf{B}}{k_BT}\right)+\exp\left(-\frac{6g\mu_B\mathbf{B}}{k_BT}\right)+\exp\left(-\frac{\Delta}{k_BT}\right)\left(\exp\left(\frac{5g\mu_B\mathbf{B}}{k_BT}\right)+\exp\left(-\frac{5g\mu_B\mathbf{B}}{k_BT}\right)\right)$$

Now consider the magnetic field parallel to the x axis (or y axis). The Zeeman effect can be written in terms of the $J^+$ and $J^-$ operators ($H_{zeeman}$= $g\mu_B B(J^+ + J^-)/2$) acting on the states $|\pm J_m\rangle$:

$J^+|+6\rangle = 0$ $\qquad$ $J^-|+6\rangle = (12)^{1/2}|+5\rangle$

$J^+|-6\rangle = (J(J+1)-J_m(J_m+1))^{1/2}|J_m+1\rangle = (12)^{1/2}|-5\rangle$ $\qquad$ $J^-|-6\rangle = 0$

$J^+|+5\rangle = (J(J+1)-J_m(J_m+1))^{1/2}|J_m+1\rangle = (12)^{1/2}|+6\rangle$ $\qquad$ $J^-|+5\rangle = |+4\rangle$ ignore

$J^+|-5\rangle$ = couples to $|-4\rangle$ hence it can be ignored $\quad J^-|-5\rangle = (12)^{1/2}|-6\rangle$

The energy of the system can be found by diagonalising the matrix elements of the total Hamiltonian.

| $H_{tot}$ | $\|+6\rangle$ | $\|-6\rangle$ | $\|+5\rangle$ | $\|-5\rangle$ |
|---|---|---|---|---|
| $\|+6\rangle$ | 0 | | $(3)^{1/2}g\mu_B\mathbf{B}$ | |
| $\|-6\rangle$ | | 0 | | $(3)^{1/2}g\mu_B\mathbf{B}$ |
| $\|+5\rangle$ | $(3)^{1/2}g\mu_B\mathbf{B}$ | | $\Delta$ | |
| $\|-5\rangle$ | | $(3)^{1/2}g\mu_B\mathbf{B}$ | | $\Delta$ |

The eigenvalues of the energy levels can be calculated from the above matrix;

$$\lambda^2 - \Delta\lambda - 3(g\mu_B\mathbf{B})^2 = 0. \tag{7.10}$$

Hence the roots of the quadratic are,

$$|\pm 6\rangle = \Delta/2 - 1/2(\Delta^2 + 12(g\mu_B\mathbf{B})^2)^{1/2} = E_6$$

$$|\pm 5\rangle = \Delta/2 + 1/2(\Delta^2 + 12(g\mu_B\mathbf{B})^2)^{1/2} = E_5. \tag{7.11}$$

It follows from $\mathbf{m}_i$=-(dF/dB) (where F is the free energy) that the magnetic moment for the terbium ion is

$$m_X = \frac{2g\mu_B}{Z}\left(\frac{6g\mu_B\mathbf{B}}{\sqrt{\Delta^2 + 12(g\mu_B\mathbf{B})^2}}\right)\left(\exp\left(-\frac{E_6}{k_BT}\right) - \exp\left(-\frac{E_5}{k_BT}\right)\right). \tag{7.12a}$$

Here $$Z = 2\left(\exp\left(-\frac{E_6}{k_BT}\right) + \exp\left(-\frac{E_5}{k_BT}\right)\right). \tag{7.12b}$$

A factor of 2 is introduced into equation 7.12 as the energy levels are doubly degenerate. The non-linear least squares fitting program was re-run, fitting the magnetic moment (in Bohr magnetons) verses applied magnetic field with a curve following the equation $B_J(g\mu_B\mathbf{B}/k_BT)\times(2m_x + m_z)/3$. The magnetic moment per atom in a direction perpendicular to the applied field is multiplied by two as it is assumed the three directions x, y, z have equal weighting and that $m_x$ and $m_y$ are identical. This is a standard conjecture used in powder diffraction techniques. Once again the theoretical curve was fitted to the magnetic moment data allowing three parameters to vary: the temperature T, the crystal field splitting $\Delta$, and $J_{eff}$. This crude Hamiltonian

approximation to the crystal field splitting in the ground state of a terbium ion should yield a better approximation to the magnetic moment data, as a function of applied field m(**B**), than equation 7.6.

For the 10.2K data, T = 12.18K, CFΔ = 75.89K, and $J_{eff}$ = 4.63.

For the 5.2K data, T = 6.98K, CFΔ = 92.85K, and $J_{eff}$ = 5.30.

For the 2.4K data, T = 3.38K, CFΔ = 96.51K, and $J_{eff}$ = 5.38.

The crystal field splitting (CFΔ) corresponds to an energy level splitting of approximately 7.5meV (11.6K=1meV); this value is in accord with the inelastic scattering data for terbium metaphosphate glass, see figure 7.2 and 7.3. A crystal field splitting of Δ=102K was determined from NMR experiments in a ternary erbium lanthanum doped metaphosphate glass (Goudemond et al. 1997). A $J_{eff}$ smaller than 6 is expected since at a temperature of 4K fewer than the total 2J+1=13 levels will be populated.

The partial terbium structure factor $S_{TbTb}(\mathbf{Q})$ can be extracted from the difference cross section by rearranging equation 7.4, and taking $\langle J_z \rangle$ to be the $J_{eff}$ value at 5.2K (i.e. 5.30), J(J+1) =42, hence J(J+1) it is not effected by the crystal field if only the ground and 1$^{st}$ excited state are considered, and $f^2(\mathbf{Q})$ has been calculated using equation 7.5. The partial structure factor describing the terbium-terbium correlation is characteristic of an amorphous material; however it appears to be skewed; the structure factor increases systematically with increasing **Q** (figure 7.15). When the data is multiplied by a straight line the $S_{TbTb}(Q)$ spectrum (insert in figure 7.15) of terbium metaphosphate glass closely resembles the structure factors measured in other amorphous material (Hoppe et al. 1995b, 1998b); the partial structure factor is expected to oscillate about unity and the frequency of the oscillations gives information on the correlation distances. Unfortunately, the data is not good enough to Fourier transform and consequently an accurate terbium-terbium correlation length has not been extracted. However the distance can be estimated, from figure 7.15, to be approximatly ($Q=2\pi/a$) 6.2Å. This is in accord with the lanthanum-lanthanum correlation distance (6.4Å) measued by Hoppe et al. (1998b) in $LaP_3O_9$ glass, using x-ray diffraction. A correlation distance greater than 6 Å suggests there is no clustering of rare earth ions with in the sample, a result which is particularly pertinent for optical and magneto-optical devices.

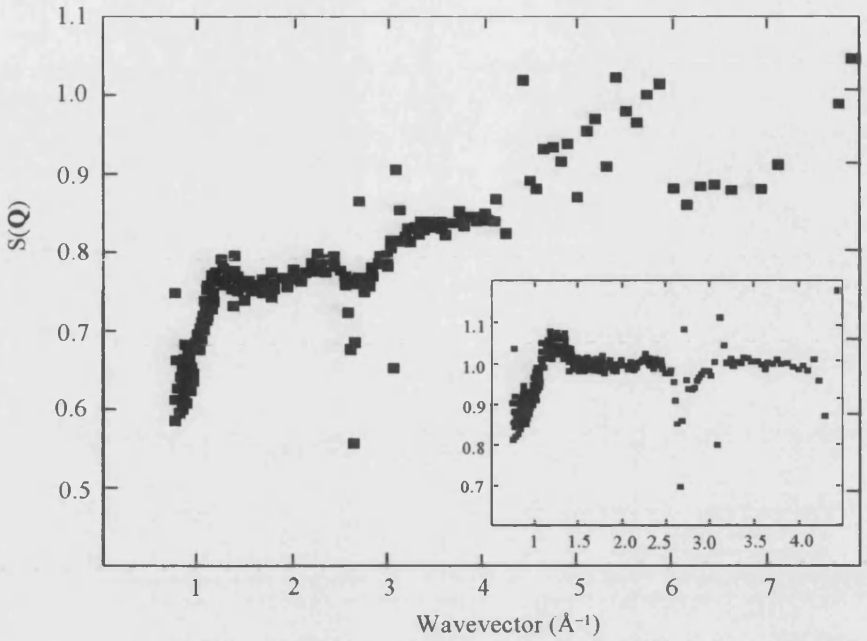


Figure 7.15. The $S_{TbTb}(Q)$ of terbium metaphosphate glass $(Tb_2O_3)_{0.247}(P_2O_5)_{0.753}$. The insert is the same data scaled by y=0.04x+0.69.

The offset in the S(**Q**) is believed to be due to poor wavelength dependent absorption corrections in the high field and no field terbium data runs. This problem has been attributed to insufficient quality of the background runs, the most likely origins being that the boron carbide is not totally 'black' at short wavelengths, the vanadium spectrum is shifted or that multiple scattering effects have not been included. Although this meant that the spectrum could not be Fourier transformed, it has demonstrated the possibilities of this new technique for probing the correlation between paramagnetic ions at separation distances in excess of 4Å.

## 7.3 CONCLUSIONS

Inelastic magnetic neutron scattering has been measured in lanthanide (Pr, Nd, Tb, Dy, Ho, Er, and Tm) doped metaphosphate glass, to examine the form of the magnetic contribution to the low energy excitations. Neutron scattering has also been used to investigate a new technique suitable for measuring the rare earth correlation distance in a metaphosphate glass host i.e. $(Tb_2O_3)_{0.247}(P_2O_5)_{0.753}$. The conclusions that are drawn from this chapter are summarised below:

1) The crystal field lifts the (2J+1) degeneracy associated with the energy levels of a free ion, according to the site symmetry of the rare earth ion in the host. This effect has been well documented in many crystalline materials, and it has been shown to exist in the ground state of metaphosphate glasses doped with trivalent lanthanides. Since the local symmetry of the rare earth ion in an amorphous material varies from site to site the spectrum suffers a degree of broadening; however the majority of the features can be assigned crystal field transitions, by comparing these samples to other materials containing the same paramagnetic ion.

2) The significance of the crystal field has also be seen in the total neutron scattering data. The crystals field and Zeeman effect on the magnetic moment of $(Tb_2O_3)_{0.247}(P_2O_5)_{0.753}$ as a function of applied field have been estimated using a simple model involving the two lowest crystal field states. The effective total angular moment $J_{eff}$ was determined to be approximately 5.10, and the crystal field splitting was in the region of 90K.

3) The paramagnetic moment per gram of terbium metaphosphate glass is 66.8emu $g^{-1}$. The resultant saturation magnetisation, **M**, (magnetic moment per unit volume) and magnetic susceptibility per unit volume are $2.41\times10^{5}Am^{-1}$ and 0.040 (at field strengths of 7.5T) respectively.

4) The terbium terbium correlation distance could not be determined from the data; however it has been shown that this method will work and it is a viable way of measuring the nearest neighbour distance between two paramagnetic ions in these metaphosphate glasses.

# CHAPTER EIGHT

# BASIC THEORY AND INSTRUMENTATION OF ULTRASONIC EXPERIMENTS

Ultrasonic methods have been utilised for the last 30 years as a diagnostic tool in the fields of solid state physics and material science. It is employed here to study the elastic properties of metaphosphate glasses and their dependence on thermodynamic quantities such as pressure and temperature. This is achieved by measuring the velocity and attenuation of a high frequency (excess of 16KHz) stress waves propagating through a sample. The waves travel through the sample by disturbing the positions of the atoms; internal restoring forces then act to return the atom to its equilibrium, thus causing oscillations and resulting in the transferral of energy along the system. Elastic stiffness describes the response of a sample to an applied stress. In this chapter the ultrasonic techniques are explained; a theory section describes the quantities being measured, which is simplified by the fact that samples being analysed are glass, which is isotropic, and not crystalline materials. A second section explains the experimental method and apparatus used. Finally the data correction procedures are discussed

## 8.1. THEORY OF ELASTICITY FOR ISOTROPIC MATERIALS

A sample is said to be elastic if it regains its original form after applied forces are removed. The mechanical properties of a perfectly elastic sample obeys Hooke's law, which states that there is a linear relationship between the stress tensor $\sigma$ (force/area) and strain tensor $\varepsilon$ (extension/length). The constant of proportionality is the second order elastic stiffness tensor component (SOEC). This relationship only holds in the long wavelength limit of the phonon dispersion curve, and is associated with the linear section in the acoustic branch. All real materials possess anharmonic vibrational

contributions, and in the majority of materials this means the sample resists compression to a volume smaller than equilibrium more strongly than expansion to a larger volume. The nonlinearity of interatomic forces with atomic displacement, which produces the departure from Hookes law, describes macroscopic phenomena such as thermal expansion, heat conduction, and is a consequence of the electrostatic interaction between two atoms. Analysis of nonlinear behaviour is considered in terms of higher order elastic stiffness constants TOEC (third order) and FOEC (fourth order), the SOEC pressure derivatives, and the Grüneisen parameters, which are a measure of the strength of the anharmonic effects.

### 8.1.1. ELASTIC BEHAVIOUR

Stress is defined as the force per unit area acting on a surface element of the sample, and is proportional to the direction in which the force acts and the orientation of the surface element. It can be described in terms of the stress tensor, $\sigma_{ij}$, where the subscripts i, j denote the direction in which the stress component acts and the direction of the normal to the plane in which the stress is applied respectively, see figure 8.1.

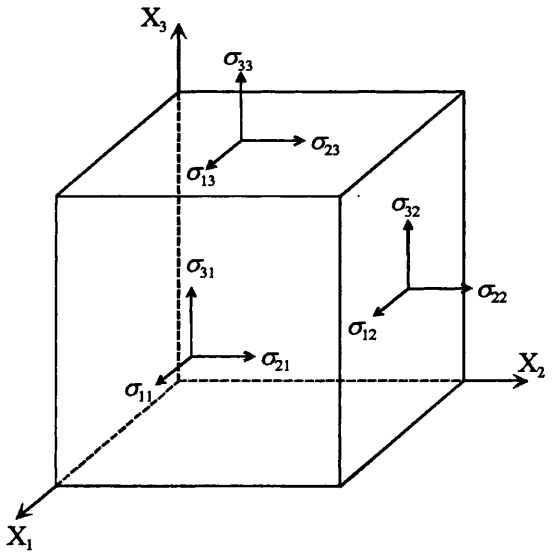


Figure. 8.1 The stresses acting on a parallelepiped.

The stress tensor can be represented by a 3×3 matrix:

$$\sigma_{ij} = \begin{bmatrix} \sigma_{11} & \sigma_{12} & \sigma_{13} \\ \sigma_{21} & \sigma_{22} & \sigma_{23} \\ \sigma_{31} & \sigma_{32} & \sigma_{33} \end{bmatrix} \qquad (8.1)$$

If it is assumed that there are no torques present in the sample, the matrix is said to be symmetric, i.e. $\sigma_{ij} = \sigma_{ji}$. Therefore only six different stress components are required to completely define the forces acting on the system. Three are extensional $\sigma_{11}$, $\sigma_{22}$, $\sigma_{33}$, and three are shearing $\sigma_{12}$, $\sigma_{13}$, $\sigma_{23}$.

Displacement of a body can occur through three different processes: rigid body translation $s_T$, rigid body rotation $s_R$, local deformation s. It is the latter process, called strain $\varepsilon$, which occurs when an ultrasonic wave is propagated through a medium. Deformation is said to be elastic if the body regains its size and or shape after the external forces have been removed. To a first order approximation, it is possible to describe the strain tensor $\varepsilon_{kl}$ as:

$$\varepsilon_{kl} = \frac{1}{2}\left(\frac{\partial s_k}{\partial x_k} + \frac{\partial s_l}{\partial x_l}\right) = \frac{1}{2}\left(s_{kl} + s_{lk}\right) \qquad (8.2)$$

$\varepsilon_{kl}$ is defined as the extension (as a fraction of total length) a body undergoes when an external force is applied, $s_k = x'_k - x_k$, where $x_k$, $x'_k$ are the positions of a point before and after deformation, and l, k define the direction of the deformation 1,2,3, see figure 8.2.

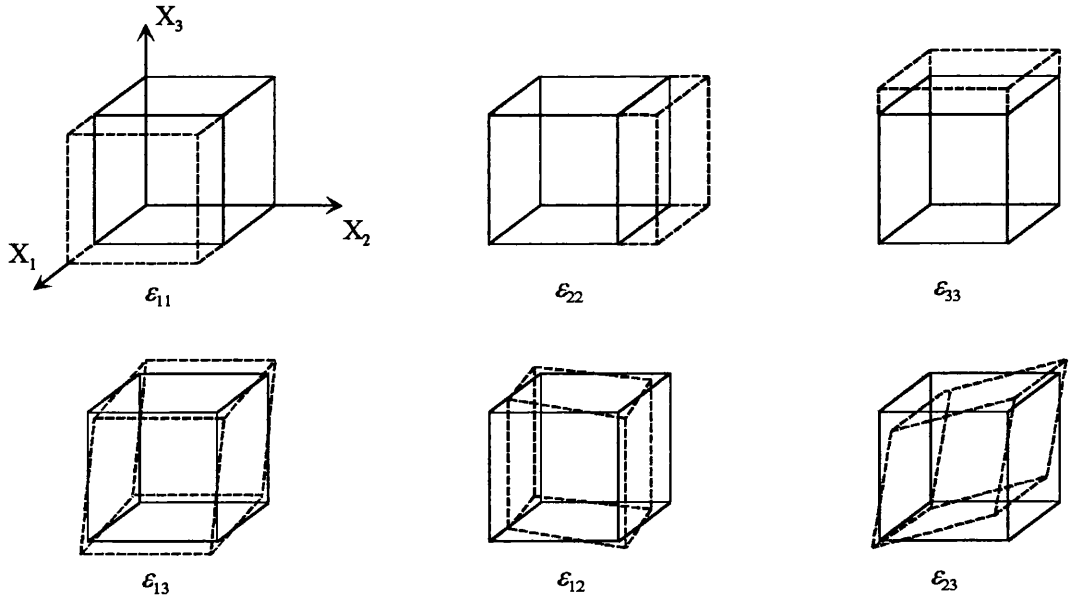


Figure 8.2. The effect of strain on a parallelepiped.

As with its stress counterpart, the strain tensor is symmetric $\varepsilon_{kl} = \varepsilon_{lk}$ and can be described by a 3×3 matrix (equation 8.3) of which only six components are independent and specify the state of the system.

$$\varepsilon_{kl}=\begin{bmatrix}\varepsilon_{11} & \varepsilon_{12} & \varepsilon_{13}\\ \varepsilon_{21} & \varepsilon_{22} & \varepsilon_{23}\\ \varepsilon_{31} & \varepsilon_{32} & \varepsilon_{33}\end{bmatrix} \tag{8.3}$$

The second order elastic stiffness tensor component $C_{ijkl}$, is the constant of proportionality relating stress to strain in Hookes law

$$\sigma_{ij} = C_{ijkl}\,\varepsilon_{kl}. \tag{8.4}$$

The equations only holds if the sample exhibits linear elastic behaviour; this condition is met when small deformations are considered. In theory each of the nine stress components depend linearly on each of the nine strain components; hence the SOEC tensor is a forth rank tensor, and in principal it has 81 coefficients. As stated previously, the stress and strain tensors are symmetric and each has six individual components; therefore there are only (6×6) 36 different combinations:

$$C_{ijkl} = C_{ijlk} = C_{jikl} \tag{8.5}$$

If elastic materials are being exclusively analysed, a further restriction can be implemented. This is possible because strain depends only on its final state, and is not a function of the path taken; hence it is possible to write:

$$C_{ijkl} = C_{ijlk} = C_{jikl} = C_{klij} \tag{8.6}$$

This reduces the number of independent elastic components to 21. The notation used can be simplified following Voigt by replacing two indices with a single subscript, this is permitted as ij = ji = I and kl = lk = J.

| Tensor Notation | 11 | 22 | 33 | 23 32 | 13 31 | 12 21 |
|---|---|---|---|---|---|---|
| Matrix Notation | 1 | 2 | 3 | 4 | 5 | 6 |

Hooke's law can be written employing matrix notation, where $C_{IJ}$ (=$C_{JI}$) are the twenty-one separate coefficients.

$$\begin{bmatrix}\sigma_1\\ \sigma_2\\ \sigma_3\\ \sigma_4\\ \sigma_5\\ \sigma_6\end{bmatrix}=\begin{bmatrix}C_{11} & C_{12} & C_{13} & C_{14} & C_{15} & C_{16}\\ C_{12} & C_{22} & C_{23} & C_{24} & C_{25} & C_{26}\\ C_{13} & C_{23} & C_{33} & C_{34} & C_{35} & C_{36}\\ C_{14} & C_{24} & C_{34} & C_{44} & C_{45} & C_{46}\\ C_{15} & C_{25} & C_{35} & C_{45} & C_{55} & C_{56}\\ C_{16} & C_{26} & C_{36} & C_{46} & C_{56} & C_{66}\end{bmatrix}\begin{bmatrix}\varepsilon_1\\ \varepsilon_2\\ \varepsilon_3\\ \varepsilon_4\\ \varepsilon_5\\ \varepsilon_6\end{bmatrix} \tag{8.7}$$

In general, increasing the symmetry of the sample being studied reduces the number of SOEC needed to characterise a material. Metaphosphate glasses are isotropic, and are uniform throughout and in all directions. The elastic constants should therefore be independent of the axes along which the stress is applied; this leads to another restriction, the three coordinate axes x,y,z, and the three coordinate planes xy, yz, zx are equivalent:

$$C_{12} = C_{13} = C_{23} \qquad C_{44} = C_{55} = C_{66} \qquad C_{11} = C_{22} = C_{33} \tag{8.8}$$

and all other components are zero. It follows that an isotropic sample can also be completely specified by two constants, known as Lamé's constants. By letting $C_{12} = C_{13} = C_{23} = \mu$ and $C_{44} = C_{55} = C_{66} = \lambda$, it is found $C_{11} = C_{22} = C_{33} = \lambda + 2\mu$. In ultrasonic experiments the quantities being measured are $C_{11}$ and $C_{44}$: these can be found from the longitudinal and shear velocities respectively. Three other elastic parameters are also of interest: Young's modulus E, the ratio of stress to strain for a material where application of stress is along a single axis, the bulk modulus B (= -Vdp/dV), the ratio of hydrostatic pressure P to the fractional change in volume, and Poisson's ratio $\sigma$, the ratio of strain perpendicular and parallel to the applied stress (Pollard 1977).

The propagation of sound waves through a medium relies upon the vibration of atoms about their equilibrium position, when a stress is applied. In general three types of plane wave can be transmitted: one longitudinal wave, in which atomic motion is in the same direction as wave propagation, two shear waves, in which particle oscillations are in a direction perpendicular to the wave. The equation of motion describing the behaviour of a propagating wave originates from Newton's third law. The wave equation can be obtained by equating the net force due to the internal stresses with the product of the acceleration of a particle exhibiting simple harmonic motion, and mass per unit volume (Thurston and Brugger 1964, Pollard 1977)

$$\frac{\partial \sigma_{ij}}{\partial x_j} = \rho_o \frac{\partial^2 u_i}{\partial t^2} \quad . \tag{8.9}$$

Here $u_i$ is the displacement of an atom in the direction i, at a time t, and a position x, and $\rho_0$ is the mass density of the sample. If Hooke's law is applied to equation 8.9, $\sigma_{ij}$ can be replaced with $C_{IJ}\,\varepsilon_{kl}$. It is possible to solve this equation using Christoffel's method (Pollard 1977, Beltzer 1988, Auld 1990). He demonstrated that the equation

of motion could be rewritten in terms of a plane travelling wave $u_i=u_0\exp[i(\mathbf{kx}-\omega t)]$ where $\omega$ is the angular frequency, **k** is the wavevector and $u_0$ is maximum amplitude, given that the density $\rho_0$, the direction of propagation n, and the elastic constants $C_{ijkl}$ are known

$$\left(C_{ijkl}n_j n_k k^2 - \rho\omega^2\delta_{il}\right)u_l = 0 \qquad (8.10)$$

where $\delta_{il} = u_i/u_l$. Equation 8.10 is called Christoffel's equation and can be expanded in full using tensor notation. For an isotropic material the roots of the equation can be simplified to consist of three mutually perpendicular waves of which one is longitudinal and two are identical shear waves (all wave velocities will be independent of there propagation direction). In solving Chirstoffel's equation the adiabatic elastic constants are linked with the longitudinal $v_L$ and shear $v_S$ wave velocities ($\omega$/k) and the density. A summary of the results are shown below (equation 8.11):

SOEC
$$C^s_{11} = \rho v_L^2$$
$$C^s_{44} = \rho v_S^2$$

Bulk modulus
$$B^s = \frac{1}{3}\left(3C^s_{11} - 4C^s_{44}\right) = \rho(3v_L^2 - 4v_S^2)/3$$

Young's modulus
$$E^S = \frac{C^s_{44}(3C^s_{11} - 4C^s_{44})}{(C^s_{11} - C^s_{44})} = \rho v_S^2 \frac{(3v_L^2 - 4v_S^2)}{(v_L^2 - v_S^2)}$$

Poisson's ratio
$$\sigma^S = \frac{(C^s_{11} - 2C^s_{44})}{2(C^s_{11} - C^s_{44})} = \frac{(v_L^2 - 2v_S^2)}{2(v_L^2 - v_S^2)} \qquad (8.11)$$

The superscript S indicates the changes are adiabatic.

### 8.1.2. ANHARMONIC VIBRATIONAL BEHAVIOUR

Real materials exhibit anharmonic vibrational behaviour; this is a direct result of the nature of the interatomic potential between two atoms (see figure 8.3). When the separation between the two atoms is greater than $x_0$ (the equilibrium separation), the atoms feel attractive forces. At smaller separations repulsive forces arise from overlapping of the electron cloud, and the Pauli exclusion principle.

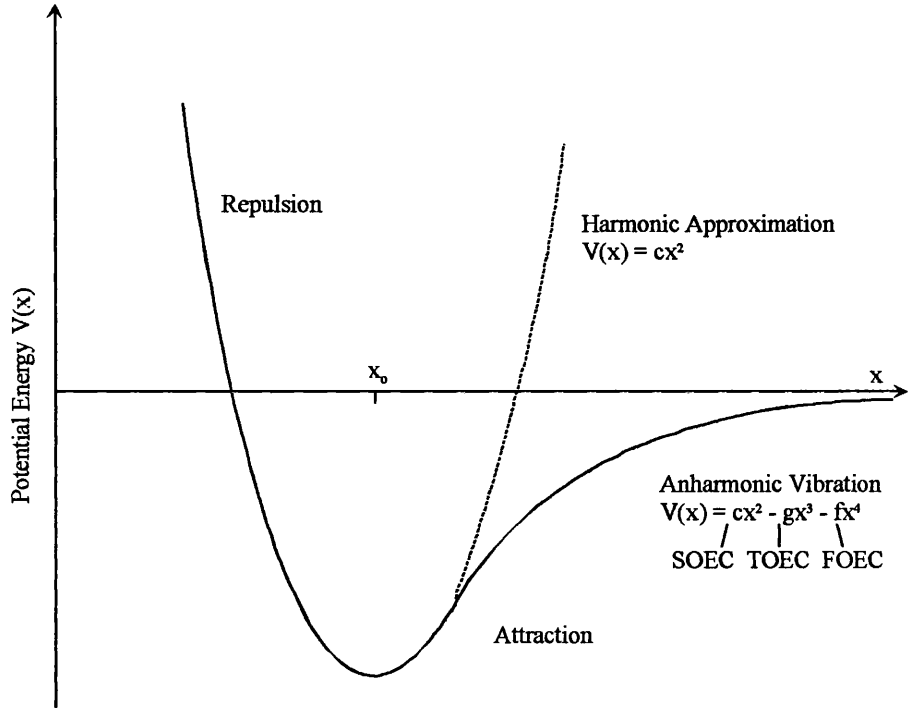


Figure 8.3. Interaction potential V(x) versus atomic separation x. The parabola represents the harmonic approximation, and $x_0$ is the equilibrium separation.

It is convenient to describe the lattice vibrations in a solid in terms of quasi-particles called phonons. In the harmonic approximation the individual phonons are independent harmonic vibrations and thus can be superimposed. The approximation is represented as the quadratic curve in figure 8.3 and is equivalent to Hooke's law. Analysis of this nature does not account for many properties of real materials such as the temperature and pressure dependences of the elastic constants, thermal conductivity, specific heat and thermal expansion. If a quasi-harmonic approximation is adopted, the vibrations are still treated as quadratic, but the normal mode frequencies $\omega$ are considered to depend on the equilibrium volume of the sample. In this model, the anharmonicity of atomic vibrations, due to temperature, can be described in terms of the thermal Grüneisen parameter $\gamma^{th}$ (Brugger and Fritz 1967, Barron et al. 1980, Sato and Anderson 1980):

$$\gamma^{th} = \frac{3\alpha V}{K^S C_p} = \frac{3\alpha V}{K^T C_v} \quad . \tag{8.12}$$

Here $\alpha$ is the linear coefficient of thermal expansion, $V$ is the volume, $K^T$, $K^S$ is the isothermal and isentropic compressibility respectively, C is the specific heat at

constant volume (subscript $V$) or constant pressure (P). The thermal Grüneisen parameter can be defined as the weighted average of the mode Grüneisen parameters $\gamma_i$:

$$\gamma^{th} = \frac{\sum(\gamma_i c_i)}{\sum c_i} \tag{8.13}$$

$c_i$ is the Einstein specific heat capacity $\left(=\left[k_B(h\nu/k_BT)^2 \exp^{h\nu/k_BT}\right]/\left(\exp^{h\nu/k_BT}-1\right)^2\right)$ where $k_B$ is the Boltzmann constant, h is Planck's constant, $\nu$ is the phonon frequency). For each mode of vibration there is a mode gamma $\gamma_i$. In an isotropic medium there are only two independent acoustic mode Grüneisen parameters. One ($\gamma_L$) represents the contribution from the long wavelength longitudinal acoustic phonons to the lattice vibrational anharmonicity and the other ($\gamma_S$) describes the effects of the shear wave. In general $\gamma_i$ represents the first order vibrational anharmonicity of the long wavelength acoustic phonon modes,

$$\gamma_i = -\left[\frac{\partial(\ln\omega_i)}{\partial(\ln V)}\right]_T \tag{8.14}$$

the negative sign is included because in normal materials the mode frequency $\omega$ decreases as the volume $V$ is increased; the majority of solid materials show resistance to compression; hence the Grüneisen parameter is positive. Three Grüneisen parameters can be determined from ultrasonic experiments, using the elastic stiffness constants and their hydrostatic pressure derivatives: the longitudinal $\gamma_L$, shear $\gamma_S$, mean $\gamma^{el}$ Grüneisen parameters (Senin 1994)

$$\gamma_L = -\left[\frac{1}{6C_{11}}\left(3B+2C_{11}+C_{111}+2C_{112}\right)\right] = -\frac{1}{6C_{11}}\left[C_{11}-3B^T\left(\frac{\partial C_{11}}{\partial P}\right)\right]$$

$$\gamma_S = -\left[\frac{1}{6C_{44}}\left(3B+2C_{44}+\frac{1}{2}\left(C_{111}+C_{123}\right)\right)\right] = -\frac{1}{6C_{44}}\left[C_{44}-3B^T\left(\frac{\partial C_{44}}{\partial P}\right)\right] \tag{8.15a}$$

Here B is the bulk modulus and the $C_{IJK}$ are the third order elastic stiffness tensor components (TOEC). The third and fourth order elastic stiffness tensor constants (TOEC and FOEC) are associated with the measurement of the finite strains produced when an elastic wave is propagated through a medium which is subject to a static stress. The TOEC provide information on the cubic coefficients of the strain

Hamiltonian, which defines the vibrational anharmonicity of the long wavelength acoustic phonons; they are the result of the asymmetry of the lattice vibrations as described by the higher order terms in the interatomic potential energy (see figure 8.3) (Brugger 1964, Thurston and Brugger 1964). The higher order terms $-gx^3-fx^4$ arise from coupling, via interactions, between the different modes. The acoustic mode gammas can also be found from the SOEC and their pressure derivatives, see the right hand equalities of equation 8.15a. The mean long wavelength acoustic Grüneisen parameter is defined as;

$$\gamma^{el} = \left(\frac{\gamma_L}{v_L^3} + \frac{2\gamma_S}{v_S^3}\right) \Bigg/ \left(\frac{1}{v_L^3} + \frac{2}{v_S^3}\right) = \frac{\gamma_L + 2\gamma_S}{3} \qquad (8.15b)$$

At low temperatures the Einstein specific heat (equation 8.13) can be approximated by a $v^{-3}$ weighting, where v is the wave velocity. The right hand side of equation 8.15b only holds for the Debye continuum model at room temperature and above (Barron 1955, Brugger and Fritz 1967). This model makes the assumptions that the optical branch can be ignored and all acoustic modes obey the Debye distribution function. In an amorphous material the acoustic modes and thermal phonons in the long wavelength limit can be regarded as Debye-like phonons: non-dispersive quasi-harmonic plane waves. Hence it is expected that their behaviour can be described using Debye theory; this approximation breaks down at low temperatures where the excess low energy modes become proportionally more significant. The Debye temperature $\Theta_D$ is required when describing the thermal properties (density of states, specific heat, thermal energy) of a system, and is proportional to a maximum vibrational frequency $\omega_m$ of the modes ($\omega_m$ acts as a cut off frequency characteristic of the sample), $k_B\Theta_D = \hbar\,\omega_m$ (Hook and Hall 1994). Its value is related to the interatomic forces between atoms; high $\Theta_D$ suggests a strongly bonded system. The Debye mean sound velocity can be calculated from the longitudinal and shear wave velocity

$$\bar{v}_D = \left(\frac{1/v_L^3 + 2/v_S^3}{3}\right)^{-\frac{1}{3}} \qquad (8.16)$$

and the Debye temperature $\Theta_D$ is

$$\Theta_D = \frac{h}{k}\left(\frac{3\rho An}{4\pi M}\right)^{\frac{1}{3}} \bar{v}_D. \qquad (8.17)$$

Here A is Avogadro's number, n is the number of atoms per unit formula, and M is the molecular weight. The $\Theta_D$ of diamond is approximatly 1000K, lead approximatly 100K and vitreous silica 496K (Senin 1994).

The variations of the SOECs and bulk modulus with applied external pressure are required to determine the long wavelength acoustic mode Grüneisen parameters, and help to describe the non-linearity of the atomic forces with respect to atomic displacements. The pressure derivatives can either be evaluated using a combination of second and third order elastic constants, or the second equality derives equation 8.18 in terms of experimentally measured quantities: the second order elastic stiffness $C_{IJ}$, the bulk modulus B, the (longitudinal or shear) natural velocity of a stress wave propagating through a solid $W_X$:

$$\left(\frac{\partial C_{11}^s}{\partial P}\right)_{T,P=0} = -\frac{1}{9B}\left(C_{111}+6C_{122}+2C_{123}\right)-\frac{2}{9B}\left(6C_{11}-6C_{44}+C_{111}-C_{123}\right)$$

$$=2C_{11}\left(\frac{d\left[\left(W_L/W_{L0}\right)-1\right]}{dP}\right)_{T,P=0}+\frac{C_{11}}{3B^s}$$

$$\left(\frac{\partial C_{44}}{\partial P}\right)_{T,P=0} = -\frac{1}{6B}\left(6C_{11}-6C_{44}-C_{111}-C_{123}\right) = 2C_{44}\left(\frac{d\left[\left(W_S/W_{S0}\right)-1\right]}{dP}\right)_{T,P=0}+\frac{C_{44}}{3B^s}$$

$$\left(\frac{\partial B^s}{\partial P}\right)_{T,P=0} = -\frac{1}{9B}\left(C_{111}+6C_{112}+2C_{123}\right)$$

$$=\frac{2}{3}\left(3C_{11}\frac{d\left[\left(W_L/W_{L0}\right)-1\right]}{dP}-4C_{44}\frac{d\left[\left(W_S/W_{S0}\right)-1\right]}{dP}\right)_{T,P=0} \qquad (8.18)$$

$W_{X0}$ is the natural velocity at zero pressure ($W_{X0} = v_X$). The natural velocity is defined by the zero pressure path length of a sample divided by the transit time of the ultrasonic wave at a given pressure. Hence $W_X$ is a measure of the wave speed ignoring the fact the volume of the sample will be reduced when pressure is applied (see section 8.2.1); in contrast the velocity v, depends on the path length of the stressed sample (Thurston and Brugger 1964, Thurston 1965). The discrepancy

between W and v is rectified by the addition of a 1/3B correction term in the pressure derivatives of $C_{11}$ and $C_{44}$. The bulk modulus can be expressed to its first order approximation in pressure as

$$B(P) = B_o + P\left(\frac{\partial B}{\partial P}\right)_{P,T=0} \tag{8.19}$$

Generally the bulk modulus becomes smaller with increasing pressure.

The velocity and attenuation of the longitudinal and shear waves with temperature provide an excellent measure of the effect of vibrational anharmonicity in a real material. If the sample is harmonic, there is no acoustic absorption. In all real materials the vibrational anharmonicity results in energy losses from the ultrasonic wave as heat. There are many acoustic loss mechanisms which include: scattering from defects, phonon-phonon interactions, thermoelastic and frictional heating. A detailed account of all the possible losses is given by Truell et al (1969). The energy of the wave decays following an exponential law:

$$u_i = u_0 \exp(-\alpha x)\exp i(\mathbf{k}x - \omega t) \tag{8.20}$$

where $\alpha$ is the attenuation factor, $u_o$ and $u_i$ are the initial and final amplitude after the wave has travelled a distance x, $\mathbf{k}$ is the wavevector ( $|\mathbf{k}| = 2\pi/\lambda$) and $\omega$ is the angular frequency (see figure 8.4). The attenuation is measured in $dBcm^{-1}$, (= $\alpha/l_0$, if $l_0$ is the unstressed thickness of the sample in the direction of wave propagation). In a sample, which exhibits harmonic behaviour only, the velocity of a wave propagating through a sample would be constant when there is a change in temperature. Allowing for anharmonic contributions: the velocity of a crystalline solid increases with decreasing temperature, up to a certain point, and below this temperature its gradient tends to zero. In rare earth metaphosphate glasses, like many other amorphous materials, the gradient steepens as the temperature is decreased (Saunders et al. 1994, Senin et al. 1993a,b, 1994a, b, Farok et al. 1994). This characteristic has been attributed to long wavelength phonon vibrational anharmonicity and phonon scattering from low energy excess modes (Carini et al 1995a).

Thermal expansion is another property governed by atomic motion, and hence can be used as a technique for looking at the macroscopic inelastic behaviour of a material; it

has already been seen that the volume thermal expansion is proportional to the thermal Grüneisen parameter $\gamma^{th}$ (equation 8.12). As the temperature is lowered, the long wavelength acoustic modes make up an increasing proportion of the phonon population: $\gamma^{el}$ tends to $\gamma^{th}$. In general softening of the low energy long wavelength acoustic modes can be linked to anomalous trends in the thermal expansion. The coefficients of expansion at low temperatures are negative for tetrahedrally bonded glasses, $SiO_2$, $GeO_2$, and $BeF_2$, but positive for $B_2O_3$, $As_2S_3$, and $As_2$ $Se_3$ (Barron et al 1980); these two distinct regimes are also found in higher order elastic data. The long wavelength acoustic modes in tetrahedrally bonded amorphous materials display anomalous characteristics such as a decrease in velocity with pressure and negative Grüneisen parameters; the latter group exhibits normal positive behaviour (Acet et al. 1998). However this simple link between thermal and acoustic characteristics ignores any contribution that the low energy excess modes make to thermal expansion.

## 8.2. ULTRASONIC METHOD AND APPARATUS

All of the ultrasonic results were collected using the pulse echo overlap technique. This technique is based on the pulse echo method. A short duration stress wave is introduced into a sample via a piezoelectric crystal transducer bonded onto one of two parallel surfaces. An applied RF voltage, usually in the form of a pulsed sine wave, drives the quartz at its fundamental (or odd harmonic) frequency, resulting in the deformation of the glass and the production of a stress wave. The ultrasonic wave packet propagates through the sample until it reaches the opposite surface where upon arrival it is reflected back. As the piezoelectric effect is reversible, the transducer acts not only as a source, but as a receiver for the returning echo. After travelling twice the length of the sample ($2l_0$) a small amount of the wave total energy stresses the transducer, which in turn produces a voltage; the majority of the wave is reflected at the bond transducer interface. The electric signal is amplified by a receiver and displayed on a cathode ray oscilloscope (C.R.O.). This process is repeated several times. The multiple reflections, called an echo train, occur at a separation equal to the time it takes for the ultrasonic wave to travel twice the sample length. The wave amplitude decreases exponentially during each transition, as the wave suffers some energy losses due to scattering or absorption; these processes limit the number of successive echoes viewed on the C.R.O. For a schematic of an echo train see figure

8.4. The velocity (equation 8.21) and attenuation (equation 8.20) can be calculated by studying the pulse echo pattern. Absolute attenuation cannot be measured due to the extrinsic energy losses associated with coupling the ultrasonic wave into the glass sample. However relative changes in the attenuation can be recorded as a function of temperature, and to a lesser extent pressure.

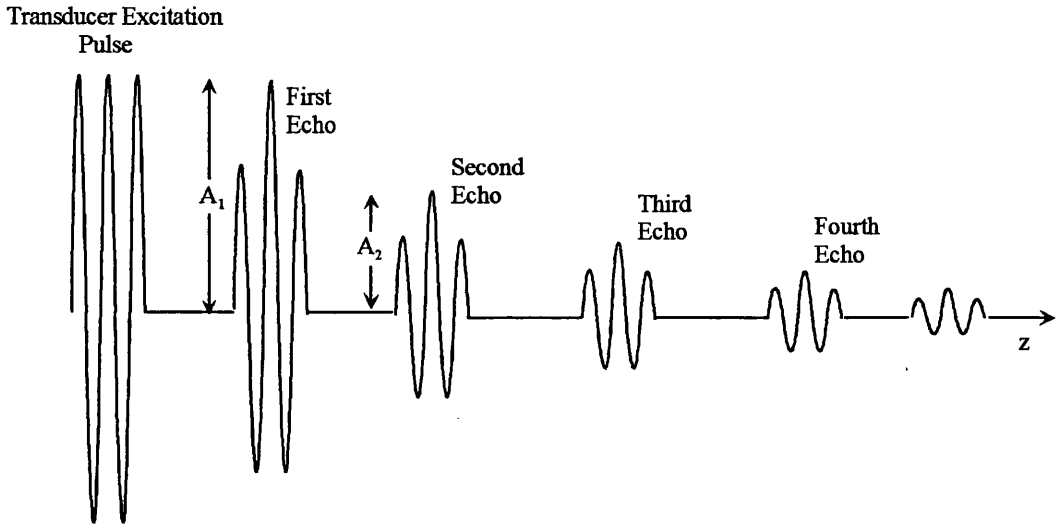


Figure 8.4. The pulse train display as seen on an oscilloscope screen, showing the relationship between amplitude and distance.

### 8.2.1. PULSE ECHO OVERLAP TECHNIQUE

The pulse echo overlap technique was introduced by May in 1958, and in subsequent years was developed by Papadakis (1964, 1967). In this method two adjacent ultrasonic pulses are highlighted electronically (strobed) and the period between them is estimated. The first echo is then delayed by the corresponding frequency, which allows for superposition of any pair of echoes. As the temperature and/or pressure of the sample are changed the echoes become unaligned; small adjustments to the frequency allows for the two overlapped waves to remain in phase. This technique enables velocity changes to be measured to an accuracy of one part in $10^5$. The apparatus is represented in block diagram form in figure 8.5.

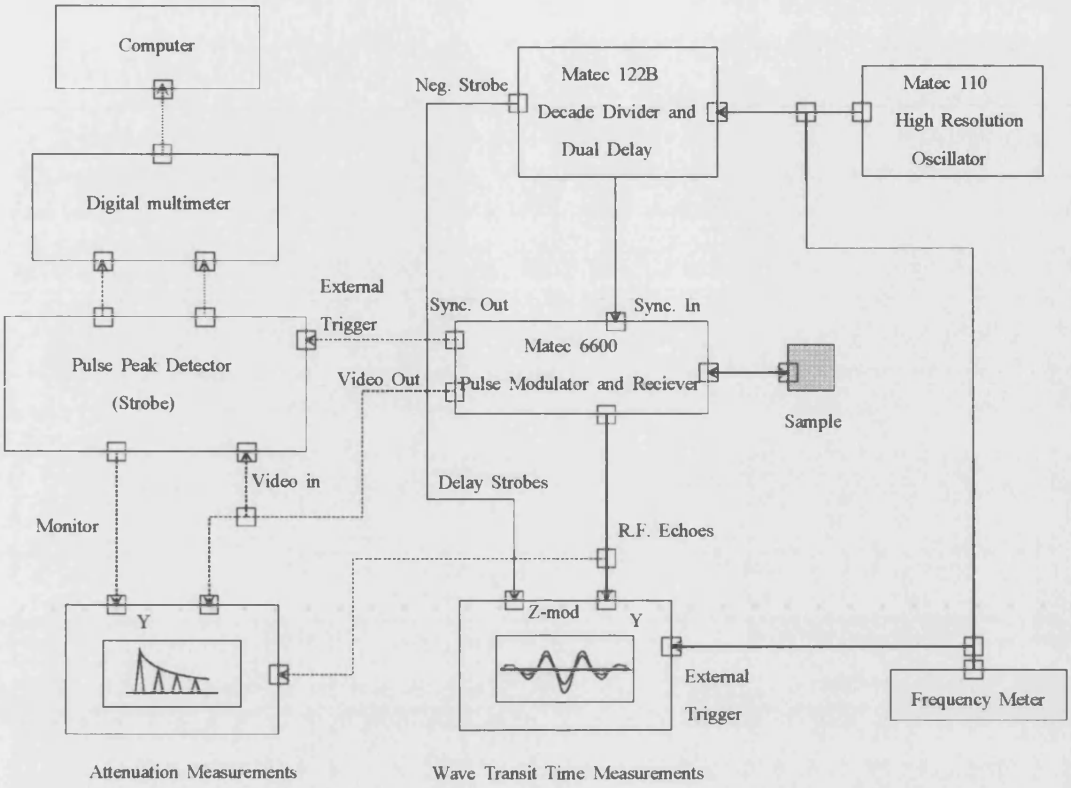


Figure 8.5. Schematic diagram of the pulse echo overlap system

A square wave is generated in the Matec 110 frequency source, which in turn triggers a high voltage (1000V) R.F pulse (figure 8.6.a). This pulse is tuned to leave the Matec 6600 with a carrier frequency corresponding to the resonant frequency of the quartz transducer; hence the propagated stress wave has a maximum amplitude. The frequency with which the R.F. pulses stress the piezoelectric crystal is low, allowing for the total decay of all the subsequent echoes before a new pulse is introduced. This is achieved by using a decade divider (Matec 122B), which divides the repetition of the triggering pulse by a factor of a thousand (figure 8.6.b and c). The transducer acts as both a generator and a receiver for the ultrasonic wave travelling through the sample. The reflected echoes are amplified and the pulse train is displayed on a cathode ray oscilloscope (figure 8.6.d).

a) Triggering square wave signal from the high resolution oscillator

b) Divided synchroniser (1/1000)

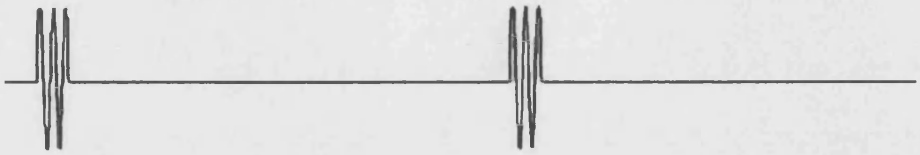

c) Radio frequency pulses to the transducer

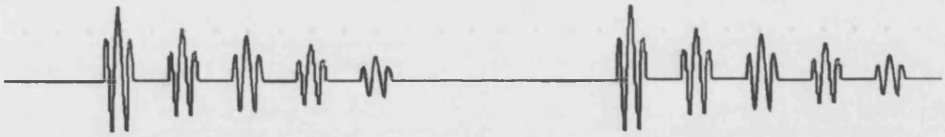

d) Radio frequency echo train

e) Z modulation - intensification of two echos

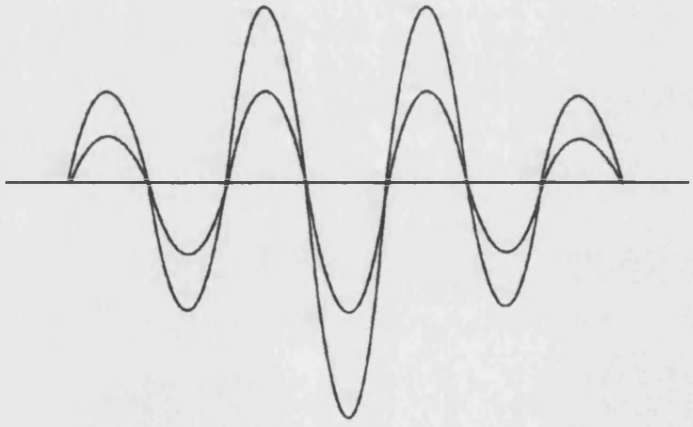

f) Overlap of two succsessive echos

Figure 8.6. The signal at various points in the pulse echo overlap system.

Two echoes are then chosen to be intensified, usually the 2nd and 3rd as they have a substantial amplitude and are less likely to suffer interference and distortion from the

driving pulse. Echo selection is accomplished by feeding a pair of square pulses, via the strobe generator (Matec 122B), into the Z modulation of the oscilloscope (figure 8.6.e). The intensity of echo train on the oscilloscope is then reduced, so that only the two echoes are visible. The strobed pulses are subsequently overlapped by adjusting the frequency f of the pulse synthesiser (Matec 110) until it equals the reciprocal of the time T for the wave to travel twice the sample width. This has the effect of triggering the oscilloscope at a quick repetition rate: with each sweep only an individual echo is scanned. When the synthesiser introduces the next external trigger, the following echo is displayed. By adjusting the time base the pulses can be overlaid (figure 8.6.f).

The echoes are superimposed by comparing each cycle on the C.R.O. using the vernier control on the high resolution frequency source. From the overlap frequency, the value of which can be read from a frequency meter, the natural velocity of the wave W can be calculated:

$$W = 2l_0/T = 2l_0f \qquad (8.21)$$

where $l_0$ is the thickness of the sample at room temperature and zero pressure. As the temperature and/or pressure is altered, there is a change in the ultrasonic wave velocity and also the period between consecutive pulses. As the overlapped waves move out of phase, they have to be realigned by altering the frequency of the synthesiser. The major difficulty incurred in overlaying the echos lies in deciding which cycles produce the true overlap. This problem arises due to the virtual impossibility of producing symmetric pulses, because of factors such as: attenuation of the beam, phase shifts during reflection, sample transducer bonding (Kittinger 1977). To minimise this error, a cycle near the centre of the first echo is chosen and compared with several subsequent echoes to see if the overlap remains in phase thought out the echo train; also the pulse amplitude and receiver gain on the Matec 6600 is lowered to see if the two cycles have the same characteristics. This problem is only significant when calculating absolute velocities, and does not effect the accuracy of the relative measurements.

The ultrasonic echo train is displayed on two C.R.O.s. The second trace is used to measure the attenuation of the beam as it propagates through the sample. Once again

two peaks are highlighted, this time by the pulse peak detector. The peak voltage of each pulse is then measured using a digital multimeter and fed directly into a computer where attenuation is calculated using

$$\alpha = 20\log_{10}\left(\frac{V_1}{V_2}\right). \qquad (8.22)$$

Here V is the voltage of two consecutive echoes, and the attenuation, $\alpha$, is measured in dB. Measurements of attenuation are complicated by extrinsic factors which arise due to the method and execution of the experiment. Extrinsic losses have been extensively reviewed by Truell, Elbaum and Chick in 1969, and are summarised below:

a) Diffraction losses. The transducer has a finite size thus the beam diverges, $\Delta\theta$, resulting in a spread of energy and possibly side wall reflections, and intermediate echoes; $\Delta\theta = 1.22\lambda/D$ where $\lambda$ is the wavelength, and D is the diameter of the transducer.

b) Non-parallelism of the surfaces. Different areas of the transducer detect different phases of the wave, which is the result of the wavefront being reflected at an angle. The transducer is phase sensitive, so the wave appears to have a decreased amplitude. After polishing, the parallelism of the sample surfaces was checked using optical interference methods; they were found to be parallel to within a wavelength of sodium light.

c) Transmission losses. A large acoustic impedance is required at the boundaries, to maximise reflection. The transmission coefficient equals $4R_1R_2/(R_1+R_2)^2$, where $R_1$, $R_2$, are the characteristic impedance's of the sample ($=\rho c$, where $\rho$ is the density and c is the velocity of the wave through the material) and the surrounding medium.

Minimisation of these effects is necessary if the relative changes of attenuation due to the intrinsic properties of the sample are to be studied. The above factors must to be considered when setting up the experiments.

### 8.2.2. PIEZOELECTRIC TRANSDUCERS AND BONDING

In piezoelectric crystals, such as quartz, application of a stress changes the materials' polarisation, and hence the electric field; if the stress is small, the relationship is linear. The piezoelectric effect is reversible, and a change in the electric field will result in a

strain, i.e. it converts mechanical to electrical energy, and vice versa. Piezoelectricity can be defined using

$$P = -d\sigma + \varepsilon_o \chi E$$

$$\varepsilon = -s\sigma + dE \qquad (8.23)$$

where P is the polarisation, E is the electric field , $\varepsilon$ is the strain, $\sigma$ is the applied stress and $\varepsilon_o$, $\chi$, s, d are the permittivity, susceptibility, elastic compliance and piezoelectric constant respectively (Hooke and Hall 1994). As stated in section 8.1.1, all second order elastic stiffness constants can be derived from the longitudinal and shear velocities ($C_{11}=\rho v_L^2$ and $C_{44}=\rho v_S^2$) of a stress wave propagating through an anisotropic sample. By using a quartz crystal cut in either the x or y direction a longitudinal or shear wave can be propagated through the sample. The transducers used were circular with a diameter of 6 mm and a natural frequency of 10 Mhz. The thickness of the transducers corresponds to half the wavelength of sound in quartz; therefore the x cut transducer has a thickness of 0.19 ± 0.02mm, and the shear transducer is 0.29 ± 0.02mm and can be distinguished as it has a flat edge cut parallel to the polarisation direction. The crystal is coated in gold; one of the surfaces is completely covered forming the earth, and the other surface is coaxially coated, where the outer ring completes the earth connection and the middle electrode acts as the high voltage connection. The transducer is bonded onto the sample using one of two bonding substances. These are employed to reduce energy losses due to reflection of the beam at the transducer sample interface. It is necessary that the bonding liquid is stable over the temperature range being explored and should not react with the sample. For measurements made at room temperature and above Dow resin 276-V9 (Dow-Corning Coup.) was used, and for temperatures below this Nonaq stopcock grease (Fisher Scientific Co.) (Bateman 1967). Prior to bonding, the sample surface was cleaned with acetone to eliminate any dirt that could act as a scattering centre; a small amount of the relevant bonding material is then placed onto the sample. It is important to make the bond as thin and as uniform as possible; consequently pressure is applied to the transducer once it is placed on the bonding substance (usually via a finger). In the case of resin, heat had to be applied (with a hot air blower) to lower the viscosity, and thus make it easier to remove any unwanted excess. After bonding a

connection is then made from the earth electrode to the base of the sample with conductive silver dag. This was performed to improve the earth connection.

### 8.2.3. ULTRASONIC TEMPERATURE MEASUREMENTS

Measurements of ultrasonic velocity and attenuation were made as a function of temperature. Low temperature measurements, between 15 - 290K, were recorded using a closed cycle liquid helium cryostat, Cryophysics Model 22C cryodyne refrigerator system. The operation and specifications of this equipment is described in detail by Fanggao (1996). Helium gas is initially compressed, with the heat involved in this process being removed by heat exchangers. The gas is then allowed to expand, which results in the temperature of the system being reduced. The cold head of the sample holder is kept continually at a temperature of 10K, and temperature variation is achieved through the use of a coil heater which is attached to a temperature controller. The sample is kept under a vacuum, by a combination of rotary and diffusion pumps, allowing for increased efficiency when cooling the sample, easier temperature control ($\pm$ 0.1K), and a more stable bond. For measurements above room temperature the sample is heated in an oil bath. The transducer and sample are placed in a covered aluminium tube and then lowered into an container filled with silicone oil 200/20cs (Dow Corning). The temperature is controlled via a thermostat, and is monitored using a nickel-chromium/nickel-aluminium thermocouple with an accuracy of $\pm$ 0.5°C; the maximum temperature is 230K. In both high and low temperature investigations the temperature of the sample was changed slowly, approximately five minutes for 5K, as glass samples have a fairly poor thermal conductivity and thermal equilibrium is required.

### 8.2.4. ULTRASONIC HYDROSTATIC PRESSURE MEASUREMENTS

The apparatus for ultrasonic measurements under pressure is shown in figure 8.7. The pressure on a sample is changed by placing it in a cylinder filled with a viscous liquid, which is compressed between two end pistons. The cylinder and pistons are made from EN26 nickel alloy carbon steel (cylinder dimensions are 115mm high, with a diameter of 12.7mm), and the oil is Dow Corning 200/1000cs silicone fluid, which has a working temperature of between 303 and 503K. The pressure is increased using an hydraulic pump, which can reach a maximum of 0.25GPa. Only the lower pressure

region is of interest here; hence a maximum pressure of 0.15GPa is used. As the top piston is forced towards the fixed lower piston, an increase in pressure is transmitted to the sample through the liquid. The change is recorded using a manganin gauge mounted upon the top piston next to the sample. The resistance of the gauge as a function of pressure is recorded with the aid of a Rascal-Dana 5004 digital multimeter, which has a sensitivity of 1mΩ. From the value of resistance, the pressure can be calculated:

$$P = \frac{\left((R/R_o)-1\right)}{2.4\times10^{-3}} \quad \text{(Kbar)} \qquad (8.24)$$

where R and $R_o$ are the resistance's corresponding to a pressure P and an initial pressure $P_o$ respectively (1 Kbar = 0.1 Gpa) (Sidek 1989). The applied pressure can be determined to within 1%, and as the temperature coefficient of resistance for manganin is small $10\times10^{-6}$ °$C^{-1}$, this will have a negligible contribution to the error. The apparatus has been equipped with two safety measures. The sample is protected by an alarm device, which prevents crushing of the sample in the eventuality of a leak in the PTFE and 'O' ring seals. The second device shields the experimenter by enclosing the equipment in a 7mm thick steel cabinet. It is possible to measure the ultrasonic wave velocities as a function of pressure at different temperatures (293-400K). This can be achieved since the apparatus has been fitted with a cylindrical heating element that is wrapped around the external wall of the oil container. The desired temperature is set using a Eurothem mini 17-90B temperature controller, and monitored on the external wall with a NiCr/NiAl thermocouple. When the required temperature is reached the electric current through the heating element is automatically reduced, and when the temperature drops below the desired value the current flow is increased. This leads to slight oscillations in temperature; however these are sufficiently damped by the thermal mass of the pressure cell; a second thermocouple recording the temperature of the silicone oil within the bore, is kept constant to ± 0.3K. Once the sample has been placed in the holder, the pressure is slowly increased to the required maximum, and then reduced to the initial pressure. This action is performed to both check the seals for leaks, and to eliminate any fluctuations which may occur from pressurising, and consequently thinning, of the bond fluid. The sample is then pressurised in steps of approximately 0.01 GPa. As the pistons are forced together (moved apart), the oil is warmed up (cooled); hence the

measurements have to be taken slowly due to the fact that thermal equilibrium has to be established between each reading.

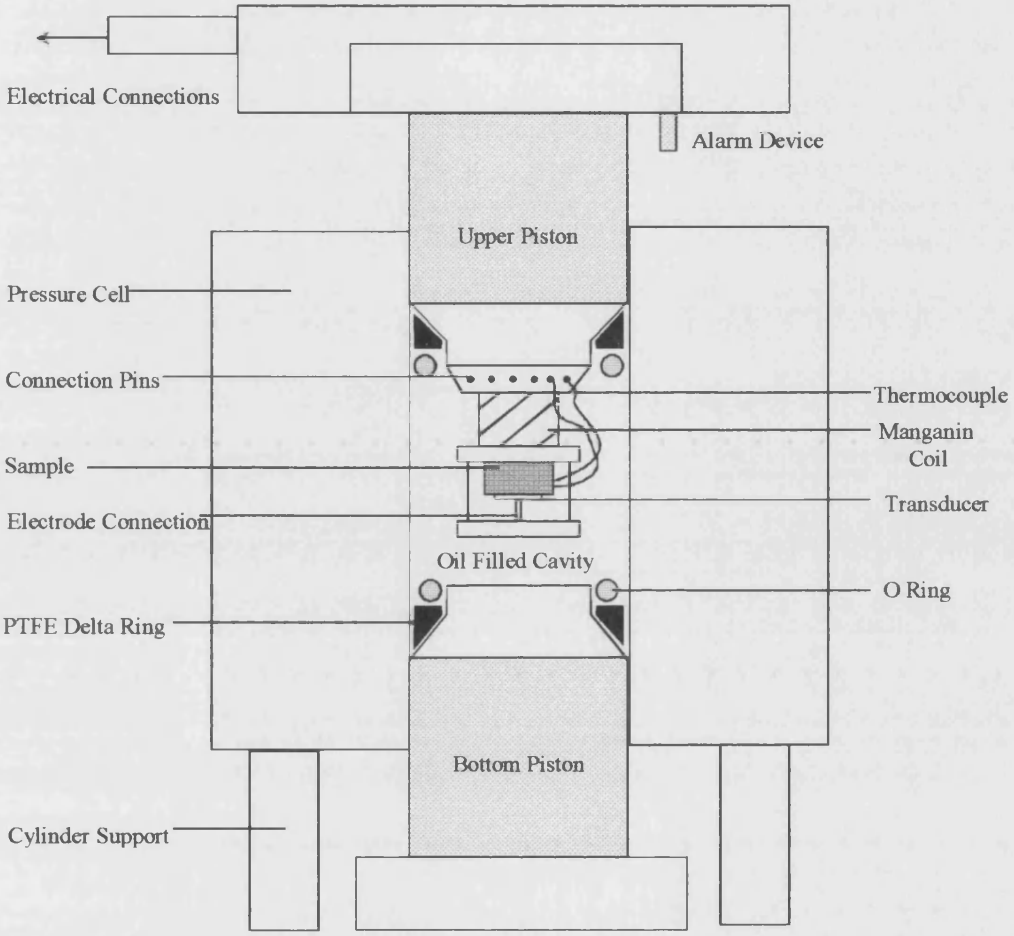


Figure 8.7. The hydrostatic pressure apparatus.

## 8.3. DATA CORRECTION PROCEDURES

In the temperature dependent ultrasonic velocity experiments the overlap frequency f (in KHz), as defined in equation 8.21, and the attenuation (in dB), equation 8.20 and 8.22, were measured as a function of temperature. All the relative attenuation measurements have been normalised into $dBcm^{-1}$ for ease of comparison; this is simply achieved by dividing the attenuation by the thickness of the sample. In the hydrostatic pressure measurement the velocity was investigated as two thermodynamic parameters, the pressure and temperature, were changed. The pressure is calculated from the resistance of a manganin gauge placed on the sample holder, and is converted into Kbar using the simple relationship in equation 8.24. The bulk of the

data corrections were completed using two Fortran 77 programs written by Dr. Q. Wang, University of Bath: nvt.exe transforms the overlap frequency in KHz to natural velocity ($ms^{-1}$) (including corrections for transducer effects, see below) and pressure in Kbar to GPa, Sonic2.exe. uses the natural velocity at zero pressure ($W_{S0}$ or $W_{L0}$) and the gradient of the natural velocity with pressure $\left(\partial W_X / \partial P\right)$ to calculate the long wavelength acoustic mode parameters: B, E, $\sigma$, $C_{11}$, $C_{44}$, $\partial C_{11}/\partial P$, $\partial C_{44}/\partial P$, $\partial B/\partial P$, $\gamma_L$, $\gamma_S$, $\gamma^{el}$. The natural ultrasonic wave velocity ($W_S$ or $W_L$) represents the speed at which the ultrasonic wave travels through a sample ignoring the effect that stress has on the path length, and hence velocity (equation 8.21) (Thurston and Brugger 1964, Thurston 1965). The natural velocity is initially corrected for transducer effects, i.e. the error due to the finite time it takes for the pulse to travel through the piezoelectric crystal and bonding material into the sample is eliminated. Multiple internal reflections within the parallel faces of the transducer and the acoustic impedance mismatch between the sample and the transducer result in the outgoing pulse consisting of a superposition of partial pulses with successively smaller amplitudes (there is a time lag between each partial pulse depending on how many multiple reflections it has undergone), and subsequently distortion of the pulse envelope (lengthened, delayed and 180° out of phase with the incoming pulse) (Kittinger 1977). The transducer contributes several other errors to the measurements that the experimenter must be aware of: changes in the thickness of the bonding material with temperature or pressure, increment of approximately 0.02%, diffraction losses (longitudinal losses are twice that of the shear wave) less than 1% error, pressure dependence of transducer resonant frequency, error depends on the mode, for a more detailed account see Wang (1993). At zero pressure there is no difference between the natural and true velocity, $W_0 = v_0$, hence the SOEC (i.e. $C_{11} = (\rho W^2_L)_{P=0} = (\rho v^2_L)_{P=0}$) can be calculated directly from the measured frequency. As pressure is increased the elastic constants only suffer small changes, however their pressure derivatives can exhibit significant differences. Using hydrostatic pressure experiments, the product of the unstressed density of the sample, $\rho_0$, with the square of the natural velocity ($\rho_0 W^2$) can be evaluated as a function of pressure (acting on the original area). Thurston and Brugger (1964) and Thurston (1965) showed that the first order

pressure derivative of the elastic constant $C_x$ (= $\rho v^2$) evaluated at atmospheric pressure, can be calculated directly from the raw data, $(d(\rho_0 W^2)/dP)_{P=0}$, using:

$$\left[\left(\rho v^2\right)' - \left(\rho_0 W^2\right)'\right]_{P=0} = \rho_0 v_0^2 \left(s^T_{kkii} - 2N_k N_m s^T_{kmii}\right)_{P=0}. \qquad (8.25)$$

Here the quantity in parenthesis on the right hand side of the equality describes the volume compressibility $\chi^T$ ($=s_{kkii}$, s is the elastic compliance) minus twice the linear compressibility in the direction N; these terms appear in equation 8.25 as applied pressure changes the density and path length respectively. The superscript T denotes that all the pressure derivatives are measured at constant temperature- isothermal. The quantity $(\rho_0 W^2)'_{P=0}$ can be calculated directly from the natural velocity ($W_x$) versus pressure graphs by fitting the gradient with straight line(s), using a method of linear regression, (these fits are depicted in figures 9.5, 9.6, 9.8-9.13, 9.20, 9.21 by the straight red lines); $(\rho_0 W^2)'_{P=0} = 2\rho_0 v_0^2 f'/f_0$, this equation retains its integrity when the frequency and its derivative (f' and $f_0$) are replaced with the natural velocity (W' and $W_0$) as the two quantities vary only by a constant $2l_0$. For a cubic crystal the linear compressibility $N_k N_m s^T_{kmii}$ equals $\chi^T/3$, for all propagation directions, the computer programs have made the assumption that this relationship holds for amorphous materials. Therefore equation 8.25 becomes,

$$\left(\rho_o v^2\right)'_{P=0} = \left(\frac{\partial c_{IJ}}{\partial P}\right)_{P=0} = \rho_0 v_0^2 \left(\frac{2W'}{W_0} + \frac{1}{3B^T}\right)_{P=0} = \left|\left(\rho_0 W^2\right)'_{P=0} + \frac{C^S_{IJ}}{3B^T}\right|_{P=0} \qquad (8.26)$$

where $B^T$ is the isothermal bulk modulus and is the reciprocal of the compressibility $1/\chi^T$. In the absence of specific heat data the adiabatic bulk modulus, $B^s$, has been used instead of $B^T$, this replacement produces negligible error. The above equation is equivalent to equation 8.18. $C_{IJ}$ and $B^s$ can be calculated from the intercept of the natural velocity versus pressure graphs (for each temperature). These values will also have some pressure dependence; however these changes can be considered negligible in the correction term. A similar expression can be used to calculate the pressure derivative of the bulk modulus. From these pressure derivatives the Grüneisen parameters can be evaluated, equation 8.15a,b. It is therefore possible to compute all the SOEC and derivatives from zero pressure ultrasonic velocity measurements, and the gradient of the frequency (or natural velocity) vs. pressure curves in the low pressure region.

# CHAPTER NINE

## RESULTS AND DISCUSSION OF ULTRASONIC EXPERIMENTS, AND THE RELATIONSHIP BETWEEN THE ACOUSTIC PHONON ANHARMONICITY, EXCESS VIBRATIONAL STATES AND THERMAL EXPANSION OF GLASSES

Samarium metaphosphate glass, $Sm(PO_3)_3$, exhibits anomalous elastic behaviour such as negative elastic stiffness pressure derivatives and Grüneisen parameters (Sidek et al. 1988, Mierzejewski et al. 1988a,b, Wang et al. 1990, Carini et al. 1990, Farok et al. 1992, Senin et al. 1993b). These characteristics are the consequence of long wavelength acoustic mode softening. In contrast the non-linear longitudinal acoustic properties of lanthanum metaphosphate glass are considered 'normal': the application of pressure increases the velocity with which an ultrasonic wave travels through a sample (Sidek et al 1988, Senin 1994). Ternary metaphosphate glasses containing both samarium and lanthanum ions $(La_2O_3)_x(Sm_2O_3)_y(P_2O_5)_{0.75}$ $(x + y = 0.25)$ displays intermediate behaviour (Senin et al. 1994b); the ultrasonic velocity essentially remains unaltered when pressure is applied to this glass. The main objective of the ultrasonic experiments has been to find out how the elastic properties change when samarium replaces lanthanum in the ternary metaphosphate glass. The vibrational anharmonicity determines the thermal expansion; hence as the $Sm^{3+}$ content is increased the coefficient of expansion decreases. At low temperatures this effect is even more prominent as the soft long wavelength acoustic modes make up an increasing proportion of the phonon population. This chapter is divided into three sections. In the first (section 9.1.) the ultrasonic (shear and longitudinal) velocity and attenuation of three ternary metaphosphate glasses doped with trivalent lanthanum and samarium ions $((La_2O_3)_{0.166}(Sm_2O_3)_{0.086}(P_2O_5)_{0.748}$, $(La_2O_3)_{0.109}(Sm_2O_3)_{0.164}(P_2O_5)_{0.727}$,

$(La_2O_3)_{0.055}(Sm_2O_3)_{0.206}(P_2O_5)_{0.739}$, was initially probed as a function of temperature (15 - 290K). In section 9.2. the effect of hydrostatic pressure (0 - 0.15GPa) on the ultrasonic wave velocity is investigated, through the three ternary glasses and for binary lanthanum $(La_2O_3)_{0.225}(P_2O_5)_{0.775}$ and cerium metaphosphate glass $(Ce_2O_3)_{0.235}(P_2O_5)_{0.765}$, at a series of temperatures between room temperature and 373K. All the ultrasonic results were collected using the pulse echo overlap technique, with a 6mm transducer, and a carrier frequency of 11Mhz. Finally in section 9.3. a simple model is formulated which relates the thermal expansion of glasses with nonlinear acoustic phonons and low energy excess vibrational states. These new ideas have been compared with the linear thermal expansion data for binary samarium and lanthanum metaphosphate glasses (Acet et al. 1998)

## 9.1. TEMPERATURE DEPENDENCE OF THE ULTRASONIC WAVE VELOCITIES AND ATTENUATION IN TERNARY SAMARIUM LANTHANUM METAPHOSPHATE GLASSES

The temperature dependences of the ultrasonic wave velocity and attenuation are depicted in figure 9.1. - 9.4. The longitudinal and shear ultrasonic wave velocities are reproducible upon cycling between room temperature and 15K, and exhibit no measurable hysterysis effects. The graphs for the three ternary glasses show similar features. The velocities associated with both the longitudinal and shear modes increase with decreasing temperature, and at low temperatures (below 100K) there is a steepening in the gradient. This differs from the behaviour of crystals resulting from vibrational anharmonicity: a linear increase in velocity with decreasing temperature, and at low temperature the slope tends to zero. Many glasses, and all of the rare earth metaphosphate glasses previously studied, (Bridge and Patel 1987, Ilisavskii et al. 1989, Saunders et al. 1994, Senin et al. 1993a,b, 1994a,b, Farok et al. 1994) exhibit this anomalous trend of a continuous increase in velocity, with a progressively increasing slope, as the temperature is lowered below ~150K. The temperature dependence of the long wavelength modes is governed by a combination of three contributions (Phillips 1981, Ilisavskii et al. 1989, Tielbürger et al. 1992, Carini et al. 1994,1995a, Sidek et al. 1998): at high temperatures an anharmonic term, at low temperatures an interaction between the acoustic phonons and the two level system (TLS) (section 2.4.1) through a thermally activated structural relaxation mechanism,

(the existence of which is justified by the peak present in attenuation data, figure 9.3., 9.4), and phonon scattering from soft anharmonic localised vibrational modes, described by the soft potential model (section 2.4.2). The longitudinal and shear wave velocities in the three ternary samples, increase in the order $(La_2O_3)_{0.109}(Sm_2O_3)_{0.164}(P_2O_5)_{0.727}$, $(La_2O_3)_{0.055}(Sm_2O_3)_{0.206}(P_2O_5)_{0.739}$, $(La_2O_3)_{0.166}(Sm_2O_3)_{0.086}(P_2O_5)_{0.748}$. In binary metaphosphate glasses lanthanum has a greater longitudinal velocity than samarium (Carini et. al 1994); hence an increase in the acoustic wave velocities might be expected with the systematic increase of the lanthanum dopant. This trend is not apparent in the data. However Bridge and Patel (1987) noticed an alternative progression in inorganic phosphate glasses. They observed that in samples of $(MoO_3)_x(P_2O_5)_{1-x}$ reducing the phosphorus pentoxide content (increasing the doping oxide) produced a corresponding decrease in the velocity; this trend holds for the mixed ternary metaphosphate glasses.

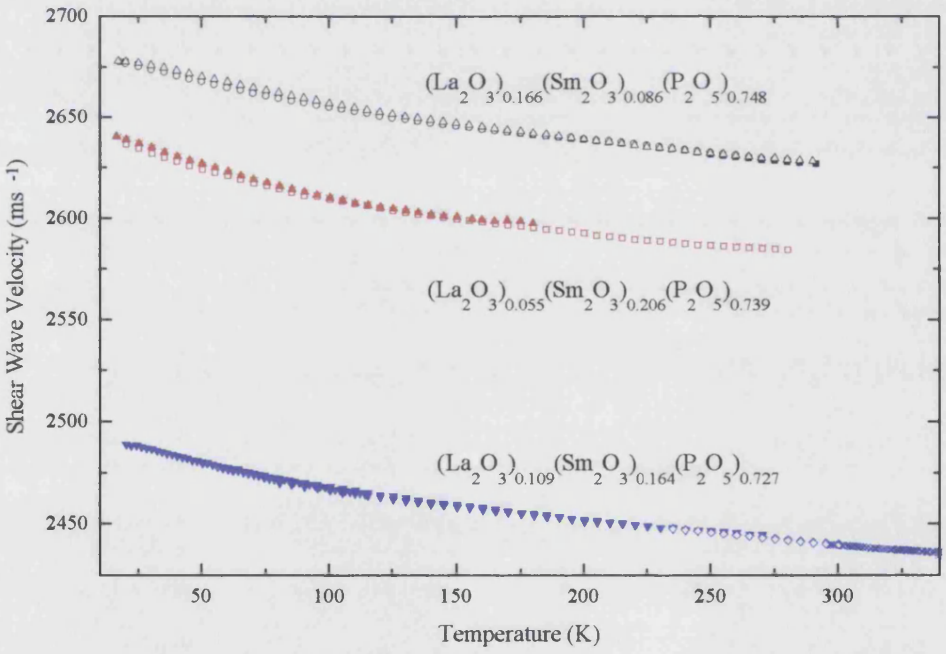


Figure 9.1. Temperature dependence of the velocities of shear 11MHz ultrasonic waves propagated in ternary samarium and lanthanum metaphosphate glasses. Different symbols refer to data obtained in different runs.

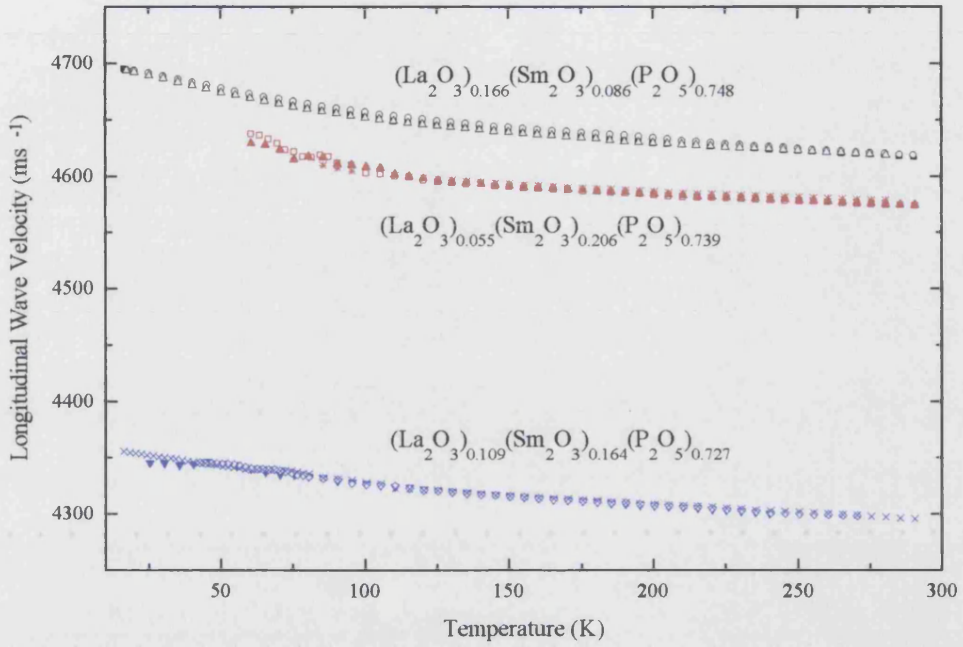


Figure 9.2. Temperature dependence of the velocities of longitudinal 11MHz ultrasonic waves propagated in ternary samarium and lanthanum metaphosphate glasses. Different symbols refer to data obtained in different runs.

The temperature dependence of the ultrasonic attenuation exhibits a broad peak centred at 75-100K; this feature is present for the three Sm-La samples and in both the longitudinal and shear modes. This peak is characteristic of many glasses and is believed to originate from the same mechanism which governs the low temperature acoustic velocity; thermally activated relaxation of localised structural defects (Anderson and Bömmel 1955, Carini et. al 1988, 1990, 1994, Tielbürger et al 1992, Senin 1994, Sidek et al 1998). As the ultrasonic wave passes through the sample it disturbs the thermal equilibrium. The relaxation process acts to restore this imbalance and can be pictured as a 'particle' moving in a double potential well between two configurations with minimum energy. Buchenau et al (1986, 1988) observed peaks in the neutron scattering spectra of vitreous $SiO_2$ which have been attributed to the same origin. They suggested the relaxation could physically be interpreted, and modelled, as the relative rotation of coupled $SiO_4$ tetrahedra through distances corresponding to approximately 0.5Å. By definition an amorphous material has topological disorder; hence the relaxation process will not be characterised by a single time $\tau$, but a

distribution of relaxation times. This has the effect of producing a peak width which is broader than that predicted by the Debye model. In the ternary metaphosphate glasses the shear mode exhibits greater attenuation than the longitudinal mode (figure 9.3), and increasing the driving frequency of the ultrasonic pulses also produces a larger attenuation (shown in figure 9.4); these characteristics appear to be typical of REMGs (Senin 1994, Carini et al 1990). In binary samarium metaphosphate glass, Carini et al. (1990, 1994) found that as the $Sm^{3+}$ ion content was increased, there was a corresponding small increase in the attenuation peak temperature, and a decrease in the peak height. Carini et al. (1990, 1994) suggested that an increase in the samarium concentration produces structural modification which probably reduces the number of relaxing particles. Examining the three ternary samples using the same criterion, that is peak position and peak height, the first characteristic is not resolvable for the shear mode within experimental error, but there seems to be a slight peak shift to higher temperatures, with increasing samarium content, in the longitudinal mode. There is no evidence to support the second trend in the REMGs samples studied. As the temperature tends to 300K the attenuation increases; however in the temperature interval studied it is ambiguous as to whether this is due to structural changes in the glass sample, or a consequence of the bonding material freezing.

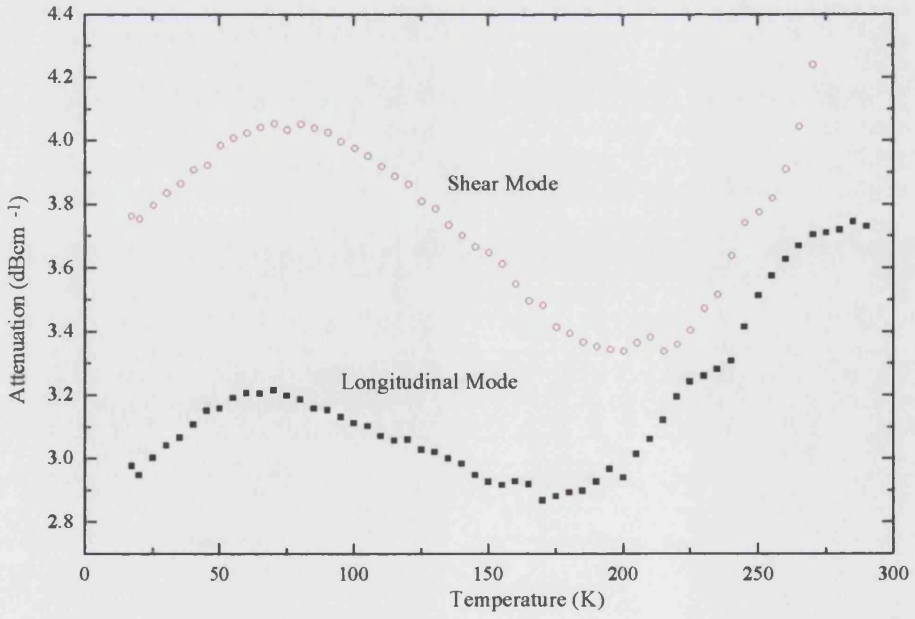


Figure 9.3. Temperature dependence of the attenuation of the longitudinal and shear 11MHz ultrasonic waves propagated in the $(La_2O_3)_{0.166}(Sm_2O_3)_{0.086}(P_2O_5)_{0.748}$ glass.

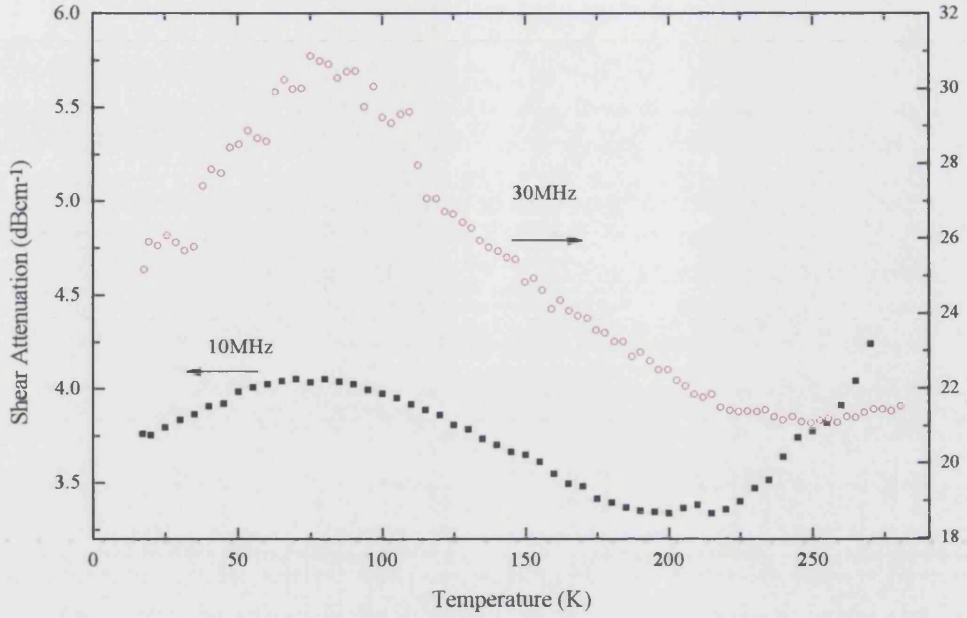


Figure 9.4. Temperature dependence of the shear ultrasonic wave attenuation propagated in the $(La_2O_3)_{0.166}(Sm_2O_3)_{0.086}(P_2O_5)_{0.748}$ glass at 11MHz and 30MHz.

## 9.2. HYDROSTATIC PRESSURE DEPENDENCE OF THE ULTRASONIC WAVE VELOCITIES AS A FUNCTION OF TEMPERATURE

The effects of pressure on the longitudinal and shear ultrasonic waves have been investigated in the three ternary samples, $(La_2O_3)_{0.166}(Sm_2O_3)_{0.086}(P_2O_5)_{0.748}$, $(La_2O_3)_{0.109}(Sm_2O_3)_{0.164}(P_2O_5)_{0.727}$, $(La_2O_3)_{0.055}(Sm_2O_3)_{0.206}(P_2O_5)_{0.739}$, and binary lanthanum $(La_2O_3)_{0.225}(P_2O_5)_{0.775}$ glass. The lanthanum glass data has been measured as a natural extreme of the ternary lanthanum samarium metaphosphate glass series (the hydrostatic pressure dependence of the ultrasonic velocities for lanthanum metaphosphate glass at 293K has previously been reported in the literature (Sidek et al. 1988, Senin et al. 1994b); however there is no data available at any other temperature). The other extremity is binary glass containing samarium; its behaviour as a function of pressure and temperature is already well documented, and hence has not been re-measured here (Mierzejewski et al. 1988a,b, Sidek et al. 1988, Wang et al. 1990, Carini et al. 1990, Senin et al. 1993a, 1994b). In addition the hydrostatic pressure dependence of the longitudinal and shear modes of cerium metaphosphate glass, $(Ce_2O_3)_{0.235}(P_2O_5)_{0.765}$, has been measured. For each sample the first table (9.1,

9.5, 9.8, 9.11 and 9.15) records the temperature dependence of the natural velocity ($W_L$ and $W_S$), the adiabatic second order elastic stiffness constants ($C_{11}$ and $C_{44}$) and bulk modulus ($B^S$). In tables 9.2, 9.6, 9.9, 9.12 and 9.16 the temperature dependence of the pressure derivatives ($\partial W_L/\partial P$, $\partial W_S/\partial P$, $\partial C_{11}/\partial P$, $\partial C_{44}/\partial P$ and $\partial B/\partial P$) are summarised. Finally the Grüneisen parameters ($\gamma_L$, $\gamma_S$ and $\gamma^{el}$), Youngs modulus (E) and Poissons ratio ($\sigma$) are tabulated (table 9.3, 9.7, 9.10, 9.13 and 9.17). The precision with which the second order elastic constants, and subsequent hydrostatic pressure derivatives, can be determined depends on the accuracy of the density, sample dimensions, pressure and overlap frequency measurements. The errors were calculated using the general error formula $E^2(y) = \left(\frac{\partial y}{\partial a}\right)^2 E^2(a) + \left(\frac{\partial y}{\partial b}\right)^2 E^2(b) + \ldots$

where y = f(a,b,..) is a function of a, b, and a, b are the measured quantities with an associated error *E*. The estimated error in the density is ± 10Kgm$^{-3}$, in the path length ± 0.001mm, the frequency ±0.3% (although the frequency equipment can measure the relative change in the overlap frequency to 1 part in $10^5$, a larger error is incurred measuring the absolute frequency due to distortion of the echo train with the worst case scenario being a one cycle miss match), the error in the pressure is difficult to estimate as it changes with applied pressure and temperature. However the errors in the hydrostatic pressure derivative of the normalised natural velocity $\partial(W_x/W_{x0}-1)/\partial P$ are of more use in calculating the errors in the pressure dependences of the SOEC and the Grüneisen parameters; the normalised natural velocity has been calculated directly from the data by fitting a least squares line to the measured results (figure 9.7): for lanthanum metaphosphate glass $\partial(W_L/W_{L0}-1)/\partial P$ = 0.0132 ± 0.0002 and $\partial(W_S/W_{S0}-1)/\partial P$ = -0.0019 ± 0.0001. The errors in $\partial W_x/\partial P$ have also been extracted using a method of linear regression (figure 9.5-9.6). The following errors have been calculated specifically for the lanthanum $(La_2O_3)_{0.225}(P_2O_5)_{0.775}$ glass sample at room temperature; however they are typical of the errors occurring in all the rare earth metaphosphate glass samples measured: $W_L$ ± 13.69ms$^{-1}$, $W_S$ ± 7.76ms$^{-1}$, $\partial W_L/\partial P$ ± 0.96ms$^{-1}$GPa$^{-1}$, $\partial W_S/\partial P$ ± 0.23ms$^{-1}$GPa$^{-1}$, $C_{11}$ ± 0.45GPa, $C_{44}$ ± 0.14GPa, $B^S$ ± 0.45GPa, E ±0.28, $\sigma$ ±0.02, $\partial C_{11}/\partial P$ ± 0.03, $\partial C_{44}/\partial P$ ± 0.003, $\partial B/\partial P$ ± 0.03, $\gamma_L$ ± 0.01, $\gamma_S$ ± 0.003, $\gamma^{el}$ ± 0.004.

For all the samples the scatter in the shear wave velocity is negligible compared with that for the longitudinal mode; hence it would seem that the scatter in the longitudinal mode velocity is a consequence of volume effects. Acet et al. (1998) suggested that the source of the scatter in the longitudinal mode velocity for the ternary samples may be a result of the different signs of the pressure responses of the $La^{3+}$ and $Sm^{3+}$ glasses, as observed in the binary samples (Sidek et al. 1988), affecting the local environment in contrasting ways. In all the samples, and for both modes, the data is reproducible upon cycling between atmospheric pressure and 0.15GPa, and show no measurable hysterysis effects.

### 9.2.1. BINARY LANTHANUM AND TERNARY LANTHANUM SAMARIUM METAPHOSPHATE GLASSES

1) Data for the sample $(La_2O_3)_{0.225}(P_2O_5)_{0.775}$ glass; $\rho = 3199 \pm 10$ Kgm$^{-3}$ $l_o = 7.600 \pm 0.001$mm, figures. 9.5. - 9.6, tables 9.1-9.3.

The experimental data for the longitudinal and shear mode natural velocities as a function of hydrostatic pressure and temperature, between room temperature and 373K, are plotted in figures 9.5 and 9.6 respectively. The natural wave velocity, at atmospheric pressure, of the longitudinal ($W_{L0}$) and shear mode ($W_{S0}$) decreases as the temperature is increased. The longitudinal ultrasonic wave velocity increases with increasing pressure ($(\partial W_L/\partial P)$ is positive), and each data set can be fitted with a single positive linear regression line (figure 9.6., table 9.1). This represents normal behaviour: the long wavelength acoustic modes stiffen under pressure. The shear mode data at the various temperatures has a negative gradient and at some temperatures (303-343K inclusive) exhibits two distinct regions, which have been fitted with two lines of differing gradients (figure 9.5, table 9.1). The fits to the data have been calculated using a method of least squares fit; these are displayed as the straight red lines on figure 9.5. These disparate gradients have been distinguished by labelling them as the low pressure (LP) or high pressure (HP) results. The low pressure region has a steeper gradient than the high pressure slope. As the temperature is increased the transition between the LP and HP regions occurs at a higher pressure $P_C$ (approximately a linear dependence, see the insert in figure 9.5) until the limiting case at 353K when the transition occurs outside the 0.15GPa range; the 353-373K data resembles the lines defined by the 'LP' low pressure label, better

than the high pressure 'HP' fit. At the highest temperatures (353-373K inclusive) the shear mode data have a anomalous beginning (up to 0.06GPa), these data however are reproducible upon cycling the pressure. It is believed that this characteristic is an artificial manifestation due to the properties of the bond at elevated temperatures, and hence these results have been ignored in the following data analysis. The negative effect of the lanthanum metaphosphate glass shear mode is very small when compared to the similar trend seen in samarium metaphosphate glass, see figure 9.7 (Sidek et al. 1988). The second order elastic stiffness constants (SOEC) and bulk modulus decrease as a function of increasing temperature; these changes however are also very small approximately 1% from room temperature to 373K. The pressure derivative of the longitudinal SOEC ($\partial C_{11}/\partial P$) is positive, and increases with temperature. When calculating ($\partial C_{11}/\partial P$), the low pressure value of the bulk modulus (which depends on both $C_{11}$ and $C_{44}$) has been used, see equation 8.26. This assumption is allowed as the change in the bulk modulus with temperature and pressure is very small; hence it produces negligible error in the correction term ($1/3B^3$). The LP and HP values are identical within experimental error (this argument is used in the data analysis of the subsequent samples where one of the modes has a natural velocity comprising of two gradients). The low pressure derivative ($\partial C_{44}/\partial P$) of $C_{44}$ is negative and increases with temperature; the high pressure dependence is positive and fluctuates about a mean value of approximately 0.15. The temperature dependence of $\partial W_S/\partial P$ (HP) and $\partial B^S/\partial P$ (HP) also oscillate about a mean value, whereas $\partial W_S/\partial P$ (LP), and $\partial B^S/\partial P$ (LP), increase with temperature in the range 313 -373K. The long wavelength Grüneisen parameters quantify the vibrational anhamonicity of a real material. The longitudinal Grüneisen parameter is positive and increases steadily with temperature. The shear Grüneisen parameters are all negative; this is synonymous with the anomalous trend of long wavelength acoustic mode softening; the sample becomes easier to squeeze with pressure. The low pressure region Grüneisen parameters increase with temperature from 313K, and the HP results are independent of temperature and fluctuate about a mean value. This pattern is perpetuated in the mean Grüneisen parameter. A negative Grüneisen parameters means that the application of pressure on the sample decreases the frequencies of the long wavelength acoustic modes, and the energies associated with these modes. The Youngs modulus and Poissons ratio decrease with temperature.

| Temp (K) | LP or HP | $W_{L0}$ ($ms^{-1}$) | $W_{S0}$ ($ms^{-1}$) | $C_{11}$ (GPa) | $C_{44}$ (GPa) | $B^S$ (GPa) |
|---|---|---|---|---|---|---|
| RT | N/A | 4570.1 | 2560.7 | 66.8 | 22.5 | 36.8 |
| 303 | LP | 4568.7 | 2650.4 | 66.8 | 22.5 | 36.8 |
| | HP | | 2649.2 | | 22.5 | 36.8 |
| 313 | LP | 4565.1 | 2650.7 | 66.7 | 22.5 | 36.7 |
| | HP | | 2647.8 | | 22.4 | 36.8 |
| 323 | LP | 4563.0 | 2649.3 | 66.6 | 22.5 | 36.7 |
| | HP | | 2645.6 | | 22.4 | 36.8 |
| 333 | LP | 4560.3 | 2648.9 | 66.5 | 22.4 | 36.6 |
| | HP | | 2644.7 | | 22.4 | 36.7 |
| 343 | LP | 4555.6 | 2646.07 | 66.4 | 22.4 | 36.5 |
| | HP | | 2640.8 | | 22.3 | 36.6 |
| 353 | N/A | 4550.8 | 2644.2 | 66.3 | 22.4 | 36.4 |
| 363 | N/A | 4546.4 | 2641.9 | 66.1 | 22.3 | 36.4 |
| 373 | N/A | 4544.8 | 2640.2 | 66.1 | 22.3 | 36.3 |

Table 9.1. The temperature dependences of natural velocity and elastic moduli for $(La_2O_3)_{0.225}(P_2O_5)_{0.775}$ glass.

| Temp (K) | LP or HP | $\partial W_L/\partial P$ ($ms^{-1}GPa$) | $\partial W_S/\partial P$ ($ms^{-1}GPa$) | $\partial C_{11}/\partial P$ | $\partial C_{44}/\partial P$ | $\partial B^S/\partial P$ |
|---|---|---|---|---|---|---|
| RT | N/A | 60.1 | -5.1 | 2.36 | 0.12 | 2.20 |
| 303 | LP | 61.5 | -39.9 | 2.40 | -0.47 | 3.03 |
| | HP | | -4.3 | | 0.13 | 2.23 |
| 313 | LP | 69.7 | -65.4 | 2.64 | -0.90 | 3.85 |
| | HP | | -6.0 | | 0.10 | 2.50 |
| 323 | LP | 70.5 | -53.1 | 2.66 | -0.70 | 3.59 |
| | HP | | -2.3 | | 0.16 | 2.45 |
| 333 | LP | 78.2 | -51.9 | 2.89 | -0.67 | 3.79 |
| | HP | | -7.5 | | 0.08 | 2.78 |
| 343 | LP | 107.8 | -50.5 | 3.75 | -0.65 | 4.61 |
| | HP | | 1.1 | | 0.22 | 3.45 |
| 353 | N/A | 133.9 | -40.1 | 4.51 | -0.47 | 5.13 |
| 363 | N/A | 146.1 | -33.2 | 4.85 | -0.36 | 5.33 |
| 373 | N/A | 142.0 | -26.1 | 4.73 | -0.23 | 5.05 |

Table 9.2. The temperature dependences of the pressure derivatives for $(La_2O_3)_{0.225}$ $(P_2O_5)_{0.775}$ glass

| Temp (K) | LP or HP | $\gamma_L$ | $\gamma_S$ | $\gamma^{el}$ | E (GPa) | $\sigma$ (GPa) |
|---|---|---|---|---|---|---|
| RT | N/A | 0.48 | -0.07 | 0.11 | 56.03 | 0.246 |
| 303 | LP | 0.50 | -0.55 | -0.20 | 56.02 | 0.247 |
| | HP | | -0.06 | 0.13 | 55.98 | 0.247 |
| 313 | LP | 0.56 | -0.90 | -0.42 | 56.00 | 0.246 |
| | HP | | -0.08 | 0.13 | 55.91 | 0.247 |
| 323 | LP | 0.57 | -0.73 | -0.30 | 55.94 | 0.246 |
| | HP | | -0.03 | 0.17 | 55.83 | 0.247 |
| 333 | LP | 0.63 | -0.72 | -0.27 | 55.91 | 0.245 |
| | HP | | -0.10 | 0.14 | 55.79 | 0.247 |
| 343 | LP | 0.86 | -0.70 | -0.18 | 55.81 | 0.245 |
| | HP | | 0.02 | 0.30 | 55.64 | 0.247 |
| 353 | N/A | 1.07 | -0.55 | -0.01 | 55.70 | 0.245 |
| 363 | N/A | 1.17 | -0.46 | 0.08 | 55.60 | 0.245 |
| 373 | N/A | 1.14 | -0.36 | 0.14 | 55.54 | 0.245 |

Table 9.3. The temperature dependence of the Grüneisen parameters, Youngs modulus, and Poison's ratio for $(La_2O_3)_{0.225}(P_2O_5)_{0.775}$ glass.

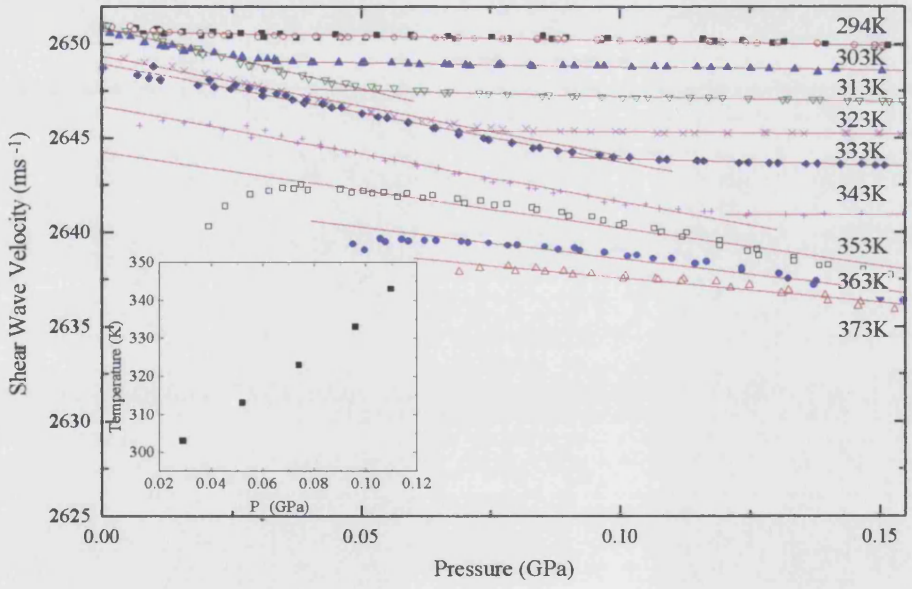


Figure 9.5. Hydrostatic pressure dependence of the velocity of the 11MHz shear ultrasonic wave in $(La_2O_3)_{0.225}(P_2O_5)_{0.775}$ glass at selected temperatures. The insert shows the variation with temperature of the pressure $P_c$ at which there is a change in $\partial W_S/\partial P$.

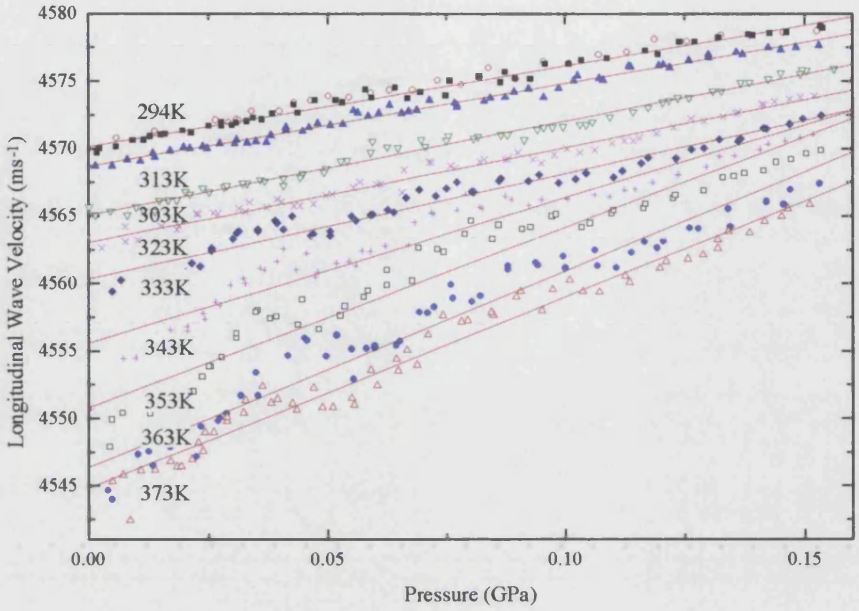


Figure 9.6. Hydrostatic pressure dependence of the velocity of the 11MHz longitudinal ultrasonic wave in $(La_2O_3)_{0.225}(P_2O_5)_{0.775}$ glass at selected temperatures, shown on the graph.

The room temperature ultrasonic data from $(La_2O_3)_{0.225}(P_2O_5)_{0.775}$ is compared with the results for two lanthanum metaphosphate glass samples, $(La_2O_3)_{0.222}(P_2O_5)_{0.778}$ and $(La_2O_3)_{0.263}(P_2O_5)_{0.737}$, previously investigated by Senin et al. (1994b) in table 9.4. The hydrostatic pressure dependence of the shear and longitudinal acoustic mode natural velocity, also at room temperature, are plotted in figure 9.7 with samarium $(Sm_2O_3)_{0.212}$ $(P_2O_5)_{0.788}$ and lanthanum $(La_2O_3)_{0.263}(P_2O_5)_{0.736}$ metaphosphate glasses (Sidek et. al 1988, Senin et al.1994b).

| Sample | $(La_2O_3)_{0.222}$ $(P_2O_5)_{0.778}$ | $(La_2O_3)_{0.225}$ $(P_2O_5)_{0.775}$ | $(La_2O_3)_{0.263}$ $(P_2O_5)_{0.737}$ |
|---|---|---|---|
| $W_{L0}$ | 4428 | 4570 | 4451 |
| $W_{S0}$ | 2491 | 2561 | 2599 |
| $C_{11}$ (GPa) | 65.9 | 66.8 | 67.6 |
| $C_{44}$ (GPa) | 20.8 | 22.5 | 23.1 |
| $B^S$ (GPa) | 38.2 | 36.8 | 36.9 |
| $E^S$ (GPa) | 52.7 | 56.0 | 57.2 |
| $\sigma^S$ | 0.270 | 0.246 | 0.241 |
| $(\partial C_{11}/\partial P)_{P=0}$ | 2.19 | 2.36 | 3.56 |
| $(\partial C_{44}/\partial P)_{P=0}$ | 0.11 | 0.12 | 0.13 |
| $(\partial B^S/\partial P)_{P=0}$ | 2.04 | 2.20 | 3.39 |
| $\gamma_L$ | 0.47 | 0.48 | 0.80 |
| $\gamma_S$ | -0.06 | -0.07 | -0.06 |
| $\gamma^{el}$ | 0.11 | 0.11 | 0.23 |

Table 9.4. The room temperature ultrasonic data for the sample $(La_2O_3)_{0.225}$ $(P_2O_5)_{0.775}$ glass compared with those for two lanthanum binary samples measured by Senin et. al. (1994b); the data is presented in order of increasing lanthanum oxide content.

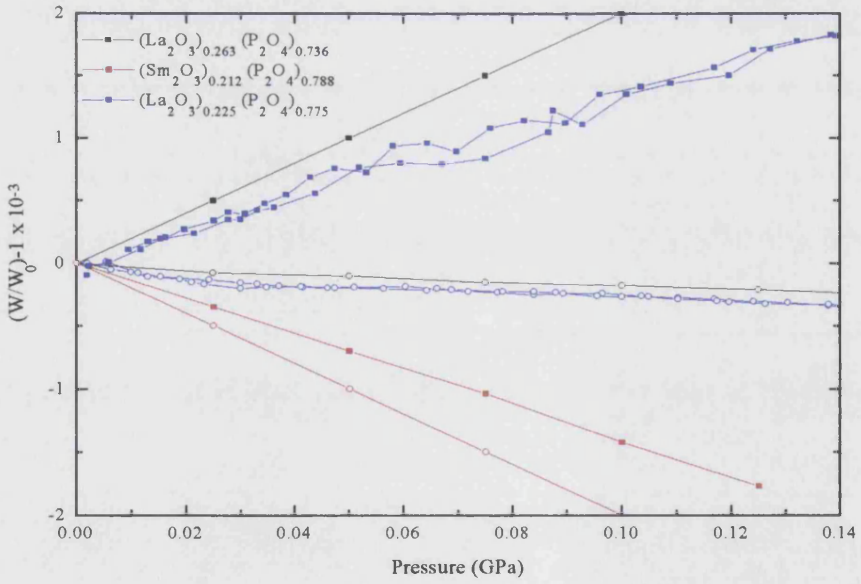


Figure 9.7. Hydrostatic pressure dependence of the relative change in the natural wave velocities of lanthanum metaphosphate glass $(La_2O_3)_{0.225}(P_2O_5)_{0.775}$ glass compared with the least squares fit lines for binary metaphosphate glasses modified with samarium and lanthanum ions as measured by Sidek et al (1988) (The squares are the longitudinal data sets and the circles are the shear modes).

Both the tabulated and plotted data are in good agreement with the previously recorded lanthanum glass results, any differences may attributed to the varying amount of $La^{3+}$ dopant in the sample. In table 9.4 the room temperature second order elastic constants, their pressure derivatives and Grüneisen parameters increase with increasing lanthanum oxide content, with the exception of the shear Grüneisen parameter which remains constant, Poisons ratio which reduces with more $La^{3+}$ ions, and the bulk modulus.

2) Data for the sample $(La_2O_3)_{0.166}(Sm_2O_3)_{0.086}(P_2O_5)_{0.748}$ glass; $\rho = 3569 \pm 10$ Kgm$^{-3}$ $l_o = 7.006 \pm 0.001$mm, figures. 9.8. - 9.9, tables 9.5-9.7.

The longitudinal ultrasonic wave velocity increases with applied pressure; the $(La_2O_3)_{0.166}(Sm_2O_3)_{0.086}(P_2O_5)_{0.748}$ sample exhibits normal behaviour and the results can be fitted with a single least squares line, see figure 9.9. The natural velocity of the shear mode shows slight long wavelength acoustic mode softening with pressure, $\partial W_S/\partial P$ is negative. The evolution of the shear mode velocity with temperature is shown in figure 9.8. The majority of shear velocity versus. pressure graphs have been fitted with a single gradient, the exceptions are the shear runs taken at 323 and 333K, where two separate straight lines with different gradients (both still negative) are needed to characterise the shape of the slope (figure 9.8.). The notation LP/HP addresses this problem, and results in the tables are labelled accordingly where necessary. The hydrostatic pressure derivatives of the bulk modulus and $C_{11}$ ($\partial C_{11}/\partial P$, $\partial B/\partial P$) are positive and slightly increasing, and $\partial C_{44}/\partial P$ is negative and approximately constant (table 9.6). The longitudinal Grüneisen parameters are positive; the shear mode Grüneisen parameters are negative and the mean acoustic mode Grüneisen parameters are slightly negative, but almost zero (Table 9.7). The acoustic mode Grüneisen parameters are very small and change only slightly with temperature in the range 290-375K

| Temp (K) | LP or HP | $W_{L0}$ ($ms^{-1}$) | $W_{S0}$ ($ms^{-1}$) | $C_{11}$ (GPa) | $C_{44}$ (GPa) | $B^S$ (GPa) |
|---|---|---|---|---|---|---|
| RT/298K | N/A | 4619.66 | 2625.93 | 76.17 | 24.61 | 43.35 |
| 313.6 | N/A | 4617.04 | 2623.66 | 76.08 | 24.57 | 43.32 |
| 323.7 | LP | 4615.33 | 2623.38 | 76.02 | 24.56 | 43.28 |
| | HP | | 2622.45 | | 24.55 | 43.30 |
| 333.9 | LP | 4614.09 | 2621.91 | 75.98 | 24.54 | 43.27 |
| | HP | | 2621.37 | | 24.53 | 43.28 |
| 344.0 | N/A | 4612.27 | 2620.56 | 75.92 | 24.51 | 43.24 |
| 354.3 | N/A | 4609.42 | 2619.15 | 75.83 | 24.48 | 43.19 |
| 364.4 | N/A | 4606.53 | 2617.71 | 75.74 | 24.46 | 43.13 |
| 374.6 | N/A | 4606.14 | 2616.16 | 75.72 | 24.43 | 43.15 |

Table 9.5. The temperature dependences of the natural velocity and the elastic moduli for $(La_2O_3)_{0.166}(Sm_2O_3)_{0.086}(P_2O_5)_{0.748}$ glass.

| Temp (K) | LP or HP | $\partial W_L/\partial P$ | $\partial W_S/\partial P$ | $\partial C_{11}/\partial P$ | $\partial C_{44}/\partial P$ | $\partial B/\partial P$ |
|---|---|---|---|---|---|---|
| RT/298 | N/A | 37.350 | -10.802 | 1.817 | -0.013 | 1.835 |
| 313.6 | N/A | 36.060 | -11.484 | 1.774 | -0.026 | 1.809 |
| 323.7 | LP | 40.330 | -32.282 | 1.914 | -0.415 | 2.468 |
| | HP | | -12.479 | | -0.045 | 1.973 |
| 333.9 | LP | 42.530 | -18.733 | 1.986 | -0.162 | 2.202 |
| | HP | | -12.893 | | -0.052 | 2.055 |
| 344.0 | N/A | 39.057 | -16.047 | 1.871 | -0.111 | 2.019 |
| 357.3 | N/A | 50.409 | -15.187 | 2.244 | -0.095 | 2.370 |
| 364.4 | N/A | 56.584 | -13.030 | 2.446 | -0.054 | 2.518 |
| 374.6 | N/A | 48.355 | -11.492 | 2.175 | -0.026 | 2.209 |

Table 9.6. The temperature dependences of the pressure derivatives for $(La_2O_3)_{0.166}$ $(Sm_2O_3)_{0.086}(P_2O_5)_{0.748}$ glass.

| Temp (K) | LP or HP | $\gamma_L$ | $\gamma_S$ | $\gamma^{el}$ | E (GPa) | $\sigma$ (GPa) |
|---|---|---|---|---|---|---|
| RT/298 | N/A | 0.351 | -0.178 | -0.002 | 62.083 | 0.261 |
| 313.6 | N/A | 0.338 | -0.190 | -0.014 | 61.986 | 0.262 |
| 323.7 | LP | 0.378 | -0.533 | -0.229 | 61.964 | 0.261 |
| | HP | | -0.206 | -0.011 | 61.932 | 0.262 |
| 333.9 | LP | 0.399 | -0.309 | -0.073 | 61.904 | 0.262 |
| | HP | | -0.213 | -0.009 | 61.886 | 0.262 |
| 344.0 | N/A | 0.366 | -0.265 | -0.054 | 61.845 | 0.262 |
| 354.3 | N/A | 0.472 | -0.250 | -0.010 | 61.775 | 0.262 |
| 364.4 | N/A | 0.530 | -0.215 | 0.033 | 61.705 | 0.262 |
| 374.6 | N/A | 0.453 | -0.189 | 0.025 | 61.649 | 0.262 |

Table 9.7. The temperature dependence of the Grüneisen parameters, Youngs modulus and Poissons ratio for $(La_2O_3)_{0.166}(Sm_2O_3)_{0.086}(P_2O_5)_{0.748}$ glass.

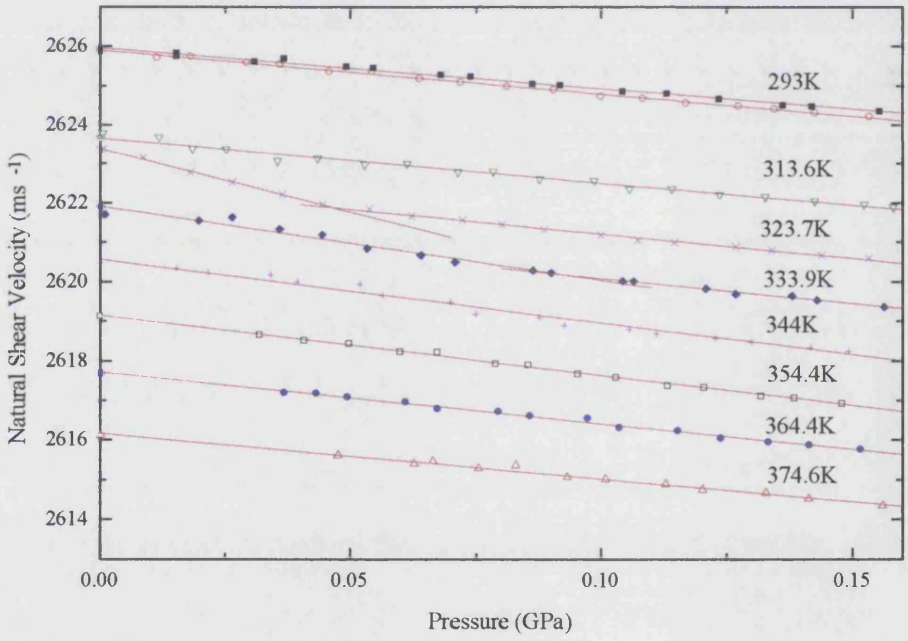


Figure 9.8. Hydrostatic pressure dependence of the velocity of the 11MHz shear ultrasonic wave in $(La_2O_3)_{0.166}(Sm_2O_3)_{0.086}(P_2O_5)_{0.748}$ glass at selected temperatures.

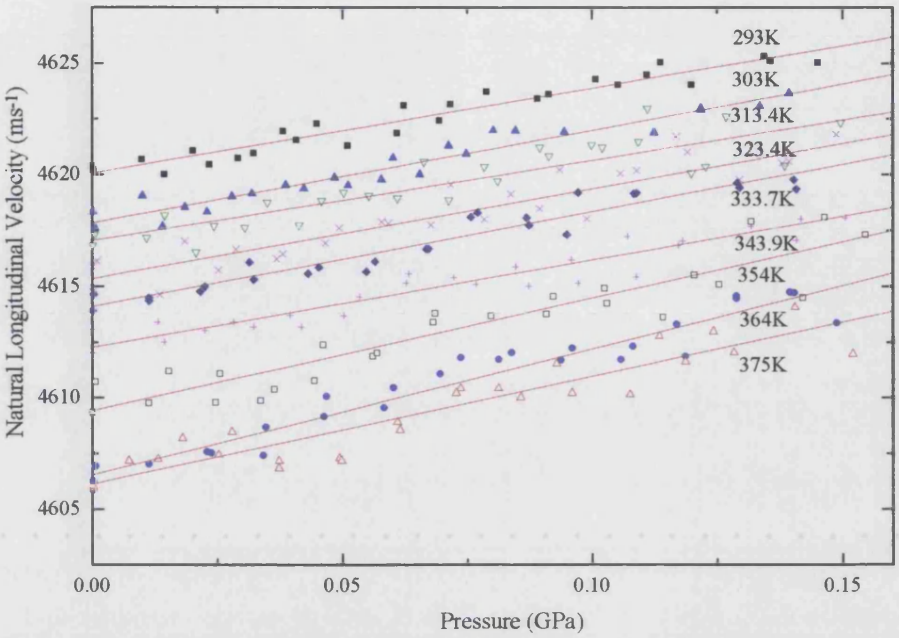


Figure 9.9. Hydrostatic pressure dependence of the velocity of the 11MHz longitudinal ultrasonic wave in $(La_2O_3)_{0.166}(Sm_2O_3)_{0.086}(P_2O_5)_{0.748}$ glass at selected temperatures.

3) Data for the sample $(La_2O_3)_{0.109}(Sm_2O_3)_{0.164}(P_2O_5)_{0.727}$ glass; $\rho = 3631 \pm 10$ Kgm$^{-3}$ $l_o = 5.296 \pm 0.001$mm. figures. 9.10 - 9.11, tables 9.8-9.10.

The ternary lanthanum samarium metaphosphate glass of composition $(La_2O_3)_{0.109}$ $(Sm_2O_3)_{0.164}(P_2O_5)_{0.727}$ exhibits normal long wavelength longitudinal acoustic mode stiffening when increasing pressure is applied (figures. 9.11). All the natural longitudinal velocity data has been fitted with a single least squares line. The shear mode velocity decreases as function of pressure and temperature; the sample shows the familiar acoustic mode softening, present in the shear mode of all three ternary glasses (figure 9.10). Once again two regions (LP/HP) need to be defined to completely characterise the behaviour of the velocity against pressure graphs. The natural shear velocity exhibits a marked change in the value of the pressure gradient at a pressure Pc, the position of which increases approximately linearly with increasing temperature, see figure 9.10, and hence provides some justification that the gradient change is a real trait such as a transition, and not some experimental manifestation. The magnitude of the gradient is smaller in the high pressure region; this seems to

suggest that the mechanism, which produces shear acoustic mode softening, diminishes at higher pressures. The hydrostatic pressure derivative $\partial B/\partial P$ of bulk modulus, and that $\partial C_{11}/\partial P$ of the longitudinal SOEC are positive and have slightly increasing values with temperature; $\partial C_{44}/\partial P$ fluctuates about zero over the temperature range investigated (table 9.9). The longitudinal Grüneisen parameter is positive and rises with temperature; the shear mode Grüneisen parameter is negative and decreasing and the mean acoustic mode Grüneisen parameter is practically zero (table 9.10).

| Temp (K) | LP or HP | $W_{L0}$ ($ms^{-1}$) | $W_{S0}$ ($ms^{-1}$) | $C_{11}$ (GPa) | $C_{44}$ (GPa) | $B^S$ (GPa) |
|---|---|---|---|---|---|---|
| RT/296 | N/A | 4292.89 | 2439.44 | 66.92 | 21.61 | 38.11 |
| 303.0 | LP | 4293.81 | 2438.61 | 66.94 | 21.59 | 38.15 |
| | HP | | 2438.33 | | 21.59 | 38.16 |
| 313.0 | LP | 4292.35 | 2437.28 | 66.90 | 21.57 | 38.14 |
| | HP | | 2436.88 | | 21.56 | 38.15 |
| 323.0 | LP | 4293.05 | 2436.50 | 66.92 | 21.56 | 38.18 |
| | HP | | 2435.22 | | 21.53 | 38.21 |
| 333.0 | LP | 4290.86 | 2435.93 | 66.85 | 21.55 | 38.13 |
| | HP | | 2433.99 | | 21.51 | 38.17 |
| 343.0 | LP | 4288.24 | 2435.31 | 66.77 | 21.53 | 38.06 |
| | HP | | 2433.31 | | 21.50 | 38.11 |

Table 9.8. The temperature dependences of the natural velocity and elastic moduli for $(La_2O_3)_{0.109}(Sm_2O_3)_{0.164}(P_2O_5)_{0.727}$ glass.

| Temp (K) | LP or HP | $\partial W_L/\partial P$ | $\partial W_S/\partial P$ | $\partial C_{11}/\partial P$ | $\partial C_{44}/\partial P$ | $\partial B/\partial P$ |
|---|---|---|---|---|---|---|
| RT/296 | N/A | 43.839 | -6.482 | 1.952 | 0.074 | 1.853 |
| 303.0 | LP | 49.713 | -13.927 | 2.135 | -0.058 | 2.212 |
| | HP | | -5.169 | | 0.097 | 2.006 |
| 313.0 | LP | 45.356 | -13.511 | 1.998 | -0.051 | 2.066 |
| | HP | | -4.461 | | 0.109 | 1.852 |
| 323.0 | LP | 43.578 | -24.481 | 1.924 | -0.245 | 2.269 |
| | HP | | -3.360 | | 0.128 | 1.771 |
| 333.0 | LP | 49.698 | -26.256 | 2.132 | -0.283 | 2.511 |
| | HP | | -3.659 | | 0.123 | 1.968 |
| 343.0 | LP | 57.035 | -28.5201 | 2.361 | -0.316 | 2.782 |
| | HP | | -6.423 | | 0.075 | 2.261 |

Table 9.9. The temperature dependences of the pressure derivatives for $(La_2O_3)_{0.109}(Sm_2O_3)_{0.164}(P_2O_5)_{0.727}$ glass.

| Temp (K) | LP or HP | $\gamma_L$ | $\gamma_S$ | $\gamma^{el}$ | E (GPa) | $\sigma$ (GPa) |
|---|---|---|---|---|---|---|
| RT/296 | N/A | 0.389 | -0.101 | 0.062 | 54.618 | 0.262 |
| 303.0 | LP | 0.442 | -0.218 | 0.002 | 54.498 | 0.262 |
| | HP | | -0.081 | 0.093 | 54.489 | 0.262 |
| 313.0 | LP | 0.403 | -0.211 | -0.006 | 54.445 | 0.262 |
| | HP | | -0.067 | 0.088 | 54.431 | 0.262 |
| 323.0 | LP | 0.388 | -0.384 | -0.127 | 54.424 | 0.262 |
| | HP | | -0.053 | 0.094 | 54.382 | 0.263 |
| 333.0 | LP | 0.442 | -0.417 | -0.131 | 54.391 | 0.262 |
| | HP | | -0.057 | 0.109 | 54.328 | 0.263 |
| 343.0 | LP | 0.506 | -0.446 | -0.128 | 54.352 | 0.262 |
| | HP | | -0.101 | 0.102 | 54.281 | 0.263 |

Table 9.10. The temperature dependences of the Grüneisen parameters, Youngs modulus and Poissons ratio for $(La_2O_3)_{0.109}(Sm_2O_3)_{0.164}(P_2O_5)_{0.727}$ glass.

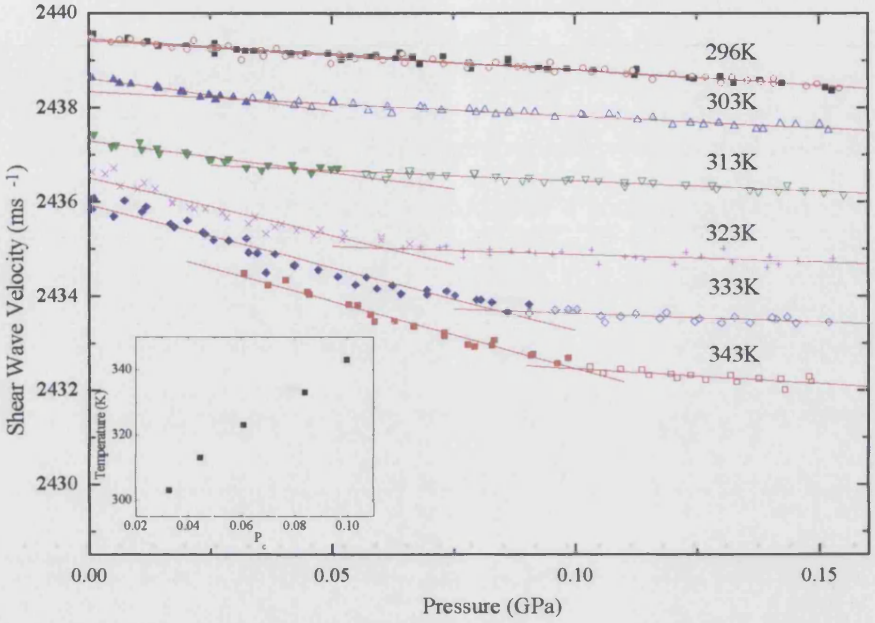


Figure 9.10. Hydrostatic pressure dependence of the velocity of the 11MHz shear ultrasonic wave in $(La_2O_3)_{0.109}(Sm_2O_3)_{0.164}(P_2O_5)_{0.727}$ glass at selected temperatures. The insert shows the variation with temperature of the pressure $P_c$ at which there is a change in $\partial W_S/\partial P$.

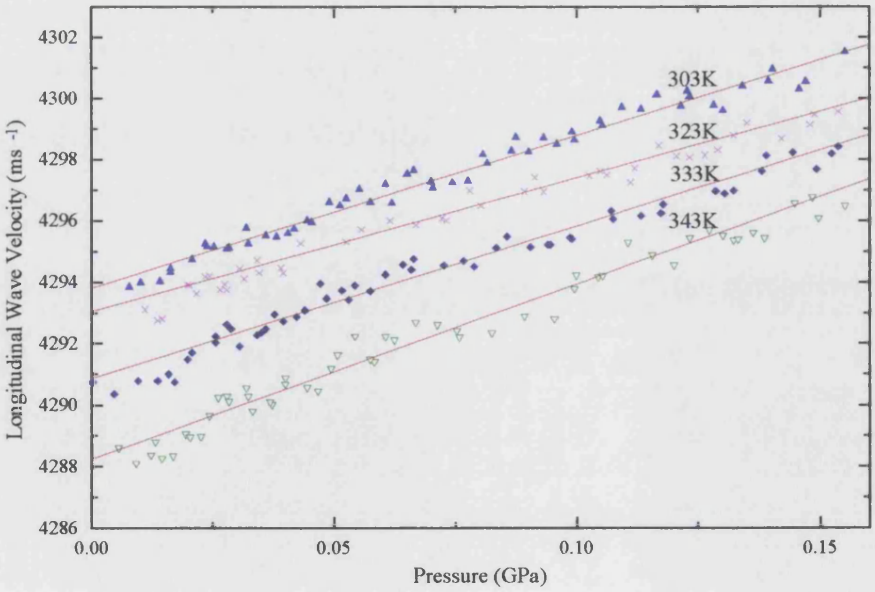


Figure 9.11. Hydrostatic pressure dependence of the velocity of the 11MHz longitudinal ultrasonic wave in $(La_2O_3)_{0.109}(Sm_2O_3)_{0.164}(P_2O_5)_{0.727}$ glass at selected temperatures.

4) Data for the sample $(La_2O_3)_{0.055}(Sm_2O_3)_{0.206}(P_2O_5)_{0.739}$ glass; $\rho = 3505 \pm 10$ Kgm$^{-3}$ $l_o = 7.416 \pm 0.001$mm, figures 9.12 - 9.13, table 9.11-9.13.

For the shear mode the $(La_2O_3)_{0.055}(Sm_2O_3)_{0.206}(P_2O_5)_{0.739}$ glass shows the same trait as the two previous ternary metaphosphate glasses: a decrease in the natural velocity with pressure (long wavelength acoustic shear mode softening). It can be seen from graph 9.12 that the majority of the shear results can be fitted with a single line. At higher temperatures (353, 363, 373K) and low pressures, a secondary line could be fitted, however these data points were ignored, as the large attenuation present in this region makes the data unreliable. The most probable cause of the feature is a change in the properties of the resin bond; similar anomalies have been observed in the binary lanthanum metaphosphate glass, (figure 9.5). The longitudinal mode behaviour is unlike that of the mixed glasses above. Two regions can be defined: in the low pressure area, the pressure gradient of the natural velocity $\partial W_L/\partial P$ is positive, that is normal stiffening behaviour; and in the high pressure region $\partial W_L/\partial P$ is negative, that there is acoustic mode softening. These trends are illustrated in figures 9.13; only the data from the 343K temperature run has been reproduced for clarity; however it does represent a typical data set. The pressure $P_c$ at which the gradient $\partial W_L/\partial P$ changes from positive to negative increases approximately linearly with temperature (figure 9.13). The origin of this anomaly may arise from the competition between the mode stiffening behaviour of the $La^{3+}$ ions and the mode softening of the $Sm^{3+}$ ions; hence in the low pressure region the effect near the lanthanum sites is dominant, and at higher pressures the samarium ion dominates. Partial replacement of Sm with La acts to suppress the longitudinal mode softening. The low pressure (below $P_c$) derivatives of the longitudinal SOEC $\partial C_{11}/\partial P$, and bulk modulus $\partial B/\partial P$ are positive; however in the high pressure region $\partial C_{11}/\partial P$, $\partial B/\partial P$ and $\partial C_{44}/\partial P$ are negative, The longitudinal Grüneisen parameter is positive in the pressure range below $P_c$ and negative at pressures above $P_c$. The shear mode Grüneisen parameter and the high pressure mean acoustic mode Grüneisen parameter are negative, see table 9.13. The low pressure mean acoustic mode Grüneisen parameters are approximately zero.

| Temp (K) | LP or HP | $W_{L0}$ ($ms^{-1}$) | $W_{S0}$ ($ms^{-1}$) | $C_{11}$ (GPa) | $C_{44}$ (GPa) | $B^s$ (GPa) |
|---|---|---|---|---|---|---|
| 295.0 | LP | 4575.13 | 2581.61 | 73.37 | 23.36 | 42.22 |
| | HP | 4583.25 | | 73.63 | | 42.48 |
| 303.0 | LP | 4574.52 | 2580.24 | 73.35 | 23.34 | 42.23 |
| | HP | 4579.86 | | 73.52 | | 42.40 |
| 313.0 | LP | 4574.12 | 2579.14 | 73.33 | 23.32 | 42.25 |
| | HP | 4578.89 | | 73.49 | | 42.40 |
| 323.0 | LP | 4573.35 | 2578.14 | 73.31 | 23.30 | 42.25 |
| | HP | 4576.17 | | 73.40 | | 42.34 |
| 333.0 | LP | 4572.77 | 2576.90 | 73.29 | 23.28 | 42.26 |
| | HP | 4577.48 | | 73.44 | | 42.41 |
| 343.0 | LP | 4567.74 | 2575.82 | 73.13 | 23.26 | 42.12 |
| | HP | 4588.15 | | 73.78 | | 42.78 |
| 353 | LP | 4565.23 | 2574.59 | 73.05 | 23.23 | 42.07 |
| | HP | 4587.74 | | 73.77 | | 42.79 |
| 363 | LP | 4561.70 | 2573.38 | 72.94 | 23.21 | 41.99 |
| | HP | 4587.32 | | 73.76 | | 42.81 |
| 373 | LP | 4558.44 | 2572.66 | 72.83 | 23.20 | 41.90 |
| | HP | 4581.52 | | 73.57 | | 42.64 |

Table 9.11. The temperature dependences of natural velocity and elastic moduli for $(La_2O_3)_{0.055}(Sm_2O_3)_{0.206}(P_2O_5)_{0.739}$ glass.

| Temp (K) | LP or HP | $\partial W_L/\partial P$ $ms^{-1}GPa^{-1}$ | $\partial W_S/\partial P$ $ms^{-1}GPa^{-1}$ | $\partial C_{11}/\partial P$ | $\partial C_{44}/\partial P$ | $\partial B/\partial P$ |
|---|---|---|---|---|---|---|
| RT/295 | LP | 51.799 | -16.724 | 2.241 | -0.118 | 2.398 |
| | HP | -62.570 | | -1.431 | -0.119 | -1.272 |
| 303.0 | LP | 33.708 | -15.810 | 1.660 | -0.102 | 1.796 |
| | HP | -32.733 | | -0.472 | -0.103 | -0.336 |
| 313.0 | LP | 32.000 | -16.335 | 1.605 | -0.111 | 1.753 |
| | HP | -27.637 | | -0.309 | -0.112 | -0.160 |
| 323.0 | LP | 28.810 | -18.613 | 1.502 | -0.153 | 1.706 |
| | HP | -11.460 | | 0.210 | -0.153 | 0.414 |
| 333.0 | LP | 31.125 | -17.073 | 1.576 | -0.125 | 1.742 |
| | HP | -23.725 | | -0.184 | -0.126 | -0.018 |
| 343.0 | LP | 92.405 | -17.841 | 3.538 | -0.138 | 3.722 |
| | HP | -108.446 | | -2.913 | -0.141 | -2.725 |
| 353.0 | LP | 101.484 | -17.169 | 3.826 | -0.126 | 3.994 |
| | HP | -105.229 | | -2.810 | -0.129 | -2.638 |
| 363.0 | LP | 111.520 | -19.455 | 4.145 | -0.166 | 4.367 |
| | HP | -116.296 | | -3.165 | -0.170 | -2.938 |
| 373.0 | LP | 130.440 | -21.910 | 4.748 | -0.211 | 5.028 |
| | HP | -80.627 | | -2.014 | -0.214 | -1.729 |

Table 9.12. The temperature dependences of the pressure derivatives for $(La_2O_3)_{0.055}(Sm_2O_3)_{0.206}(P_2O_5)_{0.739}$ glass.

| Temp (K) | LP or HP | $\gamma_L$ | $\gamma_S$ | $\gamma^{el}$ | E (GPa) | $\sigma$ (GPa) |
|---|---|---|---|---|---|---|
| RT/295 | LP | 0.478 | -0.273 | -0.023 | 59.167 | 0.266 |
| | HP | -0.580 | -0.275 | -0.377 | 59.224 | 0.268 |
| 303.0 | LP | 0.267 | -0.259 | -0.069 | 59.117 | 0.267 |
| | HP | -0.303 | -0.260 | -0.274 | 59.154 | 0.267 |
| 313.0 | LP | 0.296 | -0.267 | -0.080 | 59.077 | 0.267 |
| | HP | -0.246 | -0.268 | -0.264 | 59.110 | 0.268 |
| 323.0 | LP | 0.266 | -0.305 | -0.114 | 59.039 | 0.267 |
| | HP | -0.106 | -0.306 | -0.239 | 59.058 | 0.268 |
| 333.0 | LP | 0.289 | -0.280 | -0.091 | 58.993 | 0.267 |
| | HP | -0.220 | -0.281 | -0.260 | 59.026 | 0.268 |
| 343.0 | LP | 0.852 | -0.292 | 0.090 | 58.922 | 0.267 |
| | HP | -1.011 | -0.296 | -0.534 | 59.063 | 0.270 |
| 353.0 | LP | 0.935 | -0.280 | 0.125 | 58.863 | 0.267 |
| | HP | -0.982 | -0.285 | -0.517 | 59.018 | 0.270 |
| 363.0 | LP | 1.026 | -0.317 | 0.131 | 58.798 | 0.267 |
| | HP | -1.085 | -0.324 | -0.578 | 58.975 | 0.270 |
| 373.0 | LP | 1.200 | -0.357 | 0.162 | 58.751 | 0.266 |
| | HP | -0.750 | -0.363 | -0.492 | 58.911 | 0.270 |

Table 9.13. The temperature dependence of the Grüneisen parameters, Youngs modulus and Poissons ratio for $(La_2O_3)_{0.055}(Sm_2O_3)_{0.206}(P_2O_5)_{0.739}$ glass.

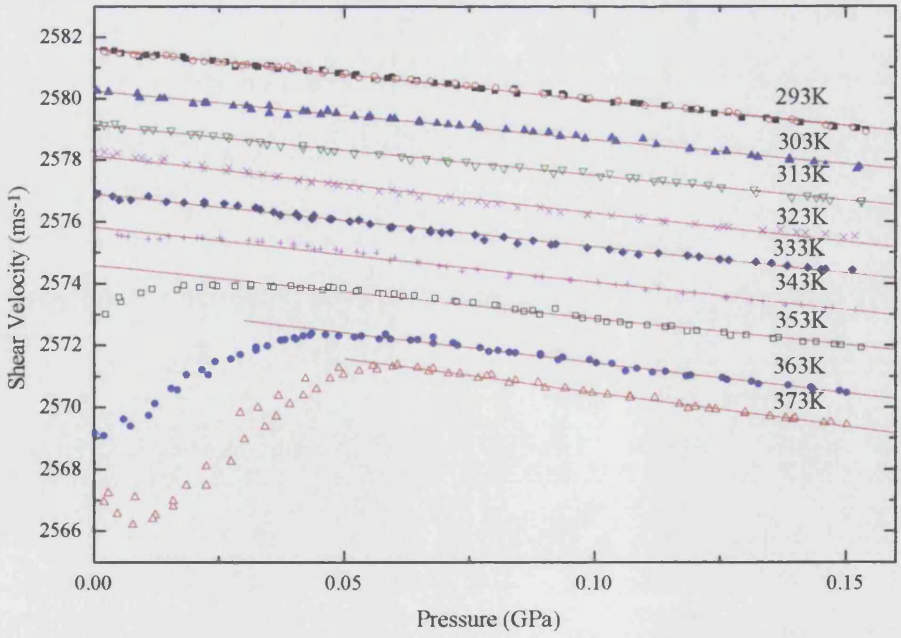


Figure 9.12. Hydrostatic pressure dependence of the velocity of the 11MHz shear ultrasonic wave in $(La_2O_3)_{0.055}(Sm_2O_3)_{0.206}(P_2O_5)_{0.739}$ glass at selected temperatures

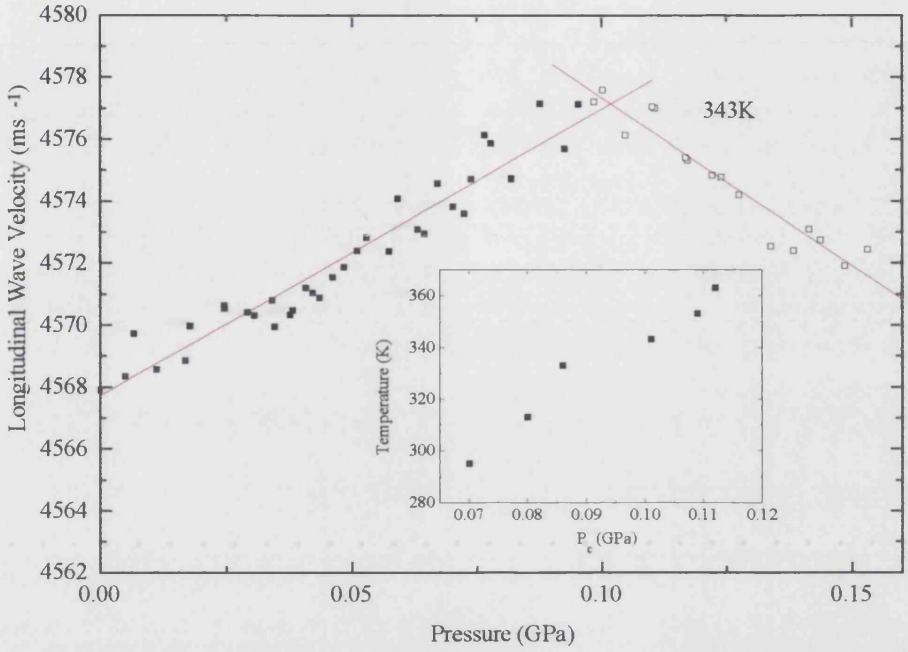


Figure 9.13. Hydrostatic pressure dependence of the velocity of the 11MHz longitudinal ultrasonic wave in $(La_2O_3)_{0.055}(Sm_2O_3)_{0.206}(P_2O_5)_{0.739}$ glass at 343K. The insert shows the variation with temperature of the pressure $P_c$ at which there is a change in $\partial W_S/\partial P$.

To put the ternary glass results into context, the hydrostatic pressure derivatives and Grüneisen parameters have been plotted with the two extremities of the series, binary lanthanum (section 9.2.1.) and samarium metaphosphate glasses (Senin et al 1994b, Senin 1994) at selected temperatures between 293-373K (figures 9.14-9.19), the room temperature data has been presented in table 9.14. It is clear from figures 9.14-9.19, that lanthanum metaphosphate glass has largest hydrostatic pressure derivatives and Grüneisen parameters; they are all positive except for $\gamma_S$; in contrast samarium doped glasses have the smallest (all negative) values. The mixed lanthanum samarium samples exhibit intermediate behaviour, characterised by small pressure dependences. The three ternary samples all exhibit shear mode acoustic softening, which is indicative of samarium metaphosphate glass. The effects are not as pronounced as in the binary materials, as the lanthanum acts to nullify this anomalous behaviour (see figures 9.14 and 9.17, the mean values for the ternary samples have been plotted). This soft acoustic mode cancellation is also illustrated clearly for the longitudinal

mode (figure 9.15 and 9.18), which displays mostly normal behaviour: the long wavelength longitudinal acoustic mode stiffens with pressure, unlike $Sm(PO_3)_3$ glass which has negative ($\partial C_{11}/\partial P$) and $\gamma_L$ (Mierzejewski et al. 1988a, Senin et al. 1993b). The only exception is the sample with the largest $Sm^{3+}$ doping, which shows longitudinal acoustic phonon softening in the higher pressure regions 0.08GPa - 0.15GPa. In the data there are two 'trends' present. The natural velocities $W_L$ $W_S$, SOEC $C_{11}$, $C_{44}$, and the bulk modulus B, increase in the sample order $(La_2O_3)_{0.109}(Sm_2O_3)_{0.164}(P_2O_5)_{0.727}$, $(La_2O_3)_{0.055}(Sm_2O_3)_{0.206}(P_2O_5)_{0.739}$, $(La_2O_3)_{0.166}(Sm_2O_3)_{0.086}(P_2O_5)_{0.748}$, (table 14) as previously stated (section 9.1.); this is in order of increasing phosphorus pentoxide content and is consistent with the observations on other phosphate glasses made by Bridge and Patel (1987). The hydrostatic pressure derivatives and the Grüneisen parameters, however, increase with the following samarium content variation: $Sm_2O_3 \rightarrow$ 20.6mol%, 8.6mol%, 16.4mol%. From graphs (figures 9.17 - 9.19) it can be seen that the samples doped with 8.6% and 16.4% samarium have values which are very similar, and the sample containing 20.6% Sm exhibits characteristics which would be expected from an increase in samarium concentration; as the ratio of samarium to lanthanum becomes greater, the long wavelength acoustic mode softening present associated with $Sm^{3+}$ makes a larger contribution to the properties of the ternary glass. As the Grüneisen parameters determine the vibrational anharmonicity, the thermal expansion for the ternary samples is expected to also be very small. In general the hydrostatic pressure derivative of the elastic stiffnesses and bulk modulus for mixed REMGs have intermediate values between the metaphosphate glasses doped with $Sm^{3+}$ and $La^{3+}$; lanthanum acts to nullify the acoustic mode softening.

| Sample | $(La_2O_3)_{0.225}$ $(P_2O_5)_{0.775}$ | $(La_2O_3)_x(Sm_2O_3)_y(P_2O_5)_{1-x-y}$ x = 0.166 y = 0.086 | x = 0.109 y = 0.164 | x = 0.055 y = 0.206 | $(Sm_2O_3)_{0.224}$ $(P_2O_5)_{0.776}$ |
|---|---|---|---|---|---|
| $\rho$ ($Kgm^{-3}$) | 3199 | 3569 | 3631 | 3505 | 3280 |
| $C_{11}$ (GPa) | 66.8 | 76.2 | 66.9 | 73.4 | 66.4 |
| $C_{44}$ (GPa) | 22.5 | 24.6 | 21.6 | 23.4 | 23.6 |
| $B^S$ (GPa) | 36.8 | 43.4 | 38.1 | 42.2 | 34.9 |
| $E^S$ (GPa) | 56.03 | 62.1 | 54.6 | 59.2 | 57.8 |
| $\Theta_D$ (K) | 348 | 364 | 336 | 353 | 360 |
| $\sigma^S$ | 0.246 | 0.261 | 0.262 | 0.266 | 0.224 |
| $(\partial C_{11}/\partial P)_{P=0}$ | 2.36 | 1.82 | 1.95 | 2.24 (-1.43) | -1.09 |
| $(\partial C_{44}/\partial P)_{P=0}$ | 0.12 | -0.01 | 0.07 | -0.12 | -0.72 |
| $(\partial B^S/\partial P)_{P=0}$ | 2.20 | 1.84 | 1.85 | 2.40 (-1.27) | -0.13 |
| $\gamma_L$ | 0.48 | 0.35 | 0.39 | 0.48 (-0.58) | -0.45 |
| $\gamma_S$ | -0.07 | -0.18 | -0.10 | -0.27 | -0.70 |
| $\gamma^{el}$ | 0.11 | 0.00 | 0.06 | -0.02(-0.38) | -0.62 |

Table 9.14. Comparison of the elastic and non-linear acoustic properties of ternary $(La_2O_3)_x(Sm_2O_3)_y(P_2O_5)_{1-x-y}$ glasses at room temperature (296K) with those of the binary lanthanum $(La_2O_3)_{0.225}(P_2O_5)_{0.775}$ and samarium $(Sm_2O_3)_{0.224}(P_2O_5)_{0.776}$ metaphosphate glasses (Data from Senin et al 1994b). For the $(La_2O_3)_{0.055}(Sm_2O_3)_{0.206}(P_2O_5)_{0.739}$ sample there are two values quoted for the hydrostatic-pressure derivatives of elastic moduli and Grüneisen parameters; these relate to the low pressure and high pressure (figures in brackets) regions. $\Theta_D$ is the Debye temperature (see equation 8.17)

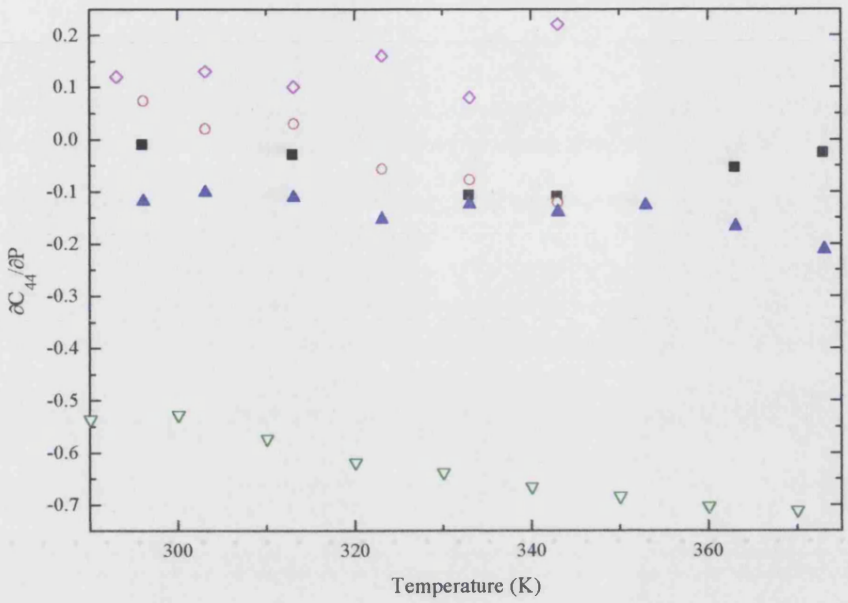


Figure 9.14. Temperature dependence of the hydrostatic pressure derivative of the shear mode elastic stiffness for binary and ternary REMGs, namely (◇) $(La_2O_3)_{0.225}(P_2O_5)_{0.775}$, (■) $(La_2O_3)_{0.166}(Sm_2O_3)_{0.086}(P_2O_5)_{0.748}$, (○) $(La_2O_3)_{0.109}(Sm_2O_3)_{0.164}(P_2O_5)_{0.727}$, (▲) $(La_2O_3)_{0.055}(Sm_2O_3)_{0.206}(P_2O_5)_{0.739}$, (▽) $(Sm_2O_3)_{0.224}(P_2O_5)_{0.776}$ (binary samarium data was taken from Carini et al. 1990).

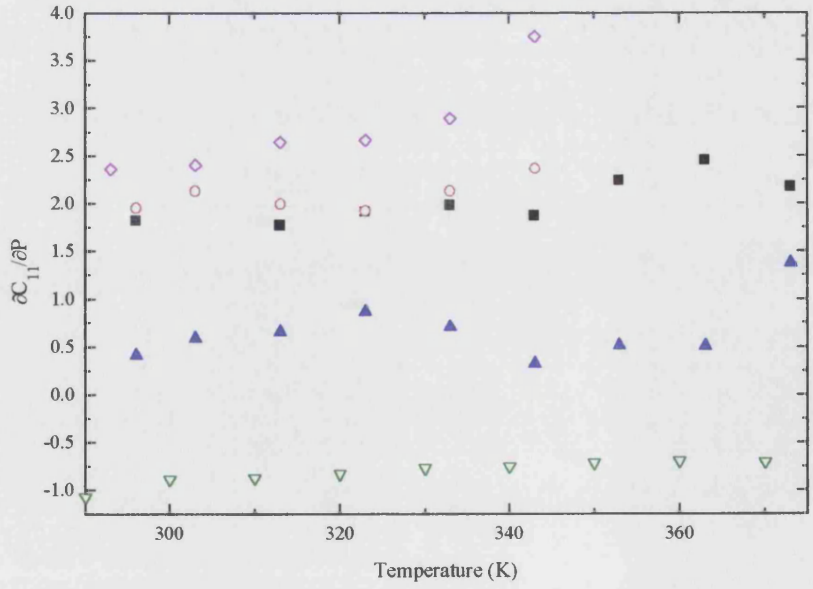


Figure 9.15. Temperature dependence of the hydrostatic pressure derivative of the longitudinal mode elastic stiffness for binary and ternary REMGs. The symbols have the same meaning as in figure 9.14.

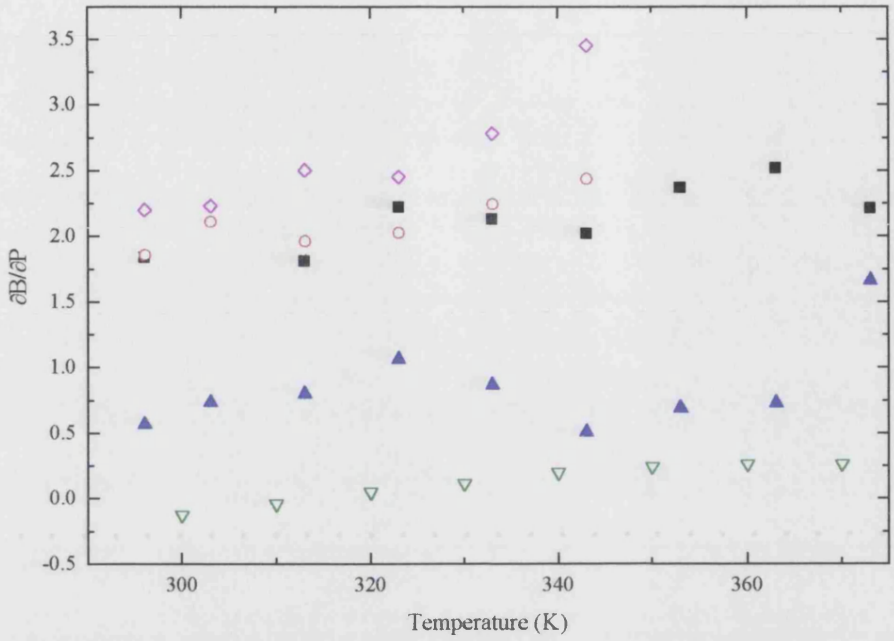


Figure 9.16. Temperature dependence of the hydrostatic pressure derivative of the bulk modulus for binary and ternary REMGs. The symbols have the same meaning as in figure 9.14.

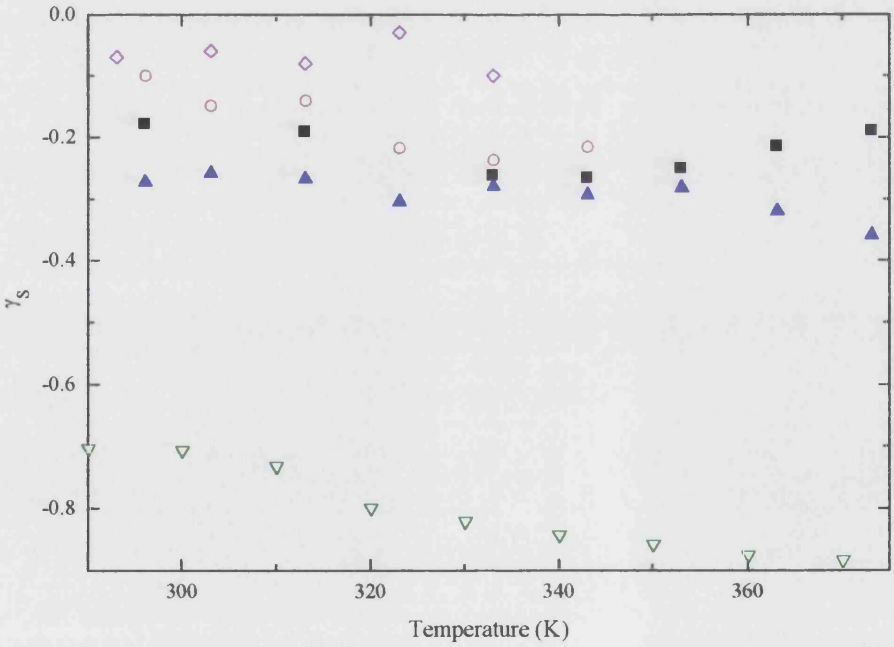


Figure 9.17. Temperature dependence of the shear mode Grüneisen parameters for binary and ternary REMGs. The symbols have the same meaning as in figure 9.14.

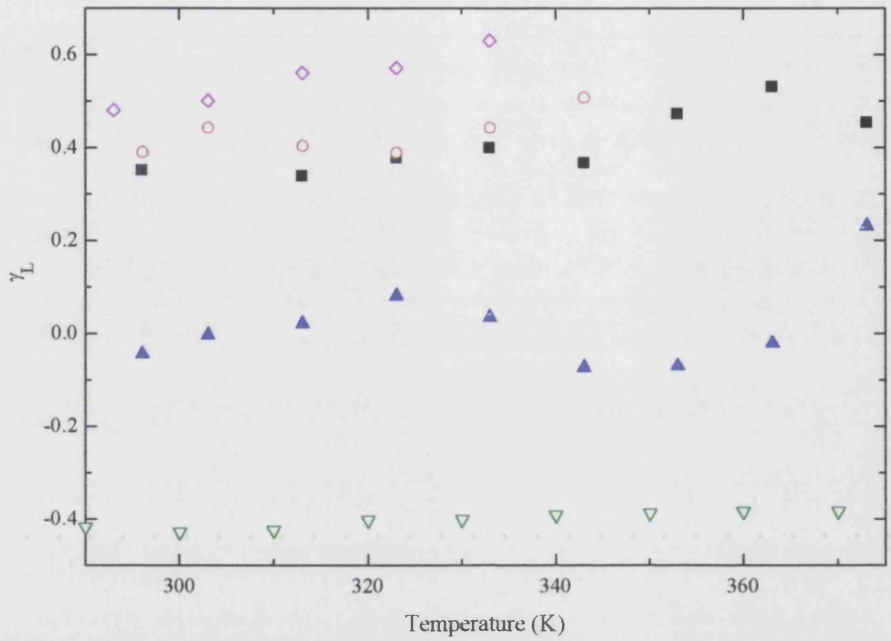


Figure 9.18. Temperature dependence of the longitudinal mode Grüneisen parameters for binary and ternary REMGs. The symbols have the same meaning as in figure 9.14.

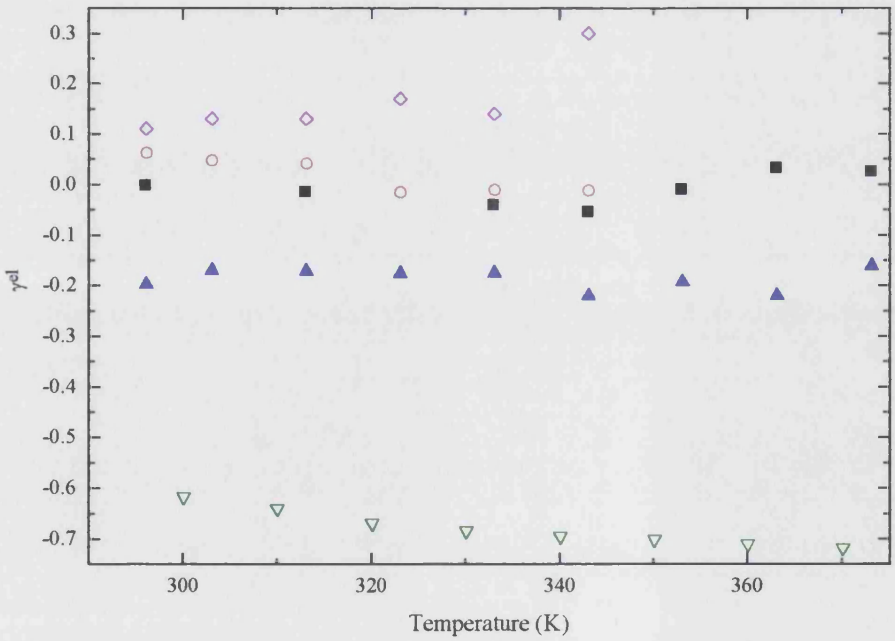


Figure 9.19. Temperature dependence of the mean mode Grüneisen parameters for binary and ternary REMGs. The symbols have the same meaning as in figure 9.14.

### 9.2.2. CERIUM METAPHOSPHATE GLASS

Data for the sample $(Ce_2O_3)_{0.235}(P_2O_5)_{0.765}$ glass; $\rho = 3120\pm 10$ Kgm$^{-3}$ $l_o = 6.099\pm 0.001$mm, figures 9.20 - 9.21, tables 9.15-9.17.

The natural shear and longitudinal velocities as a function of pressure and temperature are plotted in figures 9.20 and 9.21 respectively. The natural velocity of the shear ($W_S$) mode exhibits slight long wavelength acoustic mode softening with pressure: $\partial W_S/\partial P$ is negative; the sample become easier to squeeze as pressure is increased, see figure 9.20. The shear mode velocity data, with the exception of the results recorded at room temperature and 303K, show two distinct areas, which can be characterised by fitting two separates straight lines (by a method of least squares fit) with different gradients (both negative). The low pressure (LP) / high pressure (HP) notation addresses this problem. The low pressure region displays a steeper gradient than its high pressure counterpart (table 9.16). The transition pressure $P_c$ between the two regions increases approximately linearly as temperature is raised between 313K to 343K; in the 353K to 373K interval this pattern is repeated figure 9.20. The hydrostatic pressure results for cerium metaphosphate glass in the low pressure (LP ~ up to 0.1GPa) and the high pressure (HP ~ 0.1GPa to 0.15GPa) regions are shown in table 9.15-9.17. Below 343K the natural shear velocity at atmospheric pressure ($W_{S0}$), calculated by extrapolating the best fit line from the HP region data, decreases with increasing temperature, see table 9.15 ($W_{S0}$ at LP is temperature independent within experimental error). The mode softening effect in the sample studied is very small (approximately 1%); this suggests that the cerium displays intermediate elastic behaviour under pressure. The shear mode softening present in cerium doped glass is more prominent than in lanthanum phosphate glass, but not as dramatic as in samarium and europium metaphosphate glasses (Mierzejewski et al. 1988a,b, Sidek et al. 1988, Wang et al. 1990, Carini et al. 1990, Senin et al. 1993, 1994b, Farok 1994). The hydrostatic pressure derivative of the longitudinal mode is also characteristic of an intermediate rare earth glass; the change in $W_L$ with increasing pressure is very small and fluctuates about a mean value. The natural longitudinal velocity as a function of pressure is displayed in figure 9.21; a smooth line has been fitted using multi-peak Lorenzian fits in the graphics package Microcal Origin 4.0., and are included as a guide for the eye. Despite the scatter, the curves make it relatively easy to detect a pattern in the results; the longitudinal wave velocity appears to increase to

a peak at approximately 0.07GPa, and then reduce as the pressure is increased still further. Plausibly these peaks may arise due to the variation of the $Ce^{3+}$ ion environment associated with the topological disorder of amorphous materials. In certain arrangements the ions show 'normal' characteristics and in other environments acoustic mode softening traits. As the pressure is increased there appears to be a change in which site is dominant, thus producing the maxima in figure 9.21. However this effect is very small. In order to calculate the SOEC and pressure derivatives, it is necessary to describe the results using a series of straight lines; hence the longitudinal data has been fitted with a pair of lines, once again defined as LP, and HP regions. The hydrostatic pressure derivatives resulting from this analysis is recorded in table 9.16. Both the low pressure and high pressure intercepts decrease with increasing temperature. The changes in the second order elastic constants and bulk modulus with temperature are very small (total variation over the temperature range ~3%). The longitudinal SOEC ($C_{11}$) in the LP and HP regions, reduces with temperature, as do the high pressure shear SOEC ($C_{44}$ HP) results, and the bulk modulus in the LP domain. The shear second order constant, $C_{44}$, under lower applied pressures increases with temperature, and the HP bulk modulus is temperature independent over the range studied (see tables. 9.15-9.16.). The hydrostatic pressure derivatives of the SOEC's, $\partial C_{11}/\partial P$ (LP and HP), $\partial C_{44}/\partial P$ (HP) and $\partial B/\partial P$ (HP) are also independent of temperature with in experimental error, and are either just positive or just negative, a result characteristic of an intermediate glass. $\partial C_{44}/\partial P$ (LP) becomes significantly negative as the temperature reaches 353K and above. At these elevated temperatures $\partial B/\partial P$ (LP) jumps to higher, positive values. All the Grüneisen parameters, with the exception $\gamma_L$ (LP) are negative. The high pressure longitudinal, shear and mean Grüneisen parameters are very small and practically independent of temperature. As the temperature rises above 353K $\gamma^{el}$ (LP) and $\gamma_S$ (LP) become significantly more negative.

| Temp (K) | LP or HP | $W_{L0}$ ($ms^{-1}$) | $W_{S0}$ ($ms^{-1}$) | $C_{11}$ (GPa) | $C_{44}$ (GPa) | $B^S$ (GPa) |
|---|---|---|---|---|---|---|
| RT | N/A | 4724.99 | 2695.65 | 69.66 | 22.67 | 39.43 |
| 303 | LP | 4723.45 | 2695.53 | 69.61 | 22.67 | 39.38 |
| | HP | 4727.30 | 2695.53 | 69.72 | 22.67 | 39.50 |
| 313 | LP | 4721.62 | 2696.59 | 69.56 | 22.69 | 39.31 |
| | HP | 4724.57 | 2694.83 | 69.64 | 22.66 | 39.43 |
| 323 | LP | 4721.67 | 2695.56 | 69.56 | 22.67 | 39.33 |
| | HP | 4723.70 | 2692.66 | 69.62 | 22.62 | 39.46 |
| 333 | LP | 4720.82 | 2696.23 | 69.53 | 22.68 | 39.29 |
| | HP | 4722.80 | 2691.87 | 69.59 | 22.61 | 39.45 |
| 343 | LP | 4718.99 | 2696.83 | 69.48 | 22.69 | 39.22 |
| | HP | 4723.31 | 2691.48 | 69.61 | 22.60 | 39.47 |
| 353 | LP | 4717.77 | 2705.53 | 69.44 | 22.84 | 38.99 |
| | HP | 4722.91 | 2692.25 | 69.59 | 22.61 | 39.44 |
| 363 | LP | 4718.10 | 2717.65 | 69.45 | 23.04 | 38.72 |
| | HP | 4721.32 | 2691.95 | 69.55 | 22.61 | 39.40 |
| 373 | LP | 4717.22 | 23.33 | 69.43 | 23.33 | 38.32 |
| | HP | 4721.30 | 2691.18 | 69.55 | 22.60 | 39.42 |

Table 9.15. The temperature dependences of natural velocity and elastic moduli for $(Ce_2O_3)_{0.235}(P_2O_5)_{0.765}$ glass.

| Temp (K) | LP or HP | $\partial W_L/\partial P$ $ms^{-1}GPa^{-1}$ | $\partial W_S/\partial P$ $ms^{-1}GPa^{-1}$ | $\partial C_{11}/\partial P$ | $\partial C_{44}/\partial P$ | $\partial B/\partial P$ |
|---|---|---|---|---|---|---|
| RT | N/A | -9.21 | -25.86 | 0.32 | -0.24 | 0.64 |
| 303 | LP | 10.97 | -24.81 | 0.91 | -0.23 | 1.21 |
| | HP | -34.80 | -24.81 | -0.44 | -0.23 | -0.14 |
| 313 | LP | 32.33 | -101.29 | 1.54 | -1.51 | 3.56 |
| | HP | -18.05 | -26.57 | 0.06 | -0.26 | 0.40 |
| 323 | LP | 20.02 | -89.67 | 1.18 | -1.32 | 2.93 |
| | HP | -13.16 | -19.16 | 0.20 | -0.13 | 0.38 |
| 333 | LP | 17.90 | -87.23 | 1.11 | -1.28 | 2.82 |
| | HP | -10.00 | -21.38 | 0.29 | -0.17 | 0.52 |
| 343 | LP | 28.15 | -77.14 | 1.42 | -1.11 | 2.89 |
| | HP | -27.88 | -23.34 | -0.23 | -0.20 | 0.03 |
| 353 | LP | 32.49 | -913.1 | 1.55 | -15.22 | 21.82 |
| | HP | -31.78 | -37.22 | -0.35 | -0.43 | 0.23 |
| 363 | LP | 25.9 | -719.03 | 1.36 | -12.00 | 17.35 |
| | HP | -19.69 | -43.44 | 0.01 | -0.54 | 0.73 |
| 373 | LP | 25.98 | -824.01 | 1.37 | -13.86 | 19.85 |
| | HP | -22.88 | -33.36 | -0.09 | -0.37 | 0.41 |

Table 9.16. The temperature dependences of the pressure derivatives for $(Ce_2O_3)_{0.235}$ $(P_2O_5)_{0.765}$ glass.

| Temp (K) | LP or HP | $\gamma_L$ | $\gamma_S$ | $\gamma^{el}$ | E (GPa) | $\sigma$ (GPa) |
|---|---|---|---|---|---|---|
| RT | N/A | -0.08 | -0.38 | -0.28 | 57.07 | 0.26 |
| 303 | LP | 0.09 | -0.36 | -0.21 | 57.06 | 0.26 |
| | HP | -0.29 | -0.36 | -0.33 | 57.08 | 0.26 |
| 313 | LP | 0.27 | -1.48 | -0.89 | 57.08 | 0.26 |
| | HP | -0.15 | -0.39 | -0.31 | 57.05 | 0.26 |
| 323 | LP | 0.17 | -1.31 | -0.82 | 57.05 | 0.26 |
| | HP | -0.11 | -0.28 | -0.22 | 56.98 | 0.26 |
| 333 | LP | 0.15 | -1.27 | -0.80 | 57.06 | 0.26 |
| | HP | -0.08 | -0.31 | -0.24 | 56.95 | 0.26 |
| 343 | LP | 0.23 | -1.12 | -0.67 | 57.07 | 0.26 |
| | HP | -0.23 | -0.34 | -0.31 | 56.94 | 0.26 |
| 353 | LP | 0.27 | -13.16 | -8.68 | 57.32 | 0.25 |
| | HP | -0.27 | -0.55 | -0.45 | 56.96 | 0.26 |
| 363 | LP | 0.21 | -10.25 | -6.76 | 57.69 | 0.25 |
| | HP | -0.16 | -0.64 | -0.48 | 56.94 | 0.26 |
| 373 | LP | 0.211 | -11.54 | -7.63 | 58.18 | 0.25 |
| | HP | -0.19 | -0.49 | -0.39 | 56.91 | 0.26 |

Table 9.17. The temperature dependences of the Grüneisen parameters, Youngs modulus and Poissons ratio for $(Ce_2O_3)_{0.235}(P_2O_5)_{0.765}$ glass

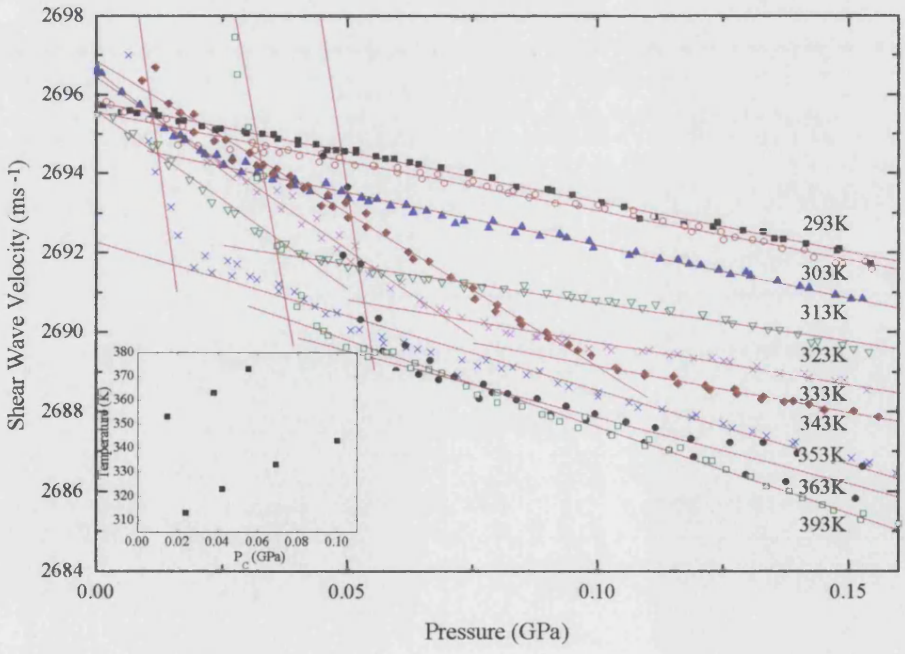


Figure 9.20. Hydrostatic pressure dependence of the velocity of the 11MHz shear ultrasonic wave in $(Ce_2O_3)_{0.235}(P_2O_5)_{0.765}$ glass at selected temperatures.

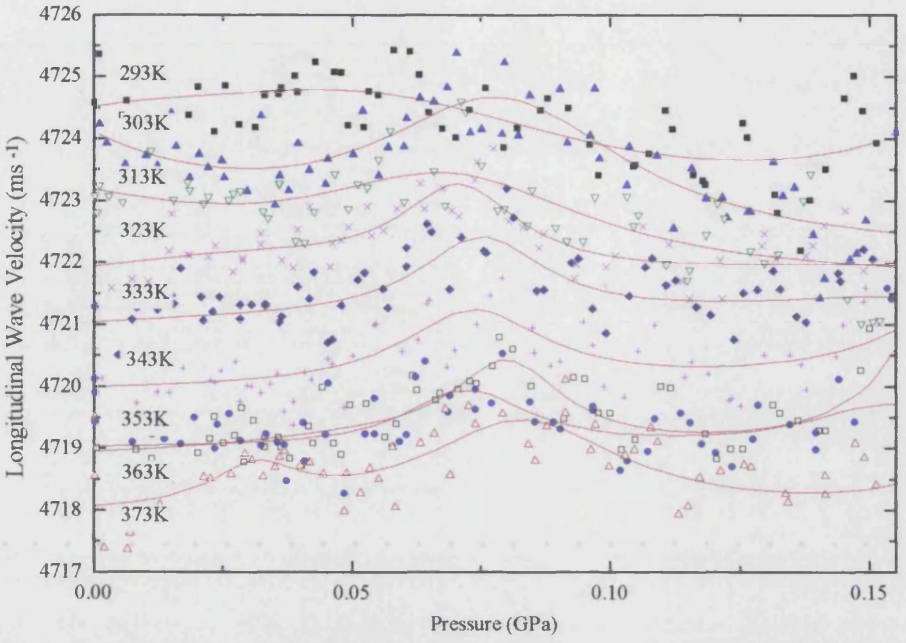


Figure 9.21. Hydrostatic pressure dependence of the velocity of the 11MHz longitudinal ultrasonic wave in $(Ce_2O_3)_{0.235}(P_2O_5)_{0.765}$ glass at selected temperatures.

## 9.3. CONTRIBUTIONS FROM THE LONG WAVELENGTH ACOUSTIC PHONONS AND EXCESS VIBRATIONAL STATES TO THE THERMAL EXPANSION OF GLASSES

The thermal expansion and pressure derivatives of the elastic stiffnesses stem from vibrational anharmonicity which is a consequence of atomic thermal motion. Since these properties have the same origins they can be directly linked. Measurement of the long wavelength Grüneisen parameters enables the effects from the acoustic modes to the thermal expansion to be separated from contributions arising from the higher energy phonon states. If the low temperature thermal expansion is dominated by the long wavelength acoustic modes, then the thermal expansion would be expected to be negative for samarium metaphosphate glass, which has negative Grüneisen parameters and positive for glasses doped with $La^{3+}$.

Thermal expansion originates from the effect of anharmonic terms in the potential energy. Consider two neighbouring atoms; the potential energy for a small

displacement x (= R - $R_o$) from their equilibrium separation $R_o$ at 0 K can be written as equation 9.1 (Kittel 1986, Anselm 1982):

$$V(x) = cx^2 - gx^3 - fx^4 \tag{9.1}$$

The probability $p_x$ that an atom will be in a state x (with energy $\varepsilon_x$) varies according to the Boltzmann distribution (Mandl 1991):

$$p_x = \frac{1}{Z} \exp^{-\frac{\varepsilon_x}{k_B T}} \tag{9.2}$$

where $k_B$ is the Boltzmann constant, T is the temperature (in Kelvin), and the normalisation constant $Z$ is defined as

$$Z = \sum_x \exp^{-\frac{\varepsilon_x}{k_B T}} . \tag{9.3}$$

The quantity $Z$ is called the partition function. Thus the probability that the atom is in state x depends only on the energy eigenvalue of the state and the temperature of the system. From equation 9.2, the mean thermal energy of the system $\langle \varepsilon \rangle$, can be calculated using

$$\langle \varepsilon \rangle = \sum_x p_x \varepsilon_x = \sum_x \frac{\varepsilon_x}{Z} \exp^{-\frac{\varepsilon_x}{k_B T}} = -\frac{\partial \ln Z}{\partial k_B T} \tag{9.4}$$

If the assumption is made, that the system is quasi-continuous, the summation in the above equation can be replaced with an integration over all possible states i.e. from $+\infty$ to $-\infty$

$$\langle \varepsilon \rangle = \frac{\int_{-\infty}^{\infty} \varepsilon_x \exp^{-\frac{\varepsilon_x}{k_B T}} dx}{\int_{-\infty}^{\infty} \exp^{-\frac{\varepsilon_x}{k_B T}} dx} \tag{9.5}$$

For the simple two particle system described by equation 9.1, $V(x) = \varepsilon_x$, and equation 9.5 can be simplified by expanding the exponential

$$\exp^{-\frac{cx^2 - gx^3 - fx^4}{k_B T}} \cong \exp^{-\frac{cx^2}{k_B T}} \left( 1 + \frac{gx^3}{k_B T} + \frac{fx^4}{k_B T} \right) \tag{9.6}$$

For displacements such that the anharmonic terms in the energy are small in comparison with $k_B T$, the symmetric $fx^4$ term can be ignored, and the bottom line of equation 9.5 becomes,

$$\int_{-\infty}^{\infty} \exp^{-\frac{\varepsilon_x}{k_B T}} dx = \int_{-\infty}^{\infty} \exp^{-\frac{cx^2}{k_B T}} \left(1 + \frac{gx^3}{k_B T}\right) \cong \left(\frac{\pi k_B T}{c}\right)^{\frac{1}{2}}. \tag{9.7}$$

Expanding the top line;

$$\int_{-\infty}^{\infty} \varepsilon_x \exp^{-\frac{\varepsilon_x}{k_B T}} dx = \int_{-\infty}^{\infty} (cx^2 - gx^3 - fx^4) \exp^{-\frac{cx^2}{k_B T}} \left(1 + \frac{gx^3}{k_B T}\right) dx = \int_{-\infty}^{\infty} cx^2 \exp^{-\frac{cx^2}{k_B T}} dx - \int_{-\infty}^{\infty} gx^3 \exp^{-\frac{cx^2}{k_B T}} dx$$
$$- \int_{-\infty}^{\infty} fx^4 \exp^{-\frac{cx^2}{k_B T}} dx + \int_{-\infty}^{\infty} \frac{cgx^5}{k_B T} \exp^{-\frac{cx^2}{k_B T}} dx - \int_{-\infty}^{\infty} \frac{g^2 x^6}{k_B T} \exp^{-\frac{cx^2}{k_B T}} dx - \int_{-\infty}^{\infty} \frac{cfgx^7}{k_B T} \exp^{-\frac{cx^2}{k_B T}} dx \tag{9.8}$$

When the odd x terms ($x^3$, $x^5$ etc.) are integrated from plus to minus infinity, they vanish. Thus leaving the top line in with only three components, that can be evaluated using standard integrals

$$\int_{-\infty}^{\infty} cx^2 \exp^{-\frac{cx^2}{k_B T}} dx = \frac{1}{2}\left(\frac{\pi (k_B T)^3}{c^3}\right)^{\frac{1}{2}}$$
$$\int_{-\infty}^{\infty} fx^4 \exp^{-\frac{cx^2}{k_B T}} dx = \frac{3f}{4}\left(\frac{\pi (k_B T)^5}{c^5}\right)^{\frac{1}{2}} \tag{9.9}$$
$$\int_{-\infty}^{\infty} \frac{g^2 x^6}{k_B T} \exp^{-\frac{cx^2}{k_B T}} dx = \frac{15g^2}{8}\left(\frac{\pi (k_B T)^5}{c^7}\right)^{\frac{1}{2}}$$

When the top line (equation 9.8) is divided by the right hand side of equation 9.7, the expression for the mean thermal energy becomes

$$\langle \varepsilon \rangle = \frac{k_B T}{2c} - \frac{3f(k_B T)^2}{4c^2} - \frac{15g^2 (k_B T)^2}{8c^3} = \frac{k_B T}{2c} - \left[\frac{3f}{4c^2} + \frac{15g^2}{8c^3}\right](k_B T)^2 \tag{9.10}$$

An analogous derivation can be made for the mean thermal displacement $\langle x \rangle$

$$\langle x \rangle = \frac{\int_{-\infty}^{\infty} x \exp^{-\frac{\varepsilon_x}{k_B T}} dx}{\int_{-\infty}^{\infty} \exp^{-\frac{\varepsilon_x}{k_B T}} dx} = \frac{3gk_B T}{4c^2} \tag{9.11}$$

The coefficient $\alpha$ of linear expansion is the extension per unit length per Kelvin:

$$\alpha = \frac{\langle x \rangle}{R_o T} = \frac{3k_B g}{4c^2 R_o} \tag{9.12}$$

The pressure derivative of the elastic modulus M can now be obtained by considering the force acting between pairs of atoms vibrating longitudinally in a linear chain,

$$F = -\frac{dV(x)}{dx} = -2cx + 3gx^2 + 4fx^3. \qquad (9.13)$$

The first term is harmonic in energy and is the Hooke's law approximation. The second term is asymmetric in the potential; its effect is to increase the force less rapidly (than expected from Hooke's law) as the displacement x is increased in the positive direction but to increase the force more rapidly as x is made more negative, reflecting the fact that interatomic repulsive forces have a shorter range than the interatomic attractive forces. The third term is symmetric with respect to x so far as the potential is concerned and causes F to increase less rapidly with |x| at large vibrational amplitude - an effect which has a pronounced influence during phonon mode softening in materials which show acoustic mode instabilities. Consider a steady uniaxial pressure applied to the chain causing the mean value of $\langle x \rangle$ to become $\langle X \rangle$ (the latter being negative and defined per unit area). The pressure can then be written as

$$P = 2c|< X >| + 3g|< X >|^2 - 4f|< X >|^3 \qquad (9.14)$$

Hence the effective elastic modulus M for a wave motion along the chain of amplitude $|\Delta x| << |< X >|$, is

$$M = dP / d|< X >| \;=\; 2c + 6g|< X >| - 12f|< X >^2| \qquad (9.15)$$

and

$$dM / d|< X >| = 6g - 24f|< X >| \qquad (9.16)$$

so its pressure derivative is

$$\frac{dM}{dP} = \frac{dM}{d|< X >|}\frac{d|< X >|}{dP} = \frac{6g - 24f|< X >|}{M} \qquad (9.17)$$

For $X \to 0$, $|< X >| \to P/2c$ hence

$$\frac{dM}{dP} = \frac{1}{M}\left(6g - \frac{12fP}{c}\right) \qquad (9.18)$$

Considering third order terms only,

$$\frac{dM}{dP} = \frac{6g}{M} \qquad (9.19)$$

The pressure gradient for the elastic modulus M and the thermal expansion coefficient (equation 9.12) is determined mainly by the third order constant g and its sign. It

follows that the thermal Grüneisen parameter (and subsequently the long wavelength acoustic mode Grüneisen parameters) is also dependent upon the value and sign of g, as it is directly proportional to the linear thermal expansion (equation 8.12). Hence for a glass the contributions of the acoustic mode vibrational anharmonicity to the thermal expansion and non-linear acoustic properties have the same sign.

At high temperatures ($T>>\Theta_D$) all the thermal phonons, and in addition occupants of other vibrational states, can be expected to contribute to the thermal expansion. As the temperature is reduced, vibrational modes in the higher-energy states freeze out first and their contributions to the thermal expansion decrease. The contributions from the acoustic phonons are determined by the mode Grüneisen parameters (equation 8.13, 8.15), which are negative for the samarium metaphosphate glass and become more negative as the temperature is reduced below room temperature (Senin et al. 1993b). Since these acoustic modes have negative Grüneisen parameters, the thermal expansion can be expected to be negative at low temperatures where these modes dominate (i.e. $g<0$ in equation 9.12). This can be seen to hold true in figures 9.22. The linear thermal expansion in the binary and ternary REMGs was presented in the paper by Acet et al. (1998), the measurements were taken using a capacitance dilatometer capable of recording length changes of 0.02Å in a sample with 6mm path length. In the case of lanthanum metaphosphate glass the acoustic mode longitudinal Grüneisen parameters are positive and the shear mode is very close to zero (table 9.3). Hence the acoustic phonon mode contribution to the thermal expansion at low temperatures is expected to be positive. Yet the thermal expansion of lanthanum metaphosphate glass is also negative at low temperatures, like that of the samarium metaphosphate glass, although over a more restricted temperature range (insert in figure 9.22). Hence there must be another contribution to the thermal expansion of lanthanum metaphosphate glasses which causes the thermal expansion coefficient to become negative. In the low temperature regime such a contribution can be expected to arise from the low energy excess vibrational states. Since the thermal expansion of samarium metaphosphate glass is negative over a wider range of temperature, it is likely that the contributions from the excess states and the acoustic modes are both negative.

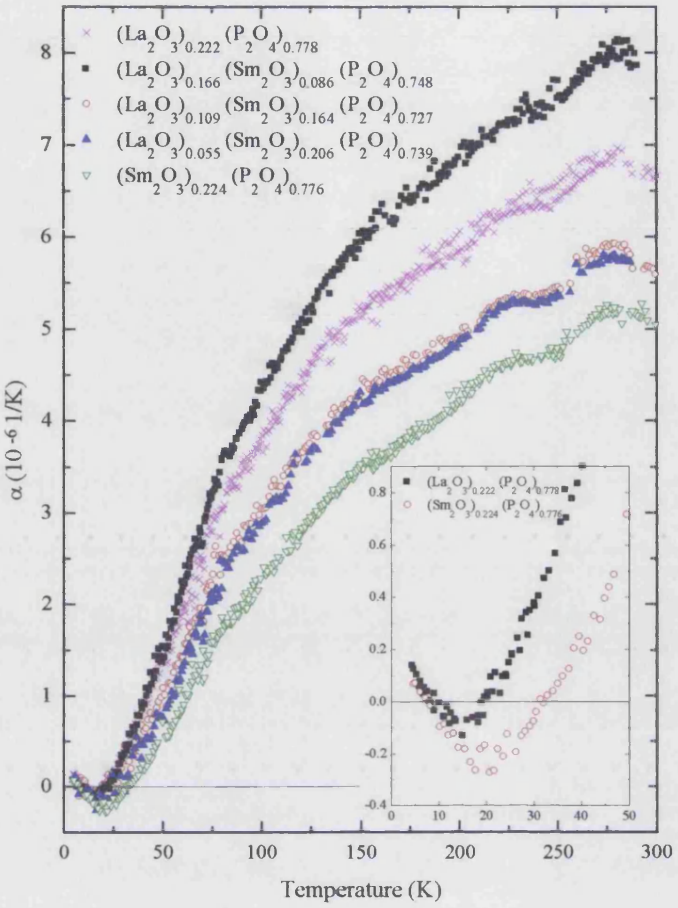


Figure 9.22. The temperature dependence of the linear thermal expansion coefficient of binary and mixed REMGs (Acet et al. 1998).

It is now necessary to develop an expression for the thermal expansion (and also for the nonlinear acoustic properties) from the soft potential model (section 2.4.2) using a similar partition function approach to that above. To recapitulate, according to the SPM (Karpov, Klinger and Ignatiev 1983) the quasi-local low-frequency modes in glasses are described by a soft anharmonic oscillator potential

$$V(x) = \varepsilon\left[\eta\left(\frac{x}{a}\right)^2 + \xi\left(\frac{x}{a}\right)^3 + \left(\frac{x}{a}\right)^4\right] \qquad (2.2)$$

Here x is the generalised coordinate of the soft mode having units of length, $a$ is a characteristic length of the order of the interatomic spacing (replaced here by $R_o$), $\varepsilon$ is the binding energy of the order of $\overline{m}v^2 \simeq 10\text{eV}$, $\overline{m}$ being the average mass of atoms making up the glass, v is the sound velocity. The values of the dimensionless

parameters $\eta$ and $\xi$ are random due to fluctuations of the structural parameters of a glass and the soft potentials correspond to $|\eta|, |\xi| << 1$.

Hence using an analogous argument to above, the contribution to the thermal expansion from the excess low-energy vibrational states has been shown to be

$$\alpha_{SPM} = -\frac{3k_B\xi}{4\varepsilon\eta^2} \tag{9.20}$$

The contribution from the excess low-energy vibrational states to the pressure gradient for the elastic modulus $M_{SPM}$ is

$$\left(\frac{dM}{dP}\right)_{SPM} = -\frac{6\varepsilon\xi}{R_o^3 M_{SPM}} \tag{9.21}$$

Hence the contributions from the excess states to the thermal expansion and to the pressure gradient for the elastic modulus $M_{SPM}$ have the same sign, and depend on the signs of the parameters $\xi$ and $\varepsilon$, $\varepsilon$ being the binding energy and hence positive. The negative thermal expansion of the lanthanum metaphosphate glass at low temperatures suggests that $\xi$ is positive. This model analysis strongly suggests that the excess modes provide negative contributions to both the thermal expansion and to the pressure derivative for the elastic modulus $M_{SPM}$ for the binary and mixed rare earth metaphosphate glasses. Excess mode contributions to these properties should occur for any glass, extending the range of universality arising from topological disorder.

## 9.4. CONCLUSIONS

The ultrasonic wave velocities and attenuations of mixed $(La_2O_3)_x(Sm_2O_3)_y(P_2O_5)_{0.75}$, metaphosphate glasses, where $(x+y=0.25)$, have been measured as a function of temperature (15-293K). The hydrostatic pressure dependence of the longitudinal and shear acoustic waves has been investigated at various temperatures between room temperature and 373K, in the ternary lanthanum samarium samples and binary $(La_2O_3)_{0.222}(P_2O_5)_{0.778}$ and $(Ce_2O_3)_{0.235}(P_2O_5)_{0.765}$. metaphosphate glasses. The results have been compared with the data for $(Sm_2O_3)_{0.224}(P_2O_5)_{0.776}$, measured by Carini et al. (1990) and Senin et al. (1994b). Finally the contributions from the acoustic mode phonons and the excess excitations, to the thermal expansion has been discussed. The results obtained provide a physical description of the vibrational anharmonicity of the glasses, and can be summarised as follows.

1) The temperature dependence of ultrasound velocity is determined by contributions from an anharmonic term at high temperatures, an interaction at lower temperatures between the acoustic phonons and the two-level systems through a thermally activated structural relaxation process (evidenced also by a broad attenuation peak) and soft anharmonic localised vibrational modes.

2) When subjected to hydrostatic pressure the longitudinal mode of $(La_2O_3)_{0.225}(P_2O_5)_{0.775}$ glass shows a normal stiffening response to pressure: the application of hydrostatic pressure increases the ultrasonic longitudinal wave velocity. The shear mode however exhibits slight softening: the application of hydrostatic pressure decreases the ultrasonic shear wave velocity. In contrast the velocities of both longitudinal and shear ultrasonic waves in the $Sm^{3+}$ modified rare earth metaphosphate glass decrease under pressure; the long wavelength acoustic-phonon modes soften. For mixed REMGs the hydrostatic-pressure derivatives of elastic stiffnesses and bulk modulus have intermediate values between those determined for the binary REMGs: introduction of $La^{3+}$ counteracts the acoustic-mode softening found in the $Sm^{3+}$ modified glasses.

3) While the acoustic-mode Grüneisen parameters of samarium metaphosphate glasses are negative, the longitudinal and mean Grüneisen parameters for the $(La_2O_3)_{0.225}(P_2O_5)_{0.775}$ glass show the more normal behaviour. The acoustic-mode Grüneisen parameters of the mixed $(La_2O_3)_x(Sm_2O_3)_y(P_2O_5)_{0.75}$ glasses have intermediate values; again evidencing that replacing $Sm^{3+}$ by $La^{3+}$ in metaphosphate glasses nullifies the acoustic-mode softening. This observation is consistent with a very small thermal expansion coefficient measured for mixed REMGs.

4) The cerium metaphosphate glass $(Ce_2O_3)_{0.235}(P_2O_5)_{0.765}$ shows intermediate characteristics; the hydrostatic pressure derivatives of the elastic stiffnessess and the acoustic mode Grüneisen parameters are very small and either slightly negative or positive depending on the mode or whether the property has been calculated for the high/low pressure region

5) Comparisons made between the thermal expansion and the non-linear acoustic properties of $(La_2O_3)_{0.222}(P_2O_5)_{0.778}$ and $(Sm_2O_3)_{0.224}(P_2O_5)_{0.776}$, based on the SPM suggest that the excess modes present due to the topological disorder in these glasses provide negative contributions to the thermal expansion and to the pressure derivative for the elastic modulus. It is likely that such excess mode contributions to these properties are a universal feature of the glassy state.

# CHAPTER TEN

## BASIC THEORY AND INSTRUMENTATION OF OPTICAL EXPERIMENTS AND AN INTRODUCTION INTO THE CONCEPTS OF LASERS AND OPTICAL FIBRES

In 1900 Max Planck demonstrated that the energy distribution of the blackbody radiation curve could be explained by assuming that radiation was either emitted or absorbed in discrete packets of energy known as quanta. This concept has since been extended to include the discontinuous energy levels present in other forms of energy occurring in materials (vibrational, rotational). Spectroscopic techniques are employed to study the interaction of electromagnetic radiation with matter (see Banwell and McCash 1994). Electromagnetic radiation interacts with particles by creating or annihilating quanta of energy, known as photons. Hence spectral investigations provide information on the energy levels, valency and local symmetry of ions incorporated in a host material. Many REMGs exhibit strong, electronic absorptions and fluorescence in the visible and near infra red region and therefore have potential in the fabrication of optical fibres and lasers. The optical spectra of rare earth ions are mainly determined by electric and magnetic dipole transitions between states of the ground $f^n$ electronic configuration. In rare earth ions the 4f electrons are partially shielded from perturbations by the external fields due to the presence of the 5s and 5p shells; hence the absorption and fluorescence are less dependent on the external crystal fields than is the case for other ions i.e. transition elements, in similar hosts. Nevertheless altering the environment of the rare earth ion does, to a certain extent, produce changes in the spectra. The host material and dopant concentration affects the electronic and optical characteristics of paramagnetic ions, such as position, intensity and shape of the fluorescence and absorption bands, excited state lifetimes, stimulated emission cross sections and ion-ion and ion-lattice interactions. To provide

a direct source of information concerning the 4f energy levels in a glass matrix having a near metaphosphate composition, electronic excitations can be examined by optical absorption and fluorescence, and lifetime measurements. Investigations of this type are necessary for assessing the potential of the materials for device applications, such as lasers, and fibre optics. The basic concepts required for the understanding of lasers and optical fibres are introduced in section 10.3 and 10.4 respectively. Section 10.4 also includes information on the manufacture of a ternary, lanthanum neodymium, metaphosphate glass fibre.

## 10.1. THEORY OF OPTICAL EXPERIMENTS

An electron can exist in any one of several discrete quantized energy levels, defined by the quantum numbers n the principal, l the orbital, m the magnetic, and s the spin $|n,l,m,s\rangle$. The energy level diagrams for free trivalent rare earth ions are shown in figure 10.1. The energy of the different levels depends on the attraction between electrons and the nucleus, the repulsion acting among the electrons in the same energy level, and the influence of the host material through crystal fields effects. Transitions can take place between these levels providing the appropriate amount of energy, has been absorbed or emitted:

$$\Delta E = nh\nu \qquad (10.1)$$

where n is an integer $\Delta E = E_f - E_i$ is the energy difference between the final and initial energy levels, h is Planck's constant and $\nu$ is the frequency of the absorbed or emitted radiation. If a beam of electromagnetic radiation incident on a sample has an incoming energy greater than or equal to $\Delta E$, there is a finite probability the electron will be excited to a higher energy level (see figure 10.3a); this absorption rate depends on the number of electrons in the ground level, and the absorption cross section. Once an electron has been excited it can revert to the ground state by emitting an integer multiple of $\Delta E$.

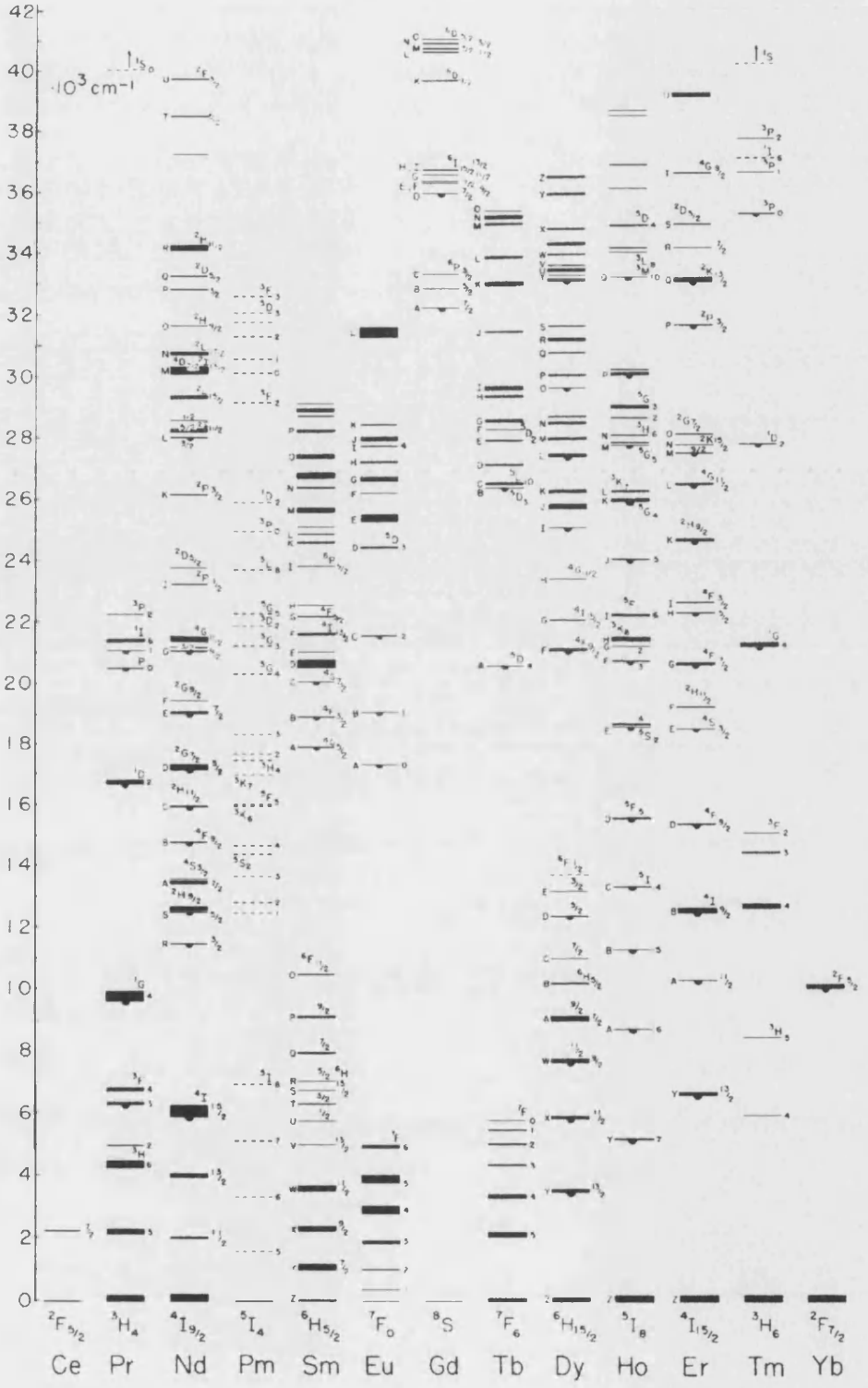


Figure 10.1. Energy level diagram of the trivalent rare earth ions (after Reisfeld 1972). Fluorescence is observed from the levels marked with a half circle.

### 10.1.1. REFLECTION, TRANSMISSION, ABSORPTION AND FLUORESCENCE

Radiant energy falling on an interface is partly reflected, partly transmitted, and partly absorbed

$$I_0 = I_r + I_t + I_a \tag{10.2}$$

where $I_0$ is the intensity of the incident radiation, and $I_r$, $I_t$ and $I_a$ are the intensities of the reflected, transmitted and absorbed signal respectively. Reflection is defined as the scattering of the light by the surface of a sample; re-direction of the incoming radiation, without altering the wavelength or frequency. If a quantum mechanical approach is considered, the elastic reflection of radiation by an atom, whose diameter is small compared with the wavelength of the incoming radiation, is called Rayleigh scattering. Electromagnetic radiation incident on the material, with energies too small to produce electron transition into higher energy levels, will drive the electron cloud to oscillate at same frequency of the incoming wave. The vibrating cloud acts as an oscillating dipole with respect to the positive nucleus; hence it re-radiates radiation at the same frequency. Transmission is the name given to the signal which emerges after the radiation has travelled through a medium. The transmission coefficient (also called the transmittance T) is defined as the ratio of the intensity of radiation after it has propagated a unit distance through the medium, to the original intensity.

Fresnel (1788-1828) developed a set of equations describing the effect of an incoming electromagnetic plane wave falling on the interface between two different dielectric materials, i.e. ignoring absorption effects ($I_0 = I_r + I_t$). He calculated the field amplitudes of the reflected and transmitted incident radiation, having an **E**-field parallel ( $\|$ ) and perpendicular to the plane ($\perp$) of incidence:

$$\begin{aligned} r_\perp &= -\frac{\sin(\theta_i - \theta_t)}{\sin(\theta_i + \theta_t)} \\ r_\| &= +\frac{\tan(\theta_i - \theta_t)}{\tan(\theta_i + \theta_t)} \\ t_\perp &= +\frac{2\sin\theta_t\cos\theta_i}{\sin(\theta_i + \theta_t)} \\ t_\| &= +\frac{2\sin\theta_t\cos\theta_i}{\sin(\theta_i + \theta_t)\cos(\theta_i + \theta_t)} \end{aligned} \tag{10.3}$$

Here r is the amplitude reflection coefficient (the ratio of reflected to incident electric field amplitudes, $E_{0r}/E_{0i}$), t is the amplitude transmission coefficient ($E_{0t}/E_{0i}$) and $\theta_i$ and $\theta_t$ are the angles of incidence and transmission respectively (Hecht 1987). The reflectance, R, is defined as the ratio of the incident and reflected beam irradiance; irradiance is proportional to the square of the field amplitude, hence $R = r^2$ and

$$R_{\perp} = \frac{\sin^2(\theta_i - \theta_t)}{\sin^2(\theta_i + \theta_t)}$$
$$R_{\parallel} = \frac{\tan^2(\theta_i - \theta_t)}{\tan^2(\theta_i + \theta_t)} \qquad (10.4)$$

In the limit of $\theta_i$ tending to zero (i.e. normal incidence) the tangent and sines are essentially equal, hence the total reflectance $R = R_{\perp} = R_{\parallel}$. By expanding the top equation of 10.3, substituting in Snells law, $n_i \sin\theta_i = n_t \sin\theta_t$, and squaring the resultant, the reflectance can be written as

$$R = \left(\frac{n_t \cos\theta_i - n_i \cos\theta_t}{n_t \cos\theta_i + n_i \cos\theta_t}\right)_{\theta_i=0} = \left(\frac{n_t - n_i}{n_t + n_i}\right)^2 \qquad (10.5)$$

where $n_t$, and $n_i$ are the refractive index of the incident and transmitted mediums, and $\cos\theta_i$ and $\cos\theta_t$ tend to one as $\theta_i$ goes to zero. From equation 10.4 is can be seen that $R_{\perp}$ is never zero, but $R_{\parallel}$ vanishes when $\theta_i + \theta_t = 90°$, this observation forms the basis of Brewster's law. Incoming radiation linearly polarized perpendicular to the plane of incidence, drives the bound electrons to vibrate causing the atom to re-radiate; the reflected and transmitted waves have **E**-fields with the same orientation as the incident wave. If the incoming **E**-field oscillations are in the incident plane, after refraction at the dielectric interface, the electrons near the surface will oscillate in a same direction as the **E**-field of the refracted wave, see figure 10.2. The flux density of the reflected wave is small as it only makes a slight angle $\theta$ with the electric dipole axis. As $\theta$ goes to zero i.e. $\theta_i + \theta_t = 90°$ the reflected wave vanishes, all the signal is transmitted (the refracted wave is partially polarized).

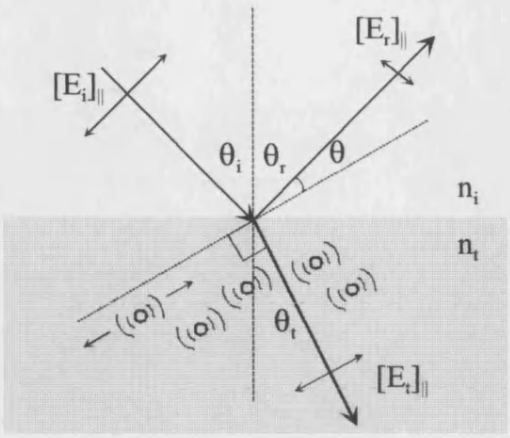


Figure 10.2. A schematic diagram showing the reflection and refraction of an incoming wave (with the **E**-field in the plane of incidence) at an interface. The figure shows the nature of the electron oscillations and Brewster's law (after Hecht 1987).

For an incoming unpolarized wave made up of two incoherent orthogonal plane polarized waves incident on a sample such that the reflected and refracted beam form a right angle, only the component of polarized light normal to the incident plane, and therefore parallel to the surface, will be reflected; the reflected light is plane polarized. When this constraint is met $\theta_i$ is called $\theta_B$, Brewster's angle i.e. $\theta_B + \theta_t = 90°$. Brewster's law can be written as,

$$\tan \theta_B = n_t / n_i \qquad (10.6)$$

Absorption of radiation occurs if the incoming photons possess enough energy to excite a ground state valence electron into a higher energy level (figure 10.3a). The absorption coefficient $\alpha$ can be determined by measuring the ratio of the wave intensity after travelling a distance x through a sample, to the incident intensity (Svelto 1989):

$$I_t = I_0 \exp^{-(\alpha x)} \qquad (10.7)$$

This is called the Beer-Lambert law. The absorption coefficient depends on material properties, the transition probability and frequency of the incoming wave. The reciprocal of the absorption coefficient, $1/\alpha$, is the distance over which a propagating wave loses $\exp^{-1} = 0.368$ of the incident flux density.

Once an atom or molecule has been excited into a higher state, it can lose its excess energy by spontaneous (figure 10.3b) or stimulated (figure 10.3c) emission. The first process can be split into two subsections: non-radiative decay describes the rapid transferral of the excited energy via intermolecular collisions and the subsequent production of heat (interaction between electrons and the dynamic lattice), or radiative recombination, the re-emission of a photon with energy $\Delta E = E_f - E_i$. Spontaneous emission depends on the population of the upper level, and occurs at any time. The emitted photons can be in any direction, have any phase, and the frequency, $\nu_{emit.}$, has a broad range.

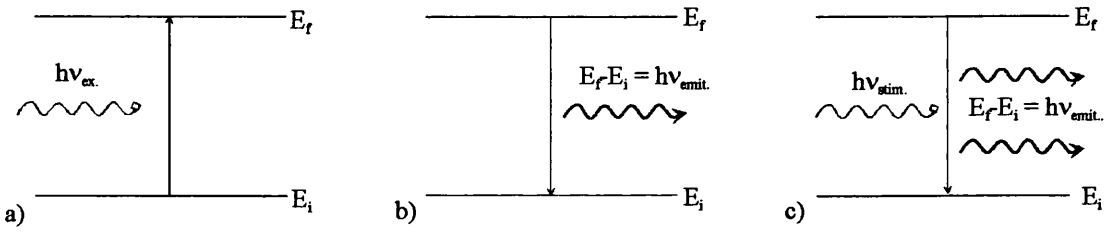


Figure 10.3. Diagram showing a) absorption from the ground state and b) spontaneous and c) stimulated emission from an excited energy level ($\nu_{stim}$= $\nu_{emit}$).

If a wave incident on the sample has the same frequency $\nu_{stim}$ as the atomic transition,$\nu_{emit}$, then there is a finite probability the wave will force the atom to undergo a transition from the excited state to the ground level; this resonance process is called stimulated emission. The atom can be considered an oscillating electric dipole, and the interaction of the associated dipole moment with the electric field of the incident electromagnetic wave instigates the emission of a photon. The emitted wave has the same phase, frequency and direction as the stimulating wave. After interacting with the atom the incident wave is not absorbed, and continues to travel through the sample activating further emissions. Each liberated photon can in turn stimulate new transitions; hence stimulated emission is a cascade effect. It is this process of amplifying of the original stimulated signal which forms the basis of lasers (Light Amplification by Stimulated Emission of Radiation). For lasing to be achieved it is necessary to find systems where the excited lifetime is sufficiently long that

stimulated emission exceeds spontaneous emission; this criteria will only be forfilled if more than two levels are involved.

Luminescence is the generic term given to the emission of electromagnetic radiation by a substance, for any reason other than a rise in temperature. Fluorescence describes the absorption of radiation of a given wavelength, followed by the emission of a photon with a different frequency. If an atom is raised into a higher energy state on being excited by an incoming electromagnetic wave, the system can lose some of its vibrational energy through non-radiative collisions and the subsequent production of heat in the sample. On reaching a lower energy level spontaneous radiation may be emitted as the atom regresses to the ground state, i.e. fluorescence is a mixture of non-radiative and radiative recombination. The majority of fluorescence follows Stokes law which states that emitted radiation has a greater wavelength than that of the incident beam (Pringsheim and Vogel 1943). However, if the energy levels near the excited state are closely spaced and the temperature is high, there is a finite probability that an excited ion may actually gain energy from the surrounding atoms, thus the photon emitted will have a greater frequency, this is know as anti-Stokes radiation. Anti-Stokes fluorescence may also arise due to multiphonon absorption from the ground state or excited state absorption (ESA) (Auzel 1973, Minscalco 1991, Lu et al. 1996). ESA involves the excitation of an ion in the metastable state to a even higher level. These processes are the basis of infrared-to-visible upconversion as seen in erbium doped glasses. Fluorescence will cease after the excitation source has been removed.

### 10.1.2. THE INTENSITY AND WIDTH OF ABSORPTION AND FLUORESCENCE TRANSITIONS

All optical transitions in absorption and fluorescence spectra have a characteristic wavelength (or frequency), intensity and linewidth which depends on the energy levels of the active ion within the host material. The intensities of the absorption or fluorescence spectral lines are determined by three main factors: the transition probability, the population of the states, the path length of the sample. The transition probability characterises the likelihood of a transition between two energy levels occurring. Calculation of the transition probabilities is very complex and requires

detailed knowledge of the quantum mechanical wave functions of the two states. All electronic transitions have a finite probability of occurring; the events which are more likely, correspond to strong intensity peaks in the optical spectra. Some of the transitions are very weak (basically zero), on these occasions the transition are classified as forbidden. Judd (1962) and Ofelt (1962) examined the intensities of transitions in rare earth ions. They concluded that the absorption spectra of the lanthanides essentially resulted from electric dipole transitions, with the magnetic and electric quadrupole transitions being significantly weaker; the majority are forbidden. The matrix elements of the electric dipole operator between two states $E_i$ and $E_f$ are only non-vanishing if they have opposite parity. In a free lanthanide ion the levels of the $4f^N$ configuration have the same parity, hence the electric dipole transitions are forbidden. In a material the crystal field potential acts, on the rare earth ion, to admix higher lying state of opposite parity (e.g. 5d) into the 4f configuration, thus allowing intra f shell transitions. Transition intensity between two energy levels also depends on the population of the states; the larger the population the stronger the spectral peak. In thermal equilibrium the population of an energy level can be determined using Boltzmann statistics:

$$\frac{N_2}{N_1} = \exp\left(-\frac{\Delta E}{k_B T}\right) \tag{10.8}$$

Where $N_1$ and $N_2$, are the number of ions in two arbitrary states, T is the absolute temperature of the material, $\Delta E$ is the energy difference between the two levels, and $k_B$ is Boltzmanns constant. From equation 10.8 it can be seen that in equilibrium $N_1$ is larger than $N_2$, and the sample is an absorber; if a non equilibrium system is created $N_2$ may become greater than the ground level $N_1$ (a population inversion), and the sample acts as an amplifier. Finally the path length contribution to the spectral peak intensity is intuitive; increasing the sample length increases the amount of energy absorbed from the beam. However this relationship is non-linear (doubling the path length does not double the absorption) and can be expressed using the Beer-Lambert law, equation 10.7. There is a similar relationship between concentration and absorption.

The features in the absorption and fluorescence spectra manifest themselves as broad peaks in intensity as a function wavelength or frequency, rather than ideal infinitesimally sharp lines. The broadening of the transition lines occur due to two

contributions: homogeneous and inhomogeneous broadening. Homogeneous broadening refers to broadening which affects the linewidth of each individual atom, and hence the system, in an identical way. The main sources of homogeneous broadening are due to collisions and the Heisenberg uncertainty principle. Collision broadening describes the effect of atomic motion, and the subsequent interactions, on the optical spectra. Collisions can result in the deformation of the atoms and as a consequence the perturbation of the energies of the outer electrons. In a gas the collisions are between atoms and other atoms or the walls of the container; in a solid the atoms interfere with the lattice phonons. This broadening will increase with temperature and/or pressure. Natural or intrinsic broadening occurs due to the finite frequency spread of the energy levels. The Heisenberg uncertainty principal states that it is not possible to know simultaneously the exactly position, x, and momentum, p, (or energy, E, and time, t) of a particle; measurements are inherently limited by the measurement process itself. Hence if an atom exists in an energy state for a limited amount of time $\delta t$ before spontaneous emission, the energy of the state will be uncertain (and vice versa);

$$\delta \mathrm{E} \times \delta \mathrm{t} \geq \hbar / 2 \tag{10.9}$$

where $\hbar = \mathrm{h} / 2\pi$. An atom with an uncertainty in its energy, has an associated uncertainty in the frequency, see equation 10.1.

$$\delta \upsilon = \frac{\delta \mathrm{E}}{\mathrm{h}} \approx \frac{\mathrm{h}}{2\pi \, \mathrm{h} \delta \mathrm{t}} \approx \frac{1}{2\pi \, \delta \mathrm{t}} \tag{10.10}$$

Inhomogeneous broadening classifies mechanisms which broaden the width of the whole system without broadening the lines of the individual atoms. In this type of broadening the individual atoms are considered to be distinguishable, and each atom has a different resonant frequency (or lineshape) for the same transition. The width of the whole system becomes spread due to the average of individual transition frequencies. One contribution to inhomogeneous line broadening is Doppler broadening. A Doppler shift in the emission frequency of an atom arises due to the motion of a particle relative to an observer (in an absorption peak this becomes a task of considering the motion of an atom relative to the frequency of the incoming radiation). The measured frequency increases as the observer and source move together and decreases as they recede.

$$\nu' = \nu\left(1 \pm \frac{v_x}{c}\right) \tag{10.11}$$

where $\nu$ is the emitted optical frequency and $v_x$ is the velocity of the atom in the direction of the observer. As the atoms are in random motion, the observed frequency $\nu'$ will depend on the magnitude and direction of $v_x$; this has the effect of making the atoms appear as though they are emitting radiation with a range of resonant frequencies. The individual Doppler shifted frequencies contribute to the broadened lineshape of the transition. Finally any phenomena which produces fluctuations in the energy levels of an atom contributes to the linewidth of the optical transition. This includes local pressure and temperature variations, and the random crystal fields felt by atoms due to the different positions they occupy within the network. For a detailed account of broadening mechanisms consult the text written by Svelto (1989).

### 10.1.3. FLUORESCENT LIFETIMES

An excited ion can decay at any time, t, from t = 0 to t = ∞. The lifetime characterises the typical time an electron exists in the excited state before returning to the ground state and depends on the active atom and the surrounding environment. Energy from the excited ion can be lost radiatively as fluorescence, or as a radiationless transition through interactions between the ion and the lattice. The total lifetime $\tau$ of an excited state is determined by a combination of all the possible radiative $\tau_{rad}$ and non-radiative $\tau_{nr}$ transitions.

$$\frac{1}{\tau} = \sum_j \left(A_{ij}^{nd} + W_{ij}^{nr}\right) \tag{10.12}$$

where $A_{ij}^{nd}$ and $W_{ij}^{nr}$ are the radiative and non-radiative transition probabilities from state i to state j. The total decay rate of the excited state, W, can be calculated directly from experiment as it is equal to the reciprocal of the total lifetime ($W=1/\tau$) which, in turn, is equal to the rate of decay of the observed fluorescence. The observed fluorescence decays, as a function of time t, following a simple exponential behaviour; $\tau$ is the time taken for the stored energy to fall to $1/e^{th}$ of its maximum value.

$$I_t = I_0 \exp^{-(t/\tau)} \tag{10.13}$$

where $I_0$ and $I_t$ are the intensities at t = 0 and t = t. As the active ions in an amorphous material lie in non-equivalent environments, it may not always be possible to approximate the fluorescence decay using a single exponential; the use of more than one exponential is required to represents the site to site variation in the probabilities of the different relaxation processes.

Non-radiative transitions essentially arise due to interactions between the network vibrations and the excited ion. This causes transitions between levels separated by energies equal to the lattice mode. If the gap between energy levels is small, non-radiative decay is essentially a single phonon process, the lifetime $\tau_{nr}$ of which is very short approximately the order of $10^{-13}$ s. If the energy gap is large (i.e. larger than the maximum phonon energy in the material), non-radiative transitions arise from multiphonon relaxations, the decay rate of which are determined by the number of phonons required to conserve energy. Most multiphonon processes are accompanied by radiative recombination. The non-radiative decay rate depends on the energy gap (the transition rate is inversely proportional to the exponential of the energy gap), the host material (including lattice-ion coupling, and crystal field effects) and the temperature (Reisfeld and Eckstein 1975, Layne et al 1977, Toratani et al. 1982).

For higher rare earth dopant concentrations non-radiative decay can also occur due to ion-ion cross relaxation mechanisms called concentration quenching. If a neodymium ion in the excited metastable state $^4F_{3/2}$ interacts with a closely coupled neighbouring $Nd^{3+}$ ion in the ground level, the excited ion can lose some of its energy by raising the ground state ion, resulting in both ions undergoing an intermediate transition to the $^4I_{15/2}$ level. The two ions then decay non-radiatively to the ground state, see figure 10.4. (Auzel 1973, Miniscalco 1991, Payne et al. 1995). It is of particular interest that according to the data collected by Miniscalco (1991) phosphates are the most resistant glass host to the phenomena of concentration quenching. Concentration quenching acts to reduce the fluorescence lifetime of the glass sample; ion-ion interactions increases the non radiative transition rate, but the radiative transition rate essentially remains constant; hence it can be seen from equation 10.12 that the total transition rate increases and the fluorescence lifetime must fall. This has a detrimental effect on the efficiency of optical devices such as lasers, and amplifiers.

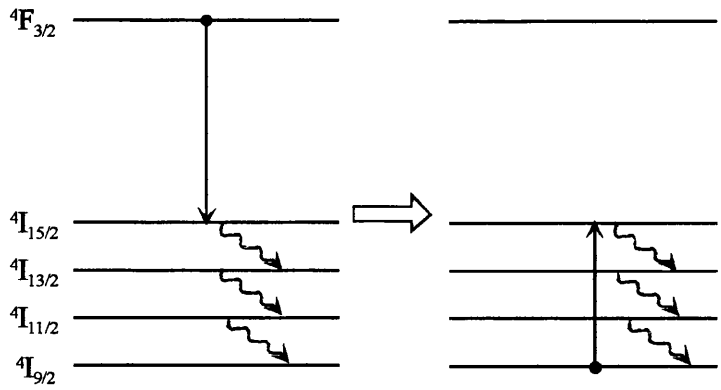


Figure 10.4. The cross relaxation process for trivalent neodymium. The two energy level systems represent a pair of interacting $Nd^{3+}$ ions. The 'wiggly' line indicates a non-radiative transition from $^4I_{15/2}$ to $^4I_{9/2}$ (after Miniscalco 1991).

A second type of concentration quenching involves the presence of hydroxyl groups in the phosphate glass (Toratani et al. 1982, Yan et al. 1995). The $OH^-$ group acts to reduce the fluorescence lifetime in phosphate glasses. Excited energy is quickly transferred between interacting ions, however it is lost whenever it is transferred to a rare earth ion which is coupled to an $OH^-$ quenching centre. Fast Fourier infrared absorption experiments have determined the water contamination in rare earth metaphosphate glasses to be less than 0.1mol% (Bowron et al. 1995); hence the rare earth content is expected to dominate the concentration quenching rate.

## 10.2. OPTICAL METHODS, APPARATUS AND DATA CORRECTION PROCEDURES

In this section the method, apparatus and data correction procedures of the various optical experiments are outlined. Initially the techniques required for the measurement of the fluorescence and absorption spectra for a selection of rare earth metaphosphate glasses are described. The subsequent experiments (determination of Brewsters angle and refractive index and the examination of concentration quenching effects) are employed to characterise and develop greater understanding of the behaviour of neodymium metaphosphate glass. Trivalent neodymium ions are technologically important and produce the most used lasing transition for research and industrial purposes. The samples for all the optical experiments were prepared in exactly the

same fashion; each sample initially had to be cut and then polished until two adjacent surfaces were flat and parallel. All the experiments were executed at room temperature

### 10.2.1. ABSORPTION AND FLUORESCENCE MEASUREMENTS

Both the absorption and fluorescence spectra were measured using an optical spectrum analyser AQ-6315A/B from Ando Electric Co. Ltd.(OSA) attached to a large calibre fused silica multimode patch cord (core diameter 400μm). The OSA allows for the measurement of a spectrum of light in the wavelength range 355-1750nm, and includes a built-in floppy disc drive and mini-printer. It has high sensitivity, high accuracy, excellent linearity and a wide dynamic range. To measure the absorption spectrum of a bulk REMG, the sample was illuminated using an approximately collimated beam from a tungsten lamp, and the optical fibre was placed next to the sample so that only the light which emerged after passing through the glass sample was recorded. The signal was investigated in the wavelength range 400 to 1750nm; the OSA had resolution of 5nm, sampling rate of 541 points, with the average number of readings at each wavelength interval being 10. All spectra were recorded four times; the position of the white light source, lens, and optical fibre were kept constant but the bulk rare earth glass sample was translated in the y and z direction (where the x direction is the optical axis); by examining the absorption through different sections of the glass, any optical path dependent features, due to the presence of internal thermal stresses etc, can be examined. The rare earth metaphosphate glasses studied were of a high optical quality and there was no measurable change in the different absorption spectra. Two background spectra were recorded for data correction purposes. A signal was measured in the absence of white light to investigate the wavelength dependence of the noise. The main sources of noise are the random fluctuations caused by spurious electronic signals produced by the detector, and amplification process of the OSA. The background noise was subtracted from each rare earth metaphosphate glass absorption spectra and the resultant $I_t$ is divided by the incoming signal $I_o$. The incident signal is the characteristic blackbody curve of the halogen bulb (this was measured after each absorption data set, being careful to retain the same geometry) minus the background noise, and multiplied (1 - R), where R is the Fresnel reflectance given in equation 10.5 (taking $n_t$

and $n_i$ to be 1.56 and 1 respectively). The absorption coefficient $\alpha$ was finally plotted as a function of wavelength by dividing the natural log of the normalised intensity $I_t/I_o$ by the sample path length, x (see equation 10.7).

The fluorescence measurements were obtained by exciting the sample with the focused beam of an argon ion laser ($\lambda$= 488nm, power 100mW). The fluorescence was collected using the same objective, split from the pump beam by a dichroic mirror and focused onto the wide core fibre. The apparatus required to measure the fluorescence of the bulk rare earth doped metaphosphate glasses are show in figure 10.5.

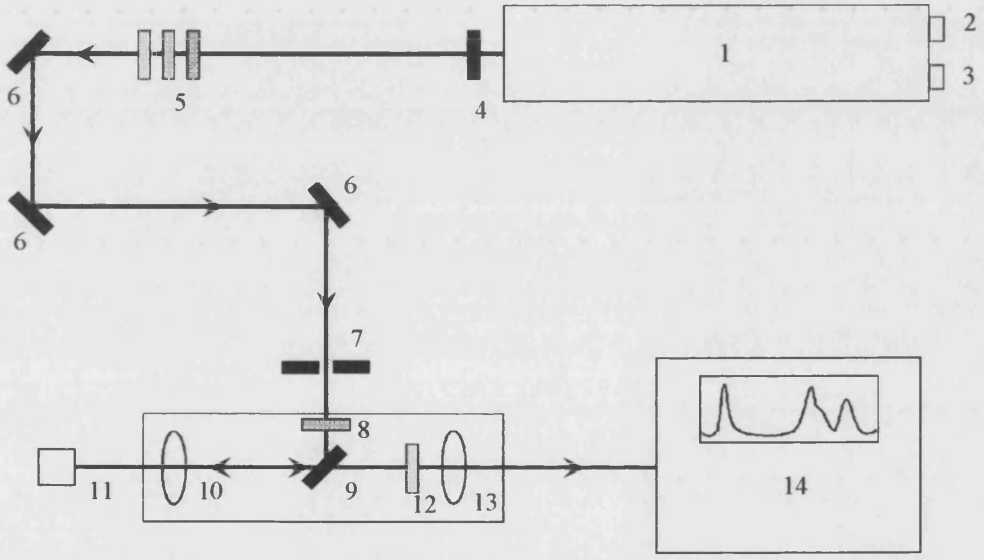


1. Argon ion laser
2. Screw to move the laser prism horizontally, required for beam alignment
3. Screw to move the laser prism vertically, required for wavelength selection
4. Safety flap
5. Neutral density filters
6. Mirrors
7. Pinhole
8. Plasma glow filter
9. Laser reflecting dichroic mirror
10. Focusing lens
11. Sample
12. Schott filter
13. Converging lens
14. Optical Spectrum Analyser (OSA)

Figure 10.5. Schematic diagram of the apparatus used for fluorescence measurements.

The fluorescence measurements were obtained by exciting the sample with a water cooled continuous wave argon ion laser, model Lexus 95 [figure 10.5 no. 1]. This laser is capable of a 4W maximum output when run in multimode operation, and has cavity length of 1m and a beam diameter of 1.3mm at the 514.5nm line. The cavity contains an argon gas plasma tube which is initially excited by ionising the gas with a high voltage. In single mode operation the back mirror is replaced with a prism wavelength selector, and the desired frequency can be chosen by changing the orientation of the prism with the screws located at the back of the laser casing [figure 10.5, no. 2,3]. The argon ion laser produces a large number of lasing lines in the green and blue regions of the visible spectrum.

On emerging from the laser tube the electromagnetic radiation passes through three neutral density filters [figure 10.5, no. 5]. These filters are optional and can be lowered into the path of the beam to reduce the intensity by varying amounts, 10%, 25% and 50%. They are usually only employed during the alignment of the optical equipment, i.e. when there is the possibility of causing damage to eyes or sensitive optical equipment. The electromagnetic radiation is then steered towards the sample using a network of mirrors [figure 10.5, no. 6]. The mirrors used in this system are broad band, visible type B1004.136 supplied by Melles Griot company, and are capable of reflecting a laser beam 45° in the wavelength range 400-700nm. They are made from BK7 having a reflectance of 99.0% and dimensions 25mm in diameter and 6mm thick. Filter no. 8, is an ID901003M filter acquired from Infrared Engineering (diameter 25mm, thickness 3mm). It is designed to block all the plasma glow lines generated in the laser cavity, due to the elevated temperatures reached, and allows only the lasers lines to pass. On hitting the dichroic mirror [figure 10.5, no. 9] the beam is passed though an angle of 45°. The dichroic mirror, from AG-electro Optics company, is highly reflective of the main argon ion laser wavelengths but is transparent to other wavelengths i.e. the returning fluorescence signal is allowed to pass through. The radiation is focused onto the sample using a long working distance objective lens [figure 10.5, no.10]. This lens is an SLWD PLN Achro from Nikon and has 20X magnification, 0.35 numerical aperture, and 20mm working distance. The lens is coated to protect it from carbonisation caused by the heating effect of the laser beam. The sample [figure 10.5, no.11] is mounted on a micropositioner with x, y, z

micrometers (Ealing Electro Optics plc.) allowing for maximisation of the laser focusing and consequently the signal. After exciting the sample the subsequent fluorescence is collected by the objective lens and passed though the dichroic mirror and a Schott colour glass filter OG515 [figure 10.5, no. 12]. The latter, purchased from Melles Griot, acts to block any stray laser light from reaching the OSA which would contribute to the noise of the spectrum. Finally the fluorescence is focused onto the wide core fibre by a condensing lens supplied by the Baker company [figure 10.5, no. 13]. This has 20X magnification and a focal length of 3mm. The end of the wide core fibre is mounted on another x y z, micropositioner which permits it to be positioned at the focal point. Safety is important at all times, goggles are always warn when the laser is on, the neutral density filters should be lowered when aligning the laser; a safety flap [figure 10.5, no. 4] has been fitted which automatically cuts the laser beam if the interlock is tripped by opening the door.

Two fluorescent wavelength ranges were examined, 400-1750nm for the glasses doped with erbium and neodymium and 400-1150nm for the remaining six rare earth doped samples, where there was no structure present beyond 1150nm in the preliminary runs. The sampling rate was 350 points (550 for Nd, and Er), averaged 30 times at each wavelength interval, with a resolution of 5nm. The fluorescence signals were corrected by measuring and subtracting the background spectra over the same wavelength range.

### 10.2.2. BREWSTERS ANGLE MEASUREMENTS

Brewsters angle $\theta_B$ measurements were made on a bulk sample of $(Nd_2O_3)_{0.010}(La_2O_3)_{0.260}(P_2O_5)_{0.730}$. The ternary neodymium lanthanum metaphosphate glass was mounted upon a spectrometer capable of measuring the angle, $\theta$, the surface of the glass made with the direction of propagation of the laser beam, to an accuracy of $\pm$ 1 minute. The incoming argon ion laser beam was polarised parallel to the plane of incidence. Measurements of the reflected beam intensity were made between $\theta$ = 40-70° in one degree intervals, using a photodiode. The experiment was repeated twice (increasing and decreasing angle) and at three different wavelengths, namely 457nm, 488nm and 514nm. Brewsters angle can be determined from finding the angle at which the E-field oscillations are confined normal to the incident plane, and hence

the reflectance, R, falls to zero. The reflectance in equation 10.5 can be rewritten using Snells law to give,

$$R = \frac{-n^2 \cos\theta + \sqrt{n^2 - \sin^2\theta}}{n^2 \cos\theta + \sqrt{n^2 - \sin^2\theta}} \qquad (10.14)$$

where n is the refractive index of the sample, here ternary metaphosphate glass (Fowles 1974). The measured data does not take this exact form, but can be represented by modifying equation 10.14 by the addition of two parameters: A is the scaling factor between the reflectance and the measured intensity I, B accounts for the fact that the intensity never completely falls to zero (this is a consequence of imperfections in the polished surface of the sample and background light). Hence equation 10.14 becomes:

$$I = A\left(\frac{-n^2 \cos\theta + \sqrt{n^2 - \sin^2\theta}}{n^2 \cos\theta + \sqrt{n^2 - \sin^2\theta}}\right) + B \qquad (10.15)$$

The intensity data as a function of angle was fitted using a method of non-linear least squares fitting which minimises the square of the errors in the x and y direction. $\theta_B$ and the refractive index are directly linked, see equation 10.6; hence on finding Brewsters angle $\theta_B$ the refractive index can be calculated.

### 10.2.3. FLUORESCENT LIFETIMES MEASUREMENTS

The lifetime of a series of neodymium, and neodymium lanthanum doped phosphate glasses have been measured to investigate the effect of $Nd^{3+}$ concentration quenching in these metaphosphate glasses. As previously stated, phosphate glasses manufactured using the techniques outlined in chapter three produces glass samples close to the metaphosphate composition, regardless of the starting concentration ratios. Hence, if a change in concentration of active ion, in this case neodymium, is required, it is necessary to add an additional rare earth oxide to act as a 'dummy' dopant: the sum of neodymium oxide and 'dummy' rare earth oxide equals 25mol%. For lifetime experiments lanthanum oxide was chosen. Trivalent lanthanum has a closed shell configuration i.e. no unpaired electrons; consequently it is transparent at the pumping and $Nd^{3+}$ fluorescence wavelengths (see figure 11.11).

A sample of neodymium lanthanum metaphosphate glass was illuminated using a nitrogen laser with characteristic wavelength of 337nm and a pulse lifetime the order of 200ps. The intensity of the fluorescence was recorded as a function of time using a silicon detector fed directly into a storage oscilloscope. The lifetime measurements were averaged 257 times, and three separate readings were taken on each sample. Filters were installed between the samples and the photodiode to eliminate emission arising from the $^4F_{3/2} \rightarrow {}^4I_{9/2}$ transition at 899.5nm. The peak at 1324.8nm ($^4F_{3/2} \rightarrow {}^4I_{13/2}$) is very weak in comparison with the $^4F_{3/2} \rightarrow {}^4I_{11/2}$ ($\lambda$ = 1056.1nm) transition, so it can be assumed, that within experimental error, the measured fluorescence lifetime arises solely from the $^4F_{3/2} \rightarrow {}^4I_{11/2}$ transition. The measurement apparatus has a resistance and hence an associated response lifetime. This was calculated by directly measuring the lifetime of the laser pules; it was found to have a value of 2.0μs. This is sufficiently small enough to be sure that the measured fluorescence lifetime is the result of $Nd^{3+}$ ion transitions, and is not affected by the response of the system.

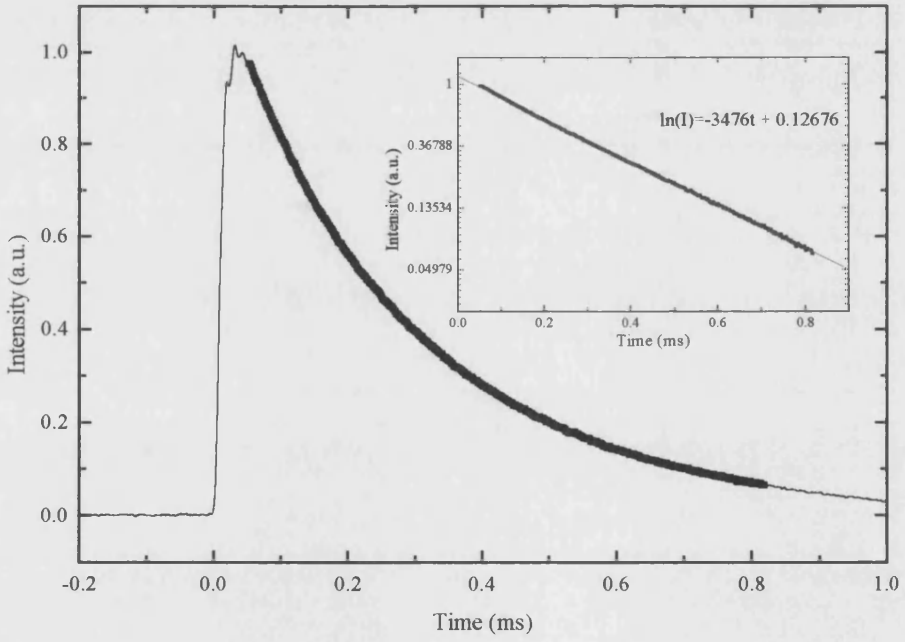


Figure 10.6. The decay of fluorescent intensity with time, in $(Nd_2O_3)_{0.009}(La_2O_3)_{0.240}(P_2O_5)_{0.751}$. The insert shows the same data, but the exponential intensity decay has been plotted on a logarithmic scale.

To find the time $\tau$ it takes for the intensity of the neodymium ions to fall e-fold, at various concentrations, the intensity data was initially normalised using $(I_t-I_o)/(I_m-I_o)$ where $I_t$, is the intensity at time t, and $I_o$, $I_m$ are the minimum, and maximum intensities respectively (see figure 10.6). The exponential section of the resulting spectrum was then isolated. This is subsequently plotted on a semi-logarithmic scale (see insert in figure 10.6). The lifetime is finally calculated by fitting a least squares line to the data, the gradient of which is equal to $-1/\tau$ (equation 10.13).

## 10.3. BASIC LASER THEORY

The first material to exhibit light amplification by stimulated emission was a three level pulsed ruby laser (1960). Four level laser systems were soon to develop, and in many cases have replaced ruby lasers (He-Ne, and Nd:YAG); an example of a four level lasing scheme is shown in figure 10.7. Before a sample will exhibit lasing three conditions must be satisfied:

a) A population inversion must be created. This requires more atoms in the upper lasing level than the lower lasing level, and is usually achieved either by optical or electrical pumping. A population inversion can only occur in systems containing more than two energy levels.

b) The excited state has to be a metastable state; the lifetime of the spontaneous emissions must be sufficiently long lived that stimulated emission transitions dominate.

c) The emitted photons must be confined in the system long enough that they stimulate other emission, thus perpetrating the cascade effect. This is usually achieved by placing reflecting mirrors at either end of the optical cavity.

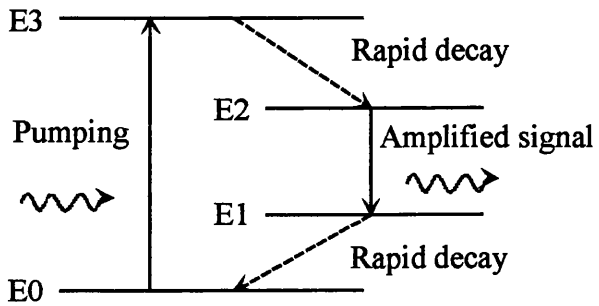


Figure 10.7. Four level laser scheme.

Absorption of pump radiation excites ground state (labelled E0 in figure 10.7) electrons into an energy level (E3) higher than the upper lasing transition level (E2). The ion (or molecule) subsequently loses some of its excess energy through non-radiative relaxations into the energy level E2. In a lasing material the decay from E3→E2 is rapid ($\tau_{32}$ is small) and level E3 will remain almost empty. If E2 is a metastable state, the spontaneous lifetime $\tau_{21}$ is much longer than $\tau_{32}$ and the ions cannot readily decay to the ground state; thus the population of level E2 increases. Once a population inversion ($N_2 > N_1$ where $N_2$ and $N_1$ are the population (per unit volume) of the upper and lower lasing levels) has been established, a photon from a spontaneous emission event (with wavelength corresponding to the energy gap $\Delta E$ = E2-E1) will produce a simulated emission photon, which in turn stimulates further radiative transitions, resulting in a cascade effect. In a three level lasing system the lower lasing level is the ground state; hence to create a population inversion over half the ground state ions have to be raised into the upper lasing level. In a four level system the lower lasing level is not thermally populated, so any electrons excited to E2 are immediately available for a population inversion. The non-radiative transition rate between E1→E0 is usually rapid, which helps to maintain a favourable ratio between $N_1$ and $N_2$ with moderate pumping. Hence, in general, it is much easier to produce a population inversion in a four level system than in one with three levels. A comprehensive text on the field of lasers is written by Svelto (1989)

The gain coefficient $\alpha_g$ characterises the increase in the beam irradiance as it propagates through the medium; it can be determined from the product of the stimulated emission cross section $\sigma$ and the population inversion between the initial and final laser levels ($N_2$-$N_1$) (Weber et al 1981, Svelto 1989):

$$\alpha_g = \sigma\left(N_2 - N_1\right). \tag{10.16}$$

The stimulated emission cross section has dimension of area, and depends only on the particular transitions.

### 10.3.1. NEODYMIUM GLASS LASERS

Neodymium doped lasers have received the greatest commercial application of any of the solid state glass lasers produced due to efficient pumping by flashlamps and lasers sources, the presence of strong absorption bands in the visible and near infra red, and their ease of operation at ambient temperatures because the neodymium dopant is a four level lasing system (Kishida et. al 1979, Hall and Weber 1991, Miura et al. 1997). The host material can either be in the form of crystals (i.e. $Y_2Al_5O_{12}$) or glasses (i.e. phosphate or silicate). Glasses have many advantages over crystalline hosts. (Kozlovsky et al. 1986, Rapp 1987, Urquhart 1988, Weber 1990, Elliot 1990, Hall and Weber 1991):

a) Glasses are usually easier to fabricate with uniform composition compared with high quality crystals. They can be produced in an array of sizes and shapes, which leads to lower costs. Glass properties can also be optimised to minimise undesirable effects such as low thermal conductivity.

b) The topological disorder associated with an amorphous material produces variations in the local field, and broadening of the Stark energy levels (~100$cm^{-1}$). As a consequence glass materials exhibit characteristics that can be exploited in laser fabrication. Splitting of the energy level means that glasses have wider and stronger pump absorption bands than their crystalline counterparts. Lasing can be achieved throughout this homogeneously broadened level; hence rare-earth glass lasers have a degree of tunability not readily available in crystals. It also makes them the preferred material for short pulse generation (>1ns) using the technique of mode locking.

c) Glasses can usually be doped with larger concentrations of active ion than crystalline hosts.

d) Oxide glass hosts are optically transparent over a wide range of wavelengths. Transparency at short wavelengths is required so the optical pump efficiency is optimised, and transparency at longer wavelengths is desired to maximise the output intensity of the laser radiation.

Phosphates have emerged, with silicates, and to a lesser extent fluorides, as the principal glasses used for lasers. Phosphates do not offer the extreme property values (lifetime, effective linewidth, emission cross section, low optical losses) that can be exhibited by some of the other glass laser hosts, but have gained commercial success

through good overall combination of characteristics (Marion and Weber 1991). While silicates generally have a greater resistance to environmental effects, such as water contamination, silica can only incorporate very small amount of lanthanide ions (upper limit of ~1wt%) before clustering, phase separation and concentration quenching effects the efficiency of the material; this is a result of the compact network formed by the silica tetrahedra $S_iO_4$ and the bridging oxygen ions (Payne et al. 1995). While silicates might be attractive for pulsed operation, phosphates are more useful in the field of continuous wave operation. Phosphates generally have narrower emission bandwidth than silicate laser glasses having similar concentrations, hence they require a lower pumping threshold; the emission cross section, and subsequently gain (equation 10.16), is inversely proportional to the fluorescence linewidth, so a sharper bandwidth means a lower threshold power (Deutschbein and Pautrat 1968, Urquhart 1988, Weber 1990). Rare earth metaphosphate glasses have also shown resistance to water contamination, which is essential if these materials are to be used in optical devices.

## 10.4. OPTICAL FIBRES

Optical fibres are dielectric fibres which can conduct light from one point in space to another i.e. glass fibres that function as waveguides for light. Consider light propagating though a fibre, which has a higher refractive index than its' surrounding medium (air or a cladding material); the light will be totally internally refracted, if it is coupled into the fibre such that it falls upon the fibre cladding interface at angle equal to or greater than the critical angle $\theta_c$. The critical angle is defined as

$$\sin\theta_c = \frac{n_c}{n_f} \qquad (10.17)$$

where $n_c$ and $n_f$ are the refractive index of the cladding and fibre respectively, ($n_c < n_f$) see figure 10.8. If the light strikes the fibre cladding interface at an angle less than the critical angle (the angle of incidence of the light on the face of the fibre $\theta_i$ is greater than $\theta_{max}$, see figure 10.8), the wave will only be partially reflected at each reflection.

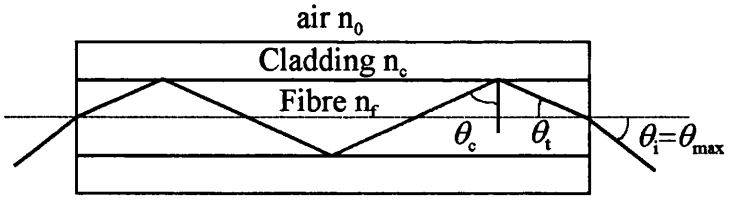


Figure 10.8. Total internal reflection in an optical fibre. $\theta_{max}$ is the maximum value of the incident angle $\theta_i$ for which the light waves will be totally internally reflected. The refractive index of the fibre $n_f$ needs to be greater than the refractive index of the cladding $n_c$.

The cladding is wrapped around the fibre to protect it from the environment; the presence of dirt, oil, and moisture on the surface of the fibre would result in leakage of light. An optical fibre carries information by guiding and confining light in the core of the optical fibre through a number of total internal reflections. The efficiency is determined by the quality of the fibre cladding interface and the absorption characteristics of the material; both effects limit the number of total internal reflections.

Optical fibres can support more than one guided waveforms (or modes). The total number of modes that can propagated in a fibre depends on the V parameter (Marcuse 1981):

$$V = \frac{2\pi a}{\lambda} NA \tag{10.18}$$

where $\lambda$ is the free-space wavelength of the light being carried by the core and a is the core radius. For a step profile circular fibre the core will only support a single mode if $0<V<2.405$ (Synder and Love 1996). The numerical aperture NA of a clad fibre is the square root of the light gathering power of the fibre cladding system. It can be calculated from

$$NA = n_0 \sin\theta_{max} = \left(n_f^2 - n_c^2\right)^{1/2} \tag{10.19}$$

where $n_0$ is the refractive index of the air, and $\theta_{max}$ defines the half-angle of the light acceptance cone of the fibre (Hecht 1987).

Rare earth doped fibre lasers and amplifiers provide low cost, easily manufactured, alternative to crystalline mediums, and which more importantly produce lasing wavelengths that have potential for telecommunications, sensing, medicine and spectroscopy. High quality fibre lasers have many desirable properties: low scattering and absorption losses, and good optical confinement which results in a large population inversion density as the light is confined in the transverse direction over the distance required for its absorption, as a consequence the pumping thresholds can be lower. Another advantage of the fibre geometry is that the high surface area to volume ratio means they exhibit efficient heat dissipation. Two extensive reviews of the field of fibre lasers have been written by Urquart (1988) and Hall and Weber (1991).

### 10.4.1. FABRICATION OF SILICON CLAD NEODYMIUM DOPED LANTHANUM METAPHOSPHATE GLASS FIBRE

A clad fibre has been produced by drawing a rod of rare earth doped phosphate glass placed inside a tube of silica. Lanthanum metaphosphate glass doped with 1mol% of neodymium ($(Nd_2O_3)_{0.010}(La_2O_3)_{0.260}(P_2O_5)_{0.730}$) was chosen as the fibre core material. This sample exhibits little or no concentration quenching (see section 11.2.3), unlike binary neodymium metaphosphate glass, yet produces a significant amount of fluorescence and retains the traits that make the metaphosphate composition desirable in device application, most notably resistance to water contamination.

Manufacture of an optical fibre was executed using a fibre drawing tower (figure 10.9). A hollow silica tube (outer diameter 20mm, wall thickness 2mm) was first lowered into a resistance ring furnace until it's middle occupied the central localised heat zone (~8-10mm). The furnace was then heated to approximately 2100°C. While the furnace was operational it was flooded with argon to prevent oxidisation of the graphite furnace element. At this temperature the silica softened and by pulling the end section of the tube, the hollow silica rod necked thus producing a tapered end. The furnace was then cooled to 1900°C and a cylinder of neodymium glass ($(Nd_2O_3)_{0.010}$ $(La_2O_3)_{0.260}$ $(P_2O_5)_{0.730}$) was placed into the silica tube. The tapered end, of the now closed silica tube, was slowly and carefully pulled down by hand and attached to a rotating drum. The fibre was then fed into the electric resistance furnace

at a rate of 10mm $min^{-1}$ and the drum rotated to give a pull rate of 10-13m $min^{-1}$. As the tube passed through the hot zone in the furnace the temperature of the preform increased and consequently it collapsed onto the rod as it was drawn into a fibre. Collapsing and drawing are performed simultaneously to reduce the internal thermal stresses which might arise due to the different thermal expansions of the two mediums, and can result in cracking at the interface.

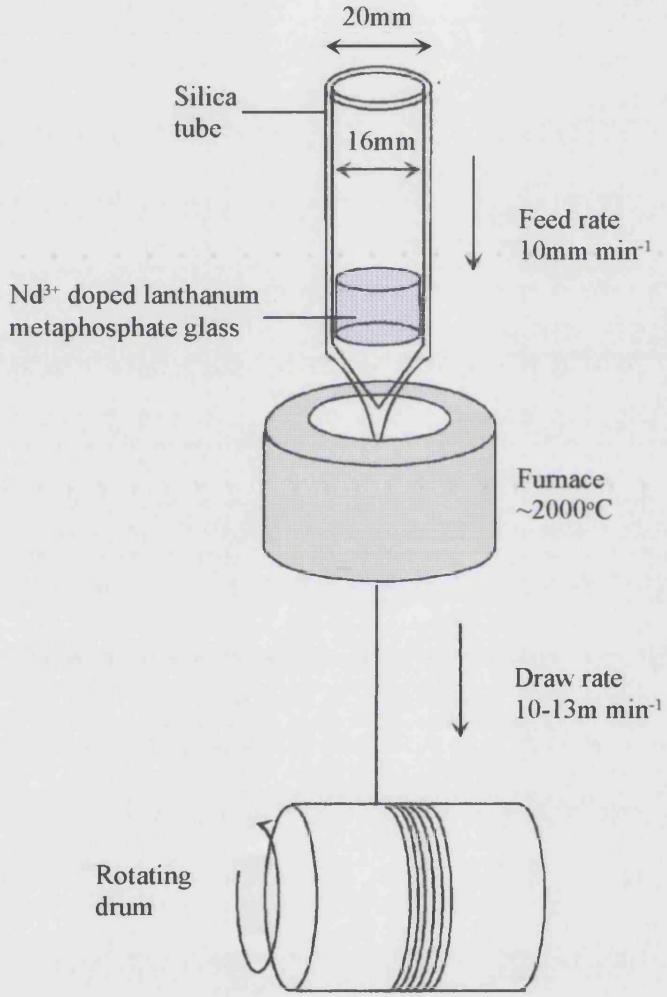


Figure 10.9. A schematic of the fibre drawing set apparatus.

The ratio of the feed ($v_{feed}$) and draw ($v_{draw}$) velocities give the ratio of the cross sectional areas of the rare earth doped phosphate rod ($R_{rod}$) to the fibre core ($R_{fibre}$) (it is also the ratio of the cross sectional area of the silica tube to the cladding):

$$\frac{R_{rod}^2}{R_{fibre}^2} = \frac{v_{draw}}{v_{feed}} \qquad (10.20)$$

A length of fibre of approximately 10m was drawn and coiled onto the rotating drum. During the fibre pulling process it was decided to vary the draw rate so that the final optical fibre had an a selection of radiuses. The external diameters were measured using a micrometer and found to vary between approximately 0.4 and 0.7mm.

Upon cleaving the optical fibre the end of the REMG core shattered. It is believed that this is probably a consequence of thermal stresses which are introduced into the fibre as a results of a thermal expansion mis-match between silica and $Nd^{3+}$ doped lanthanum metaphsophate glass. The linear thermal expansion of amorphous silica is one of the lowest of all of the glass hosts. At 300°C the measured linear thermal expansion for supersil, which is a high quality fused $SiO_2$ supplied by Heraus, is $\sim 7\times10^{-7}K^{-1}$. There is limited thermal expansion data available for REMGs, but the low temperature dependency of lanthanum metaphosphate glass is shown in figure 9.22; at 300°C the linear thermal expansion is an order of magnitude larger than that of silica ($\sim 7\times10^{-6}K^{-1}$). The fibre was redrawn in the hope that the increase in the surface area to volume ratio, associated with the production of a thinner sample, would lead to a reduction in the thermal stresses. A length of the silica clad neodymium lanthanum phosphate glass was inserted into a second silica jacket measuring approximately 0.4mm in diameter, and redraw using the same technique, but with a feed rate of 30mm $min^{-1}$ and a drum rotation rate of 1.5m $min^{-1}$. The resulting fibre was much thinner (approximately 105μm), flexible and more importantly produced a good surface upon cleaving.

This drawn sample represents the first successful attempt to create a fibre from a rare earth metaphosphate glass. Being able to produce REMGs in the form of a clad fibre allows protection of the core from environmental effects which is essential for practical applications, and represents a geometry favoured for many devices in the fields of optics and telecommunications. In section 11.2.4 the results from several basic optical experiments, which are needed to characterise the fibre, are presented.

# CHAPTER ELEVEN

## RESULTS AND DISCUSSION OF OPTICAL EXPERIMENTS

The incorporation of large quantities of dopants into glass networks modifies the energy level structure, and produces the necessary requirements for the manufacture of non-linear optical devices such as lasers and amplifiers for the telecommunication industry. Spectral investigations, such as optical absorption and fluorescence provides information on the energy levels, valency and local symmetry of ions incorporated in a host material, which are essential for understanding and using the magnetic and magneto-optical properties of rare earth metaphosphate glasses. Several rare earth metaphosphate glasses have already been examined using absorption and fluorescence techniques: samarium (Farok et al. 1992, to be published), europium (Farok et al. 1994), holmium (Farok et al. 1996). However, the present investigation provides a more extensive description of the optical spectra extending previous results by substantially increasing the wavelength range over which the spectra were recorded and studying additional metaphosphate glasses modified with praseodymium, neodymium, terbium, dysprosium and erbium. The second part of this optical investigation (section 11.2) focuses solely on the samples which have trivalent neodymium as the active ion i.e. binary neodymium or ternary neodymium lanthanum metaphosphate glasses. The effective linewidth of the $^4F_{3/2} \rightarrow {}^4I_{11/2}$ transition, lifetime as a function of concentration and the refractive index, has been determined in bulk samples, and fundamental experiments have be made to characterise the properties a silica clad optical fibre with a core of $(Nd_2O_3)_{0.010}(La_2O_3)_{0.260}(P_2O_5)_{0.730}$.

## 11.1. ABSORPTION AND FLUORESCENCE OF RARE EARTH METAPHOSPHATE GLASSES

The data for the eight rare earth metaphosphate glasses (composition given in table 11.1) are presented graphically in figures 11.1-11.8, and in table form 11.2-11.17. Each figure relates to an individual lanthanide doped metaphosphate glass and contains two graphs; the top spectrum is the absorption signal and the lower graph is the recorded fluorescence spectrum, both are plotted as a function of wavelength. The two tables per sample summarise the measured absorption and fluorescence line peaks of the glasses, compared with the same rare earth element in a different host material. The transitions, which are responsible for these peaks, are also assigned. For some of the absorption spectra features in the rare earth metaphosphate glasses, a range of wavelengths have been quoted (column 1, table 11.2, 11.4, 11.12, 11.14, 11.16); this is necessary when the absorption is very high. In such cases the position of the apex of the peak is unknown and the exact wavelength of the transition cannot be defined (unless the sample path length x is reduced), hence it is impossible to distinguish whether the line represents one or more transitions. Some of the reference absorption and fluorescence peaks (column 2, tables 11.9, 11.10, 11.11, 11.12, 11.14), are also presented as a range of wavelengths; this range encompasses all the transitions between Stark components, which are a consequence of the splitting of the active ion energy levels due to the crystal fields of the host. These individual peaks are not resolvable in glasses due to the topological disorder characteristic of these materials; however they do contribute to the inhomogeneous broadening of the peak width. The peak width also suffers a degree of thermal broadening, as all measurements were recorded at room temperature. At this temperature all the absorption features in REMGs are expected to arise from transitions originating at the ground state (with the exception of europium) as this is the only level which will be significantly populated according to the Boltzmann distribution (see equation 10.8). Generally fewer lines occur in the absorption spectra than the emission spectra of the same sample. This is because electrons which give rise to the absorption spectrum originate only from the lowest lying energy level, consequently there are fewer possible transitions than the emission spectrum in which the electrons are distributed over a range of excited states.

| Rare earth dopant | Atomic number | Final rare earth composition (mol%) |
|---|---|---|
| Pr | 59 | $(Pr_2O_3)_{0.239}(P_2O_5)_{0.761}$ |
| Nd | 60 | $(Nd_2O_3)_{0.234}(P_2O_5)_{0.766}$ |
| Sm | 62 | $(Sm_2O_3)_{0.195}(P_2O_5)_{0.805}$ |
| Eu | 63 | $(Eu_2O_3)_{0.218}(P_2O_5)_{0.782}$ |
| Tb | 65 | $(Tb_2O_3)_{0.263}(P_2O_5)_{0.737}$ |
| Dy | 66 | $(Dy_2O_3)_{0.225}(P_2O_5)_{0.775}$ |
| Ho | 67 | $(Ho_2O_3)_{0.208}(P_2O_5)_{0.792}$ |
| Er | 68 | $(Er_2O_3)_{0.239}(P_2O_5)_{0.731}$ |

Table 11.1. The composition of the rare earth metaphosphate glasses studied using absorption and fluorescence techniques.

**1) $(Pr_2O_3)_{0.239}(P_2O_5)_{0.761}$**

At present the magnetic properties are best understood for the metaphosphate glass modified by praseodymium. A comparative study of specific heat and low frequency Raman scattering at low temperatures of lanthanide metaphosphate glasses and pentaphosphate single crystals has established the presence of low energy singlet-singlet magnetic excitations in the materials containing Pr ions (Carini et al. to be published). Knowledge of the rare earth ion valence state, and how it relates to the optical absorption and fluorescence, is essential for understanding and using these magnetic properties. Generally rare earth ions in metaphosphate glasses have a valence 3, as this is the most stable state of the majority of rare earth ions. However in the case of praseodymium, uncertainty as to the valence state arises because it can be stable as $Pr^{4+}$ i.e. $PrO_2$, $PrF_4$ or even as mixed valence (+3 and +4) oxidation states, as in the case of $Pr_6O_{11}$.

a) Absorption Spectrum

All the peaks correspond to transitions between the ground state $^3H_4$ and excited states inside the $4f^2$ configuration of the $Pr^{3+}$ ion. Within the wavelength range studied, all the transition were of an electric dipole nature (Sayer et al. 1955). The

characteristic peaks have been documented in the absorption spectrum of many different materials doped with trivalent praseodymium ions, yttria-stabilized zirconia single crystals (Savoini et al. 1997), ZBLAN glass (Remilieux et al. 1996), chloride (Moeller and Brantley 1950, Sayer et al.1955), sulphate glass (Lakshman and Ratnakaram 1988), ethylsulfate crystals (Gruber 1963) and $CsCdBr_3$ (Merdoch and Cockroft 1996)

| Wavelength (nm) $(Pr_2O_3)_{0.239}(P_2O_5)_{0.761}$ | Wavelength (nm) (Carnall et al. 1968) | Transition (Carnall et al. 1968) |
|---|---|---|
| 439.2 | 431.7 | $^3H_4 \rightarrow {}^3P_2$ |
| 447.3 | 450.2 | $^3H_4 \rightarrow {}^1I_6$ |
| | 454.4 | $^3H_4 \rightarrow {}^3P_1$ |
| 467.5 | 467.5 | $^3H_4 \rightarrow {}^3P_0$ |
| 482.4 | | |
| 589.0 | 576.9 | $^3H_4 \rightarrow {}^1D_2$ |
| 1010.2 | 1007.9 | $^3H_4 \rightarrow {}^1G_4$ |
| 1426.0 - 1561.0 | 1458.8 | $^3H_4 \rightarrow {}^3F_4$ |
| | 1558.7 | $^3H_4 \rightarrow {}^3F_3$ |

Table 11.2. The measured wavelengths of the absorption lines in $(Pr_2O_3)_{0.239}(P_2O_5)_{0.761}$ compared with the energy levels of a $Pr^{3+}$ aquo-ions in a dilute acid solution (Carnall et al. 1968).

b) Fluorescence Spectrum

The strong fluorescence in $Pr^{3+}$ ions originates from the $^3P_0$, $^3P_1$, $^1D_2$ levels. The 640nm ($^3P_0 \rightarrow {}^3F_2$) transition dominates the spectrum and produces a characteristic red-orange luminescence when the sample is excited. This has also been observed in the fluorescence spectrum of $Pr^{3+}$ doped zinc tellurite glass (Kanoun et al. 1990). These workers also recorded a strong peak at 494nm corresponding to the $^3P_0 \rightarrow {}^3H_4$ transition; however as the Pr concentration was increased (from 0.5 to 12wt%), they found the $^3P_0 \rightarrow {}^3H_4$ was reabsorbed and the $^3P_0 \rightarrow {}^3H_6$ luminescence transition was enhanced. In praseodymium metaphosphate glass, which by definition contains a large concentration of $Pr^{3+}$ ions, the 500nm feature is not visible. Regions of the spectrum are similar to the data collected in $Pr^{3+}$ doped materials such as zirconia single crystals

(Savoini et al. 1997), $CsCdBr_3:Pr^{3+}:Tm^{3+}$ crystal (Merdoch and Cockroft 1996), ZBLAN (Remillieux et al. 1996), and triply ionized Pr (Sugar 1965).

| Wavelength (nm) $(Pr_2O_3)_x(P_2O_5)_{1-x}$ | Wavelength (nm) (Carnall 1968) | Transition (Carnall 1968) |
|---|---|---|
| 612.3 | 601.0 | $^1D_2 \rightarrow {}^3H_4$ |
| | 615.4 | $^3P_0 \rightarrow {}^3H_6$ |
| | 621.2 | $^3P_1 \rightarrow {}^3F_2$ |
| 640.8 | 643.0 | $^3P_0 \rightarrow {}^3F_2$ |
| 681.3 | 675.7 | $^3P_1 \rightarrow {}^3F_3$ |
| | 690.6 | $^1D_2 \rightarrow {}^3H_5$ |
| 700.8 | 696.9 | $^3P_1 \rightarrow {}^3F_4$ |
| | 701.8 | $^3P_0 \rightarrow {}^3F_3$ |
| 724.8 | 724.6 | $^3P_0 \rightarrow {}^3F_4$ |
| 882.3 | 859.1 | $^1D_2 \rightarrow {}^3F_2$ |
| | 877.2 | $^3P_1 \rightarrow {}^1G_4$ |

Table 11.3. The measured wavelengths of the fluorescence lines in $(Pr_2O_3)_{0.239}(P_2O_5)_{0.761}$ compared with the energy levels of $Pr^{3+}$ aquo-ions in a dilute acid solution (Carnall et al. 1968).

Correspondence between glass spectra and those of materials known to contain $Pr^{3+}$ ions leads to the conclusion that in the metaphosphate glass praseodymium ion exists in a trivalent state - in spite of the fact that the starting material $Pr_6O_{11}$ is a mixed valence (+3 and +4) oxide. The optical transitions assigned to the energy levels of the praseodymium ions indicate that both the absorption and fluorescence spectra show only transitions characteristic of trivalent praseodymium ions. This conclusion is important for continuing development of an understanding of the physical nature of the large distribution of low lying CF excitations, which determine the low temperature thermal and optical properties (Carini et al. 1997,1998).

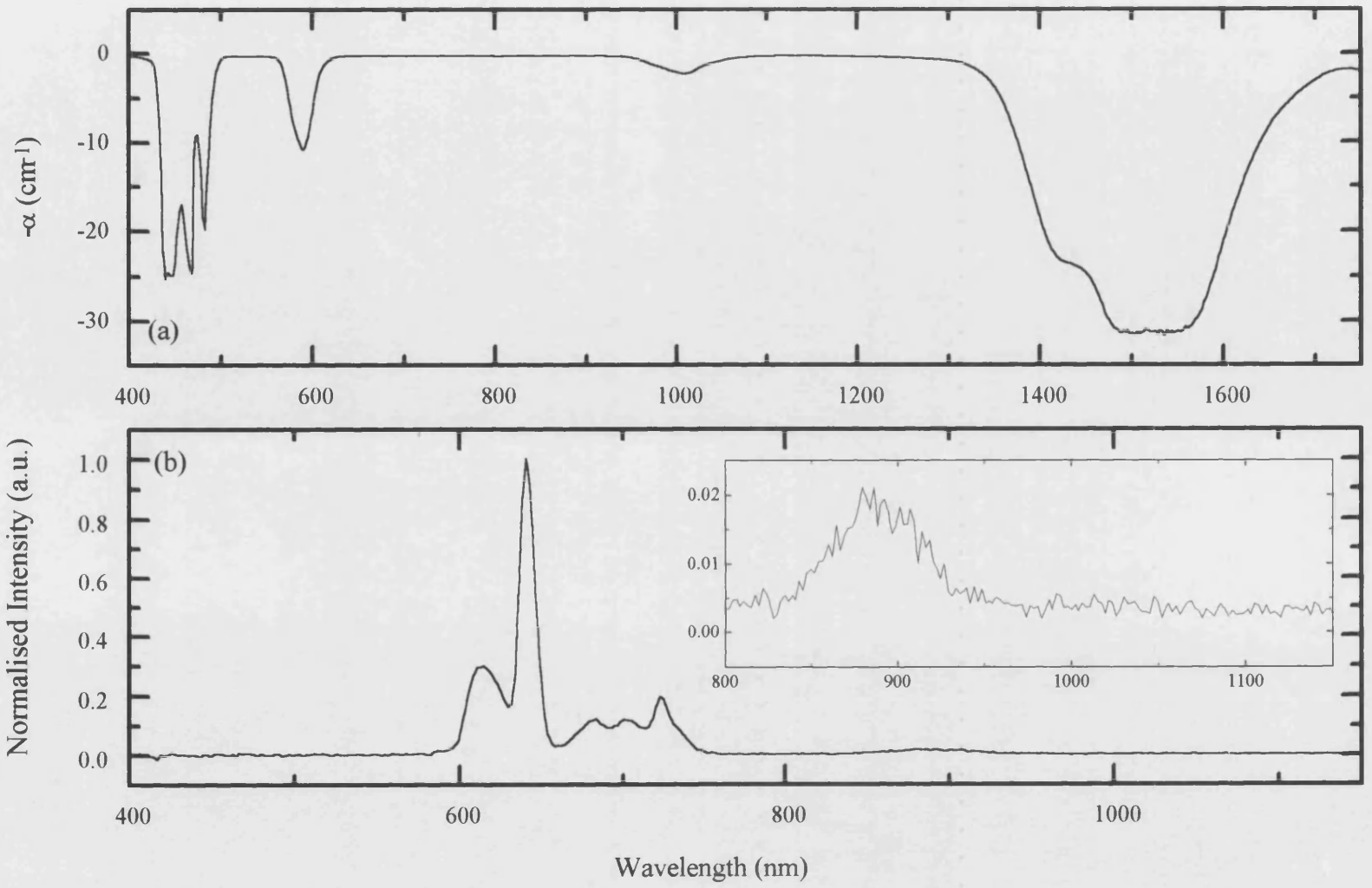


Figure 11.1. The (a) absorption and (b) fluorescence spectra of praeseodymium metaphosphate glass

**2) $(Nd_2O_3)_{0.234}(P_2O_5)_{0.766}$**

Neodymium doped lasers have received the greatest commercial application of any of the bulk glass lasers produced, due to efficient pumping by flashlamps and laser sources on account of the strong absorption bands in the visible and near infra red region, and ease of operation at ambient temperatures, see section 10.3.1 (Weber 1990). The $^4F_{3/2} \rightarrow {}^4I_{11/2}$ transition at 1060nm represents the most widely used lasing transition in a glassy host; it is stimulated using a four level pumping system. Trivalent neodymium has been made to lase in many different glass hosts, silicates, phosphates, borates, fluorides and in many different geometries, bulk, fibres, microspheres (Urquart 1988, Hall and Weber 1991, Kiyotaka et al. 1997).

a) Absorption Spectrum

All the absorption peaks arise from exciting electron in the ground $^4I_{9/2}$ state.

| Wavelength (nm) $(Nd_2O_3)_{0.234}(P_2O_5)_{0.766}$ | Wavelength (nm) (Carnall et al. 1968) | Transition (Carnall et al. 1968) |
|---|---|---|
| 429.7 | 432.8 | $^4I_{9/2} \rightarrow {}^2P_{1/2}$ |
| 462.1 | 465.0 | $^4I_{9/2} \rightarrow {}^4G_{11/2}$ |
| 468.9 | 472.7 | $^4I_{9/2} \rightarrow {}^2G_{9/2}, {}^2D_{3/2}, {}^2P_{3/2}$ |
| 477.0 | 479.5 | $^4I_{9/2} \rightarrow {}^2K_{15/2}$ |
| 514.8 | 515.4 | $^4I_{9/2} \rightarrow {}^4G_{9/2}$ |
| 518.5 | 525.9 | $^4I_{9/2} \rightarrow {}^4G_{7/2}$ |
| 529.6 | 534.0 | $^4I_{9/2} \rightarrow {}^2K_{13/2}$ |
| 574.2 - 599.8 | 577.6 | $^4I_{9/2} \rightarrow {}^2G_{7/2}$ |
| | 583.0 | $^4I_{9/2} \rightarrow {}^4G_{5/2}$ |
| 626.8 | 636.0 | $^4I_{9/2} \rightarrow {}^2H_{11/2}$ |
| 682.2 | 684.7 | $^4I_{9/2} \rightarrow {}^4F_{9/2}$ |
| 734.8 - 759.1 | 748.8 | $^4I_{9/2} \rightarrow {}^4F_{7/2}, {}^4S_{3/2}$ |
| 787.5 - 818.5 | 803.6 | $^4I_{9/2} \rightarrow {}^2H_{9/2}$ |
| | 810.8 | $^4I_{9/2} \rightarrow {}^4F_{5/2}$ |
| 865.8 - 883.3 | 883.9 | $^4I_{9/2} \rightarrow {}^4F_{3/2}$ |
| 1600.2-1713.5 | 1693.8 | $^4I_{9/2} \rightarrow {}^4I_{15/2}$ |

Table 11.4. The measured wavelengths of the absorption lines in $(Nd_2O_3)_{0.234}(P_2O_5)_{0.766}$ compared with the centres of $Nd^{3+}$ band systems in an aqueous solution (Carnall et al. 1968).

The absorption spectrum for neodymium metaphosphate glass is reminiscent of the spectra for neodymium ions in polymetric metaphosphate glass (Weber et al. 1981), chloride solution (Moeller and Brantley 1950), borophosphate (Jiang and Jiang, 1991) and APG-1:$Nd^{3+}$ (average power glass) (Payne et al. 1995).

b) Fluorescence Spectrum

The fluorescence spectrum of neodymium metaphosphate consists of three strong peaks centred at 899, 1056, and 1325 nm. The fluorescence peak positions are in accord with the results for neodymium doped silicate glasses (Weber 1990, Betts et al. 1991).

| Wavelength (nm) $(Nd_2O_3)_{0.234}(P_2O_5)_{0.766}$ | Wavelength (nm) (Urquart 1988) | Transition (Urquart 1988) |
|---|---|---|
| 899.5 | 900 | $^4F_{3/2} \rightarrow {}^4I_{9/2}$ |
| 1056.1 | 1060 | $^4F_{3/2} \rightarrow {}^4I_{11/2}$ |
| 1324.8 | 1350 | $^4F_{3/2} \rightarrow {}^4I_{13/2}$ |

Table 11.5. The measured wavelengths of the fluorescence lines in $(Nd_2O_3)_{0.234}(P_2O_5)_{0.766}$ compared with the peaks of $Nd^{3+}$ doped $(SiO_2)_{0.945}(GeO_2)_{0.050}(P_2O_5)_{0.005}$ (Urquart 1988)

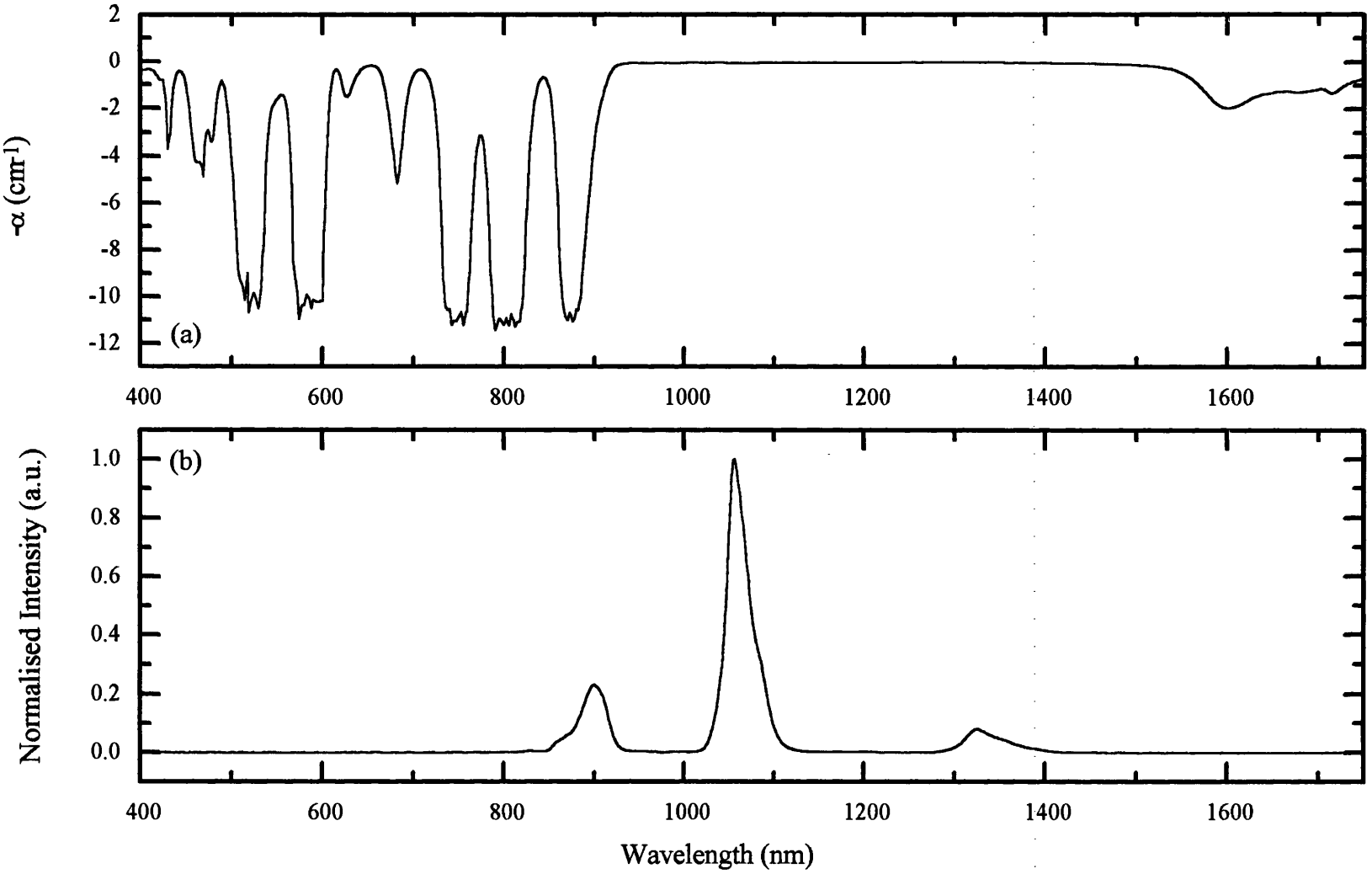


Figure 11.2. The (a)absorption and (b) fluorescence spectra of neodymium metaphosphate glass

### 3) $(Sm_2O_3)_{0.195}(P_2O_5)_{0.805}$

Samarium atoms can form almost equally stable compositions as divalent $4f^6 5d^0$ or trivalent $4f^5 5d^1$ ions. A previous investigation of the absorption and fluorescence of samarium metaphosphate glass by Farok et al. (1992, to be published), established that the spectra were typical of $Sm^{3+}$, showing no signs of peaks which characterise $Sm^{2+}$ ions. These investigations only recorded the absorption spectrum in the range 315-700nm and the fluorescence spectrum between 550-850nm. The present study increases both these ranges and shows many new features, especially in the absorption spectrum.

a) Absorption Spectrum

| Wavelength (nm) $(Sm_2O_3)_{0.195}(P_2O_5)_{0.805}$ | Wavelength (nm) (Reisfeld et al. 1974) | Transition (Reisfeld et al. 1974) |
|---|---|---|
| 439.2 | 438.5 | $^6H_{5/2} \rightarrow {}^4M_{17/2}, {}^4G_{9/2}, {}^4I_{15/2}, {}^4M_{19/2}$ |
| 471.6 | 450.0 | $^6H_{5/2} \rightarrow {}^4F_{5/2}$ |
| | 461.9 | $^6H_{5/2} \rightarrow {}^4I_{13/2}$ |
| | 476.6 | $^6H_{5/2} \rightarrow {}^4I_{9/2}, {}^4M_{15/2}, {}^4I_{11/2}$ |
| | 503.0 | $^6H_{5/2} \rightarrow {}^4G_{7/2}$ |
| 528.3 | 528.0 | $^6H_{5/2} \rightarrow {}^4F_{3/2}$ |
| 560.7 | 564.0 | $^6H_{5/2} \rightarrow {}^4G_{5/2}$ |
| 944.1 | 942.1 | $^6H_{5/2} \rightarrow {}^6F_{11/2}$ |
| 1077.7 | 1080.0 | $^6H_{5/2} \rightarrow {}^6F_{9/2}$ |
| 1227.5<br>1257.3 | 1230.0 | $^6H_{5/2} \rightarrow {}^6F_{7/2}$ |
| 1374.7<br>1409.8 | 1378.2 | $^6H_{5/2} \rightarrow {}^6F_{5/2}$ |
| 1478.7 | 1494.1 | $^6H_{5/2} \rightarrow {}^6H_{15/2}$ |
| 1529.0<br>1589.4 | 1546.1<br>1587.0 | $^6H_{5/2} \rightarrow {}^6F_{3/2}$ |

Table 11.6. The measured wavelengths of the absorption lines in $(Sm_2O_3)_{0.195}(P_2O_5)_{0.805}$ compared with the spectrum of samarium doped borate glass (Reisfeld et al. 1974).

The absorption spectrum depicts transitions from the ground state $^6H_{5/2}$ to higher levels of the $4f^5$ configurations. The strongest absorption peaks occur at wavelengths greater than 1000nm. The spectrum is similar to those found for samarium phosphate glass (Reisfeld 1972) and $Sm^{3+}$ doped $LaCl_3$ crystals (Carnall et al. 1968).

b) Fluorescence Spectrum

The spectral lines define transitions from the $^4G_{5/2}$ level to components of the ground $^6H_j$ and first excited $^6F_j$ multiplets. The most intense peak has been attributed to the $^4G_{5/2} \rightarrow {}^6H_{9/2}$ samarium transition; it is this peak which is responsible for the lasing observed in $Sm^{3+}$ doped silica fibre glasses (Hall and Webber 1991). The characteristics of the graph are shared with other samarium doped phosphate glasses (Farok et al. 1992, to be published) and samarium borate glass (Reisfeld et al. 1974).

| Wavelength (nm) $(Sm_2O_3)_{0.195}(P_2O_5)_{0.805}$ | Wavelength (nm) | Transition |
|---|---|---|
| 562.8 | 563* | $^4G_{5/2} \rightarrow {}^6H_{5/2}$ |
| 597.3/601.8 | 600* | $^4G_{5/2} \rightarrow {}^6H_{7/2}$ |
| 644.5 | 647* | $^4G_{5/2} \rightarrow {}^6H_{9/2}$ |
| 705.3 | 707* | $^4G_{5/2} \rightarrow {}^6H_{11/2}$ |
| 787.0 | 775.2 | $^4G_{5/2} \rightarrow {}^6H_{13/2}$ |
| 850.0 | | |
| 868.8 | 869.7 | $^4G_{5/2} \rightarrow {}^6F_{1/2}$ |
| 886.0 | 875.5 | $^4G_{5/2} \rightarrow {}^6H_{15/2}$ |
| 901.0 | 887.3 | $^4G_{5/2} \rightarrow {}^6F_{3/2}$ |
| 931.0 | 925.9 | $^4G_{5/2} \rightarrow {}^6F_{5/2}$ |
| 946.0 | | |
| 1028.5 | 1010.0 | $^4G_{5/2} \rightarrow {}^6F_{7/2}$ |

Table 11.7. The measured wavelengths of the fluorescence lines in $(Sm_2O_3)_{0.195}(P_2O_5)_{0.805}$ compared with samarium phosphate glass peaks as measured by Reisfeld and Boehm (1972) (*). The smaller features, which occur at longer wavelengths have, been labelled by calculating the possible transition based on the energy level diagram of aqueous $Sm^{3+}$ (Carnall et al. 1968)

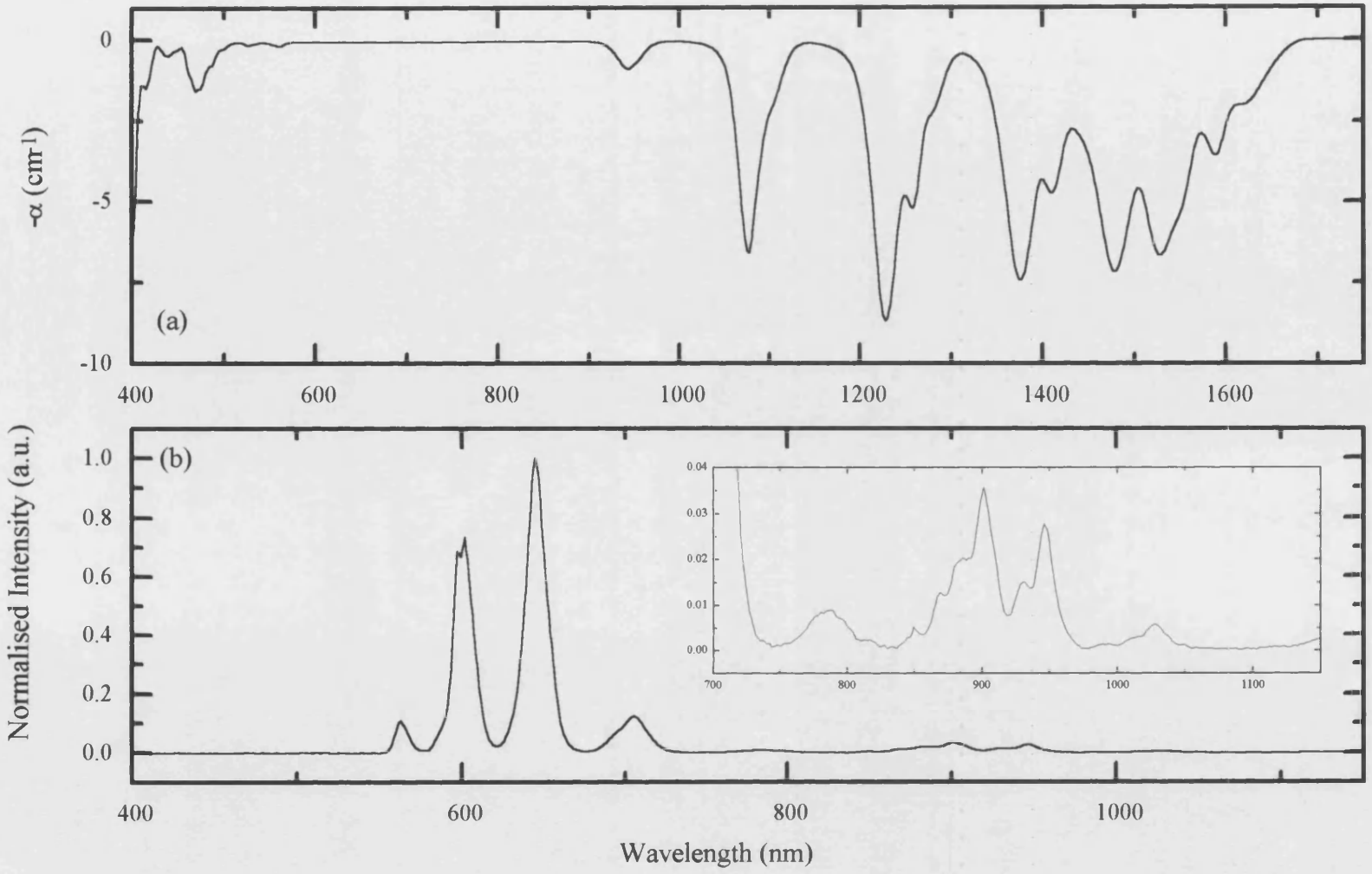


Figure 11.3. The (a) absorption and (b) fluorescence spectra of samarium metaphosphate glass

**4) $(Eu_2O_3)_{0.218}(P_2O_5)_{0.782}$**

Glasses containing $Eu^{+3}$ ions are amongst those which can exhibit laser induced refractive index gratings using four wave mixing techniques (French and Powell 1991, Durville et al. 1986), a particularly interesting and potentially useful feature. Permanent, but erasable, photoinduced modulation of the refractive index occurs due to changes in the local structure of the glass, induced by non-radiative decay of the europium ion by multiphonon emission after optical excitement of the $5D^2$ state. The experimental data has been described in terms of a double minima potential well (section 2.4.1) where the refractive index depends on which potential well (configuration) the $Eu^{3+}$ ions occupy in the host matrix.

As with samarium, europium can exhibit pressure dependent and volume sensitive, mixed valence. Europium can enter a host in either its divalent ($4f^7 5s^2$ - $^8S_{7/2}$) or trivalent ($4f^6 5s^2$ - $^7F_0$) state, making it necessary to ascertain its valence state in any particular host matrix. This has been achieved by Farok et al. (1994) who measured the optical absorption (between 200-600nm) and fluorescence (300-720nm) and compared them with the spectra reported for divalent and trivalent europium ion in various hosts. No evidence was found to suggest the presence of divalent europium ions, a conclusion which is verified here.

a) Absorption Spectrum

As the first three manifolds of $Eu^{3+}$ are very close, the ground state $^7F_0$, and first two excited states $^7F_1$ and $^7F_2$, can be populated at room temperature and therefore contribute to transitions in the absorption spectrum. The relative concentration of the $^7F_0$, $^7F_1$ and $^7F_2$ levels can be calculated using the Boltzmann distribution; at a temperature of 300K $C_0 = 0.792$, $C_1 = 0.200$, $C_2 = 0.008$ respectively, thus transitions from the $^7F_2$ level are very weak. The $^7F_0 \rightarrow {}^5D_0$ electric dipole transition is forbidden (Judd 1962, Ofelt 1962); hence this must be a magnetic dipole interaction, which are usually much less intense, explaining why it is only just visible in the $(Eu_2O_3)_{0.218}(P_2O_5)_{0.782}$ spectrum. The absorption spectrum of other europium phosphate glasses were recorded by Reisfeld and Boehm (1972), Farok et al. (1994) and Van Deun et al. (1998).

| Wavelength (nm) $(Eu_2O_3)_{0.218}(P_2O_5)_{0.782}$ | Wavelength (nm) (Cormier et al. 1993) | Transition (Cormier et al. 1993) |
|---|---|---|
| 414.9 | 414.1 | $^7F_1 \rightarrow {}^5D_3$ |
| 464.8 | 464.6 | $^7F_0 \rightarrow {}^5D_2$ |
| | 471.9 | $^7F_1 \rightarrow {}^5D_2$ |
| | 526.1 | $^7F_0 \rightarrow {}^5D_1$ |
| 532.3 | 533.1 | $^7F_1 \rightarrow {}^5D_1$ |
| 576.8 | 578.9 | $^7F_0 \rightarrow {}^5D_0$ |
| 589.0 | 588.9 | $^7F_1 \rightarrow {}^5D_0$ |
| 612.0 | 615.6* | $^7F_2 \rightarrow {}^5D_0$* |

Table 11.8. The measured wavelengths of the absorption lines in $(Eu_2O_3)_{0.218}(P_2O_5)_{0.782}$ compared with $Eu^{3+}$ ion doped sodium disilicate glass (Cormier et al. 1993) (*This transition is labelled from DeShazer and Dieke 1963)

The $^7F_1 \rightarrow {}^5D_2$ transition at 472nm is not observable in $Eu^{3+}$ metaphosphate glass (figure 11.4), neither is it observed in the absorption spectrum of europium doped flurophosphate glass measured by Van Deun et al. (1998).

b) Fluorescence Spectrum

Fluorescence is observed from the $^5D_0$ level to the ground $^7F_j$ multiplet. The $^5D_0$ level cannot be directly excited ($^5D_0 \rightarrow {}^7F_0$ is a forbidden electric dipole transition (Judd 1962, Ofelt 1962)), hence the $^5D_0$ must be populated by non-radiative decay from a higher state i.e. $^5L_6$. The selection rules determined by Judd-Ofelt theory only allows electric dipole transitions for which $\Delta J = 2$, 4, and 6, if the fluorescence starts from a J=0 state (Van-Deun et al. 1998). The $^5D_0 \rightarrow {}^7F_1$ transition is a magnetic dipole transition (DeShazer and Dieke 1963). The fluorescence spectrum of trivalent europium ions in many different hosts has been well documented: phosphate glass (Reisfeld 1972, Farok et al. 1994, Ebendorff-Heidepriem and Ehrt 1996), fluorophosphate (Van-Deun et al. 1998), fluorozirconate glass (Adam et al. 1987), sodium disilicate glass (Comier et al. 1993), crystalline hexagonal $LaCl_3$ (DeShazer and Dieke 1963).

| Wavelength (nm) $(Eu_2O_3)_{0.218}(P_2O_5)_{0.782}$ | Wavelength (nm) (Brecher et al. 1974) | Transition (Brecher et al. 1974) |
|---|---|---|
| 591.3 | 587.3 - 594.7 | $^5D_0 \rightarrow {}^7F_1$ |
| 612.3 | 611.5 - 620.6 | $^5D_0 \rightarrow {}^7F_2$ |
| 653.5 | 648.5 - 654.4 | $^5D_0 \rightarrow {}^7F_3$ |
| 700.8 | 687.6 - 701.7 | $^5D_0 \rightarrow {}^7F_4$ |
| 745.8 | 737.8 - 756.5 | $^5D_0 \rightarrow {}^7F_5$ |
| 812.5 | 800.7 - 831.5 | $^5D_0 \rightarrow {}^7F_6$ |

Table 11.9. The measured wavelengths of the fluorescence lines in $(Eu_2O_3)_{0.218}(P_2O_5)_{0.782}$ compared with the measured spectrum in europium pentaphosphate crystal (Brecher et al. 1974).

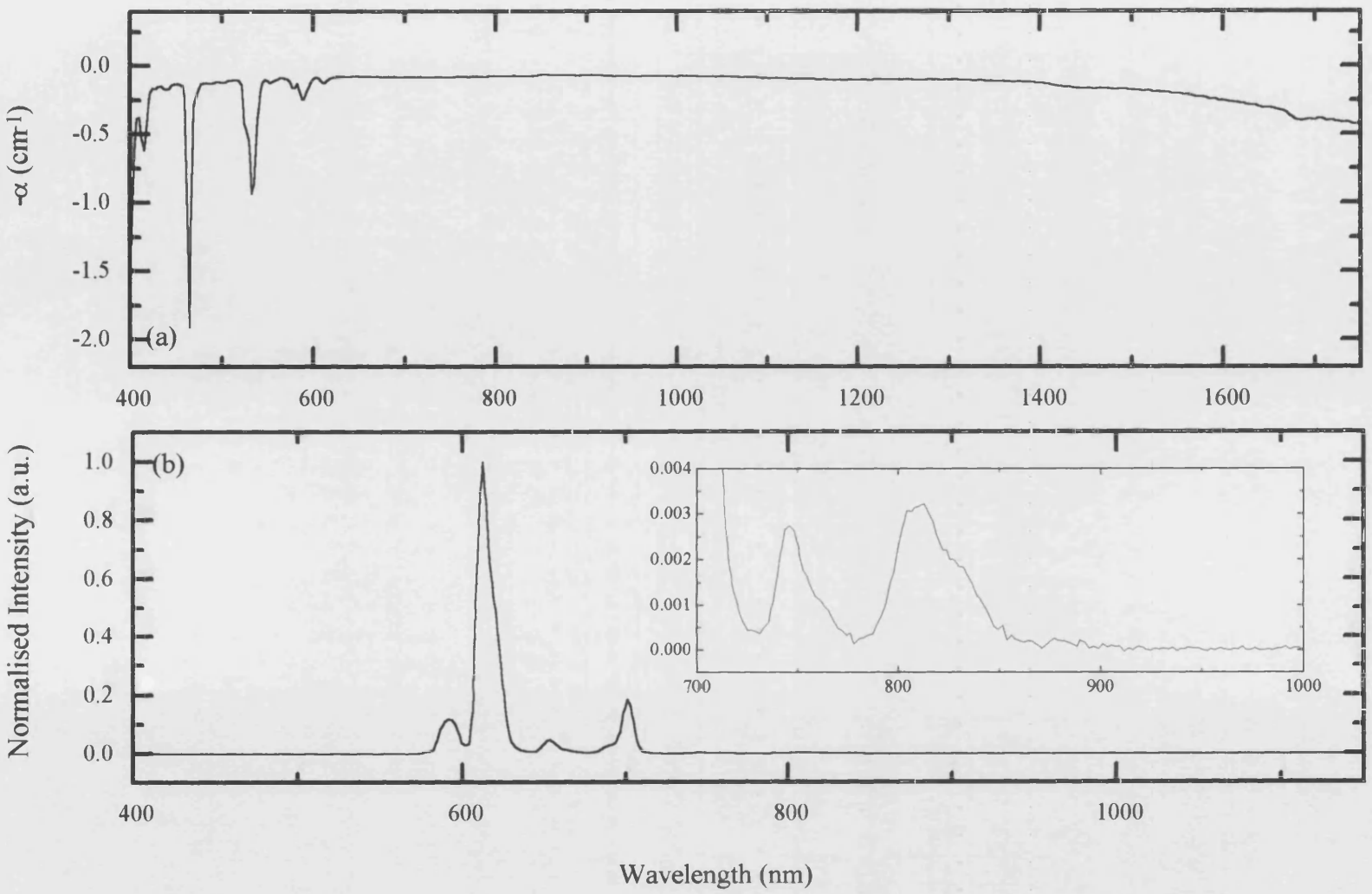


Figure 11.4. The (a) absorption and (b) fluorescence spectra of europuim metaphosphate glass

**5) $(Tb_2O_3)_{0.263}(P_2O_5)_{0.737}$**

The optical spectra of the terbium ion has received relatively little attention. In the hosts studied it gives out an intense green fluorescence dominated by the 550nm ($^5D_4 \rightarrow {}^7F_5$) line; a similar emission is exhibited on quenching of $Tb^{3+}$ phosphate glass melts. This phenomena, referred to as cooling induced luminescence, was observed by Cronin et al. (1982), who suggested that it originates from thermally induced shifts in the oxidation-reduction balance in the melt. It is uncertain whether this produces terbium luminescence directly (through induced shifts in the valency from $Tb^{4+}$ to $Tb^{3+}$) or involves the phosphorus with the energy released being transferred to the terbium ion. Terbium ions can exhibit 3+ (electronic configuration of ion $4f^8$) or 4+ ($4f^7$) valence.

a) Absorption Spectrum

Two absorption peaks are recorded in terbium metaphsophate glass between 400 and 1750nm. Both arise from transitions between the $^7F_6$ ground state and higher excited states. The first feature is relatively small, and only the beginning of the second peak falls within the range studied.

| Wavelength (nm) $(Tb_2O_3)_{0.263}(P_2O_5)_{0.737}$ | Wavelength (nm) (Thomas et al. 1963) | Transition (Thomas et al. 1963) |
|---|---|---|
| 485.1 | 488.0 - 488.7 | $^7F_6 \rightarrow {}^5D_4$ |
| 1750+ | 1784.8 - 1791.9 | $^7F_6 \rightarrow {}^7F_0$ |

Table 11.10. The measured wavelengths of the absorption lines in $(Tb_2O_3)_{0.263}(P_2O_5)_{0.737}$ compared with the transitions in Tb doped $LaCl_3$ (Thomas et al. 1963).

b) Fluorescence Spectrum

All the fluorescence lines observed in terbium metaphosphate glass, in the wavelength range examined, are electric dipole transitions originating from the $^5D_4$ energy level. From studying the energy level diagram of trivalent terbium there appears to be no transition which would result in a broad peak centred approximately at 838nm. The spectrum was measured repeatedly and this feature was always present. This peak is likely to arise from impurities in the sample, incorporated during the fabrication of the

glass, or perhaps the presence of $Tb^{4+}$ ions. The feature is very weak and there are no other peaks in the spectrum that can be attributed to the presence of a 'foreign' ion. Hence it is likely that the impurity ions only exist in the sample in small quantities. All the other peaks in the fluorescence spectrum are observed at wavelengths similar to the ones measured in $Tb^{3+}$ borate glass (Reisfeld 1972) and trivalent terbium doped fluorapatite (Tachihante et al. 1993). In those two materials the $^5D_4 \rightarrow {}^7F_5$ transition is the strongest; in contrast the $(Tb_2O_3)_{0.263}(P_2O_5)_{0.737}$ glass peak at 619nm ($^5D_4 \rightarrow {}^7F_3$) has the largest intensity (see figure 11.5). Relative changes in the intensity can be attributed to compositional variation of the host and dopant concentration.

| Wavelength (nm) $(Tb_2O_3)_{0.263}(P_2O_5)_{0.737}$ | Wavelength (nm) (Thomas et al. 1963) | Transition (Thomas et al. 1963) |
|---|---|---|
| 550.0 | 541.9 - 547.5 | $^5D_4 \rightarrow {}^7F_5$ |
| 584.5 | 583.3 - 587.2 | $^5D_4 \rightarrow {}^7F_4$ |
| 619.0 | 618.4 - 621.5 | $^5D_4 \rightarrow {}^7F_3$ |
| 655.8 | 644.5 - 648.2 | $^5D_4 \rightarrow {}^7F_2$ |
| 670.8 | 664.5 - 667.8 | $^5D_4 \rightarrow {}^7F_1$ |
| 683.5 | 676.2 - 677.0 | $^5D_4 \rightarrow {}^7F_0$ |
| 838.8 | | |

Table 11.11. The measured wavelengths of the fluorescence lines in $(Tb_2O_3)_{0.263}(P_2O_5)_{0.737}$ compared with the spectrum of $Tb^{3+}$ in hexagonal $LaCl_3$ (Thomas et al. 1963).

Comparison between the absorption bands of the terbium metaphosphate glass and those reported for $Tb^{3+}$ ion shows a good agreement, establishing that all the bands, except for the 838nm, are typical of a 3+ valence state.

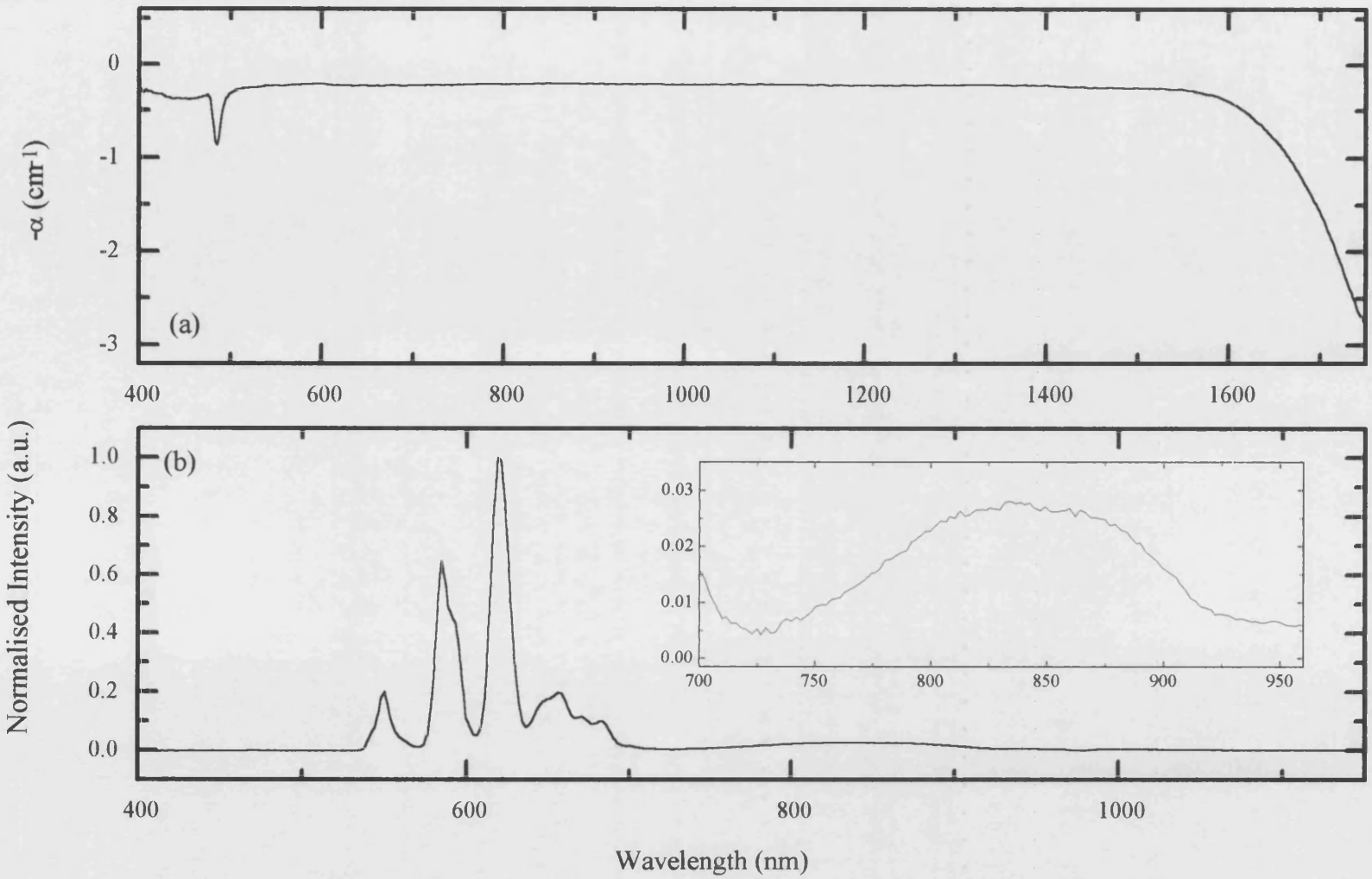


Figure 11.5. The (a) absorption and (b) fluorescence spectra of terbium metaphosphate glass

### 6) $(Dy_2O_3)_{0.225}(P_2O_5)_{0.775}$

Investigations in dysprosium doped materials are still relatively sparse, as $Dy^{3+}$ exhibits relatively weak fluorescence in the visible region of the spectrum. Attention has been focused on the mid-infrared transitions 1.8, 2.9 and 4.3μm (Schweizer et al. 1996). However the optical parameters obtained by Nagli et al. (1997) suggests that the dysprosium doped silicate glass has the potential to produce a blue-green solid state laser.

a) Absorption Spectrum

The measured absorption bands originate from excitation of the $^6H_{15/2}$ ground state. The $^6H_{15/2} \rightarrow {}^6H_{9/2}, {}^6F_{11/2}$ peak has the largest absorption factor of any of the rare earth doped metaphosphate glasses. The absorption spectrum of dysprosium metaphosphate glass is similar to the spectrums of silicate glass (Nagli et al. 1997), tellurite and fluoride glasses (Tanabe et al. 1995) and lanthanum sulphide glass (Schweizer et al. 1996) doped with trivalent $Dy^{3+}$ ions.

| Wavelength (nm) $(Dy_2O_3)_{0.225}(P_2O_5)_{0.775}$ | Wavelength (nm) (Seltzer et al. 1996) | Transition (Seltzer et al. 1996) |
|---|---|---|
| 424.3 | 428.3* | $^6H_{15/2} \rightarrow {}^4G_{11/2}$ |
| 451.3 | 446.7 - 456.2 | $^6H_{15/2} \rightarrow {}^4I_{15/2}$ |
| 474.3 | 464.7 - 479.1 | $^6H_{15/2} \rightarrow {}^4F_{9/2}$ |
| 749.7 | 750.0 - 750.3<br>750.7 | $^6H_{15/2} \rightarrow {}^6F_{3/2}$<br>$^6H_{15/2} \rightarrow {}^6F_{1/2}$ |
| 798.3 | 791.5 - 802.4 | $^6H_{15/2} \rightarrow {}^6F_{5/2}$ |
| 892.8 | 889.0 - 907.5<br>949.7 - 992.0 | $^6H_{15/2} \rightarrow {}^6F_{7/2}$<br>$^6H_{15/2} \rightarrow {}^6H_{5/2}$ |
| 1091.2 | 1032.6 - 1112.0 | $^6H_{15/2} \rightarrow {}^6H_{7/2}, {}^6F_{9/2}$ |
| 1233.0 - 1299.1 | 1218.0 - 1351.0 | $^6H_{15/2} \rightarrow {}^6H_{9/2}, {}^6F_{11/2}$ |
| 1667.7 | 1657.8 - 1688.0 | $^6H_{15/2} \rightarrow {}^6H_{11/2}$ |

Table 11.12. The measured wavelengths of the absorption lines in $(Dy_2O_3)_{0.225}(P_2O_5)_{0.775}$ compared with transitions present in dysprosium doped yttrium scandium gallium garnet (Seltzer et al. 1996). * This transitions has been compared with aqueous $Dy^{3+}$ (Carnall et al. 1968).

b) Fluorescence Spectrum

All the fluorescence peaks arise from transitions beginning at the $^4F_{9/2}$ energy level; this state is populated due to non-radiative transitions from higher levels. The $^4F_{9/2} \rightarrow {}^6H_{13/2}$ transition corresponds to a peak observed in dysprosium doped fluoroindate, fluorozirconate, tellurite, and gallium sulfide glasses at 575nm (Tanabe et al. 1995). The fluorescence spectrum of dysprosium is also documented in a crystalline yttrium scandium gallium garnet host (Seltzer et al. 1996).

| Wavelength (nm) $(Dy_2O_3)_{0.225}(P_2O_5)_{0.775}$ | Wavelength (nm) (Nagli et al. 1997) | Transition (Nagli et al. 1997) |
|---|---|---|
| 574.0 | 570 | $^4F_{9/2} \rightarrow {}^6H_{13/2}$ |
| 661.8 | 650 | $^4F_{9/2} \rightarrow {}^6H_{11/2}$ |
| 754.8 | 750 | $^4F_{9/2} \rightarrow {}^6H_{9/2}$, $^6F_{11/2}$ |

Table 11.13. The measured wavelengths of the fluorescence lines in $(Dy_2O_3)_{0.225}(P_2O_5)_{0.775}$ compared with the luminescence spectrum of $Dy^{3+}$ doped silicate glass (Nagli et al. 1997).

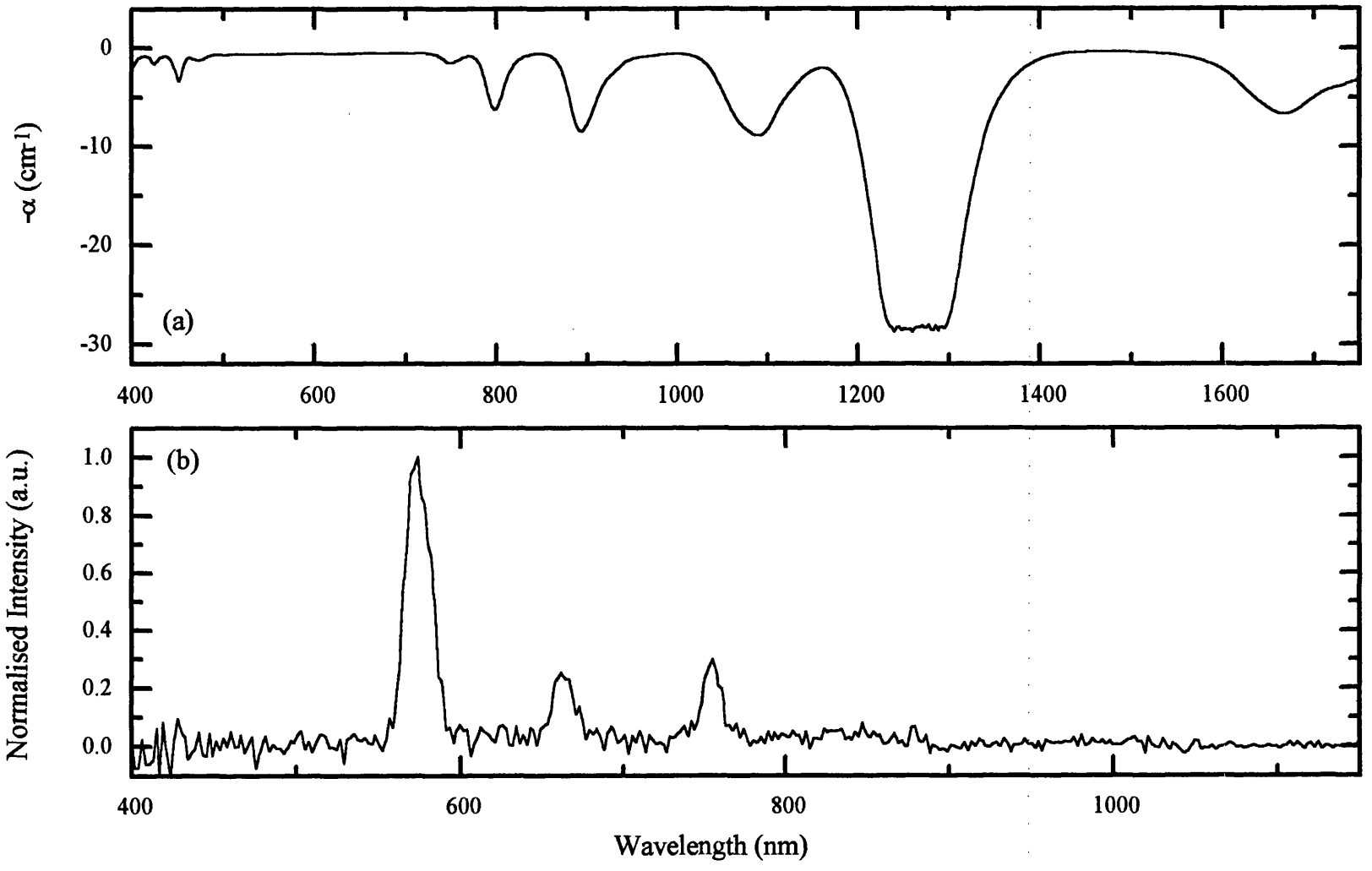


Figure 11.6. The (a) absorption and (b) fluorescence spectra of dysprosium metaphosphate glass

7) $(Ho_2O_3)_{0.208}(P_2O_5)_{0.792}$

An effect of the alexandrite type has been observed in holmium metaphosphate glass: its perceived colour changes when this glass is viewed in different light sources (Farok et al. 1996). This interesting effect has been attributed to two optical windows in the absorption spectrum of the glass between 554-626nm in the yellow-orange region of the visible spectrum, and a narrower band in the green between 497-526nm. These optical windows are seen in figure 11.7. Trivalent holmium has featured as the active ion dopant (or co-dopant with $Er^{3+}$ and $Tm^{3+}$) in many mid-infrared lasers, manufactured from hosts such as garnets (Gruber et al. 1992), YAG crystal (Kalisky et al. 1991),and $LiNbO_3$ (Lorenzo et al. 1996). The crystal field varies between hosts and detailed knowledge of the optical spectra are required to understand the capabilities and limitations of the sample. The absorption and fluorescence spectra of holmium metaphosphate glass have been previously investigated by Farok et al. (1996) up to wavelengths of 700nm. The present investigations extend the absorption and fluorescence to 1750nm and 1150nm respectively.

a) Absorption Spectrum

| Wavelength (nm) $(Ho_2O_3)_{0.208}(P_2O_5)_{0.792}$ | Wavelength (nm) (Caspers et al. 1970) | Transition (Caspers et al. 1970) |
|---|---|---|
| 418.9 | 414.4 - 414.8 | $^5I_8 \rightarrow {}^5G_5$ |
| 447.3 - 458.1 | 445.5 - 447.7 | $^5I_8 \rightarrow {}^5G_6$ |
| | 448.6 - 449.2 | $^5I_8 \rightarrow {}^5F_1$ |
| | 463.3 - 466.9 | $^5I_8 \rightarrow {}^3K_8$ |
| | 469.7 - 470.7 | $^5I_8 \rightarrow {}^5F_2$ |
| 485.1 | 479.1 - 481.9 | $^5I_8 \rightarrow {}^5F_3$ |
| | 531.3 - 535.2 | $^5I_8 \rightarrow {}^5F_4$ |
| 536.4 | 536.9 - 537.8 | $^5I_8 \rightarrow {}^5S_2$ |
| 640.3 | 635.5 - 641.3 | $^5I_8 \rightarrow {}^5F_5$ |
| | 747.2 - 752.4 | $^5I_8 \rightarrow {}^5I_4$ |
| 884.7<br>911.7 | 878.0 - 884.4 | $^5I_8 \rightarrow {}^5I_5$ |
| 1152.0<br>1188.4 | 1131.7 - 1145.2 | $^5I_8 \rightarrow {}^5I_6$ |

Table 11.14. The measured wavelengths of the absorption lines in $(Ho_2O_3)_{0.208}(P_2O_5)_{0.792}$ compared with the spectrum from $LaF_3$:Ho crystals (Caspers et al. 1970).

All the transitions commence from the $^5I_8$ ground state of the holmium ion. The two optical windows, which determines the colour of the holmium metaphosphate glass sample have been observed in $(Ho_2O_3)_{0.208}(P_2O_5)_{0.792}$ between 499-521nm and 557-622nm. The trends in the absorption spectrum can be seen in the spectrum of aqueous $Ho^{3+}$ (Carnall et al. 1968) and $LiNbO_3$ (Lorenzo et al. 1996). The $^5I_8 \rightarrow {}^5I_4$ transition is not observed in the $LiNbO_3$ sample either.

b) Fluorescence Spectrum

The $^5F_4$ and $^5S_2$ states are so close in the $Ho^{3+}$ ion, that transitions from the individual energy level cannot be distinguished within the broadening associated with the topological disorder of a glass. The fluorescence spectrum of $Ho^{3+}$ ion is dominated by two peaks at 550nm and 660nm. The luminescence from the $(Ho_2O_3)_{0.208}(P_2O_5)_{0.792}$ sample shares many common features with a previously studied holmium metaphosphate glass in the overlapping wavelength range, (Farok et al. 1996), and $Ho^{3+}$ doped $LaF_3$ crystals (Caspers et al. 1970)

| Wavelength (nm) $(Ho_2O_3)_{0.208}(P_2O_5)_{0.792}$ | Wavelength (nm) (Lorenzo et al. 1996) | Transition (Lorenzo et al. 1996) |
|---|---|---|
| 550.0 | 543 | $^5S_2, {}^5F_4 \rightarrow {}^5I_8$ |
| 660.3 | 648 | $^5F_5 \rightarrow {}^5I_8$ |
| 752.5 | 757 | $^5S_2, {}^5F_4 \rightarrow {}^5I_7$ |
| 965.5<br>986.5 | 973 | $^5F_5 \rightarrow {}^5I_7$ |
| 1013.5 | 1017 | $^5S_2, {}^5F_4 \rightarrow {}^5I_6$ |

Table 11.15. The measured wavelengths of the fluorescence lines in $(Ho_2O_3)_{0.208}(P_2O_5)_{0.792}$ compared with the fluorescence spectrum of $LiNbO_3$:$Ho^{3+}$ (Lorenzo et al. 1996).

The optical absorption and fluorescence spectra conform with those expected if the holmium ions are present as $Ho^{3+}$ (electronic configuration of the ion is $4f^{10}$).

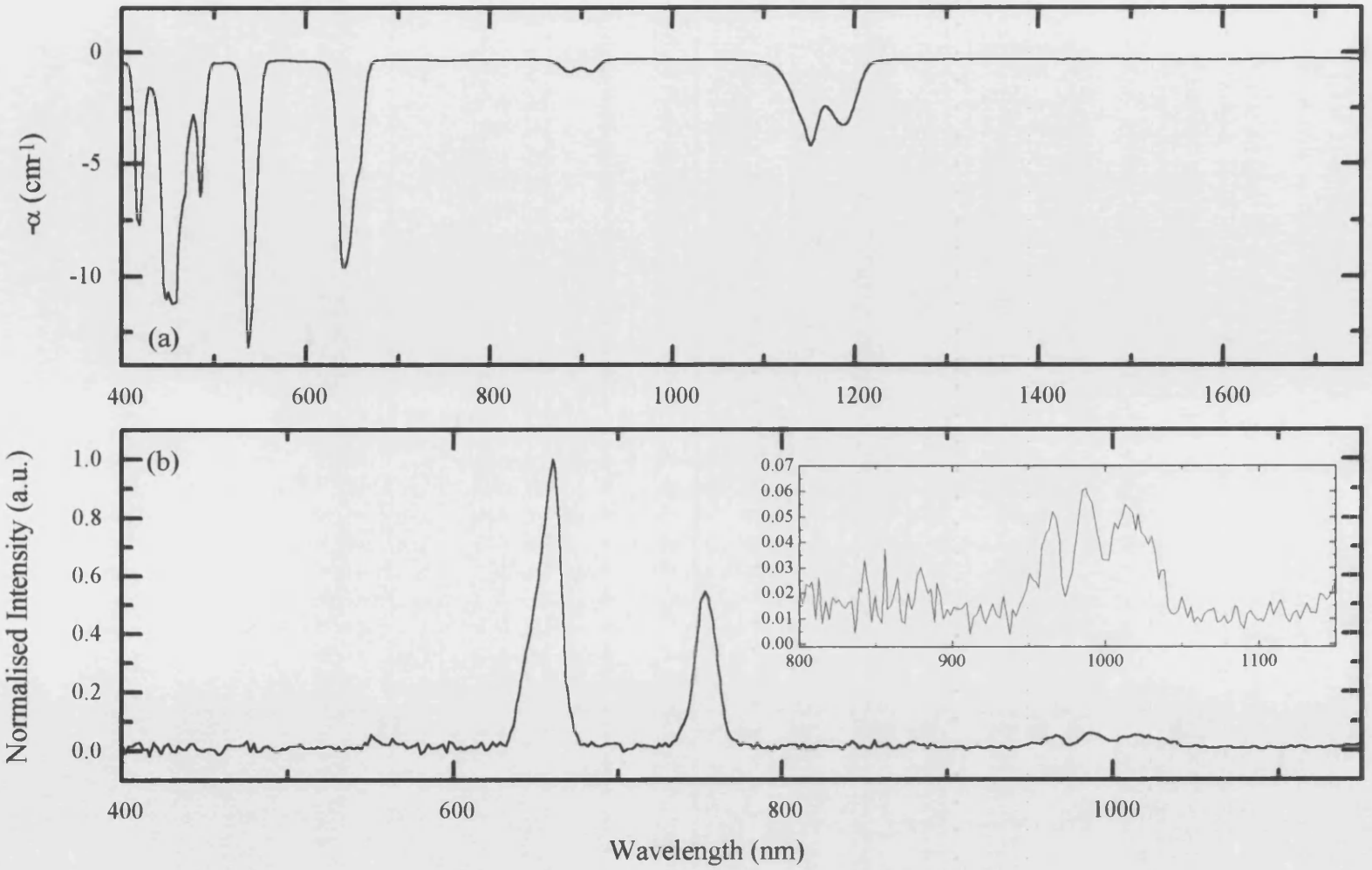


Figure 11.7. The (a) absorption and (b) fluorescence spectra of holmium metaphosphate glass

**8) $(Er_2O_3)_{0.239}(P_2O_5)_{0.731}$**

Investigations into the properties of erbium as an active ion have become popular in the search to produce a lasing wavelength which exploits the 1.55μm optical window in silica. Lasing, infrared-to-visible up-conversion, and amplifying have been achieved in $Er^{3+}$ doped phosphate glasses, in both bulk and fibre form (Hall and Weber (1991), Lu (1996), Miniscalco (1991).) The erbium ions most significant fluorescence band occurs in the near infra red between 1500-1600nm corresponding to the $^4I_{13/2} \rightarrow {}^4I_{15/2}$ transition, this wavelength exhibits low transmission loss in the atmosphere but is strongly absorbed in water, making it "eye safe". A peak is also observed in the absorption spectra at approximately 1550nm; this indicates the presence of a three level lasing system (Urquart 1988).

a) Absorption Spectrum

All transitions are excited from the $^4I_{15/2}$ ground state.

| Wavelength (nm) $(Er_2O_3)_{0.239}(P_2O_5)_{0.731}$ | Wavelength (nm) (Carnall et al. 1968) | Transition (Carnall et al. 1968) |
|---|---|---|
| 406.8 | 408.6 | $^4I_{15/2} \rightarrow {}^2G_{9/2}, {}^4F_{9/2}$ |
| 444.6 | 445.4 | $^4I_{15/2} \rightarrow {}^4F_{3/2}$ |
| 451.3 | 450.8 | $^4I_{15/2} \rightarrow {}^4F_{5/2}$ |
| 487.4 | 487.9 | $^4I_{15/2} \rightarrow {}^4F_{7/2}$ |
| 524.2 | 526.0 | $^4I_{15/2} \rightarrow {}^4G_{11/2}, {}^2H_{11/2}$ |
| 544.5 | 546.5 | $^4I_{15/2} \rightarrow {}^4S_{3/2}$ |
| 652.5 | 658.6 | $^4I_{15/2} \rightarrow {}^4F_{9/2}$ |
| 798.3 | 810.0 | $^4I_{15/2} \rightarrow {}^4I_{9/2}$ |
| 980.5<br>1004.8 | 987.8 | $^4I_{15/2} \rightarrow {}^4I_{11/2}$ |
| 1493.5<br>1532.7-1543.5 | 1541.8 | $^4I_{15/2} \rightarrow {}^4I_{13/2}$ |

Table 11.16. The measured wavelengths of the absorption lines in $(Er_2O_3)_{0.239}(P_2O_5)_{0.731}$ compared with the energy levels of the $E_r^{3+}$ free ion (Carnall et al. 1968).

This absorption spectrum shows similar characteristics to the absorption spectra of trivalent erbium perchlorate solution (Moeller and Brantley 1950), $Er^{3+}$ doped

phosphate glasses (Zheng et al. 1986, Qi et al. 1992, Lu et al. 1996), and erbium silicate glasses (Betts et al. 1991, Miniscalco 1991).

b) Fluorescence Spectrum

The luminescence transitions originate from the excited erbium energy levels $^4I_{15/2}$, and $^4S_{3/2}$. All of the fluorescence peaks, in the wavelength range studied, are weak except for the $^4I_{13/2} \rightarrow {}^4I_{15/2}$ transition (this also corresponds with the largest absorption peak). The fluorescence in erbium doped phosphate glasses has also been explored by Qi et al. (1992), and erbium doped silicate systems by Miniscalco (1991).

| Wavelength (nm) $(Er_2O_3)_{0.239}(P_2O_5)_{0.731}$ | Wavelength (nm) (Zheng et al. 1985) | Transition (Zheng et al. 1985) |
|---|---|---|
| 558.0 | 546 | $^4S_{3/2} \rightarrow {}^4I_{15/2}$ |
| 846.9 | 841 | $^4S_{3/2} \rightarrow {}^4I_{13/2}$ |
| 1566.4<br>1601.5 | 1552 | $^4I_{13/2} \rightarrow {}^4I_{15/2}$ |
| 1723.0 | 1680 | $^4S_{3/2} \rightarrow {}^4I_{9/2}$ |

Table 11.17. The measured wavelengths of the fluorescence lines in $(Er_2O_3)_{0.239}(P_2O_5)_{0.731}$ compared with radiative transitions for erbium doped phosphate glass (Zheng et al.1985).

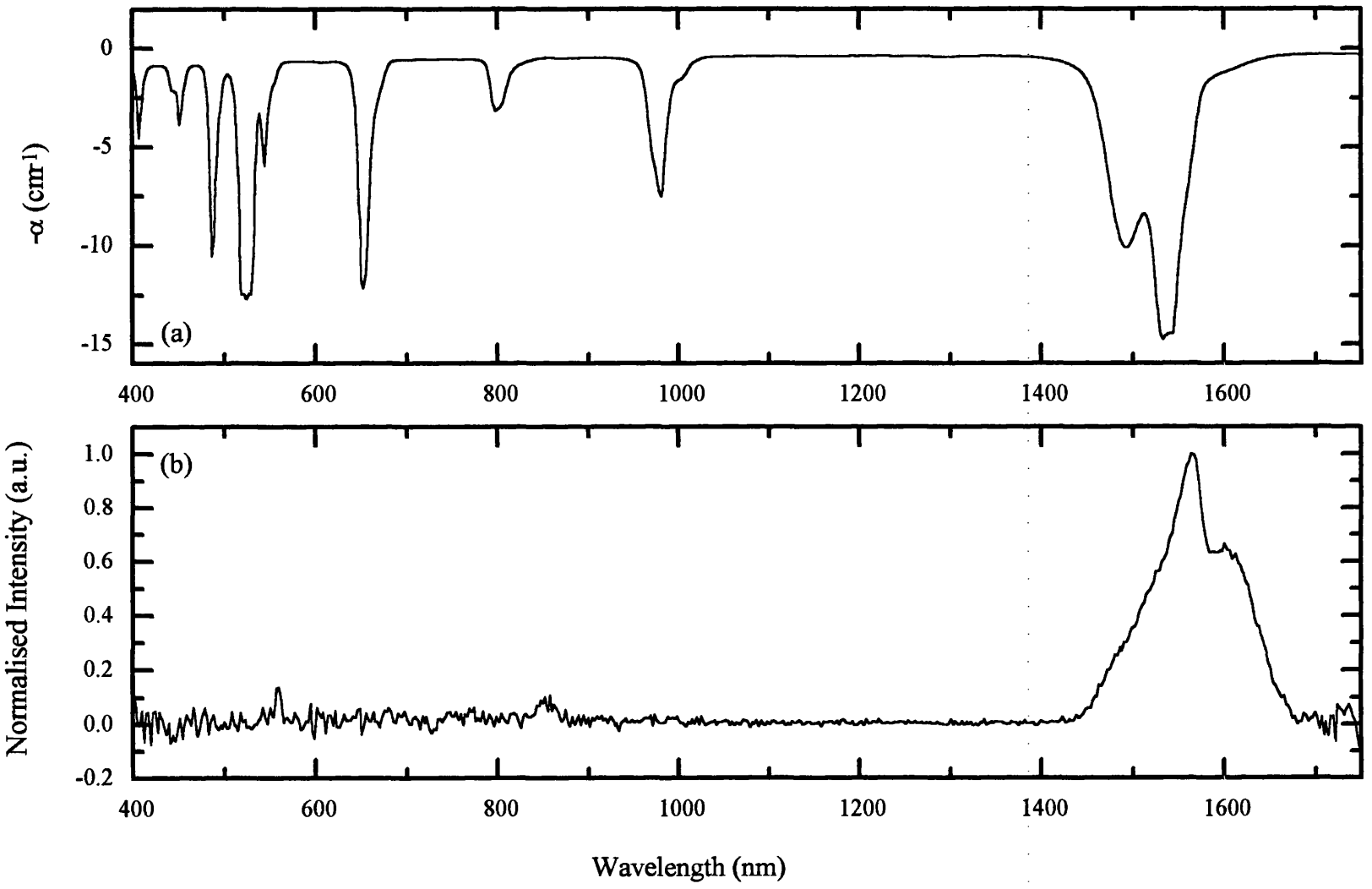


Figure 11.8. The (a) absorption and (b) fluorescence spectra of erbium metaphosphate glass

## 11.2. INVESTIGATION OF THE OPTICAL PROPERTIES OF BULK AND FIBRE NEODYMIUM DOPED METAPHOSPHATE GLASSES

Rare earth doped fibre lasers and amplifiers provide a low cost, easily manufactured, alternative to their crystalline counterparts. More importantly they produce wavelengths required for the telecommunications, sensing and spectroscopy device applications. Some of the first lasers and amplifiers, manufactured in the early 1960's, were constructed from $Nd^{3+}$ doped barium crown glasses (Miniscalco 1991). The $^4F_{3/2} \rightarrow {}^4I_{11/2}$ transition in neodymium at 1060nm is the most widely used lasing transition of any from the rare earth ions in glassy hosts. The following experiments have been performed to examine some of the host dependent properties that would affect the optical performance of real neodymium metaphosphate glass devices.

### 11.2.1. THE EFFECTIVE LINEWIDTH OF THE NEODYMIUM $^4F_{3/2} \rightarrow {}^4I_{11/2}$ TRANSITION IN METAPHOSPHATE GLASS

The emission cross section, and gain, of a material are inversely proportional to the fluorescence linewidth; hence a narrow bandwidth corresponds to a lower threshold power required for lasing action (Deutschbein and Pautrat 1968, Urquhart 1988, Weber 1990, Wilson and Hawkes 1998). As the luminescence band corresponding to the $^4F_{3/2} \rightarrow {}^4I_{11/2}$ transition in neodymium metaphosphate glass $(Nd_2O_3)_{0.234}(P_2O_5)_{0.766}$ is not symmetric (see figure 11.9), an effective fluorescence linewidth $\Delta\lambda_{eff}$ has been measured instead of the full-width half-maximum linewidth. The effective linewidth $\Delta\lambda_{eff}$ has been obtained be integrating over the band and dividing by the peak intensity (Weber 1990, Jiang and Jiang 1991, Marion and Weber 1991). $\Delta\lambda_{eff}$ is host dependent. The numerical integration was achieved using Simpson's rule (Jeffrey 1985):

$$\int_a^b f(x)dx = \frac{h}{3}[f(a) + 4f(a+h) + 2f(a+2h) + 4f(a+3h) + \ldots \ldots + 4f(a+(n-1)h) + f(b)] \quad (11.1)$$

Here n is an even number of sub-intervals of equal length h=(b-a)/n, in the integral $[f(x)]_b^a$.

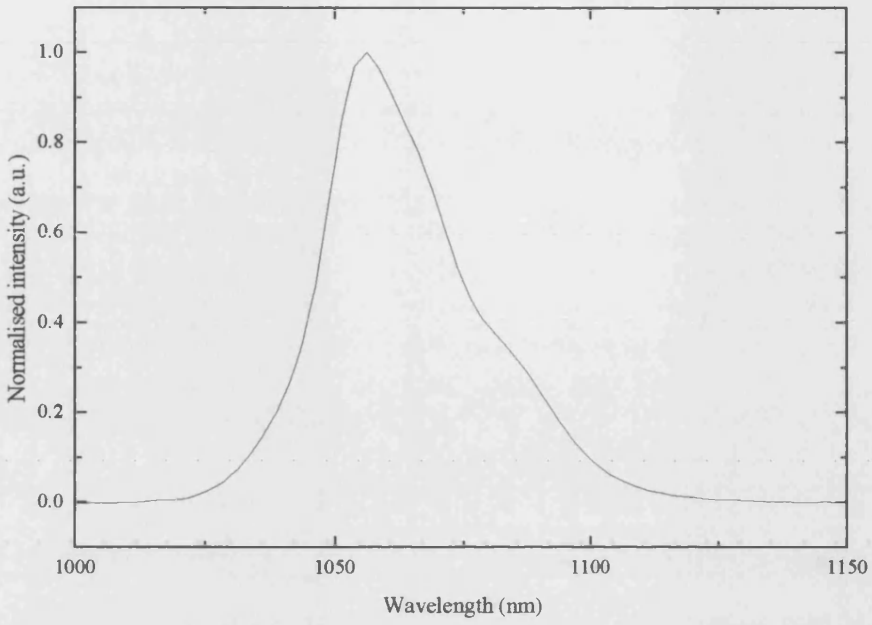


Figure 11.9. The $^4F_{3/2} \rightarrow {}^4I_{11/2}$ transition in neodymium metaphosphate glass $(Nd_2O_3)_{0.234}(P_2O_5)_{0.766}$.

| Host glass | Effective linewidth (nm) | Refractive index |
|---|---|---|
| silicate | 31-55 | 1.46-1.75 |
| germinate | 36-43 | 1.61-1.71 |
| tellurite | 26-31 | 2.0-2.1 |
| phosphate | 22-35 | 1.49-1.63 |
| borate | 34-38 | 1.51-1.69 |

Table 11.18. The effective linewidth and refractive index of the $^4F_{3/2} \rightarrow {}^4I_{11/2}$ transition of trivalent neodymium in different oxide glasses (Weber 1990, and references therein).

The effective fluorescence linewidth of the $^4F_{3/2} \rightarrow {}^4I_{11/2}$ transition is 34.1±0.5nm. This lies within the $\Delta\lambda_{eff}$ range tabulated by Weber (1990) for the same $Nd^{3+}$ transition in different phosphate hosts, and is comparable to the effective linewidth in other oxide glasses, see table 11.18. The bandwidth in neodymium metaphosphate glass is narrower than the average silicate effective linewidth; hence it should have a lower

threshold pump efficiency; however it has a near maximum effective linewidth compared with other phosphate hosts; this would result in good tunability required in device applications, and might facilitate mode-locking operation which requires lasing over a broad spectrum.

### 11.2.2. BREWSTERS ANGLE IN NEODYMIUM METAPHOSPHATE GLASS

The experimental procedures required to measure Brewsters angle in neodymium metaphsophate glass has been outlined in section 10.2.2. Brewsters angle $\theta_B$ has been determined in a bulk sample of $(Nd_2O_3)_{0.010}(La_2O_3)_{0.260}(P_2O_5)_{0.730}$ by measuring the polarised reflected beam intensity as a function $\theta$, the angle the surface of the glass makes with the direction of propagation of the laser beam (see figure 11.10).

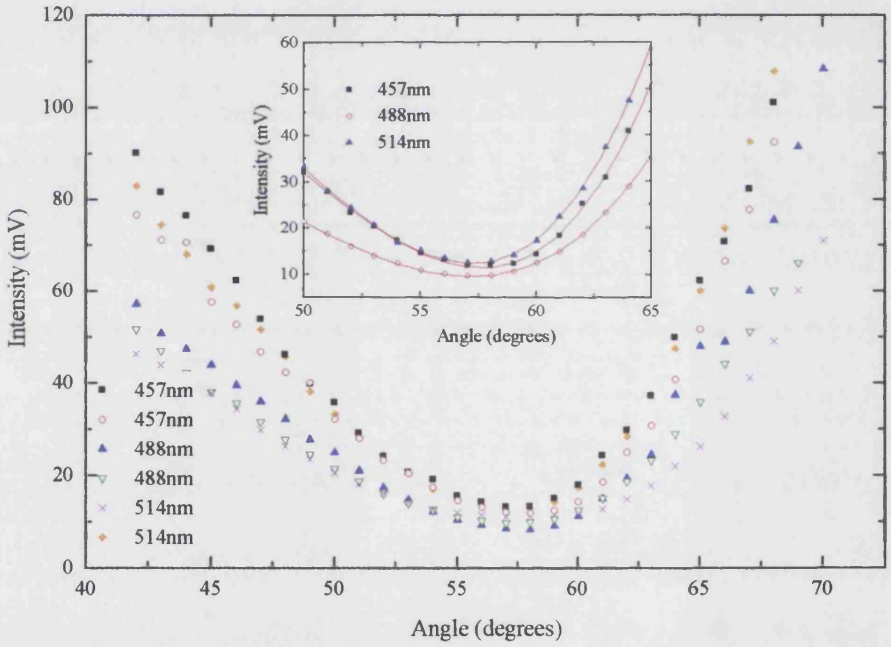


Figure 11.10. Graph showing the intensity of the reflected argon ion beam, polarised in the plane of incidence, as a function of incident angle and laser wavelength in $(Nd_2O_3)_{0.010}(La_2O_3)_{0.260}(P_2O_5)_{0.730}$. Two runs were recorded at each wavelength. The inset displays the best fit lines calculated for three wavelengths.

The intensity of the measurements never falls to zero; this is probably a result of imperfections on the surface of the sample, which will produce scattering of the incomming light. Brewsters angle and the refractive index (using $\tan \theta_B = n_t/n_i$,

equation 10.6) have been calculated at three different lasing wavelengths (457nm, 488nm, and 514nm) and are displayed in table 11.19. The refractive index of a material is a measure of the relative velocity of light propagating in free space compared with the velocity of light travelling through a medium; $n=\sqrt{\mu_r \varepsilon_r}$ where $\mu_r$ and $\varepsilon_r$ are the relative permeability and relative permativity of the medium respectively.

| Wavelength (nm) | Brewsters angle, $\theta_B$ (±0.35°) | Refractive index, n (±0.02) |
|---|---|---|
| 457 | 57.39 | 1.56 |
| 488 | 57.24 | 1.55 |
| 514 | 57.48 | 1.57 |

Table 11.19. The Brewster angle and refractive index measured in $(Nd_2O_3)_{0.010}(La_2O_3)_{0.260}(P_2O_5)_{0.730}$. The error in $\theta_B$ has been determined by the fitting procedure.

Weber (1990) presented the common refractive index ranges of trivalent neodymium in different oxide hosts, see table 11.18. The average value for the $(Nd_2O_3)_{0.010}(La_2O_3)_{0.260}(P_2O_5)_{0.730}$ sample, 1.56, falls in the middle of the range for phosphate hosts. The three wavelengths at which the Brewsters angle have been measured are too close to be able to observe any wavelength dependency in the refractive index; the Brewsters angles and refractive indexes are identical within experimental error. The frequency dependence, $\omega$, of the refractive index can be described in terms of the properties of the atoms in the medium (Hecht 1987);

$$n^2(\omega) = 1 + \frac{Nq_e^2}{\varepsilon_0 m}\sum_j \frac{f_j}{\omega_{0j}^2 - \omega^2 + i\gamma_j\omega} \qquad (11.2)$$

Here $q_e$ and m are the charge and the mass of the electron respectively, N is the number of atoms per unit volume having natural resonances $\omega_{0j}$, and $f_j$ (the oscillator strength) is a factor which characterises how strongly the atom exhibits each of its resonant frequencies. The resonant frequencies $\omega_{0j}$ characterises the frequencies at which the atom absorbs or emits radiant energy. As the wave travels though the

material part of the signal is absorbed, this incorporated into equation 11.2 by the damping factor $\gamma$. The above expression is called the dispersion equation. As $\omega$ approaches $\omega_{0j}$, $(\omega_{0j}^2-\omega^2)$ decreases and the refractive index increases; a positive slope $(dn/d\omega)$ is called normal dispersion. In the limit of $\omega$ tending to a the resonant frequency, $(\omega_{0j}^2-\omega)$ becomes very small compared with $i\gamma\omega$ and the refractive index becomes almost totally imaginary. The absorption of radiant energy is the dominant effect. The regions immediately surrounding the different resonant frequencies are called absorption bands; here the refractive index reduces as the frequency of the source is increased ($dn/d\omega$ is negative); this is known as anomalous dispersion. The change in n is large near the resonant frequencies, and approximately constant further away from $\omega_{0j}$.

Extensions to this experiment could be made by studying a wider range of wavelengths and improving the polishing on the sample surface.

### 11.2.3. LIFETIMES OF NEODYMIUM DOPED LANTHANUM METAPHOSPHATE GLASSES

To measure the effect of neodymium concentration on the fluorescence lifetime in metaphosphate glass six ternary neodymium lanthanum metaphosphate glasses have been manufactured, see table 11.20. Lanthanum has been employed as the 'dummy' dopant as it exhibits no absorption in the wavelength range studied, see figure 11.11.

As expected, the absorption coefficient (equation 10.7) of neodymium glass reduces with decreasing $Nd^{3+}$ content (figure 11.11). For a sample absorbing energy from an incoming beam, the more active ions the beam passes, be it due to an increase in path length or concentration, the more energy will be absorbed from it. The relationship is not linear, doubling the concentration does not produce twice the absorption (see equation 10.7). The $(Nd_2O_3)_{0.010}(La_2O_3)_{0.260}(P_2O_5)$ spectrum contains the same characteristics as the neodymium metaphosphate glass $(Nd_2O_3)_{0.234}(P_2O_5)_{0.766}$. The transitions responsible for the peaks are presented in table 11.4.

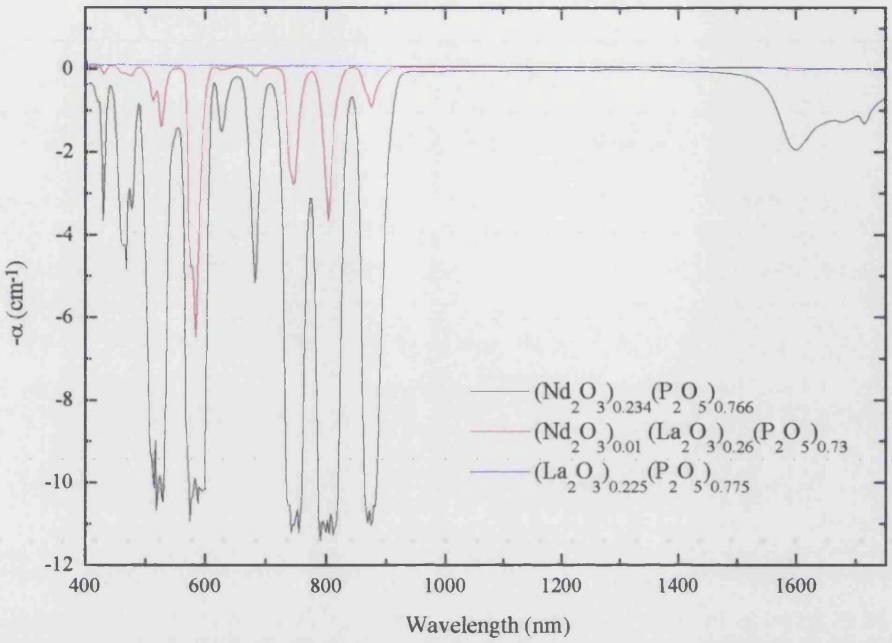


Figure 11.11. The absorption spectra of binary neodymium $((Nd_2O_3)_{0.234}(P_2O_5)_{0.766})$ and lanthanum $((La_2O_3)_{0.225}(P_2O_5)_{0.775})$ metaphosphate glasses and ternary neodymium lanthanum metaphosphate glass $(Nd_2O_3)_{0.010}(La_2O_3)_{0.260}(P_2O_5)_{0.730}$.

The fluorescent lifetimes of the neodymium lanthanum metaphosphate glasses have been measured at room temperature, using the pulsed 337nm line of a nitrogen laser to excite the ions. The decay curves plotted on a semi-logarithmic scale are shown in figure 11.12. The lifetimes are displayed in figure 11.13 and table 11.20 as a function of $Nd^{3+}$ concentration; they were calculated using the density of the sample and the composition determined by the EPMA, (column 1 and 2 in table 11.20). The photoluminescence curves used to determine the 1/e decay times are exponential within experimental error. The error in the lifetime is ±0.5%, and represents the standard deviation associated with the quality of the linear regression fit to the data, but does not include uncertainties in the experimental method. The error in neodymium concentration $C_{Nd}$ was calculated using the general error formula taking the error in the density to be $\pm 10 Kgm^{-3}$ and the error in the composition to be ±0.005mol%.

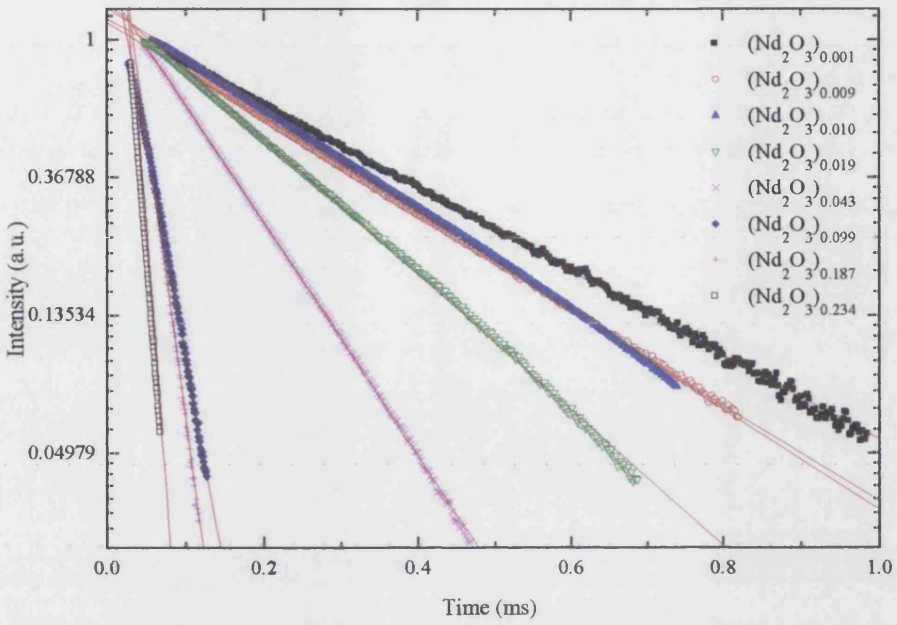


Figure 11.12. The fluorescence decay curves after excitation by a 337nm pulse. The intensity is plotted on a logarithmic scale. The key corresponds to the neodymium oxide content, the full composition of the glasses are given in table 11.20.

| Composition (mol%) | Density ($Kgm^{-3}$) (±10$Kgm^{-3}$) | $C_{Nd} \times 10^{20}$ (ions $cm^{-3}$) (±2.5%) | Lifetime (μs) (±0.5%) |
|---|---|---|---|
| $(Nd_2O_3)_{0.234}(P_2O_5)_{0.766}$ | 3372 | 42.92 | 14.7 |
| $(Nd_2O_3)_{0.187}(P_2O_5)_{0.813}$ | 3105 | 39.19 | 24.0 |
| $(Nd_2O_3)_{0.099}$ $(La_2O_3)_{0.147}$ $(P_2O_5)_{0.754}$ | 3257 | 20.63 | 31.7 |
| $(Nd_2O_3)_{0.043}$ $(La_2O_3)_{0.190}$ $(P_2O_5)_{0.767}$ | 3167 | 8.85 | 118.0 |
| $(Nd_2O_3)_{0.019}$ $(La_2O_3)_{0.226}$ $(P_2O_5)_{0.755}$ | 3155 | 3.86 | 204.6 |
| $(Nd_2O_3)_{0.010}$ $(La_2O_3)_{0.260}$ $(P_2O_5)_{0.730}$ | 3294 | 2.07 | 269.5 |
| $(Nd_2O_3)_{0.009}$ $(La_2O_3)_{0.240}$ $(P_2O_5)_{0.751}$ | 3189 | 1.84 | 286.9 |
| $(Nd_2O_3)_{0.001}$ $(La_2O_3)_{0.258}$ $(P_2O_5)_{0.741}$ | 3264 | 0.21 | 331.8 |

Table 11.20. The lifetimes of a series of ternary neodymium lanthanum metaphosphate glasses, manufactured with increasing neodymium content.

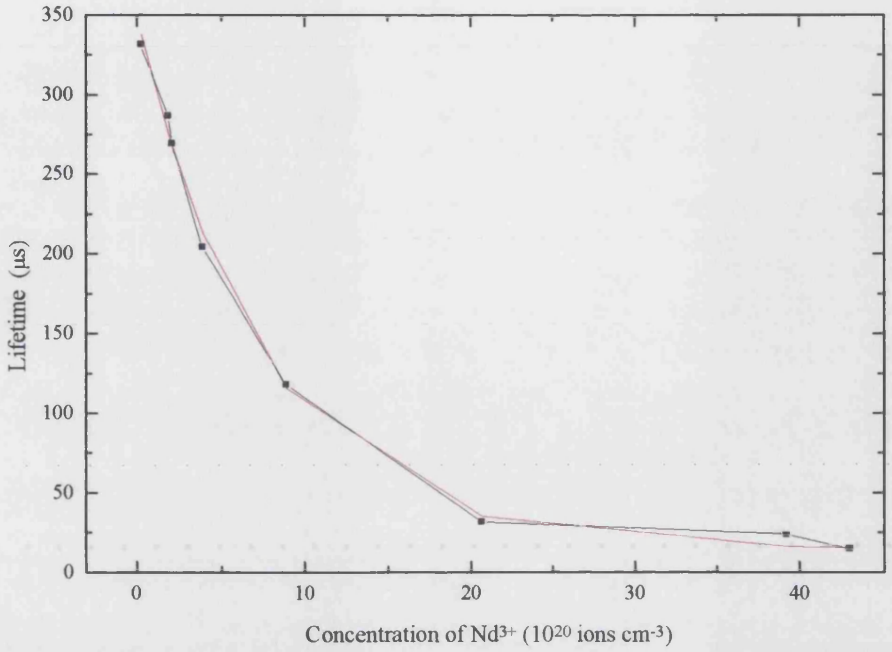


Figure 11.13. The lifetime of a series of ternary neodymium lanthanum metaphsophate glasses, plotted as a function of $Nd^{3+}$ ion concentration. The black line serves as a guide for the eye, and the red line is a second order exponential fit to the data points.

As the concentration of the $Nd^{3+}$ ions is increased the fluorescence lifetime decreases, due to concentration quenching (ion-ion cross relaxation processes) between the neodymium ions (section 10.1.3). The concentration at which the neodymium fluorescence lifetime falls by a factor of two have been compared for different glass hosts by Miniscalco and references therein (1991).

To estimate $\tau_0$ the lifetime in the limit of zero neodymium concentration, the data has been fitted with a second order exponential decay, defined by $\tau=333.0\exp(-C_{Nd}/7.4) +14.8\exp(-C_{Nd}/6219.5)$. Fitting the data with a single exponential produced larger deviations from experimental data at larger concentrations. This is believed to be a consequence of measuring the fluorescence without using a monochromator, although the $^4F_{3/2}\rightarrow{}^4I_{9/2}$ and $^4F_{3/2}\rightarrow{}^4I_{13/2}$ transitions are weak compared to $^4F_{3/2}\rightarrow{}^4I_{11/2}$, they may contribute in a small way to the fluorescence lifetimes. Extrapolating the equation to zero concentration gave a $\tau_0$ equal 347.8μs. Consequently the quenching concentration (Q) corresponding to $\tau_0/2$ can be read from figure 11.13, Q =

$5.8\times10^{20}$ions $cm^{-3}$. This Q value is in accord with the data presented in table 11.21, and lies in approximatly in the middle of the range found for neodymium doped phosphate glasses. The neodymium quenching concentration in metaphosphate glasses is comparable to the maximum values in silicates, and is higher than the other glasses tabulated in 11.21 (Miniscalco 1991); phosphates are generally more resistant than other glass hosts to the effects of concentration quenching, and Nd doped metaphosphate glass is not an exception.

| Glass type | Quenching concentration Q ($10^{20}$ions $cm^{-3}$) |
|---|---|
| Silicate | 3.9-6.0 |
| Phosphate | 3.9-8.6 |
| Fluorophosphate | 3.0-4.0 |
| Flurozirconate | 4.2 |
| Fluoroberyllate | 3.8-5.3 |

Table 11.21. $Nd^{3+}$ concentrations for a factor of two reduction (Q) in the $^4F_{3/2}$ lifetime. The range of concentrations represents the different values for various multi-component glass (Miniscalco 1991 and references therein).

## 11.2.4. CHARACTERISATION OF SILICA CLAD NEODYMIUM DOPED LANTHANUM METAPHOSPHATE GLASS FIBRES

Preliminary experiments and calculations have been made to characterise the nature of a silica clad optical fibre, with $Nd^{3+}$ doped core of composition $(Nd_2O_3)_{0.010}$ $(La_2O_3)_{0.260}(P_2O_5)_{0.730}$ (see section 10.4). An electron micrograph of the doubly silica coated fibre has been taken using a scanning electron microscope (SEM), and is shown in figure 11.14. The picture of the fibre exhibits several points of interest. The outer silica cladding is very prominent, this has an outer diameter of 110μm, and a thickness of 18.8μm. Between the inner and outer cladding layer there exists a several pockets of air; these can be avoided in future by increasing the temperature during the second fibre drawing process. The inner cladding has an outer diameter of 66.2μm and a thickness of approximately 3.8μm; this has totally collapsed onto the

$(Nd_2O_3)_{0.010}(La_2O_3)_{0.260}(P_2O_5)_{0.730}$ fibre. The diameter of the ternary neodymium lanthanum metaphosphate glass fibre is 58.6μm. There is an error of 5% associated with these diameters due to the measurement technique and deviations of the fibre from a cylindrical geometry.

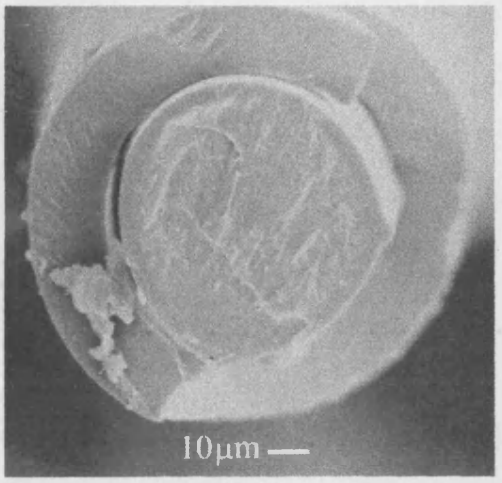


Figure 11.14. An electron micrograph of the cross section of the double silica clad ternary neodymium lanthanum metaphosphate glass $(Nd_2O_3)_{0.010}(La_2O_3)_{0.260}(P_2O_5)_{0.730}$.

1) The efficiency with which the fibre will pass light down its length depends on the quality of the interface and the absorption properties of the material. Scattering from surface imperfections and energy absorption will limit the maximum number of reflections the light wave can undergo before loss of signal. The first experiment was to check that the majority of light focused onto the optical fibre was confined to the core. A small length of the fibre, approximatly 3cm, was mounted in a copper v-groove sample holder. The 633nm line emerging from a He-Ne laser was reflected from two mirrors, which were required for beam steering, and then focused onto the end of the fibre using a high power lens mounted on an xyz micro-positioner. The output signal was passed through a second lens. The projected clad fibre image showed a bright central region which corresponded to confinement of almost all the transmitted light in the core; there appears to be no, or very little light escaping into the double silica jacket. The image is also speckled, a characteristic of multimode propagation.

2) To quantify the intrinsic attenuation losses in the neodymium fibre, a standard cutback technique has been employed. Light from a He-Ne (633nm) laser is coupled into a long fibre (approximatly 650mm) using the same set up as above (1). The intensity of the emerging signal ($I_0$) was converted into voltage using a large surface area silica photodiode and fed into a digital multimeter (model 199 from Keithley Instruments) capable of measuring voltages to an accuracy of 10μV. Without changing the coupling set up of the fibre, a section (of known length) is cleaved off and the output ($I_t$) is once again measured. The fractional transmittance in the length of fibre removed is calculated from the ratio of the two signal output measurements (equation 10.7), as the input conditions (and related extrinsic losses) are identical. The experiment was repeated three times at different intervals along the same fibre, hence also allowing the uniformity of the fibre to be examined (table 11.22).

Within experimental error the absorption coefficient appears to be approximately independent of path length and constant along the length of the fibre examined. This suggests that the attenuation mechanisms are due to evenly distributed intrinsic losses associated with the fibre and any extrinsic contributions are minimal. Intrinsic loss mechanisms in fibres can generally be split into two categories: scattering losses, absorption losses. Scattering losses in glasses are predominantly of the Rayleigh type; incoming light is scattered by objects which are small in comparison with its wavelength (typically $\lambda/10$ or less). Rayleigh scattering arises from the structural disorder associated with amorphous materials and the resulting fluctuations in the refractive index. These scattering losses are proportional to the fourth power of the frequency (section 10.1.1. Hecht 1987, Wilson and Hawkes 1998). Scattering will also occur from the surface of the fibre and impurities at the fibre cladding interface. Absorption losses are due to the presence of impurity ions in the fibre such as: traces of transition metals or hydroxyl groups ($OH^-$). Impurity ions can be introduced into the medium in small quantities from the starting oxides which are used to fabricate the fibres.

| Δ length (±0.05cm) | $I_0$ (±2mV) | $I_t$ (±2mV) | $\alpha$ (±0.003cm$^{-1}$) |
|---|---|---|---|
| 18.75 | 18 | 30 | 0.027 |
| 21.80 | 49 | 99 | 0.032 |
| 10.90 | 134 | 182 | 0.028 |

Table 11.22. Cutback measurements in silica clad ternary neodymium lanthanum metaphosphate glass $(Nd_2O_3)_{0.010}(La_2O_3)_{0.260}(P_2O_5)_{0.730}$. $I_0$ and $I_t$ are the measured intensities before and after a length of fibre has been cut off, and $\alpha$ is the absorption coefficient of the fibre.

From this experiment the coupling efficiency can be estimated. The laser voltage measured before the focusing lens was 400 ± 2 mV, the signal emerging from a fibre of length 5cm was 182 ± 2 mV; hence the coupling efficiency is approximatly 46%. If fibre lasers of this type are to be constructed, there will be additional scattering and absorption losses at the two mirrors at either end of the cavity; hence if a population inversion is to be maintained the light coupling needs to be maximised. Two methods of doing this would be to polish the input surface of the fibre to reduce scattering losses, and to cut the fibre surface at an angle equal to Brewsters angle.

3) The absorption spectrum in the optical fibre has been measured in a similar way as for the bulk samples (section 10.2.1), except that the white light source was focused onto the fibre fixed in a v-groove copper mount. The absorption has been recorded in three samples of $(Nd_2O_3)_{0.010}(La_2O_3)_{0.260}(P_2O_5)_{0.730}$ with different lengths (60.0mm, 183mm, and 418.5mm). The spectra, corrected for background noise and divided by the white light spectrum i.e. $I/I_0$, has been scaled using the absolute absorption measurement at 633nm taken from the cut back experiment (using equation 10.7, and $\alpha = 0.029\text{cm}^{-1}$). Loss is commonly measured in units of decibel per m; a decibel is a standard way of comparing the ratio of two different power ($P_1$and $P_2$) levels. The number n of dB can be calculated using,

$$n = -10\log_{10}\left(\frac{P_2}{P_1}\right) \qquad (11.3)$$

where the power P is proportional to the intensity I. The absorption spectra from the neodymium lanthanum fibre is converted into decibel using equation 11.3, and finally dividing by the path length of the sample; the attenuation is expressed in terms of $dBm^{-1}$ (see figure 11.14).

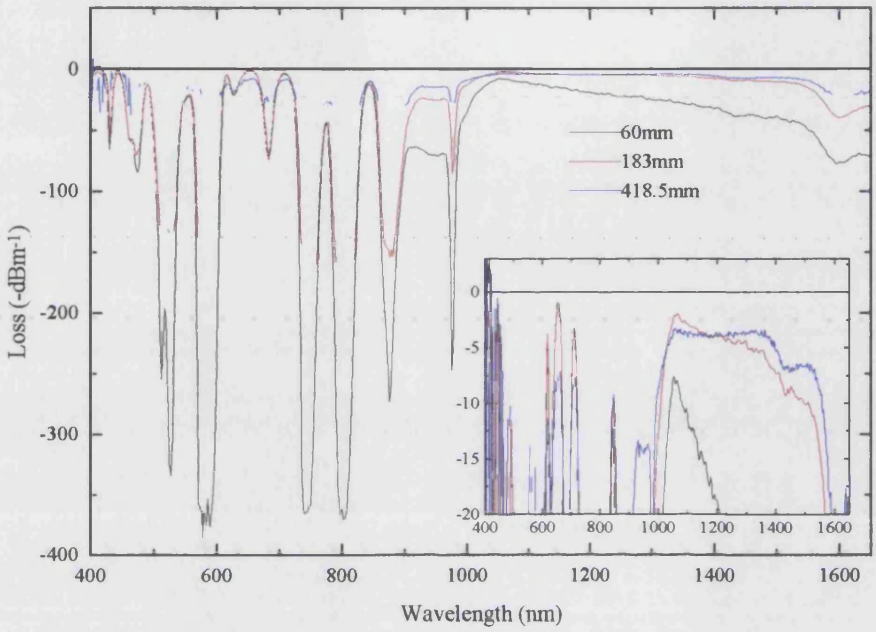


Figure 11.14. The absorption spectra in different lengths of silica clad ternary neodymium lanthanum metaphosphate glass $(Nd_2O_3)_{0.010}(La_2O_3)_{0.260}(P_2O_5)_{0.730}$. The insert is an expansion of the data in the region 2 to -20 $dBm^{-1}$.

The breaks in the spectra in figures 11.14, at increased path lengths 183mm and 418.5mm, correspond to wavelengths at which all the signal is absorbed, and the transmitted intensity falls to zero. Figures 11.14 exhibit features characteristic of the $(Nd_2O_3)_{0.010}(La_2O_3)_{0.260}(P_2O_5)_{0.730}$ and $(Nd_2O_3)_{0.234}(P_2O_5)_{0.766}$ bulk samples, see figure 11.11. All the peaks (except for the one occurring at 975nm) can be accounted for by assuming electron transitions from the ground $^4I_{9/2}$ state to higher multiplets. The absorption peaks in $(Nd_2O_3)_{0.234}(P_2O_5)_{0.766}$ have been assigned transitions in table 11.4. The peak at 975nm occurs in the three different samples (each run was repeated and the feature was still present). This peak is unlikely to be a consequence of the measurement technique, as all spectra were corrected for background signal, and normalised to the incident spectrum. The line probably arises due to impurity atoms in

the fibre. These have not been incorporated during the manufacture of the bulk sample: the 975nm peak is not present in the absorption spectra of the bulk material cut from the same ingot of glass, figure 11.11; therefore impurities must have been included during the fabrication of the fibre. Another unexpected feature in these spectra is the increase in absorption with increasing wavelength (larger than 1000nm) and reducing path lengths. In the 1000-1500nm range, which corresponds to an optical window in the neodymium ion, there is expected to be no absorption by the $Nd^{3+}$ ion, and the attenuation is due to the scattering and absorption losses detailed in 11.2.4(2). Optical windows are regions of the energy spectrum associated with the least Rayleigh scattering from the host medium. If the losses are intrinsic to the sample, the absolute attenuation in $dBm^{-1}$ is expected to be constant in the same sample, at the same wavelength, regardless of the path length over which the spectrum was measured. This systematic increase in absorption with decreasing measurement path length could be a consequence of extrinsic losses, such as coupling of the light in and out of the sample, or the excitation of cladding modes. In the smaller samples extrinsic losses will make up an increasing proportion of the total losses, and hence these effects will still be significant even after dividing the absorption spectrum by the path length.

The absorption in these fibres is large (see insert in figure 11.14) compared with the high purity optical fibres manufactured from silica for the telecommunications purposes. Typically absorption values for optical fibres required in the telecommunications industry, in the chosen optical transmission window, must have losses less than $0.5dBkm^{-1}$; hence signals can travel at least 80 kilometres before amplification. The minimum attenuation recorded in the 60mm fibre had a value of $0.88dBm^{-1}$ at 652.9nm. Optical fibres used for lasing and amplification have different criteria than low loss fibres such as, stability, reliability, low loss at signal wavelength. These devices are fabricated on a shorter length scale, so loss characteristics are less important. The attenuation in the ternary lanthanum metaphosphate glass is comparable to the absorption measured in neodymium LHG-5 glass laser (Kozlovsky et al. 1986); LHG-5 is a phosphate glass manufactured by Hoya Optics. The absorption coefficient in LHG-5 glass at 801nm is $9cm^{-1}$, and in the 60mm fibre the absorption is $366.4dBm^{-1}$ (figure 11.14) which corresponds to $\alpha$ $=0.843cm^{-1}$

(equation 10.7 and 11.3). The attenuation in the $(Nd_2O_3)_{0.010}(La_2O_3)_{0.260}(P_2O_5)_{0.730}$ glass is the result of a combination of intrinsic and extrinsic losses such as: impurities, structural imperfections, quality of the fibre cladding interface, bends in the fibre.

4) When light travels from a more optically dense medium to a less optically dense medium, there occurs a 'critical' angle $\theta_c$ at which the light is no longer transmitted out of initial material; $\theta_c$ marks the onset of total internal reflection. The critical angle can be calculated using equation 10.17. The refractive index of the $(Nd_2O_3)_{0.010}(La_2O_3)_{0.260}(P_2O_5)_{0.730}$ fibre $n_f$ has been determined in section 11.2.2 to be 1.56 and the refractive index of the silica cladding $n_c$ is 1.458; the critical angle has a value of 69.2°.

5) The numerical aperture (NA) defines the maximum angle $\theta_{max}$ at which light incident on the surface of the core (air/fibre interface) will generate total internal reflections at the fibre cladding boundary; the NA can be calculated using equation 10.19. For the silica clad ternary neodymium lanthanum metaphosphate glass NA is 0.55 and $\theta_{max}$ is 33.7°. Fibres have been fabricated with a range of numerical apertures between 0.2 and 1.0 (Hecht 1987). The number of modes propagating through the fibre can be calculated using equation 10.18 The core radius determined from the electron micrograph is 29.3μm, hence the V parameter, for light propagating down the fibre with a wavelength of 528nm, is 192. In a step profile fibre, where V>>1, the number of bound modes $M_{bm}$ can be calculated using (Synder and Love 1996)

$$M_{bm} = \frac{V^2}{2}. \qquad (11.4)$$

Hence the number of modes propagating in the $(Nd_2O_3)_{0.010}(La_2O_3)_{0.260}(P_2O_5)_{0.730}$ fibre is 18432. For monomode propagation of the 528nm argon ion lasing line the V number has to < 2.405, hence the maximum fibre core radius would be 0.37μm.

6) The gain coefficient $\alpha_g$ is proportional to the stimulated emission cross section $\sigma$ and the population inversion between the initial and final lasing levels $N_2$-$N_1$ (see equation 10.16). The simulated emission cross section for a neodymium ion is approximately $4\times10^{-20}cm^2$. Gain only occurs in samples in which a population inversion can be achieved, consequently in a four level lasing system the number of

ions per unit volume in the initial state $N_1$ compared with $N_2$ is very small and effectively can be ignored. Assuming steady state conditions, $N_2$ in the $(Nd_2O_3)_{0.010}(La_2O_3)_{0.260}(P_2O_5)_{0.730}$ fibre can be calculated from the rate equation governing the population of the upper lasing level:

$$N_2 = R - A_{21}N_2. \qquad (11.5)$$

Here $A_{21}$ is the Einstein A coefficient, this characterises the spontaneous emission probability of the active ions and is inversely proportion of the spontaneous emission lifetime of the lasing transition. The pump rate R is equal to P/hν, where P is the absorbed pump power in $Wcm^{-3}$, h is Plancks constant and ν is the pump frequency. If the neodymium lanthanum fibre, with cross sectional area $4.88\times10^{-5}cm^2$, is excited with 100mW using the 528nm argon ion lasing line the pump rate R is $5.44\times10^{21}$ions $s^{-1}cm^{-3}$. The lifetime of $(Nd_2O_3)_{0.010}(La_2O_3)_{0.260}(P_2O_5)_{0.730}$ has been measured (section 11.2.2) and was found to be 269.5μs; therefore the population of the upper lasing level $N_2$ is $1.47\times10^{18}$ions $cm^3$, and the gain coefficient is $0.059cm^{-1}$. The average absorption coefficient in $(Nd_2O_3)_{0.010}(La_2O_3)_{0.260}(P_2O_5)_{0.730}$ fibres has been measured (section 11.2.4(2)); at 528nm the absorption coefficient $\alpha$ is $0.738cm^{-1}$. Hence there will be loss in this fibre at 528nm ($\alpha_g < \alpha$). If overall gain is to be achieved, pump power P needs to be increased; this can be done by increasing the pump rate R or increasing the coupling efficiency of light into the fibre (preferably both).

## 11.3. CONCLUSION

Knowledge of the relationship between structure of the glass host and optical properties of the active ions is essential for the design of glasses for real applications. A comprehensive picture of the fluorescence and absorption transitions, which govern the optical properties of rare earth doped metaphosphate glass in the visible and near infra red region of the spectrum, has been presented in section 11.1. In the second half of this chapter (section 11.2) the effect of the metaphosphate host on trivalent neodymium ions has been examined, in bulk and fibre form. Although the data gathered on the fibre ($(Nd_2O_3)_{0.010}(La_2O_3)_{0.260}(P_2O_5)_{0.730}$) was limited, it shows the potential of this glass for device applications such as fibre lasers. The main achievement of this part of the work was the actual fabrication of a clad fibre from a bulk sample. This has never been done in these glasses before.

1) All the rare earth ions (R=Pr, Nd, Sm, Eu, Tb, Dy, Ho, Er) studied in the metaphosphate glass host exhibit absorption and fluorescence features which have been assigned transitions using the spectra of corresponding trivalent lanthanides in variety of glass and crystalline hosts. Hence it can be concluded that rare earth ions are preferentially incorporated into metaphosphate glass as $R^{3+}$. This result is in accord with EXAFS data recorded in section 5.2; the measured rare earth ion-oxygen distances were in close agreement with those calculated from the tables of ionic radius (Shannon 1976) assuming a co-ordination number of six and a valence of 3+.

2) The effective fluorescence linewidth $\Delta\lambda_{eff}$ of the $^4F_{3/2}\rightarrow{}^4I_{11/2}$ transition neodymium metaphosphate glass $(Nd_2O_3)_{0.234}(P_2O_5)_{0.766}$ is 34.1±0.5nm.

3) Brewsters angle $\theta_B$ and the refractive index n have been calculated at three different lasing wavelengths in $(Nd_2O_3)_{0.010}(La_2O_3)_{0.260}(P_2O_5)_{0.730}$. The average $\theta_B$ was 57.37±0.35° and n was equal to 1.56±0.02. In the wavelength range 457 to 514nm there is no measurable change in either of these properties.

4) Concentration quenching effects on the lifetime of the $^4F_{3/2}\rightarrow{}^4I_{11/2}$ neodymium transition were examined in a series of ternary neodymium lanthanum metaphosphate glasses. As the concentration of the $Nd^{3+}$ ions is increased the fluorescence lifetime was found to decrease, due to ion-ion cross relaxation processes between the neodymium ions. The lifetimes varied from 14.7μs (±0.5%) in $(Nd_2O_3)_{0.234}(P_2O_5)_{0.766}$ ($42.92 \times 10^{20}$ $Nd^{3+}$ions $cm^{-3}$) to 331.8μs in $(Nd_2O_3)_{0.001}(La_2O_3)_{0.258}(P_2O_5)_{0.741}$ ($0.21\times 10^{20}$ $Nd^{3+}$ ions $cm^{-3}$). The concentration at which the neodymium fluorescence lifetime falls by a factor of two is $5.810^{20}$ $Nd^{3+}$ions $cm^{-3}$; this represents a better resistance to concentration quenching than that displayed in the majority of glass hosts.

5) Cutback measurements in silica clad ternary neodymium lanthanum metaphosphate glass $(Nd_2O_3)_{0.010}(La_2O_3)_{0.260}(P_2O_5)_{0.730}$ have determined the absorption coefficient $\alpha$ to be $0.029cm^{-1}$ at 633nm. Within experimental error this value appears to be constant through out the fibre.

6) The absorption spectrum in the optical fibre has been measured in three samples with different path lengths. The minimum attenuation recorded in the 60mm fibre is $0.88dBm^{-1}$ at 652.9nm. This is in accord with other fibres manufactured for laser applications.

7) For the silica clad ternary neodymium lanthanum metaphosphate glass the critical angle $\theta_c$ has a value of 69.2°; the numerical aperture NA is 0.55 and $\theta_{max}$ is 33.7°. The V number of the fibre is 192, which corresponds to the fibre propagating 18432 bound modes when light of 528nm passes. The gain coefficient was estimated to be approximatly $0.059cm^{-1}$ at 528nm.

# CHAPTER TWELVE

## CONCLUSIONS

Rare earth metaphosphate glasses are doped with large quantities of lanthanides, $(R_2O_3)_{0.25}(P_2O_5)_{0.75}$, and consequently exhibit a number of fundamentally interesting acoustic, optical, and magnetic properties. The structure and properties of a series of REMGs have been investigated using a variety of techniques. This chapter is a general synopsis of the work and results collected; if more detailed summary is required, the separate conclusion sections 5.3, 7.3, 9.4 and 11.3, which have been divided according to experimental technique, can be consulted.

The short range structure of REMGs has been probed using the powerful combination of x-ray diffraction and EXAFS techniques. These investigations, made with collaborators at the University of Kent at Canterbury, have increased existing structural information (Bowron et al. 1994, 1995, 1996a, 1996b) by significantly extending the range of samples studied. Previous x-ray diffraction measurements investigated the structure of metaphosphate glasses doped with trivalent lanthanum, praseodymium, europium and terbium ions only; the metaphosphate glasses examined in this thesis have been doped with Ce, Nd, Sm, Gd, Dy, Ho, and Er. The glass series exhibited the lanthanide contraction: as the atomic number is increased there is a corresponding decrease in the peak positions of the gaussian fits to the t(r) data assigned as the R-O and R-(O-)P correlations. The nearest neighbour correlation distances were in accord with the glass former comprising of a three-dimensional network of corner linked $PO_4$ tetrahedra. The EXAFS measurements have been made at three different temperatures 293K, 145K, and 79K. The spectra were recorded at several temperatures to investigate whether changes in the structure account for the anomalous thermal, acoustic and optical properties that occur at low temperatures. However no significant change was observed in the short range structure, from 79K

to 293K, within the experimental error associated with the EXAFS method. An interesting variation on this experiment would be the use of EXAFS to examine the structure of REMGs as a function of pressure. It has been seen from the ultrasonics work that the elastic properties of these samples vary significantly with pressure and not always in the same manner, i.e. lanthanum exhibits normal elastic behaviour and samarium displays mode softening. The measured nearest neighbour distances and co-ordination numbers of the rare earth ions are in agreement with previous results; the trivalent rare earth ions, $R^{3+}$, have a similar local environment to that of rare earth ions in the metaphosphate crystals (Hong 1974a and b, Matuszewski et al. 1988), with rare earth ions being co-ordinated to approximately 6 non-bridging oxygens. The occurrence of the lanthanide contraction has been verified using the EXAFS technique. The measured rare earth ion-oxygen distances were in close agreement with those calculated from the tables of ionic radius (Shannon 1976) assuming a co-ordination number of six and a valence of 3+. The R-P correlation distance was determined to be between 3.3 and 3.6 Å, and a second oxygen was found to be situated at approximately 4Å from the rare earth ion. There was no evidence of rare earth-rare earth correlations within the distance (~4Å) examined by the x-ray diffraction and EXAFS probes. Neutron scattering has been employed to investigate these R-R correlations. The potential of a new method, which is based on isotropic substitution but utilises the fact that the scattering length of a paramagnetic ion can be changed by the application of a field, has been investigated. The difference of the no field and applied field spectra should allow for the partial structure factor to be isolated and the correlation distance between two paramagnetic ions to be calculated. The method has been tested on $(Tb_2O_3)_{0.247}(P_2O_5)_{0.753}$; however due to the background runs being of insufficient quality, the first order difference cross section $S_{TbTb}(\mathbf{Q})$ is skewed, and the terbium-terbium correlation length could not be extracted. Nevertheless, this investigation shows that experiments of this type can be used to determine the correlation distance between paramagnetic ions in amorphous materials, and a repeat experiment in the future should allow determination of the distance between dopant ions in REMGs. Subsidiary data on the magnetic moment of terbium metaphosphate glass as a function of applied field has been measured. The data cannot be fitted with a Brillouin function with a fixed J value of 6, and a simple model which incorporates crystal field and Zeeman splitting terms has been produced, thus

evidencing the significance of crystal field splitting in these material. Inelastic magnetic neutron scattering has been used to examine the form of the magnetic contribution to the low energy excitations in metaphosphate glasses doped with Pr, Nd, Tb, Dy, Ho, Er, and Tm. Although all the spectra suffer a degree of broadening due to the variation of the rare earth ion environments throughout the glassy host, a significant degree of structure is still present. The features in the spectra arise from neutron induced electron transitions between the energy levels of the ground state split by the crystal field. The majority of the features can be assigned to crystal field transitions, by comparing these samples to other materials containing the same paramagnetic rare earth ion. A semi-classical crystal field model has been discussed in relation to the measured data.

The elastic and optical properties of rare earth metaphosphate glasses have been investigated. The temperature dependence of the longitudinal and shear mode ultrasonic wave velocities has been determined in ternary samarium lanthanum metaphosphate glasses $(La_2O_3)_x(Sm_2O_3)_y(P_2O_5)_{0.75}$ where $(x+y=0.25)$. The velocities of the ultrasonic waves increased as the temperature was decreased; this trend has been attributed to contributions arising from an anharmonic term at high temperatures, and at lower temperatures interactions between the acoustic phonons with the two-level systems and soft anharmonic localised vibrational modes. The effects of pressure on the ultrasonic wave velocities have been examined to find out how the elastic properties change when samarium replaces lanthanum in three ternary metaphosphate glasses. In lanthanum glass the longitudinal and mean Grüneisen parameters and the longitudinal mode velocity display the normal stiffening response to pressure. In contrast samarium metaphosphate glass exhibits acoustic mode softening with hydrostatic pressure; the acoustic mode Grüneisen parameters of the $Sm^{3+}$ metaphosphate glasses are negative. For ternary REMGs the hydrostatic-pressure derivatives of elastic stiffness and bulk modulus have intermediate values between those determined for the binary REMGs: introduction of $La^{3+}$ counteracts the acoustic-mode softening found in the $Sm^{3+}$ modified glasses. The vibrational anharmonicity of a sample determines both the pressure derivatives of the elastic stiffness and the thermal expansion. By comparing the long wavelength Grüneisen parameters of $(La_2O_3)_{0.222}(P_2O_5)_{0.778}$ and $(Sm_2O_3)_{0.224}(P_2O_5)_{0.776}$ with low temperature

thermal expansion, the effects of the acoustic modes on theses properties can be separated from contributions arising from the higher energy phonon states. The results have been interpreted with in the framework of the soft potential model. It was concluded that the excess modes, due to the topological disorder in these glasses, provide negative contributions to the thermal expansion and the pressure derivative of the elastic moduli. Such excess mode contributions may well be present in the thermal expansion of all glasses. Future work would include a study of the non-linear elastic properties and low temperature thermal expansion of a number of amorphous materials. The optical spectra mainly examine the electric dipole transitions between the ground state and significantly higher energy multiplets; this is in contrast to inelastic magnetic neutron scattering, which investigates the magnetic dipole transitions between the low lying electronic states. The absorption and fluorescence spectra have been measured in a series of metaphosphate glasses doped with Pr, Nd, Sm, Eu, Tb, Dy, Ho and Er. Knowledge of the optical properties of REMGs is essential if these materials are to be used in real device applications. Transitions have been assigned to individual features in the spectra by comparing the data with previously recorded spectra of corresponding lanthanides in variety of glass and crystalline hosts. It was concluded that the rare earth dopants are incorporated into metaphosphate glass as trivalent ions; this is in accord with the EXAFS data. The optical properties of neodymium doped metaphosphate glasses have been investigated further. The lifetime dependence of the $^4F_{3/2} \rightarrow {}^4I_{11/2}$ neodymium transition was examined as a function of $Nd^{3+}$ concentration; neodymium doped metaphosphate glasses were found to exhibit resistance to concentration quenching comparable to, or better than, other amorphous hosts. A silica clad fibre has been pulled from a bulk sample of $(Nd_2O_3)_{0.010}(La_2O_3)_{0.260}(P_2O_5)_{0.730}$. The ternary neodymium lanthanum metaphosphate glass fibre was found to have a diameter of 58.6μm, and a refractive index of n=1.56±0.02; this corresponds to a V number of 192, which means the fibre supports 18432 bound modes when light of 528nm passes. Being able to produce these first optical fibres has improved the potential of creating devices from these glasses. Current work is being undertaken to produce a mono-mode fibre (this fibre requires a diameter of less than 0.74μm), and follow-on experiments such as studying magneto-optical effects, and producing a fibre laser.

# PUBLICATIONS

- Elastic and nonlinear acoustic properties and thermal expansion of rare-earth metaphosphate glasses. Acet M., Brennan T., Cankurtaran M., Saunders G. A., Zähres H., Phil. Mag. B, 77, 6, 1633, (1998).

- An EXAFS study of rare earth phosphate glasses in the vicinity of the metaphosphate composition. Anderson R., Brennan T., Mountjoy G., Newport R.J. Saunders G.A. J. Non-Cryst. Sol. 232-234, 286, (1998).

- An EXAFS study of rare earth (R=La, Ce, Pr, Nd, Sm, Eu, Gd, Tb, Dy, Ho, Er) phosphate glasses near the metaphosphate composition. Anderson R., Brennan T., Mountjoy G., Newport R. J., Saunders G. A., Submitted to J. Mat. Res.

- The fluorescence and absorption spectra of rare earth metaphosphate glasses Brennan T., Knight J. C. Saunders G. A., Submitted to J. Phys. Chem. Glass.

- A rare earth $L_3$-edge EXAFS and $L_1$-edge XANES study of Nd and Ce phosphate glasses near the ultraphosphate composition, Mountjoy G., Cole J. M., Brennan T., Newport R.J. Saunders G.A., Wallidge G. W., In preparation.

# REFERENCES


Acet M., Brennan T., Cankurtaran M., Saunders G. A., Zähres H., Phil. Mag. B, **77**, 6, 1633, (1998).

Adam J. L., Ponçon V., Lucas J., Boulon G., J. Non. Cryst. Sol. **91**, 191, (1987).

Anderson R., Brennan T., J. M. Cole, Mountjoy G., Newport R. J., Saunders G. A., J. Matt. Res (to be published).

Anderson O. L., Bömmel H. E., J. Am. Ceram. Soc. **38**, 4, 125, (1955).

Anderson P. W. , Halperin B. I., Varma C. M., Phil. Mag. **8**, 25, 1, (1971).

Anselm A., Introduction to Semiconductor Theory, Mir Publishers, Moscow, (1982).

Auld B. A., Acoustic Fields and Waves in Solids, Vol. 1 (second edition), Robert E. Krieger Publishing Company Inc., Florida, (1990).

Auzel F. E., Proc. IEEE, **61**, 6, 758, (1973).

Balcar E., Lovesey S. W., Theory of Magnetic Neutron and Photon Scattering, Clarendon Press, Oxford, (1989).

Banavar J. R., Phillips J. C., Phys. Rev. B. **28**, 8, 4716, (1983).

Banwell C. N., McCash E. M., Fundamentals in Molecular Spectroscopy, fourth ed., McGraw Hill Interantional Ltd., London, (1994).

Barron T. H. K., Phil. Mag., Ser. **7**, 46, 720, (1955).

Barron T. H. K., Collins J. G., White G. K. , Advances in Phys. **29**, 4, 609, (1980).

Bateman T. B., J. Acous. Soc. Am., **41**, 4, 2, 1011, (1967)

Bell R.J., Dean P., Philo. Mag. **25**, 1381, (1972).

Beltzer A. I., Acoustics of Solids, Springer-Verlag, Berlin, (1988).

Bethe H. A., Annln. Phys. **3**, 133, (1929).

Betts R. A., Rühl F. F., Kwok T. M., Zheng G. F., Int. J. Optpelec. **6**, 1/2, 47, (1991).

Birgeneau R. J., J. Phys. Chem. Sol. **33**, 56, (1972).

Bleany B., Proc. Roy. Soc. **A276**, 19, (1963).

Bowron D. T., A Study of Rare Earth Doped Silicate and Phosphate Glasses PhD.Thesis, University of Kent at Cantenbury (1994).

Bowron D. T., Newport R. J., Rainford B. D., Saunders G. A., Senin H. B., Phys. Rev. B. **51**, 9, 5739, (1995).

Bowron D. T., Saunders G. A., Newport R. J. , Rainford B. D., Senin H. B., Phys. Rev. B. **53**, 9, 5268, (1996a).

Bowron D. T., Bushnell-wye G., Newport R. J., Rainford B. D., Saunders G. A., J. Phys. Condens. Matt. **8**, 3337, (1996b).

Bradbury M. I., Newman D. J. , Chem. Phys. Lett. **1**, 44, (1967).

Brecher C. J., Chem. Phys. **61**, 6, 2297, (1974).

Bridge B., Patel N. D., J. Mat. Sci. **22**, 781, (1987).

Brodin A., Fontana A., Börjesson L., Carini G. , Torell C. M. , Phys. Rev. Lett. **73**, 15, 2067, (1994).

Brow R. K., Kirkpatrick R. J. Turner G. L. J. Non Cryst. Sol. **116**, 39, (1990).

Brow R. K. , J. Am. Ceram. Soc. **76**, 4, 913, (1993).

Brown J. P., International Tables for Crystallography, **Vol. C**, (1988).

Brugger K. , Phys. Rev. **133**, 6A, A1611, (1964).

Brugger K., Fritz T. C., Phys. Rev. **157**, 3, 524, (1967).

Bruni S., Cariti F., Corrias A., Gatskell P. H., Lai A., Musinu A., Piccaluga G. J.,Phys. Chem. **99**, 41, 15229, (1995).

Buchenau U., Prager M., Nucker N., Dianoux A. J., Ahmed N. , Phillips W. A., Phys. Rev. B. **34**, 8, 5665, (1986).

Buchenau U. , Zhou H. M., Nucker N., Gilroy K. S., Phillips W. A., Phys. Rev. Lett. **60**, 13, 1318, (1988).

Buchenau U., Galperin Yu. M., Gurevich V. L., Phys. Rev. B. **43**, 6, 5039, (1991).

Buchenau U. , Galperin Yu. M., Gurevich V. L., Parshin D. A., Ramos M. A. , Schober H. R., Phys. Rev. B. **46**, 5, 2798, (1992).

Bushnell-Wye G., Finney J. L., Turner J., Huxley D. W., Dore J. C., Rev. Sci. Instrum., **61**, 1, 1153, (1992).

Carini G., Cutroni M. , Fredrico M., Tripodo G., Phys Rev. B, **37**, 12, 7021, (1988)

Carini G., Cutroni M. , D'Angelo G., Fredrico M., Galli G., Tripodo G., Saunders G. A., Wang Q., J. Non. Cryst. Sol. **121**, 288, (1990).

Carini G., D'Angelo G., Fredrico M., Tripodo G., Saunders G. A., Senin H. B., Phys. Rev. B. **50**, 5, 2858, (1994).

Carini G., D'Angelo G., Tripodo G., Fontana A., Leonardi A., Saunders G. A., Brodin A., Phys. Rev. B. **52**, 13, 9342, (1995a).

Carini G., D'Angelo G., Tripodo G., Saunders G. A., Phil. Mag. B. **71**, 4, 539, (1995b).

Carini G., D'Angelo G., Tripodo G., Fontana A., Rossi F., Saunders G. A., Europhys. Lett. **40**, 4, 435, (1997).

Carini G., D'Angelo G., Tripodo G., Bartolotta A., Fontana A., Rossi F., Saunders G. A., Phil. Mag. B., **77**, 2, 449, (1998).

Carini G., D'Angelo G., Tripodo G., Fontana A., Rossi F., Saunders G. A., (to be published)

Carnall W.T., Fields P.R., Rajnak K., J. Chem. Phys. **49**, 10, 4424, (1968).

Caspers H. H., Rast H. E., Fry J. L., J. Chem. Phys. **53**, 8, 3208, (1970).

Cervinka L., Bergerová J., Trojan M, J. Non-Cryst. Sol. **192&193**, 121, (1995).

Chaboy J., Tyson T. A. Phys. Rev. B. **49**, 9, (1994).

Ching, W. Y., Phys. Rev. B. **26**, 12, 6610, (1982).

Cormier G., Capobianco J. A., Morrison C. A., Monteil A., Phys. Rev. B. **48**, 22, 16290, (1993).

Cronin D. J., Blackburn D. H., Haller W. K., Nature **295**, 680, (1982).

Crozier E. D., Nuc. Instr. Meth. Phys. Res. B, **133**, 134, (1997).

Cusack N. E., The Physics of Structurally Disordered Matter, An Introduction, Adam Hilger, Bristol, (1987).

DeShazer L. G., Dieke G. H., J. Chem. Phys. **38**, 9, 2190, (1963).

Deutschbein O. K., Pautrat C. C., IEEE J. Quant. Elec. **QE-4**, 48, (1968).

Dieke G. H., Sarup R., J. Chem. Phys. **29**, 4, 741, (1958).

Durville F. M., Behrens E. G., Powell R. C. , Phys. Rev. B. **34**, 6, 4213, (1986).

Ebendorff-Heidepriem H., Ehrt D., J. Non. Cryst. Sol. **208**, 205, (1996).

Eberhhart J.P., Structure and Chemical Analysis of Material, John Wiley and Sons, Chichester, (1991).

Eccleston R. S., Osborn R., Kitchener B. G. B., The HET mini-manual, RAL report (1998).

Elliott S. R., Physics of Amorphous Materials, Second Edition, Longman Scientific and Technical, Essex, (1990).

Elliott S. R., Nature (Review Article) **354**, 445 (1991).

Fanggao C., Dielectric and Ultrasonic studies of Polethylene Plaques and Cable Insulators, PhD.Thesis, University of Bath, (1996).

Farok H. M., Saunders G. A., Poon W.. Vass H.. J. Non. Cryst. Sol. **142**, 175, (1992).

Farok H. M., Senin H. B., Saunders G. A., Poon W., Vass H., J. Mat. Sci. **29**, 2487, (1994).

Farok H. M., Saunders G. A., Lambson W. A., Kruger R., Senin H. B., Bartlet S., Takel S., Phys. Chem. Glasses **37**, 3, 125, (1996).

Farok H. M., Flourescence and Raman Spectra of Rare Earth Phosphate Glasses and Crystals, PhD Thesis, University of Bath, (1997).

Farok H. M., Saunders G. A., Poon W., Crain J., Vass H. , Honle W., Schönherr E., To Be Published.

Fert A., Campbell I. A., J. Phys. F: Metal Phys. **8**, 3, L57, (1978).

Fontana A., Carini G., Brodin A., Torell C. M., Börjesson L., Saunders G. A., Phil. Mag. B. **71**, 4, 525, (1995).

Ford P. J., Graham Jr. C. D., Saunders G, A. , Senin H. B. , Cooper J. R., J. Mat. Sci. Lett. **13**, 697, (1994).

Fowles G. R., Introduction to Modern Optics (Second Edition), Dover Publications, New York (1974).

French V. A., Powell R. C., J. Appl. Phys. **69**, 2, 913, (1991).

Fulde Lowenhaupt Adv. Phys. **34**, 86, (1985).

Ed. Furrer A., Magnetic Neutron Scattering, World Scientific Publishing Co. London, (1995).

Galeener F. L., Mikkelsen Jr. J. C. Sol. Stat. Comm. **30**, 505, (1979).

Galeener F. L., Wright A. C. Sol. Stat. Comm. **57**, 8, 677, (1986).

Gaskell, P. H., Tarrant I. D. Philo. Mag. B. **42**, 2, 265, (1980).

Gladden L. F., J. Non Cryst. Sol. **119**, 318, (1990).

Goudemond I.P., Keartland J. M., Hoch M. J. R., Senin H. B., Saunders G. A., Extended Abstracts of the XXII th Congress Ampere, Kanzan Vol 2 Aug (1994).

Goudemond I. P., Keartland J. M., Hoch M. J. R., Saunders G. A., Phys. Rev. B, 56, **14**, 56, (1997).

Greaves G. N., J. Non. Cryst. Sol., **71**, 203, (1985).

Greaves G. N., Gurman S. J., Gladdens L. F., Spence C. A., Cox P. Sales B. C. Boatner L. A., Jenkins R. N. Philo. Mag. B. **58**, 3, 271, (1988).

Greaves G. N., Phil. Mag. B., **60**, 6, 793, (1989).

Gruber J., J. Chem. Phys. **38**, 4, 946, (1963).

Guillot B., Guissani Y., Phys. Rev. Lett. **78**, 12, 2401, (1997).

Gurman S. J., Binstead N., Ross I., J. Phys. C: Sol. Stat. Phys. **17**, 143, (1984).

Gurman S. J., Binstead N., Ross I., J. Phys. C: Sol. Stat. Phys. **19**, 1845, (1986).

Hall D. W., Weber M. J., Handbook of Laser Science and Technology, Supplement 1: Lasers, CRC Press, Boca Raton, **137**, (1991).

Harani R., Hogarth C. A., Ahmed M. M., Morris D. F. C., J. Mat. Sci. lett. **3**, 843, (1984).

Harris R., Plischke M., Zuckermann M. J., J. Phys. F: Metal Phys. **5**, 763, (1972).

Hayes T. M, Boyce J. B., Sol. Stat. Phys. **37**, 173, (1982).

Hecht E., Optics, (Second Edition), Addison-Wesley Pub. Com., Wokingham, (1987).

Hong H. Y-P., Acta. Cryst. **B30**, 468, (1974a).

Hong H. Y-P., Acta. Cryst. **B30**, 1857, (1974b).

Hook J. R., Hall H. E., Solid State Physics (Second Edition), John Wiley & Sons, Chichester, (1994).

Hoppe U., Walter G., Kranold R., Stachel D., Barz A., J. Non Cryst. Sol. **192/193**, 28, (1995a).

Hoppe U., Walter G., Stachel D., Hannon A. C., J. Phys. Sci. **50**, 7, 684, (1995b).

Hoppe U. J. Non. Crys. Sol. 195, 138, (1996).

Hoppe U., Walter G., Barz A., Stachel D., Hannon A. C., J Phys.: Condens. Matter, **10**, 261, (1998a)

Hoppe U., Kranold R., Stachel D., Barz A., Hannon A., J. Non. Cryst. Sol., **232-234**, 44, (1998b).

Hosemann R., Hentschel M. P., Schneisser U., Bruchner R., J. Non. Cryst. Sol. **83**, 223, (1986).

Hsieh Y. Y., Blume M., Phys. Rev. B. **6**, 7, 2684, (1972).

Hutchings M.T., (Ed. Seitz F., Turnbull D. Academic New York). Sol. Stat. Phys. **16**, 227, (1964)

Ilisavskii Yu. V., Kulakova L. A., Tikhonov V. V., Sov. Phys. Sol. Stat. **31**, 8, 1363, (1989).

Jeffrey A., Mathematics for Engineers and Scientists, Van Nostrand Reinhold Co. Ltd., Berkshire (1985)

Jiang S., Jiang Y., Glastech. Ber. **64**, 291, (1991).

Jiles D., Introduction to Magnetism and Magnetic Materials, Chapman and Hall, London, (1995).

Jagannathan A., Orbach R., Phys. Rev. B, **41**, 5, 3153, (1990).

Joyner R. W., Martin K. J., Meehan P., J. Phys. C: Sol. Stat. Phys., **20**, 4005, (1987).

Judd B. R., Phys. Rev. **127**, 750, (1962).

Kalisky Y., Kagan J., Sagie D., Brenier A., Pedrini C., Boulon G., J. Appl. Phys., **70**, 8, 409, (1991).

Kaneyoshi T. Amorphous Magnetism, CRC press, Florida, (1984).

Kang Sun , Risen Jr. W. M., Sol. Stat. Comm. **60**, 9, 697, (1986).

Karpov V. G., Klinger M., Ignat'ev F. N., Sov. Phys. JEPT **57**, 2, 439, (1983).

Keartland J. M., Goudemond I.P., Hoch M. J. R., Senin H. B., Ford P. J., Saunders G. A., Phisica B. **397**, 194, (1994).

Kelly F. M., MacDonald D. K. C., Canad. J. Phys. **32**, 147, (1953).

Kishida S., Washio K., Yoshikawa S., Kato Y., Appl., Phys., Let., **34**, 4, 273, (1979).

Kittel C., Kroemer H., Thermal Physics (Second Edition), W. H. Freeman and Company, New York (1980).

Kittel C., Solid State Physics (Sixth Edition), John Wiley and Sons Ltd., Canada, (1986).

Kittinger E. Ultrasonics, **15**, 30, (1977).

Knopp G., Knorr K., Wehr H., Murani A. P., J. Mag. and Mag. Mat. **52**, 326, (1985).

Kozlovsky W. J., Fan T., Y., Byer R. L., Opt. Lett., **11**, 12, 788 (1986).

Lakkad S. C. , J. Apl. Phy. **42**, 11, 4277, (1971).

Lakshman S. V. J., Ratnakaram Y. C., J. Non. Cryst. Sol. **101**, 75, (1988).

Layne C. B., Lowdermilk W. H., Weber M. J., Phys. Rev. B., **16**, 1, 10, (1977).

Lea K. R., Leask. M. J. M., Wolf W. P., J. Phys. Chem. Sol. **23**, 1381, (1962).

Lesniak K., J. Phys.: Condens. Matt., **2**, 5563, (1990).

Loong C. K., Soderholm L., Hammonds J. P., Abraham M. M. Boatner L. A. Edelstein N. M. J. Appl. Phys. **73**, 10, 6069, (1993a).

Loong C. K., Soderholm L., Hammonds J. P., Abraham M. M. Boatner L. A. Edelstein N. M., J. Phys: Condens. Mat. **5**, 5121, (1993b).

Loong C. K., Soderholm L., Goodman G. L., Abraham M. M. Boatner L. A., Phys. Rev. B, **48**, 9, 6124, (1993c).

Lorenzo A., Bausá L. E., Sanz Garcia J. A., Garcia Solé J., J. Phys.:Condens. Matt., **8**, 5781, (1996).

Lovesey S.W., Theory of Neutron Scattering from Condensed Matter Vol. 1 and 2 (1987).

Loewenhaupt M., Prager M., Zeitschrift Fur Physik B, **62**, 195, (1986).

Lu Y.-L., Lu Y.-Q., Ming N.-B., Appl. Phys. B, **62**, 287, (1996).

Mandl F. Statistical Physics, 2nd ed., John Wiley and Sons, Chichester, (1991).

Marion J. E., Weber M. J., Eur. J. Sol. Stat. Inorg. Chem. **28**, 271, (1991).

Mason W. P., Physical Properties and the Properties of Solids, D Van Nostrand Company Inc., Princeton, (1958).

Marcuse D., Principles of Optical Fibre Measurements, Academic Press, London (1981).

Martin S. W., J. Sol. Stat. Chem. (Review Article) **28**, 163, (1991).

Matsubara E., Waseda Y., Ashizuka M., Ishida E., J. Non. Cryst. Sol. **103**, 117, (1988).

Matuszewski J., Kropiwnicka J., Znamierowska T., J. Sol. State Chem. **75**, 285, (1988).

May J. E., IRE Natl. Conv. Record, **6**, 134, (1958).

Mierzejewski A., Saunders G. A., Sidek H. A. A., Bridge B., J. Non. Cryst. Sol. **104**, 323, (1988a).

Mierzejewski A., Saunders G. A., Sidek H. A. A., Hampton R. N., Al-Mummar I. J., Sol. Stat. Ionics, **28-30**, 778, (1988b).

Miniscalco W. J., J. Lightwave Tech. **9**, 234, (1991).

Miura K., Tanaka K, Hirao K., J. Non Cryst., Sol., **213**, 276, (1997).

Moeller T., Brantley J. C., Analy. Chem. **22**, 3, 433, (1950).

Moeller T., The Chemistry of the Lanthanides, Pergasmon Press, Oxford, (1973).

Murdoch K. M., Cockroft N. J., Phys Rev. B, **54**, 7, 4589, (1996).

Musinu A., Piccaluga G. , Pinna G., Narducci D., Pizzini S., J. Non Cryst. Sol. **111**, 221, (1989).

Musinu A., Piccaluga G., J. Non. Cryst. Sol. **192/193**, 32, (1995).

Nagli L., Bunimovich D., Katzir A., Gorodetsky O., Molev V., J. Non. Cryst. Sol. **217**, 208, (1997).

Newman D. J., Stedman G. E. J. Phys. Chem. Sol. **32**, 535, (1971).

Newman D. J., Betty Ng, (Review Article) Rep. Prog. Phys. **52**, 699, (1989).

Newman D. J. Private Communication (1995).

Ofelt G. S., J. Chem. Phys, **37**, 511, (1962).

Papadakis E. P., J. Appl. Phys. **35**, 5, 1474, (1964).

Papadakis E. P., J. Acous. Soc. Am. **42**, 5, 1045, (1967).

Parshin D. A., Phys. Rev. B. **49**, 14, 9400, (1994).

Payne S. A., Marshall C. D., Bayramian A., Wilke G. D., Hayden J. S., Appl. Phys. B, **61**, 257, (1995).

Phillips J. C., (Review Article) Sol. Stat Phys. **37**, 93, (1982).

Phillips J. C., J. Non Cryst. Sol. **63**, 347, (1984).

Phillips W. A., J. Low Temp. Phys. **7**, 3/4, 351, (1972).

Phillips W. A (Ed.), Topics in Current Physics; Amorphous Solids, Low Temperature Properties, Springer-Verlag, Berlin, (1981).

Pollard H. F., Sound Waves in Solids, Pion Ltd., London, (1977).

Pringshiem P., Vogel M., Luminescence of Liquids and Solids and its Practical Applications, Interscience Publisher Ltd., N. Y., (1943).

Qi C,. Zhang X., Jaing Y., Jaing Y., Chinese Phys. **12**, 2, 345, (1992).

Rapp C. F., Handbook of Laser Science and Technology, Vol V: Optical Mat., CRC Press, Boca Raton, (1987).

Reisfeld R., J. of Res. Nat. Bur. Stand. **76A**, 6, 613, (1972).

Reisfeld R., Boehm L., J. Sol. Stat. Chem., **4**, 417, (1972).

Reisfeld R., Greenberg E., Biron E., J. Sol. Stat. Chem. **9**, 224, (1974).

Reisfeld R., Eckstein Y., J. Chem. Phys., **63**, 9, 4001, (1975).

Remilieux A., Jacquier B., Linarès C., Lesergent C., Artigaud S., Bayaerd L., Hamon L., Beylat J. L., J. Phys. D: Appl. Phys. **26**, 963, (1996).

Sales B. C., J. Non Cryst. Sol. **119**, 136, (1990).

Sato Y., Anderson O. L., J. Phys. Chem. Sol., **41**, 401, (1980).

Saunders G. A., Carini G., Conf. Proc., Alti Accademia Peloritana dei Percolanli (1994).

Savoini B., Muñoz Santiuste J. E., Gonzáles R., Phys. Rev. B., **56**, 10, 5856, (1997).

Sayer E. V., Sancier K. M., Freed S., J. Chem. Phys. **23**, 11, 2060, (1955).

Schweizer T., Hewak D. W., Samson B. N., Payne D. N., Opt. Lett. **21**, 19. 1594, (1996).

Seltzer M. D., Wright A. O., Morrison C. A., Wortman D. E., Gruber J. B., Filer E. D., J. Phys. Chem. Sol. **57**, 9, 1175, (1996).

Senin H. B., Ford P. J., Saunders G. A., Sidek H. A. A., 21st Century Phys., Nat. Phys. Conf., Two Decades of UPM., Malaysia, (1993a).

Senin H. B., Wang Q., Saunders G. A., Lambson E. F., J. Non. Cryst. Sol. **152**, 83, (1993b).

Senin H. B., The Elastic and Nonlinear Acoustic Vibrational Properties of Vitreous $SiO_2$ and Rare Earth Phosphate Glass PhD. Thesis, University of Bath (1994).

Senin H. B., Saunders G. A., Li J., Ford P. G., Phys. Chem. Glasses, **35**, 3, 109, (1994a).

Senin H. B., Saunders G. A., Jiaqiang Li, Ford P. J., J. Mat. Sci. **29**, 562, (1994b).

Shannon R. D., Acta Cryst., **A32**, 751. (1976).

Sidek H. A. A., Senin H. B., Saunders G. A., Hampton R. N., Draper R. C. J., Bridge B., Phil. Mag. Lett. **57**, 1, 49, (1988).

Sidek H. A. A., An Ultrasonic Study of the Elastic Properties and Acoustic Mode Vibrational Anharmonicity in Glasses and Crystals, PhD. Thesis, University of Bath (1989)

Sidek H. A. A., Senin H. B., Saunders G. A., Ball D., Cankurtaran M., Federico M., Phys. Chem. Glasses, **39**, 1, 17, (1998)

Smith R. I., Hull S., User Guide for the Polaris Diffractometer at ISIS, Tech. Rep. (1997).

Snyder A. W., Love J. D., Optical Waveguide Theory, Chapman and Hall, London, (1996).

Soderholm L., Loong C.-K., Goodman G. L., Dabrowski B. D., Phys. Rev. B., 43, **10**, 7923, (1991).

Soper A. K. , Howells W. S., Hannon A. C., ATLAS: Analysis of Time of Flight Diffraction Data from Liquid and Amorphous Materials Rutherford Appleton Laboratory Report (1989).

Squires G.L. , Introduction to the Theory of Thermal Neutron Scattering, Cambridge University Press, Cambridge, (1978).

Stevens K. W. H. , Proc. Phys. Soc. Lon. **A65**, 209, (1952).

Stedman G. E., Newman D. J. , J. Phys. Chem. Sol. 32, 109, (1971).

Sugar J., J. Op. Soc. Am. **55**, 9, 1058, (1965).

Surovtsev N. V., Novikov V. N., Duval E., J. Phys.: Condens. Mat. 10, L113, (1998).

Svelto O., (Translated by Hanna D. C.), Principles of Laser, third ed., Plenum Press, New York, (1989).

Tachihante M., Zambon D., Arbus A., Zahir M., Sadel A., Cousseins J. C., Mat. Res. Bull., **28**, 605, (1993).

Tanabe S., Hanada T., Watanabe M., Hayashi T., Soga N., J. Am. Ceram. Soc., **78**, 11, 2917, (1995).

Tielbürger D., Merz R., Ehrenfels R., Hunklinger S., Phys. Rev. B, **45**, 6, 2750, (1992).

Thomas K. S., Singh S., Dieke G. H., J. Chem. Phys., **38**, 9, 2180, (1963).

Thurston R. N., Brugger K., Phys. Rev., **133**, 6A, A1604, (1964).

Thrurston R. N., Proc. IEEE, **53**, 10, 1320, (1965).

Torantani H., Izumitani T., Kuroda H., J. Non Cryst. Sol. **53**, 303, (1982).

Truell R., Elbaum C., Chick B. B. , Ultrasonic Methods in Solid State Physics, Academic Press, London, (1969).

Turberfield K. C., Passell L., Birgeneau R. J. , Bucher E., Phys. Rev. Lett. **25**, 11, 752, (1970).

Turberfield K. C., Passell L., Birgeneau R. J. , Bucher E. J., Appl. Phys. **42**, 4, 1746, (1971).

Urquart P., IEE Proceedings Pt. J. **135**, 6, 385, (1988).

Van Deun R., Binnemans K., Görller-Walrand C., Adam J. L., J. Phys.:Condens. Matt. **10**, 7231, (1998).

Van Hove L., Phys. Rev., **95**, 1, 249, (1954).

Van Vleck J. H., The Theory of Electric and Magnetic Susceptibilities, Oxford University Press, London, (1965).

Van Wazer J. R., Phosphorus and it's Compounds Vol.1 Intersciense Publishers Inc. New York (1959).

Varshni Y. P., Phys. Rev. B. **2**, 10, 3953, (1970).

Wang J., Brocklesby W. S., Lincoln J. R., Townsend J. E., Payne D. N., J. Non Cryst. Sol., **163**, 261, (1993)

Wang Q., Saunders G. A., Lambson E. F., Bayot V., Michenaud J.-P. J. Non. Cryst. Sol., **125**, 287, (1990).

Wang Q., Nonlinear Elastic Properties and Vibrational Anharmonicity of Very High Purity Quartz, PhD Thesis, University of Bath, (1993).

Warren B. E., Biscoe J., J. Am. Ceram. Soc. **21**, 259, (1939).

Warren B. E., Marvel G., Rev. Sci. Instrum., **36**, 2, 196, (1965)

Warren B. E., X-Ray Diffraction Addison-Wesley Publishing Company Inc. (1969).

Weber M. J., Saroyan R. A., Ropp R. C., J. Non. Cryst. Sol. **44**, 137, (1981).

Weber M. J., J. Non. Cryst. Sol. **123**, 208, (1990).

Willis B. T., Thermal Neutron Diffraction, Oxford University Press, Oxford, (1970).

Wilson J., Hawkes J., Optoelectronics, an Introduction, 3rd Edition, Prentice Hall Europe, London, (1998).

Windsor C.G., Pulsed Neutron Scattering, Taylor and Francis Ltd., London, (1981).

Wright A. C., Hulme R. A., Grimley D. I., Sinclair R. N., Martin S. W., Price D. L., Galeener F. L., J. Non-Cryst. Sol., **129**, 213, (1991).

Yan Y., Faber A. J., de Waal H, J. Non Cryst. Sol., **181**, 283, (1995)

Yeung Y. Y., Newman D. J., J. Chem Phys. **82**, 8, 3747, (1985a).

Yeung Y. Y. , Newman D. J., J. Chem Phys. **83**, 9, 4691, (1985b).

Zachariasen W. H., J. Am. Chem. Soc. **54**, 3841, (1932).

Zeller R. C., Pohl R. O., Phys. Rev. B. **4**, 6, 2029, (1971).

Zheng H-X ., Wu G-Z., Gan F., Chinese Phys. **6**, 4, 828, (1986).